Recombination Models for Defects in Silicon Solar Cells

Von der Fakultät für Mathematik und Physik
der Gottfried Wilhelm Leibniz Universität Hannover
zur Erlangung des Grades

Doktorin der Naturwissenschaften
- Dr. rer. nat. -

genehmigte Dissertation

von
Dipl.-Phys. Silke Steingrube
geb. Dreißigacker
geboren am 08.08.1982 in Hannover

2011

Referent: Prof. Dr. R. Brendel
Korreferent: PD Dr. C. Tegenkamp
Tag der Promotion: 06.07.2011

Kurzfassung

Rekombination von Ladungsträgern über Defekte ist ein wesentlicher Verlustmechanismus in Solarzellen. In dieser Arbeit werden Rekombinationsmodelle für drei Typen von Defekten in Solarzellen aus kristallinem Silizium (c-Si) entwickelt und analysiert. Zunächst wird ein Modell zur Beschreibung der Injektionsabhängigkeit der effektiven Oberflächenrekombinationsgeschwindigkeit S_{eff} von SiN_x- und $\mathrm{Al_2O_3}$-passivierten c-Si-Oberflächen entwickelt. Dieses beruht auf einer geschädigten Zone nahe der Siliziumoberfläche. Es wird eine geeignete Parametrisierung erarbeitet, welche die gemessene effektive Oberflächenrekombinationsgeschwindigkeit S_{eff} an den untersuchten Grenzflächen bei allen relevanten Injektions- und Dotierdichten reproduzieren kann. Mit Hilfe dieses Modells werden mögliche mikroskopische Ursachen für die Schädigung erörtert.
Anschließend wird die Grenzfläche zwischen amorphem und kristallinem Silizium behandelt. Es wird ein Shockley-Read-Hall (SRH) Modell zur näherungsweisen Beschreibung der amphoteren Eigenschaften der Grenzflächendefekte vorgestellt. Im Gegensatz zum exakten Modell kann das approximative Modell in geschlossener Form gelöst werden und ist daher leicht in Bauteil-Simulatoren integrierbar. Es werden Fehlergrenzen dieses approximativen Modells abgeleitet, um seine Anwendbarkeit abzuschätzen. Für typische Injektionsdichten an Grenzflächen ist der Fehler des SRH-Modells gering, wenn die Korrelationsenergie der donor- und akzeptorartigen Defektverteilung positiv ist und die Eigenschaften geladener Defekte durch asymmetrische Einfangquerschnitte für Elektronen und Löcher beschrieben werden. Zudem muss die Defektverteilung zwischen den Quasi-Fermi-Niveaus für Traps liegen. In Niedriginjektion, wie bei der Anwendung auf den pn-Übergang einer Solarzelle oder bei geringen Beleuchtungsstärken, kann es jedoch zu großen Abweichungen kommen.
Weiterhin werden ohne Beleuchtung gemessene Strom-Spannungs-Charakteristiken (I-V-Kurven) von c-Si-Solarzellen mit Dioden-Idealitätsfaktoren $n_{\mathrm{D}} > 2$ in Vorwärtsrichtung, d.h. mit Spannungsbereichen in denen der Strom subexponentiell ansteigt, analysiert. Solche „geshunteten" I-V-Kurven werden bei fast allen Solarzellen beobachtet, jedoch kann ihre Ursache bislang nicht zufriedenstellend erklärt werden. Motiviert durch ortsaufgelöste Messungen, werden diese I-V-Kurven durch Rekombinationsströme in stark geschädigten Bereichen des pn-Übergangs modelliert. Die hohe Defektdichte erfordert ein Konzept, welches die Kopplung zwischen Defekten berücksichtigt, d.h. über die SRH-Annahmen hinausgeht. Der hier gemachte Ansatz erklärt sowohl den Grenzfall der SRH-Rekombination für nicht gekoppelte Defekt-Energieniveaus bei geringen Defektdichten ($n_{\mathrm{D}} \leq 2$) als auch den Fall $n_{\mathrm{D}} > 2$ für gekoppelte Niveaus bei hohen Defektdichten. Möglicherweise erstmalig können somit die I-V-Kennlinnien geshunteter Zellen, in Abhängigkeit von der Stärke der Schädigung, sowohl in Durchlass- als auch in Sperrichtung reproduziert werden.
Abschließend werden die entwickelten Modelle für Grenzflächendefekte mittels SENTAURUS-DEVICE-Simulationen auf verschiedene Solarzellen angewendet. So wird die Eignung dieser Modelle für Bauteil-Simulatoren demonstriert und die Auswirkungen der untersuchten Defekte auf die I-V-Kurven analysiert.

Schlagworte: Solarzellsimulationen, Defekte, Rekombination

Abstract

Recombination of charge carriers via defects is a substantial loss mechanism in solar cells. In this work, recombination models for three defect types in crystalline silicon (c-Si) solar cells are developed and analyzed.

First, a model is developed to describe the injection dependence of the effective surface recombination velocity S_{eff} of both SiN_x and Al_2O_3 passivated c-Si surfaces. This model relies on a damaged layer in the silicon close to the interface. A suitable parametrization is given that allows to reproduce the measured effective surface recombination velocity S_{eff} of the investigated interfaces for all relevant injection densities and dopant densities. With the help of this model, we discuss possible reasons for the damage on a microscopic scale.

Second, the interface between amorphous and crystalline silicon is investigated. A Shockley-Read-Hall (SRH) model is suggested to approximate the amphoteric properties of the defects at the interface. In contrast to the exact model, the approximate model has a closed-form-solution and is therefore easily integrated into device simulators. Physically motivated error bounds are derived which can help to decide in which cases the simplified model may be applied. For typical injection densities at interfaces, the error of the SRH model is small if the correlation energy of the donor- and acceptor-like defect distribution is positive and if the properties of charged defects are described by asymmetric capture cross sections for electrons and holes. In addition, the defect distribution must lie in between the quasi-Fermi levels for traps. In low-injection, e.g. when applied to the p-n junction of a solar cell or at low illumination levels, it may fail dramatically.

Further, dark current-voltage curves (I-V curves) of c-Si solar cells having diode-ideality factors $n_{\text{D}} > 2$ in forward direction, i.e. increase sub-exponentially in certain voltage ranges, are analyzed. These "shunted" I-V curves are observed for most solar cells, but the reason for their behavior cannot be explained satisfactorily up to date. Motivated by spatially resolved measurements, these shunts are modeled by recombination currents in highly defective, localized regions of the p-n junction. The high defect density in these regions requires a concept that takes the coupling between defect levels into account, and thus, goes beyond the assumptions made in the SRH theory. The approach made here explains both the SRH-limit for decoupled levels at low defect densities ($n_{\text{D}} \leq 2$), and the case $n_{\text{D}} > 2$ for coupled defects at high defect densities. This allows, possibly for the first time, to reproduce the I-V curves of cells with nonlinear shunts in dependence of the severeness of the disturbance, for both forward and reverse bias.

Finally, the developed models for interface defects are applied to various solar cells by means of SENTAURUS-DEVICE simulations. Thereby, we demonstrate the suitability of these models for device simulators and analyze the influence of the investigated defects on the I-V characteristics.

Key words: solar cell simulations, defects, recombination

Contents

Chapter 1

Introduction

Solar cell development is most efficient if experiment and simulation are combined. To make simulations reliable, accurate and physically motivated models are required. These models not only need to accurately reproduce experimental data, they rather need to be simple enough such that they can be solved in a device-simulator within reasonable computation time. Hence, models that are derived from microscopic observations or quantum-mechanical relations, often need to be parametrized in a suitable way by comparison with experimental data.

Recombination via defects is an efficient recombination mechanism in device-grade silicon. Already in 1952, the Shockley-Read-Hall (SRH) statistics for recombination via an isolated defect in a semiconductor bandgap was derived [Hal52, Sho52]. Although this model describes the recombination properties of many defects well, there exist defect types, for example coupled defects, which need to be described by an extension of the original SRH statistics [Sch95]. Others, e.g. correlated defects, require different models [Vai86].

1.1 Purpose of this work

Often defects are detrimental to solar cell performance, but their recombination mechanisms cannot be described with the commonly used models. This work addresses this problem by developing physically motivated models for three particular defects types. These models must be parametrized by means of physically meaningful parameters to yield reliable results and to be suitable for device simulations. Further, we suggest an approximate model for a computationally intensive recombination statistics and investigate the parameter range in which this approximation is valid.

In particular for high-efficiency cells made on high-quality crystalline silicon (c-Si) material, recombination at the cell surfaces may limit the cell efficiency.

Recombination-active surface defects are for example non-saturated dangling bonds (DBs) which result from the disturbance of the crystal symmetry. Also, process related extrinsic surface defects may occur, for instance due to dislocations or chemical residues and metallic depositions on the surface [Abe00]. Essentially three quantities influence the surface recombination rate considerably: (i) the density of defects at the surface in combination with (ii) their cross sections for electron or hole capture, and (iii) the concentrations of electrons and holes at the surface, because each electron needs a hole to recombine, and vice versa. These quantities can be addressed to develop techniques to *electrically passivate* these defects, i.e. to make them recombination-inactive. Today's research focuses in particular on low-temperature passivation techniques for two main reasons [e.g. Abe00]. On the one hand, low-temperature processes are more energy-efficient and may also be more cost-efficient compared to their high-temperature counterparts. On the other hand, high-temperature passivation techniques are restricted to float-zone (FZ) and Czochralski (Cz) material due to the high sensitivity of the charge carrier lifetime in multicrystalline silicon against thermal treatment at high temperatures [Mac00, Sch04b, Sto98]. A widely-used low-temperature technique is the plasma enhanced chemical vapor deposition (PECVD) of amorphous silicon nitride (SiN_x) layers at temperatures between 350 °C and 400 °C [Abe97]. SiN_x layers address both issues (i) and (iii). The high density of atomic hydrogen released into the silicon during fabrication [Kot95] accounts for the passivation of DBs. The high density of positive fixed charges at the SiN_x/c-Si interface causes holes to be repelled from the interface. SiN_x gives excellent passivation properties comparable to e.g. alnealed (aluminum anneal) SiO_2 on highly doped crystalline p-type silicon (p-Si) surfaces [Lau96, Sch04a]. However, the presence of these fixed charges has major drawbacks. On the one hand, it was shown that SiN_x passivation is not applicable to the rear of p-Si Passivated Emitter and Rear Cells (PERC) or to the rear of Passivated Emitter and Rear Locally-diffused (PERL) cells, because the inversion layer may couple to the p-type-contacts (parasitic shunting) [Dau02a]. This reduces the short circuit current drastically. On the other hand, it is well known that the passivation quality at p-Si with an acceptor density $N_\mathrm{A} < 10^{17}\,\mathrm{cm}^{-3}$ deteriorates strongly at low illumination conditions [Abe95b, Elm97, Ker02b, Leg96]. Since this phenomenon is not well understood, strategies are missing to avoid it.

Thus, the surfaces of p-Si passivated solar cells are usually diffused with dopants to exceed the critical acceptor density of $N_\mathrm{A} \approx 10^{17}\,\mathrm{cm}^{-3}$ at the interface. Thereby, a deteriorated cell performance in low-injection[1] is avoided. A similar, yet less pronounced effect, is observed for atomic layer deposited (ALD) $\mathrm{Al}_2\mathrm{O}_3$ on n-type silicon (n-Si) which is deposited at temperatures as low as $T \simeq 200 \ldots 250\,°\mathrm{C}$

---

[1] In low-injection, the excess charge carrier density is much smaller than the dopant density of the substrate. *Injection density* is used here equivalently to *excess charge carrier density*.

and contains a high negative fixed charge density.

Another material that allows for high-quality electrical passivation of silicon surfaces and is deposited at temperatures similar to those of Al_2O_3 is hydrogenated amorphous silicon (a-Si:H). In addition to its excellent passivation qualities [Oli07, Pla07], doped a-Si:H is used as an emitter or as a back surface field in a-Si:H/c-Si hetero-junction solar cells [de 09, Sch07b, Tag00, vM06, Wan04]. Recombination of free charge carriers at the a-Si:H/c-Si interface occurs mainly via DB defect states [Kor06a, Lee10b, Li08, Oli07]. Each DB can be occupied by either zero, one, or two electrons. Consequently, the recombination centers are amphoteric, meaning that they behave in either a donor-like or an acceptor-like fashion. Donor-like defects are positively charged when empty, and neutral when occupied by an electron, whereas acceptor-like defects are neutral when empty, and negatively charged when occupied. Unfortunately, the recombination statistics that describes recombination via amphoteric defects [Vai86] has no closed-form-solution and is thus computationally demanding. Hence, it is common practice in device modeling to approximate the recombination statistics by means of the simple Shockley-Read-Hall [Hal52, Sho52] theory [e.g. Gar05]. However, indications exist that the SRH approximation may fail under certain conditions [Hal86, Kli02, Sun94, Wil98]. Therefore, further approximations have been applied, such as the extended SRH formalism by Brattain and Bardeen [Bra53] and Simmons and Taylor [Sim71] that includes a distribution of defects within the bandgap. A simplified closed-form solution of the amphoteric model in which thermal emission is neglected was proposed by Hubin *et al.* [Hub92] and applied by Olibet *et al.* [Oli07]. Also a constant density of defect states has been chosen [Pla07], with donor-like properties below midgap and acceptor-like behavior above midgap. In addition, the injection dependent interface charges which arise due to the occupation of DB states is often fully neglected [Gar05, Pla07], or approximated via a fixed charge density [Oli07, Sch11].

The last issue we address in this work are nonlinear shunts[2] that originate from localized, highly disturbed regions and cause diode ideality factors $n_\mathrm{D} > 2$ in forward direction, i.e. a partly sub-exponential increase of the dark current-voltage (I-V) characteristics, [Bre01a, Bre01b, Bre03, Hau01, Que62]. Such shunts strongly influence the I-V curves and are observed in most industrially fabricated crystalline silicon solar cells, and frequently also in cell designs under development [Lan02]. The observed diode ideality factors $n_\mathrm{D} > 2$ cannot be described using SRH the-

---

[2] We define a shunt in a diode as any path where carriers flow as an alternative to being fully injected across the p-n junction [McI01]. Hence, not all currents having $n_\mathrm{D} > 2$ are necessarily shunts (cf. Chapter 6).

ory. Also, the reverse characteristics cannot be explained using SRH theory alone: whereas SRH theory predicts a saturation behavior of the reverse currents, the measured characteristics of cells with nonlinear shunts are often non-saturating and may even increase super-linear [Bre06b]. Several attempts have been made to explain large ideality factors using various models, like trap-assisted tunneling [Kam96], field-enhanced recombination [Sch95], saturation effects within the SRH model for donor-like levels [Bei93], resistance-limited action of SRH-type edge recombination currents [McI00a, McI01, vdH05], and bias-dependent band bending that extends the recombination region to the p-type surface [Küh00]. However, many of these models have either been proven wrong or they fail. For example, resistance-limited recombination can be excluded as an explanation, as will be discussed in Sec. 6.3. Moreover, the assumption of homogeneously distributed point defects in the whole depletion region [Bei93, Kam96, Sch95] was proven wrong by lock-in thermography measurements [Bre01a, Bre01b, Bre03, Hau01]. In particular, it could be shown by lock-in thermography that the ideality factor n_D exceeds 2 only locally in highly disturbed regions, whereas in all other regions, $n_\mathrm{D} \lesssim 2$ was observed as expected from SRH theory [Bre01b].

1.2 Outline

This work is organized as follows. The relevant theory is introduced in Chapter 2. Chapter 3 describes the most essential numerical models required in this work. A microscopic model that describes the surface recombination velocity at SiN_x and $\mathrm{Al_2O_3}$ passivated substrates for all relevant injection and dopant densities on both n-type and p-type silicon is developed in Chapter 4. From this model, strategies will be derived to avoid the reduced passivation at low injection levels. Chapter 5 introduces an approximate SRH model to amphoteric recombination statistics [Vai86] which is suitable for device simulations. The differences between this model and the full amphoteric statistics [Vai86] will be investigated in detail in order to determine the error bounds of the approximation. Such error bounds are helpful to device simulations, because they allow the use of an easily implementable and computationally inexpensive recombination model within these bounds. In Chapter 6, we explain the origin of shunt currents in c-Si solar cells. The applied model takes the experimental result into account that $n_\mathrm{D} > 2$ occurs only in localized highly defective regions. In these regions, the defect densities are so high, that a model is required which takes coupling into account and thus, goes beyond the standard SRH theory. In particular, we assume coupled deep-level donor-acceptor pairs (DAPs) to be present in locally, strongly disturbed regions of the p-n junction. Incorporating this effect into device simulations explains the measured I-V characteristics for both forward and reverse bias as well as the high ideality factors n_D. In Chapter 7, we employ the software

Sentaurus Device [SD] to investigate the influence of the injection dependent recombination rate at SiN_x/c-Si interfaces. Various cell designs are considered and predictions are made how the reduced passivation at low-injection densities affects the cell performance. In addition, a comparison to a-Si:H passivated cells is made. Chapter 8 summarizes the results and relates them to possible future experiments and simulations.

Chapter 2

Fundamentals

This chapter introduces the physical background of this work. We recapitulate the semiconductor device equations in Sec. 2.1 to introduce the relevant quantities. Section 2.2 treats the different recombination models applied in this work. Intrinsic recombination mechanisms and defect recombination via both isolated and coupled defect levels are discussed. Further, the description of recombination via surface-states is described. In Sec. 2.3, we consider the amphoteric defects in amorphous hydrogenated silicon (a-Si:H). A defect-pool model (DPM) [Pow93] for describing the defect density in a-Si:H is presented, and the statistics to model recombination via the amphoteric dangling bonds (DBs) [Vai86] is derived. Finally, the main features of the current-voltage (I-V) characteristics of solar cells are described in Sec. 2.4.

2.1 Fundamentals of semiconductor device modeling

To accurately model and analyze an arbitrary semiconductor device which may operate under various operating conditions, a mathematical model is required. This mathematical model consists of the basic semiconductor equations which can be derived from Maxwell's equations and the Boltzmann transport equation by taking well-known relations from solid-state physics into account.

2.1.1 Stationary semiconductor device equations

The semiconductor equations consist of Poisson's equation and the continuity equations. Together, they form a set of three coupled partial differential equations which are derived from the Maxwell equations under the assumption of an irrotational electric field, i.e. negligible influence of magnetic effects. Poisson's equation is essentially the third Maxwell equation and relates the electrostatic potential Ψ to the charge density ϱ:

$$\begin{aligned}\varepsilon\Delta\Psi &= -\varrho &\text{(2.1a)}\\ &= q(n-p-N_\mathrm{D}+N_\mathrm{A})-\varrho_\mathrm{t}. &\text{(2.1b)}\end{aligned}$$

Here Δ is the Laplacian operator $\vec{\nabla}^2$ and q is the elementary charge. The permittivity $\varepsilon := \varepsilon_\mathrm{r}\varepsilon_0$, with the relative dielectric constant ε_r and the vacuum permittivity ε_0, is assumed to be a scalar quantity. This is valid for most materials used for device fabrication because of the alignment of the atoms in a cubic lattice or an amorphous structure [Sel84]. In Eq. (2.1b), the Poisson equation is applied to semiconductors by defining the space-charge density as the sum of the mobile charge carrier density of electrons n and holes p, a charge contribution $\varrho_\mathrm{t} \geq 0$ from traps or fixed charges, and the concentrations of ionized donors N_D and ionized acceptors N_A.

The continuity equations are derived from the first Maxwell equation and state that sources and sinks of the total conduction current $\vec{j}_\mathrm{n}+\vec{j}_\mathrm{p}$ are compensated by the time response of the mobile charge $p-n$:

$$\nabla(\vec{j}_\mathrm{n}+\vec{j}_\mathrm{p})+q\frac{\partial}{\partial t}(p-n)=0. \tag{2.2}$$

In Eq. (2.2) it is assumed that electrons and holes are the only charges in the semiconductor that may change in time. Equation (2.2) can be separated into two equations by defining a charge carrier generation rate G and a charge carrier recombination rate R:

$$\nabla\vec{j}_\mathrm{n}-q\frac{\partial n}{\partial t} = q(R-G), \qquad \nabla\vec{j}_\mathrm{p}+q\frac{\partial p}{\partial t} = -q(R-G). \tag{2.3}$$

This mathematical transformation from Eq. (2.2) to Eq. (2.3) provides additional information only if models for R and G are available [Sel84]. Models for these quantities are treated in Sec. 2.2. To solve the set of partial differential equations (2.1) and (2.3), relations for the current densities $\vec{j}_\mathrm{n}$, $\vec{j}_\mathrm{p}$ and the carrier densities n, p have to be provided. These relations are introduced in the following sections 2.1.2 and 2.1.3, respectively.

2.1.2 Carrier transport

Carrier transport is modeled using the drift-diffusion approximation. It follows from the observation that the continuity equations (2.3) derived from Maxwell's equations are in the same form as those which can be derived from the Boltzmann transport equations [Sno86] if the current densities are written as:

$$\vec{j}_\mathrm{n} = -qn\vec{v}_\mathrm{n}, \qquad \vec{j}_\mathrm{p} = qp\vec{v}_\mathrm{p}. \tag{2.4}$$

Here, $\vec{v}_\mathrm{n} = \vec{\nabla}\varphi_\mathrm{n}$ and $\vec{v}_\mathrm{p} = \vec{\nabla}\varphi_\mathrm{p}$ are the electron and hole velocities, respectively, and φ_n and φ_p are the corresponding quasi-Fermi potentials (cf. Sec. 2.1.3). This semi-classical Boltzmann approach is often sufficient to describe carrier transport in semiconductors. Considering in the transport equations only the drift term caused by an electric field and the diffusion term caused by thermal energy, and neglecting both bandgap narrowing and temperature gradients, leads to the well-known drift-diffusion approximation. For Boltzmann statistics, the current densities for electrons and holes are then given by [Sno86]:

$$\vec{j}_\mathrm{n} \;=\; -q(\mu_\mathrm{n} n\vec{\nabla}\Psi + D_\mathrm{n}\vec{\nabla}n), \qquad \vec{j}_\mathrm{p} \;=\; -q(\mu_\mathrm{p} p\vec{\nabla}\Psi - D_\mathrm{p}\vec{\nabla}p), \tag{2.5}$$

where μ_n and μ_p are the effective electron and hole mobilities, respectively. For non-degenerate semiconductors, the diffusion coefficients D_n and D_p are given by the Einstein relation [Sno86]:

$$D_\mathrm{n} \;=\; \frac{\mu_\mathrm{n}}{q\beta}, \qquad D_\mathrm{p} \;=\; \frac{\mu_\mathrm{p}}{q\beta}, \tag{2.6}$$

where $\beta = 1/(k_\mathrm{B}T)$.

2.1.3 Carrier concentrations

The carrier concentrations are obtained by integrating the density of states (DOS) multiplied by the carrier occupation functions over energy. Thereby, the occupation functions of electrons $f_\mathrm{n}(E)$ and holes $f_\mathrm{p}(E)$ are Fermi functions:

$$f_\mathrm{n}(E) \;=\; \frac{1}{1+\mathrm{e}^{\beta(E-E_\mathrm{fn})}}, \qquad f_\mathrm{p}(E) \;=\; \frac{1}{1+\mathrm{e}^{\beta(E_\mathrm{fp}-E)}}, \tag{2.7}$$

where E_fn and E_fp are the quasi-Fermi levels for electrons and holes. Assuming a parabolic and isotropic band structure, yields for the carrier densities [Sel84, page 25]:

$$n \;=\; N_\mathrm{c} F_{1/2}\left(\beta(E_\mathrm{fn}-E_\mathrm{c})\right)\frac{2}{\sqrt{\pi}}, \qquad p \;=\; N_\mathrm{v} F_{1/2}\left(\beta(E_\mathrm{v}-E_\mathrm{fp})\right)\frac{2}{\sqrt{\pi}}, \tag{2.8}$$

where N_c and N_v denote the effective DOS in the conduction band and in the valence band, respectively. E_v and E_c are the valence band and conduction band edges, and $F_{1/2}$ is the Fermi integral of order 1/2:

$$F_{1/2}(x) = \int_0^\infty \mathrm{d}y\, \frac{y^{1/2}}{1+\mathrm{e}^{y-x}}. \tag{2.9}$$

$F_{1/2}$ has no closed form solution and therefore needs to be solved numerically or using approximations [Bla82, Joy77]. In the limiting cases $\beta(E_\mathrm{c}-E_\mathrm{fn}) \gg 1$ and

$\beta(E_{\mathrm{fp}} - E_{\mathrm{v}}) \gg 1$, the Fermi occupation functions in (2.8) reduce to Boltzmann statistics, and hence:

$$n = N_{\mathrm{c}}\, \mathrm{e}^{\beta(E_{\mathrm{fn}}-E_{\mathrm{c}})}, \qquad p = N_{\mathrm{v}}\, \mathrm{e}^{\beta(E_{\mathrm{v}}-E_{\mathrm{fp}})}. \tag{2.10}$$

Boltzmann statistics is valid for impurity concentrations below $N_{\mathrm{imp}} \lesssim 10^{19}\,\mathrm{cm}^{-3}$, at least in neutral regions with negligible compensation[1] [Sch98a]. The concept of using Boltzmann statistics fails, however, for heavily doped material. For most applications in this work, the impurity and carrier concentrations are below $10^{19}\,\mathrm{cm}^{-3}$. Therefore, we stick to Boltzmann statistics here.

In the following we define the band edges E_{c} and E_{v}, and the quasi-Fermi energies E_{fn} and E_{fp} to further investigate the carrier concentrations. The quasi-Fermi energies can be written as:

$$E_{\mathrm{fn}} = E_{\mathrm{i}} - q\varphi_{\mathrm{n}}, \qquad E_{\mathrm{fp}} = E_{\mathrm{i}} - q\varphi_{\mathrm{p}}, \tag{2.11}$$

where φ_{n} and φ_{p} are the quasi-Fermi potentials of electrons and holes. The carrier concentrations are determined from the *differences* between the quasi-Fermi potentials φ_{n} and φ_{p} and the electrostatic potential Ψ. Thus, without loss of generality, we may define the electrostatic potential to be zero for intrinsic material in thermal equilibrium, such that E_{i} is the Fermi energy for the intrinsic semiconductor.

The band edges can be separated into three parts:

$$E_{\mathrm{c}} = E_{\mathrm{c0}} - \delta E_{\mathrm{c}} - q\Psi, \qquad E_{\mathrm{v}} = E_{\mathrm{v0}} + \delta E_{\mathrm{v}} - q\Psi. \tag{2.12}$$

Here, E_{c0} and E_{v0} stand for the band edges of the intrinsic semiconductor, Ψ is the electrostatic potential, and δE_{c} and δE_{v} denote shifts of the band edges caused e.g. by dopants.

In the following, we derive a formulation for the carrier densities with a reduced number of parameters. Inserting Eqs. (2.11) and (2.12) into Eq. (2.10), and considering Poisson's equation for the intrinsic semiconductor in thermal equilibrium[2] leads to:

$$N_{\mathrm{c}}\, \mathrm{e}^{\beta(E_{\mathrm{i}}-E_{\mathrm{c}})} = N_{\mathrm{v}}\, \mathrm{e}^{\beta(E_{\mathrm{v}}-E_{\mathrm{i}})}. \tag{2.13}$$

The geometric average of the carrier concentrations in equilibrium, the so called *intrinsic* density, reads then:

$$n_{\mathrm{i}} := \sqrt{n_0 p_0} = \sqrt{N_{\mathrm{c}} N_{\mathrm{v}}}\, \mathrm{e}^{-\frac{\beta E_{\mathrm{g}}}{2}}, \tag{2.14}$$

---

[1] If both donors and acceptors are present in a semiconductor, an acceptor electron satisfies an acceptor impurity. This reduces the number of free charge carriers compared to the case where only one dopant is present. This effect is called (partial) compensation.

[2] In thermal equilibrium there holds $p(\Psi = 0, \varphi_{\mathrm{p}} = 0) - n(\Psi = 0, \varphi_{\mathrm{n}} = 0) = 0$.

where n_0 and p_0 are the charge carrier densities in thermal equilibrium, and E_g is the energy bandgap of the semiconductor. Thus, it follows for the carrier concentrations:

$$n = n_\mathrm{i}\,\mathrm{e}^{q\beta(\Psi-\varphi_\mathrm{n})}, \qquad p = n_\mathrm{i}\,\mathrm{e}^{q\beta(\varphi_\mathrm{p}-\Psi)}. \tag{2.15}$$

Apart from the carrier statistics and the shift energies for the energy bands, deviations from parabolic energy bands and thus, a modified DOS function, have to be considered for heavily doped semiconductors [Alt05b, Alt06c, Alt06d, Kan63, Mah80, Ove87, Sch06]. In particular for Fermi-statistics, approximations of the DOS are too complex to be implemented in semiconductor device simulations. Therefore, it is advantageous to use the formalism of the *effective intrinsic density* which leads to expressions similar to Eq. (2.15) derived for Boltzmann statistics and a parabolic band structure [Sel84]:

$$n = n_\mathrm{i,eff}\,\mathrm{e}^{q\beta(\Psi-\varphi_\mathrm{n})}, \qquad p = n_\mathrm{i,eff}\,\mathrm{e}^{q\beta(\varphi_\mathrm{p}-\Psi)}. \tag{2.16}$$

The effective intrinsic density $n_\mathrm{i,eff}$ can be written in dependence of the bandgap narrowing (BGN) ΔE_g [Alt03]:

$$n_\mathrm{i,eff} = n_\mathrm{i}\,\mathrm{e}^{\frac{\beta\Delta E_\mathrm{g}}{2}}. \tag{2.17}$$

2.1.4 Boundary conditions

The numerical solution of the semiconductor equations (2.1) and (2.3) requires the definition of suitable boundary conditions (BCs) for the carrier densities at interfaces. For Ohmic contacts, typically Dirichlet BCs are applied. Charge neutrality requires [Sch94a]

$$\varrho = n - p - N_\mathrm{D} + N_\mathrm{A} = 0. \tag{2.18}$$

The solution relates the electrostatic potential Ψ directly to the applied voltage V. As the electrons move freely across a contact boundary, the electrostatic potential Ψ is set equal to the applied voltage $V = \Psi$. For the carrier concentrations, we use $n = n_0$ and $p = p_0$ at Ohmic contacts.

In contrast to the Dirichlet BCs for metals, insulator interfaces (and all other surfaces) are described by Neumann BCs. In the absence of an external electric field, the electric field inside any insulator vanishes and the field inside the semiconductor is balanced by the interface charge density Q_it. Thus, the BC for the Poisson equation reads:

$$\vec{\nabla}_{\hat{n}}\Psi = \frac{Q_\mathrm{it}}{\varepsilon_0\varepsilon_s}, \tag{2.19}$$

where ε_s is the relative dielectric constant of the semiconductor, and $\hat{n}$ is a unit vector normal to the surface. In addition, it is assumed that no charge carriers may cross the interface, so

$$\hat{n}(\vec{j}_\mathrm{n} + \vec{j}_\mathrm{p}) = 0. \tag{2.20}$$

The current densities $\vec{j}_\mathrm{n}$ and $\vec{j}_\mathrm{p}$ in Eq. (2.20) normal to the interface are given by:

$$\hat{n}\vec{j}_\mathrm{n} \;=\; qS_\mathrm{n}(n - n_0), \qquad \hat{n}\vec{j}_\mathrm{p} \;=\; qS_\mathrm{p}(p - p_0), \tag{2.21}$$

where S_n and S_p are the surface recombination velocity parameters (cf. Sec. 2.2.8) for electrons and holes, respectively. Equation (2.20) means that either every electron present at the surface recombines with a hole, or both current densities $\vec{j}_\mathrm{n}$ and $\vec{j}_\mathrm{p}$ are zero normal to the surface.

2.1.5 Numerical challenges of the stationary device problem

To model a semiconductor device, the fundamental semiconductor equations (2.1) and (2.3) need to be solved numerically with the BCs defined in Sec. 2.1.4. The result of any device simulation is therefore only an approximation to the real solution. Before solving the semiconductor equations, a mesh is generated to discretize the device in space (cf. Appendix A.2). The partial differential equations are then solved at selected mesh nodes (finite difference method) or in the subdomains (finite element method) of the mesh, see Appendix A.2. For non-homogeneously doped semiconductor devices, the carrier densities may change over orders of magnitude within short distances, and their behavior is strongly influenced by the space charge. One possibility to overcome this problem when solving for the variables (Ψ, n, p) or $(\Psi, E_\mathrm{fn}, E_\mathrm{fp})$ is to apply an appropriate scaling to the semiconductor equations (cf. Appendix A.1). In addition, it is advantageous to use an adaptive mesh, where a refinement of nodes is applied to those regions where the unknowns change strongly (cf. Appendix A.2). To solve the semiconductor equations in the discretized space, they must be linearized (cf. Appendix A.3). The coupled system of partial differential equations is then solved in either a coupled or a decoupled approach (cf. Appendix A.3).
A detailed description of the strategies to obtain the numerical solutions of the stationary device problem goes beyond the scope of this thesis. We employ the software SENTAURUS-DEVICE [SD] to perform the solar cell device simulations in Chapters 6 and 7. The interested reader finds an elaborate description of the main strategies in Appendix A, including hints how to circumvent convergence problems.

2.2 Carrier recombination in crystalline silicon

As outlined in Sec. 2.1.1, we require a model for the net recombination rate $R - G$ to solve the set of semiconductor equations (2.1) and (2.3). There are different recombination mechanisms contributing to the total generation rate in a semiconductor.

First, we have the radiative recombination, which is the inverse process to carrier generation and is introduced in Sec. 2.2.2. Second, there is the Auger recombination, described in Sec. 2.2.3, which is the inverse process to impact ionization and becomes important for high carrier densities. Both of these processes are not avoidable; they are rather characteristic for each material. Finally, recombination through defect levels is an efficient process in solar-grade silicon under low to medium excess charge carrier densities. Note that throughout this thesis, we abbreviate the *excess charge carrier density* as *excess carrier density*. It is usually modeled in crystalline silicon (c-Si) using the Shockley-Read-Hall (SRH) statistics [Hal52, Sho52], presented in Sec. 2.2.4. This effect can be influenced by the concentration of impurities in the semiconductor, and is thus an important aspect to consider when improving solar cells. The inverse process to defect-level recombination is the emission process of charge carriers from defect levels. SRH theory is valid for defects in the bandgap as long as they are *isolated* and *not correlated*. For closely spaced defects, a coupling between them has to be taken into account, as described in Sec. 2.2.7. An example of correlated defects are amphoteric dangling bonds (DBs). The recombination theory for such defects is described in detail in Sec. 2.3. Finally, the application of SRH theory to surfaces and the influence of interface charges is described in Sec. 2.2.8.

2.2.1 Carrier generation

In a semiconductor, free charge carriers are generated by incident light of suitable wavelength. The carrier generation rate $G = \alpha_{\mathrm{np}} N_p$ can be written as the product of the absorption coefficient for electrons and holes α_{np} and the photon flux N_{p}. Thereby, N_{p} is determined by the differential equation $\mathrm{d}N_{\mathrm{p}}/\mathrm{d}z = -(\alpha_{\mathrm{np}} + \alpha_{\mathrm{fc}})N_{\mathrm{p}}$, where z denotes the position in direction of the photon flux [Gre95]. α_{fc} denotes the absorption coefficient for processes which do not generate an electron-hole pair. An example of such a process is free carrier absorption [e.g. Gre95]. Assuming the absorption coefficients α_{np} and α_{fc} to be independent of the position, one obtains:

$$G = \alpha_{\mathrm{np}} N_{\mathrm{p},0}\, \mathrm{e}^{-(\alpha_{\mathrm{np}}+\alpha_{\mathrm{fc}})(z-z_0)}, \tag{2.22}$$

where z_0 denotes the position of the surface in z-direction. Note that in general, the absorption coefficients α_{np} and α_{fc} depend on the wavelength of the incident light.

2.2.2 Radiative recombination

In the following we consider recombination of the excess charge carriers Δn and Δp. These are defined as the difference in the carrier densities out of equilibrium at a given illumination level or an applied voltage, and in thermal equilibrium, $\Delta n := n - n_0$ and $\Delta p := p - p_0$. Note that in quasi-neutral regions of a semiconductor device, there is $\Delta n = \Delta p$.

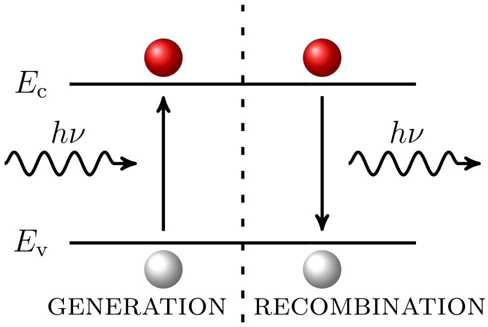

Figure 2.1: Photogeneration (left) and radiative recombination (right). ν denotes the frequency of the photons.

The process of radiative recombination and its inverse process are sketched in Fig. 2.1. An electron from the conduction band recombines with a hole in the valence band and thereby emits a photon. Since this process needs both a free electron and a free hole, the excess carrier recombination rate is proportional to the product of the electron and hole concentration np subtracted by n_0p_0:[3]

$$R_{\mathrm{Rad}} = B_{\mathrm{Rad}}(np - \underbrace{n_0p_0}_{n_{\mathrm{i,eff}}^2}) \overset{(2.10),(2.14),(2.17)}{=} B_{\mathrm{Rad}} n_{\mathrm{i,eff}}^2 \left(\mathrm{e}^{\beta(E_{\mathrm{fn}}-E_{\mathrm{fp}})} - 1 \right) \overset{\propto}{\sim} \mathrm{e}^{\beta(E_{\mathrm{fn}}-E_{\mathrm{fp}})}. \tag{2.23}$$

The approximate exponential dependence of R_{Rad} on $E_{\mathrm{fn}} - E_{\mathrm{fp}}$ holds for non-degenerate semiconductors where Boltzmann statistics is a good approximation to the correct Fermi statistics. The radiative recombination coefficient B_{Rad} is a temperature dependent material property and is thus independent of the carrier densities. It is given by [e.g. Tru03]:

$$B_{\mathrm{Rad}} = \frac{1}{n_{\mathrm{i,eff}}^2} \frac{2\pi}{h^3c^2} \int_0^\infty \mathrm{d}E \; n_{\mathrm{mat}}(E)^2 \alpha_{np}(E) \, \mathrm{e}^{-\beta E} E^2, \tag{2.24}$$

where n_{mat} is the refractive index of the semiconductor material, and the integration is performed over energy E. At a typical operation temperature $T = 300\,\mathrm{K}$ of solar cells, there is $B_{\mathrm{Rad}} = 4.733 \times 10^{-15}\,\mathrm{cm^3 s^{-1}}$ [Tru03].

2.2.3 Auger recombination

Auger recombination is an example of a non-radiative recombination process. In solar cells, it typically dominates the total recombination rate at high excess carrier densities Δn. This recombination mechanism describes the process where two charge carriers of equal polarity collide. Thereby, one of both carriers is excited to a higher energy level while the other one recombines across the bandgap with a charge carrier

---

[3] This can be explained by the law of mass action which requires $np = (n_0 + \Delta n)(p_0 + \Delta p)$, and thus it follows for $\Delta n = \Delta p$ that $np - n_0p_0 = \Delta n(n_0 + p_0 + \Delta n)$).

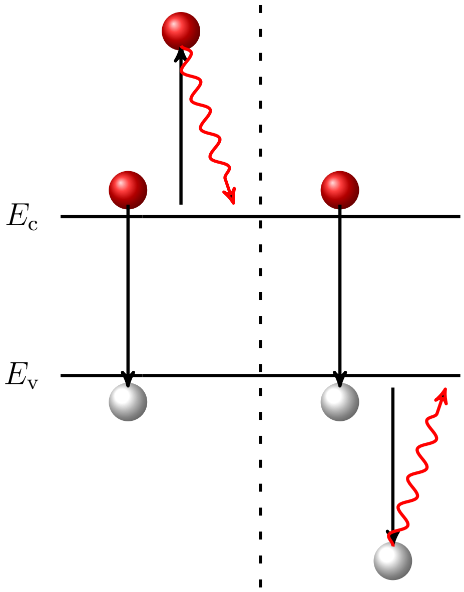

Figure 2.2: The Auger recombination process. The energy is transmitted to an electron (left) or to a hole (right).

of opposite polarity. Finally, the excited charge carrier relaxes thermally to the band edge and loses its extra energy by exciting thermal vibrations in the lattice. This process is sketched for the collision of electrons in Fig. 2.2 on the left and for holes on the right. Arguing as in Sec. 2.2.2, the Auger recombination rate is proportional to the density of all three participating charge carriers:

$$R_{\mathrm{Aug}} = R_{\mathrm{Aug,nnp}} + R_{\mathrm{Aug,npp}} = C_{\mathrm{n}}(n^2p - n_0^2p_0) + C_{\mathrm{p}}(np^2 - n_0p_0^2). \tag{2.25}$$

For the solar cell device simulations in Chapters 6 and 7, the temperature dependent material constants C_{n} and C_{p} for silicon are chosen according to Altermatt *et al.* [Alt97] which corresponds at 300 K to the measurements of Dziewior and Schmid [Dzi77], cf. Table 7.2 in Chapter 7. For the theoretical considerations in Chapters 4 and 5, we use the Auger parametrization according to Kerr and Cuevas [Ker02a]:

$$R_{\mathrm{Aug}} = np\left(1.8 \times 10^{-24} n_0^{0.65} + 6 \times 10^{-25} p_0^{0.65} + 3 \times 10^{-27} \Delta n^{0.8}\right). \tag{2.26}$$

2.2.4 SRH recombination

Recombination via defect levels constitutes a recombination process which is not due to an inherent material property. It is an important recombination process in situations where the excess carrier density Δn is less or approximately equal to the dopant density N_{dop} ($\Delta n \lesssim N_{\mathrm{dop}}$).

The SRH statistics describes recombination via an isolated defect in the bandgap [Hal52, Sho52]. According to this theory, four possible carrier transitions between defect states and the valence or conduction band are defined: the capture

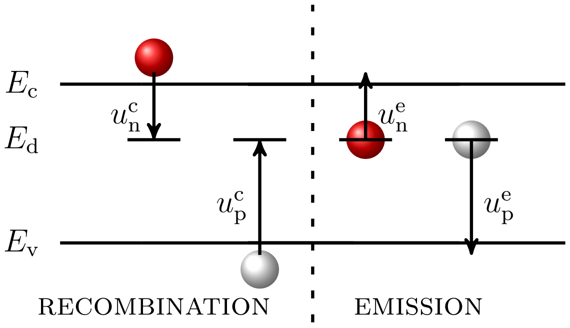

Figure 2.3: SRH defect level recombination (left) and thermal emission from defects (right). The recombination rates are labeled u_n^c and u_p^c for electrons and holes, respectively. The corresponding emission rates are u_n^e and u_p^e.

of electrons from the conduction band (u_n^c), thermal emission of captured electrons from the defect to the conduction band (u_n^e), and the mathematically-equivalent transitions of holes between the defect and the valence band, u_p^c and u_p^e, respectively. All possible carrier transition rates are sketched in Fig. 2.3. Provided there are steady-state conditions, the total carrier transition rates of electrons and holes are equal, yielding the rate equations [Sho52]:

$$u_n^c - u_n^e = u_p^c - u_p^e. \tag{2.27}$$

Hence, it is sufficient to evaluate recombination for electrons only. According to SRH statistics, a defect state is occupied by either an electron or a hole. Hence, denoting the electron occupation fraction by f, the hole occupation fraction results in $1-f$, and the expressions for the carrier transition rates become:

$$\begin{aligned} u_n^c &= c_n(1-f)N_d, & u_n^e &= e_n f N_d, \\ u_p^c &= c_p f N_d, & u_p^e &= e_p(1-f)N_d, \end{aligned} \tag{2.28}$$

where N_d is the defect density. The capture coefficients are abbreviated by c_n and c_p, and the emission coefficients by e_n and e_p:

$$\begin{aligned} c_n &= v_{th,n} n \sigma_n, & c_p &= v_{th,p} p \sigma_p, \\ e_n &= c_{n,0}\, e^{\beta(E_d-E_f)}, & e_p &= c_{p,0}\, e^{\beta(E_f-E_d)} \end{aligned} \tag{2.29a}$$

where

$$c_{n,0} = v_{th,n} n_0 \sigma_n, \qquad c_{p,0} = v_{th,p} p_0 \sigma_p. \tag{2.29b}$$

and $v_{th,n}$ and $v_{th,p}$ are the thermal velocities for electrons and holes, respectively, which are about 10^7 cm/s in silicon at room temperature; σ_n and σ_p are the cross sections of electron and hole capture, respectively, and E_d is the energy of the defect. With these Eqs. (2.28)–(2.29b), the electron occupation fraction f can be written as

$$f = \frac{c_n + e_p}{c_p + e_n + c_n + e_p}. \tag{2.30}$$

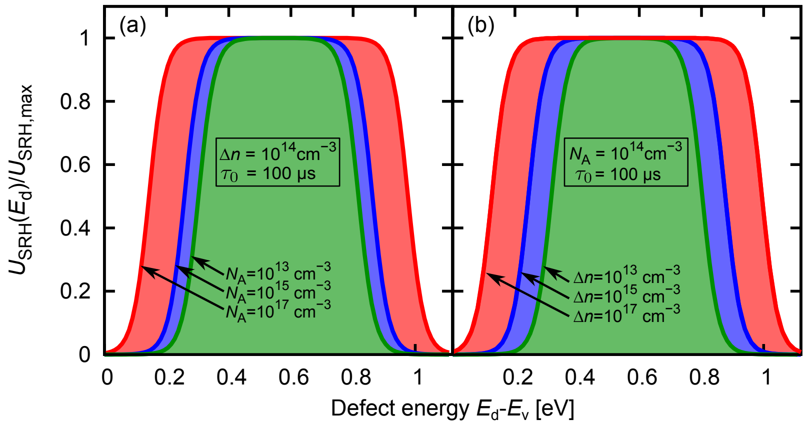

Figure 2.4: Normalized SRH recombination rate $U_{\mathrm{SRH}}(E_{\mathrm{d}} - E_{\mathrm{v}})$ as a function of defect energy with respect to the valence band edge E_{v}, calculated using Eq. (2.32) for a defect density constant in energy. The substrate material is p-Si. (a) The acceptor density N_{A} is varied for an excess carrier density $\Delta n = 10^{14}\,\mathrm{cm}^{-3}$. (b) The excess carrier density Δn is varied for an acceptor concentration $N_{\mathrm{A}} = 10^{14}\,\mathrm{cm}^{-3}$. The lifetime parameter in (a) and (b) is $\tau_0 := \tau_{\mathrm{n}} = \tau_{\mathrm{p}} = 100\,\mu\mathrm{s}$.

After some straight-forward computations, it follows for the SRH recombination rate R_{SRH} via a single defect at an energy level E_{d} in the bandgap [Hal52, Sho52]:

$$R_{\mathrm{SRH}} = N_{\mathrm{d}} \frac{np - n_{\mathrm{i,eff}}^2}{\frac{n + N_{\mathrm{c}}\,\mathrm{e}^{-\beta(E_{\mathrm{c}} - E_{\mathrm{d}})}}{v_{\mathrm{th,p}}\sigma_{\mathrm{p}}} + \frac{p + N_{\mathrm{v}}\,\mathrm{e}^{\beta(E_{\mathrm{v}} - E_{\mathrm{d}})}}{v_{\mathrm{th,n}}\sigma_{\mathrm{n}}}}. \tag{2.31}$$

Typically, each defect has a certain distribution within the bandgap. To include such distributions, Eq. (2.31) is easily generalized to a continuous defect density $D(E_{\mathrm{d}})$ within the bandgap by integrating Eq. (2.31) over the entire bandgap [Bra53, Sim71]:

$$R_{\mathrm{SRH}} = \int_{E_{\mathrm{v}}}^{E_{\mathrm{c}}} \mathrm{d}E_{\mathrm{d}}\; D(E_{\mathrm{d}}) \frac{np - n_{\mathrm{i,eff}}^2}{\frac{n + N_{\mathrm{c}}\,\mathrm{e}^{-\beta(E_{\mathrm{c}} - E_{\mathrm{d}})}}{v_{\mathrm{th,p}}\sigma_{\mathrm{p}}(E_{\mathrm{d}})} + \frac{p + N_{\mathrm{v}}\,\mathrm{e}^{\beta(E_{\mathrm{v}} - E_{\mathrm{d}})}}{v_{\mathrm{th,n}}\sigma_{\mathrm{n}}(E_{\mathrm{d}})}} =: \int_{E_{\mathrm{v}}}^{E_{\mathrm{c}}} \mathrm{d}E_{\mathrm{d}}\; U_{\mathrm{SRH}}(E_{\mathrm{d}}). \tag{2.32}$$

Here, $U_{\mathrm{SRH}}(E)$ denotes the energy dependent recombination rate. Figure 2.4 shows for the example of a p-Si substrate (i.e. $N_{\mathrm{dop}} \equiv N_{\mathrm{A}}$)[4] that U_{SRH} is quasi-constant within a wide energy range around midgap if the defect density is independent of energy. Close to the valence and conduction band edges, U_{SRH} decreases because the emission rates $u_{\mathrm{n}}^{\mathrm{e}}$ or $u_{\mathrm{p}}^{\mathrm{e}}$ dominate for shallow defect levels.[5] The boundaries of the plateau of quasi-constant recombination rate depends on both the dopant

---

[4] Note that we assume that $N_{\mathrm{D}} = 0$ in p-Si and $N_{\mathrm{A}} = 0$ in n-Si. Hence, in p-Si there is $p_0 = N_{\mathrm{A}}$ and in n-Si there is $n_0 = N_{\mathrm{D}}$. The equilibrium concentration of the minorities follows from $n_0 p_0 = n_{\mathrm{i,eff}}^2$.

[5] Shallow defect levels refer to defect levels close to the band edges.

density N_{dop} and the excess carrier density Δn. The plateau of $U_{\mathrm{SRH}}(E_{\mathrm{d}})$ shows that for deep-level defects, i.e. defects close to midgap, recombination may be described well also if the exact defect distribution is not know. Thus, in many cases it is sufficient to approximate SRH recombination via deep-level defects by a single defect level. When using this approximation, it is convenient to introduce the SRH lifetime parameters

$$\frac{1}{\tau_{\mathrm{n}}} \quad := \quad v_{\mathrm{th,n}}\sigma_{\mathrm{n}}N_{\mathrm{d}}, \qquad \frac{1}{\tau_{\mathrm{p}}} \quad := \quad v_{\mathrm{th,p}}\sigma_{\mathrm{p}}N_{\mathrm{d}}. \tag{2.33}$$

With the abbreviations:

$$n_1 \quad = \quad N_{\mathrm{c}}\,\mathrm{e}^{\beta(E_{\mathrm{d}}-E_{\mathrm{c}})}, \qquad p_1 \quad = \quad N_{\mathrm{v}}\,\mathrm{e}^{\beta(E_{\mathrm{v}}-E_{\mathrm{d}})}, \tag{2.34}$$

this leads to the simple formulation of the SRH recombination rate:

$$R_{\mathrm{SRH}} = \frac{pn - n_{\mathrm{i,eff}}^2}{\tau_{\mathrm{p}}(n+n_1) + \tau_{\mathrm{n}}(p+p_1)}. \tag{2.35}$$

2.2.5 Characteristic energy levels

In order to compare SRH theory with other defect-recombination models, it is useful to introduce characteristic energy levels. In the valence and conduction band, Fermi-Dirac statistics apply, and the characteristic energy levels are the quasi-Fermi levels (QFLs) for free holes E_{fp} and free electrons E_{fn}, respectively (cf. to Eq. (2.10)):

$$E_{\mathrm{fn}} \quad = \quad E_{\mathrm{c}} + \frac{1}{\beta}\ln\left(\frac{n}{N_{\mathrm{c}}}\right), \qquad E_{\mathrm{fp}} \quad = \quad E_{\mathrm{v}} - \frac{1}{\beta}\ln\left(\frac{p}{N_{\mathrm{v}}}\right). \tag{2.36}$$

The occupation of shallow defects is determined by the requirement that the charge carriers are in thermal equilibrium with the corresponding charge carriers in the valence or conduction band. In contrast, the occupation of deep-level defect states is determined by the process of kinetic recombination [Ros55]. It is helpful to define a characteristic energy to distinguish between shallow defects which have rather negligible effect on the total recombination rate, and deep-level defects which typically dominate the recombination rate [Ros55]. Two kinds of characteristic energy levels are commonly used: the demarcation levels (DLs) [Ros63], denoted by E_{D}, and the quasi-Fermi levels for trapped charges (TQFLs) [Sim71], denoted by E_{T}. The demarcation level E_{Dn} for electrons is defined as the energy level where the capture and the re-emission rates from and to the conduction band are equal, i.e. $u_{\mathrm{n}}^{\mathrm{c}}(E_{\mathrm{Dn}}) = u_{\mathrm{n}}^{\mathrm{e}}(E_{\mathrm{Dn}})$. The demarcation level for holes E_{Dp} is defined similarly as the energy where $u_{\mathrm{p}}^{\mathrm{c}}(E_{\mathrm{Dp}}) = u_{\mathrm{p}}^{\mathrm{e}}(E_{\mathrm{Dp}})$. Using SRH theory for the transition rates (Eq. (2.28)), these conditions can be expressed in terms of the QFLs for electrons and holes in Eq. (2.36):

$$\begin{aligned} E_{\mathrm{Dn}}^{\mathrm{SRH}} &= E_{\mathrm{c}} - (E_{\mathrm{fp}} - E_{\mathrm{v}}) + \frac{1}{\beta} \ln\left(\frac{\sigma_{\mathrm{p}} N_{\mathrm{v}}}{\sigma_{\mathrm{n}} N_{\mathrm{c}}}\right), \qquad (2.37a) \\ E_{\mathrm{Dp}}^{\mathrm{SRH}} &= E_{\mathrm{v}} + (E_{\mathrm{c}} - E_{\mathrm{fn}}) - \frac{1}{\beta} \ln\left(\frac{\sigma_{\mathrm{p}} N_{\mathrm{v}}}{\sigma_{\mathrm{n}} N_{\mathrm{c}}}\right) \qquad (2.37b) \end{aligned}$$

The TQFLs for a specific defect distribution are defined as the energy levels where one emission term in the rate equations (2.27) can be neglected. For SRH theory, two TQFLs $E_{\mathrm{Tn}}^{\mathrm{SRH}}$ and $E_{\mathrm{Tp}}^{\mathrm{SRH}}$ are obtained with $u_{\mathrm{p}}^{e}(E_{\mathrm{Tn}}^{\mathrm{SRH}}) = 0$, and $u_{\mathrm{n}}^{e}(E_{\mathrm{Tp}}^{\mathrm{SRH}}) = 0$, respectively. Applying SRH statistics (Eq. (2.28)), this results in:

$$E_{\mathrm{Tn}}^{\mathrm{SRH}} = E_{\mathrm{f}} + \frac{1}{\beta} \ln\left(\frac{c_{\mathrm{n}} + c_{\mathrm{p}}}{c_{\mathrm{n},0}}\right), \qquad E_{\mathrm{Tp}}^{\mathrm{SRH}} = E_{\mathrm{f}} - \frac{1}{\beta} \ln\left(\frac{c_{\mathrm{n}} + c_{\mathrm{p}}}{c_{\mathrm{p},0}}\right). \qquad (2.38)$$

We will show in Sec. 5.2.4 that the TQFLs E_{T} are a more general means for investigating recombination processes than the DLs.

2.2.6 Carrier lifetimes

In the following, we consider all recombination rates introduced in the previous section as independent processes, so they can be summed up to yield the total recombination rate:

$$R = R_{\mathrm{Rad}} + R_{\mathrm{Aug}} + R_{\mathrm{SRH}}. \qquad (2.39)$$

We define the carrier lifetimes for each recombination process as:

$$\tau_i = \frac{\Delta n}{R_i}, \qquad i = \mathrm{Rad,\ Aug,\ SRH}. \qquad (2.40)$$

This definition is useful because the *effective* carrier lifetime τ_{eff} of free charge carriers in the semiconductor is easily measured using the quasi-steady-state photoconductance method [Sin96] (QSSPC). It is defined as:

$$\tau_{\mathrm{eff}} = \frac{\Delta n}{R}. \qquad (2.41)$$

By definition it follows

$$\frac{1}{\tau_{\mathrm{eff}}} = \frac{1}{\tau_{\mathrm{Rad}}} + \frac{1}{\tau_{\mathrm{Aug}}} + \frac{1}{\tau_{\mathrm{SRH}}}. \qquad (2.42)$$

The carrier lifetimes for each recombination process and the resulting effective carrier lifetime are shown in Fig. 2.5 in dependence on the acceptor density N_{A} for three different excess carrier densities Δn for a p-Si substrate. The behavior of τ_{SRH} can be understood by considering the limiting cases of high-injection $N_{\mathrm{A}} \ll \Delta n$ (yellow background) and low-injection $N_{\mathrm{A}} \gg \Delta n$ (orange background). If $\tau_0 := \tau_{\mathrm{n}} = \tau_{\mathrm{p}}$, the limits are $\tau_{\mathrm{SRH}} = \tau_0$ for $N_{\mathrm{A}} \gg \Delta n$, and $\tau_{\mathrm{SRH}} = 2\tau_0$ for $N_{\mathrm{A}} \ll \Delta n$. Both the Auger

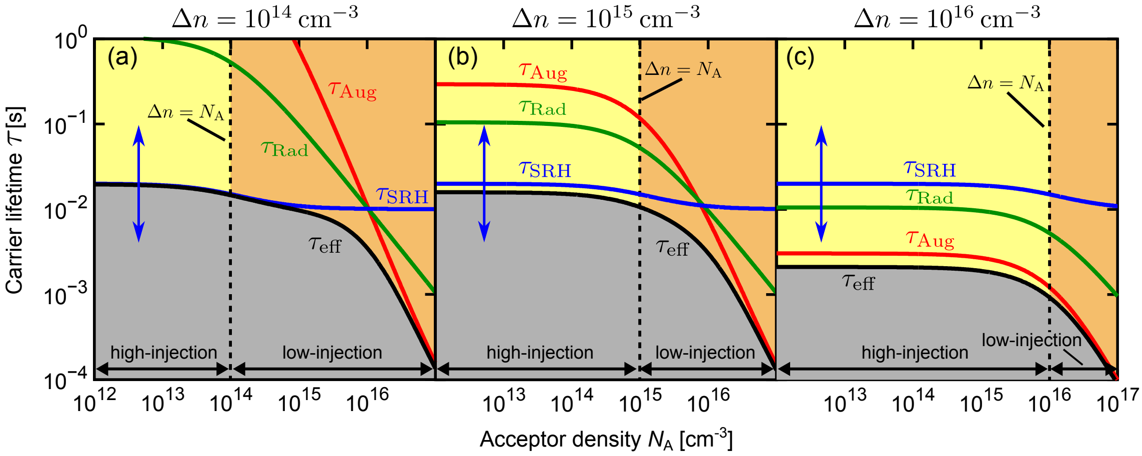

Figure 2.5: Carrier lifetimes in silicon in dependence on the acceptor concentration N_{A} for different excess carrier densities: (a) $\Delta n = 10^{14}\,\mathrm{cm}^{-3}$, (b) $\Delta n = 10^{15}\,\mathrm{cm}^{-3}$, and (c) $\Delta n = 10^{16}\,\mathrm{cm}^{-3}$. Auger lifetimes (red lines), radiative lifetimes (green lines), SRH lifetimes (blue lines), and the effective lifetimes (black lines) are shown. The vertical blue double-arrow indicates that the SRH lifetime is no fundamental material property but depends on the crystal quality. The background colors indicate high-injection conditions (yellow) and low-injection conditions (orange).

and the radiative carrier lifetimes depend in low-injection on the acceptor density N_{A} according to $\tau_{\mathrm{Aug}} \propto N_{\mathrm{A}}^{-2}$ and $\tau_{\mathrm{Rad}} \propto N_{\mathrm{A}}^{-1}$. Note that the above considerations can be made analogously for n-Si by replacing the acceptor density N_{A} with the donor density N_{D}.

For moderate dopant densities in silicon, the carrier lifetime under low to medium injection conditions is often dominated by the SRH lifetime which depends on the crystal quality, as indicated by the double-arrows in Fig. 2.5. The influence of radiative recombination is rather small in silicon which is due to the fact that silicon is an indirect semiconductor and radiative recombination can only occur in combination with phonon-assisted transitions. Thus, for high dopant densities, the carrier lifetimes are typically dominated by Auger recombination. Comparing the graphs in Fig. 2.5 shows that with increasing Δn both Auger and radiative recombination gain influence.

2.2.7 Coupled-defect level (CDL) recombination

If the defect density is so high that the wave functions of the defects overlap to a considerable amount, coupling between defects may occur. The possible carrier transition rates between two coupled defects are indicated in Figs. 2.6(a) and 2.6(b) for the case of donor-acceptor pairs (DAPs) which are lying deep in the bandgap. The derivation of the recombination statistics given in the following holds for the general case of two coupled defect levels in the bandgap. The notation is given for DAPs because these defect types are discussed in Chapter 6.

In the SRH formalism, the probability that a defect state captures a free electron or a free hole is given by the capture cross sections (CCS) σ_n and σ_p (cf. Eqs. (2.29) and (2.30)). An acceptor-like defect is often characterized by $\sigma_\mathrm{n} \ll \sigma_\mathrm{p}$, and a donor-like defect has $\sigma_\mathrm{n} \gg \sigma_\mathrm{p}$ (see also Sec. 2.3.2, and Chapters 5 and 6). Consider, for example, the transitions highlighted in Fig. 2.6 for the case that the energy level of the acceptor lies below the donor level (Fig. 2.6(a)) or above the donor level (Fig. 2.6(b)). Due to the asymmetry in the magnitude of the CCS, the donor-like state captures an electron likely (A), and transfers this electron to the acceptor-like defect (B), which then likely captures a hole (C). Using the nomenclature from the literature [Bin74, Hop63, Tho65], we refer to this type of coupled-defect level recombination as donor-acceptor-pair (DAP) recombination.

From the requirement of detailed balance in thermodynamic equilibrium, it follows that the *emission coefficients* and the *capture coefficients* of the transitions, highlighted in Figs. 2.6(a) and 2.6(b), are related via [Sch95]:

$$e_\mathrm{n}^\mathrm{D} = c_\mathrm{n}^\mathrm{D}\frac{1-f_\mathrm{n}^\mathrm{D}}{f_\mathrm{n}^\mathrm{D}}, \qquad e_\mathrm{p}^\mathrm{A} = c_\mathrm{p}^\mathrm{A}\frac{f_\mathrm{p}^\mathrm{A}}{1-f_\mathrm{p}^\mathrm{A}}, \qquad \hat{e}_\mathrm{DA} = \hat{c}_\mathrm{DA}\frac{g_1^\mathrm{D}}{g_0^\mathrm{D}}\frac{g_0^\mathrm{A}}{g_1^\mathrm{A}}\,\mathrm{e}^{-\beta(E_\mathrm{A}-E_\mathrm{D})}, \tag{2.43}$$

where

$$f_\mathrm{n,p}^\mathrm{A,D} = \left[1+\frac{g_0^\mathrm{A,D}}{g_1^\mathrm{A,D}}\,\mathrm{e}^{\beta(E_\mathrm{c}-E_\mathrm{A,D}-E_\mathrm{fn,p})}\right]^{-1}, \tag{2.44}$$

and $g_0^\mathrm{A,D}$ ($g_1^\mathrm{A,D}$) are the degeneracy factors for the unoccupied (occupied) defect states of donor-like defects (D) and acceptor-like (A) defects, respectively. The *reduced* capture and emission coefficients $\hat{c}_\mathrm{DA}$ and $\hat{e}_\mathrm{DA}$ are related to the capture and emission coefficients via [Sch95]:

$$c_\mathrm{DA} = \hat{c}_\mathrm{DA} N_\mathrm{D} N_\mathrm{A}, \tag{2.45}$$

where N_D and N_A are the defect densities of acceptor- and donor-like defects.

Assuming steady-state conditions, the DAP recombination rate is given by [Sch95]:

$$\begin{aligned} R_\mathrm{DAP} &= R_\mathrm{A} + R_\mathrm{D} + \left(\sqrt{R_\mathrm{DA}^2 - S_\mathrm{DA}} - R_\mathrm{DA}\right) \\ &\times \frac{\tau_\mathrm{n}^\mathrm{D}\tau_\mathrm{p}^\mathrm{A}(n+n_\mathrm{A})(p+p_\mathrm{D}) - \tau_\mathrm{n}^\mathrm{A}\tau_\mathrm{p}^\mathrm{D}(n+n_\mathrm{D})(p+p_\mathrm{A})}{r_\mathrm{D} r_\mathrm{A}}. \end{aligned} \tag{2.46}$$

Thereby, R_A and R_D are the net SRH recombination rates of the isolated acceptor- and donor-like defect, respectively [Sho52]:

$$R_\mathrm{A,D} = \frac{np - n_{i,\mathrm{eff}}^2}{r_\mathrm{A,D}},$$

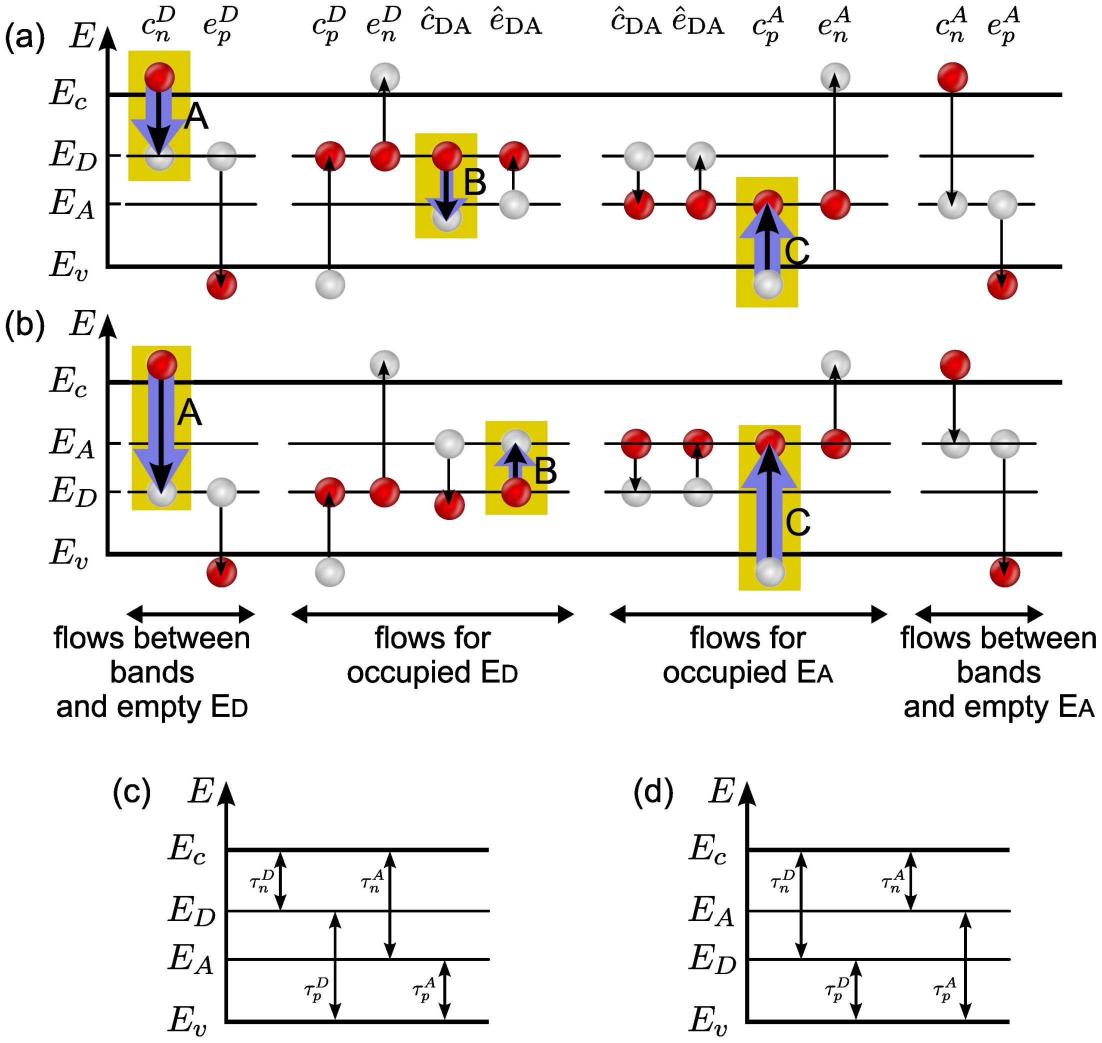

Figure 2.6: Band diagram with all charge carrier transitions according to the donor-acceptor-pair (DAP) recombination theory, considered for the case that (a) the donor-level lies above the acceptor-level and that (b) the donor-level lies below the acceptor-level. White balls indicate states occupied by a hole and red balls indicate states that are occupied by an electron. The capture and emission coefficients are labeled above the sketch. The transitions dominating for low forward biases are highlighted and the thick purple arrows illustrate the occurrence of saturation behavior. In (c)–(d), the definitions of the charge carrier lifetime parameters used in Eq. (2.46) for the transitions in (a) and (b) are indicated.

where

$$r_{\mathrm{A,D}} = \tau_{\mathrm{n}}^{\mathrm{A,D}}(p + p_{\mathrm{A,D}}) + \tau_{\mathrm{p}}^{\mathrm{A,D}}(n + n_{\mathrm{A,D}}), \tag{2.47}$$

and $n_{\mathrm{A,D}}$, $p_{\mathrm{A,D}}$ are defined according to Eq. (2.34). The inter-defect recombination rate is given by [Sch95]:

$$\begin{aligned} R_{\mathrm{DA}} \;=\; & \frac{r_{\mathrm{D}} r_{\mathrm{A}}}{2 c_{\mathrm{DA}} \tau_{\mathrm{n}}^{\mathrm{D}} \tau_{\mathrm{n}}^{\mathrm{A}} \tau_{\mathrm{p}}^{\mathrm{D}} \tau_{\mathrm{p}}^{\mathrm{A}} (1-\gamma)} + \frac{\tau_{\mathrm{n}}^{\mathrm{D}}(p + p_{\mathrm{D}}) + \tau_{\mathrm{p}}^{\mathrm{A}}(n + n_{\mathrm{A}})}{2 \tau_{\mathrm{n}}^{\mathrm{D}} \tau_{\mathrm{p}}^{\mathrm{A}} (1-\gamma)} \\ & + \gamma \frac{\tau_{\mathrm{n}}^{\mathrm{A}}(p + p_{\mathrm{A}}) + \tau_{\mathrm{p}}^{\mathrm{D}}(n + n_{\mathrm{D}})}{2 \tau_{\mathrm{n}}^{\mathrm{A}} \tau_{\mathrm{p}}^{\mathrm{D}} (1-\gamma)}, \end{aligned} \tag{2.48a}$$

and

$$S_{\mathrm{DA}} = \frac{1}{\tau_{\mathrm{n}}^{\mathrm{D}} \tau_{\mathrm{p}}^{\mathrm{A}} (1-\gamma)} \left(1 - \gamma \frac{\tau_{\mathrm{n}}^{\mathrm{D}} \tau_{\mathrm{p}}^{\mathrm{A}}}{\tau_{\mathrm{n}}^{\mathrm{A}} \tau_{\mathrm{p}}^{\mathrm{D}}} \right) (np - n_{\mathrm{i,eff}}^{2}), \tag{2.48b}$$

where

$$\gamma = \mathrm{e}^{-\beta |E_{\mathrm{A}} - E_{\mathrm{D}}|}. \tag{2.48c}$$

The definitions of the charge carrier lifetime parameters $\tau_{\mathrm{n,p}}^{\mathrm{A,D}}$ are indicated in Figs. 2.6(c) and 2.6(d). It is worth noting that the DAP recombination is an extension to the SRH formalism. In the limit of $c_{DA} \longrightarrow 0$, Eq. (2.46) is reduced to the SRH formulation of two non-coupled defects (cf. Eq. (2.35)).
At a sufficiently high injection density Δn, the recombination rate R_{DAP} may become limited by one of the three transitions highlighted in Figs. 2.6(a) and 2.6(b), respectively. Consider, for example, the transitions A→B→C in Fig. 2.6(a). Given that c_{n}^{D} and c_{p}^{A} are large (A,C), the DAP recombination may be limited by the inter-defect coefficient $\hat{c}_{\mathrm{DA}}$ for $E_{\mathrm{A}} < E_{\mathrm{D}}$ (B). Accordingly, DAP recombination may be limited by $\hat{e}_{\mathrm{DA}}$ for $E_{\mathrm{A}} > E_{\mathrm{D}}$ (cf. Fig. 2.6(b)). If R_{DAP} dominates the remaining recombination rates in a solar cell, the total recombination rate may become limited by the inter-defect coupling rate between the two defects of a DAP. This leads to a saturation behavior in the recombination currents which will be investigated in detail in Chapter 6.

2.2.7.1 Comments on simplifications

Here, we shortly comment on the approximations made in the DAP model which considers band diagrams in analogy to isolated levels. We are aware that this treatment implies some serious simplifications:

- The energy levels are considered to be constant and independent of each other. In reality, the energy of one level of the DAP depends on the occupancy state of the other level. Therefore, a DAP system must rather not be displayed in a band diagram, as this is a one-electron scheme. In our model, however, we neglect the Coulomb interaction energy (which may be in the order of 100 meV for closely spaced pairs).

- The CCS are assumed to be constant, independent of the occupancy of the coupled energy levels. It may be assumed that essentially, the ionization of one defect in a DAP causes a reduction of the CCS of the other defect in the DAP, because the electric field of this defect partly compensates the attractive field of the other defect.
- The DAPs are arranged in a regular cubic lattice. This underestimates the statistical variability because, in reality, pairs with different distances may interact. In addition, we allow each donor to interact with each acceptor within one ensemble. This overestimates the statistical variability because, in reality, the defect-charges of the one type are screened by the charges of surrounding defects of the other type.

2.2.8 SRH surface recombination

We model the recombination rate R_{surf} at the surface of c-Si or at the interface between c-Si and a passivating layer (e.g. $\mathrm{SiO_2}$, SiN_x or $\mathrm{Al_2O_3}$) using the SRH formalism for surfaces [Hal52, Sho52]:

$$R_{\mathrm{surf}} = \frac{p_{\mathrm{s}} n_{\mathrm{s}} - n_{\mathrm{i,eff}}^2}{(n_{\mathrm{s}} + n_1)/S_{\mathrm{p}} + (p_{\mathrm{s}} + p_1) S_{\mathrm{n}}}, \tag{2.49}$$

where n_1 and p_1 are defined in Eq. (2.34), and n_{s} and p_{s} are the electron and hole densities at the surface of silicon. R_{surf} depends strongly on the product $n_{\mathrm{s}} p_{\mathrm{s}}$ in excess of their densities at thermal equilibrium, $n_{0,\mathrm{s}} p_{0,\mathrm{s}} = n_{\mathrm{i,eff}}^2$. The recombination properties of the defects at the interface are defined by their *surface velocity parameters* S_{n} and S_{p} and by the energy of the defect state E_{d} with respect to the band edges E_{v} and E_{c}. Similar to the SRH lifetime parameters in the volume of a semiconductor (Eq. (2.33)), one may use the CCS σ_{n} and σ_{p} for electron and hole capture, respectively, and the interface defect density N_{s}. They are related to S_{n} and S_{p} via:

$$S_{\mathrm{n}} = N_{\mathrm{s}} \sigma_{\mathrm{n}} v_{\mathrm{th,n}} \quad \text{and} \quad S_{\mathrm{p}} = N_{\mathrm{s}} \sigma_{\mathrm{p}} v_{\mathrm{th,p}}. \tag{2.50}$$

As R_{surf} is approximately proportional to the injection density Δn, it is convenient to asses the recombination properties by means of the *surface recombination velocity* $S := R_{\mathrm{surf}}/\Delta n$.

Passivating dielectric layers often contain a high density of fixed charges, Q_{f} (unless additional manipulation is applied [Web94]). These charges attract (repel) the excess carriers to (from) the silicon surface, such that the excess charge density is different for electrons and holes. Thus, n_{s} and p_{s} are difficult to quantify experimentally, and S is not an easily measurable quantity. The attraction and repulsion of charge

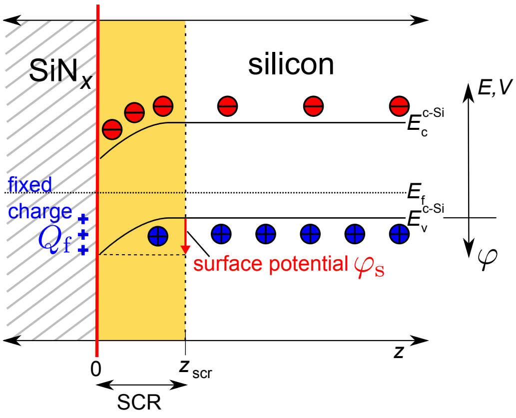

Figure 2.7: Sketch of the band edge diagram at the SiN$_x$/c-Si interface. Δn is measured at a distance z_{SCR} from the silicon surface where the band bending φ_s is negligible.

carriers to and from the surface induces a space-charge region (SCR) in the silicon as a consequence of the requirement for charge neutrality. One refers to the excess carrier density Δn at a depth z_{SCR} further below the silicon surface in the quasi-neutral region, where the space charge has become negligible and the energy bands are flat (cf. Fig. 2.7). At this depth, Δn is easily measurable. One calls

$$S_{\text{eff}} := \frac{R_{\text{surf}}}{\Delta n(z_{\text{SCR}})} \tag{2.51}$$

the *effective* surface recombination velocity. We will refer to $\Delta n(z_{\text{SCR}})$ as Δn within this entire work.

A charge present at the interface induces a band bending φ_s near the surface to account for charge neutrality in the whole device, as shown in Fig. 2.7 for the example of a SiN$_x$/c-Si interface with a strongly positive Q_f. If Q_f is the only charge present at the interface, φ_s can be computed by numerically solving the equation [Gro66, Kin55, You61]

$$\frac{Q_f^2}{c} = n(\mathrm{e}^{q\beta\varphi_s} - q\beta\varphi_s - 1) + p(\mathrm{e}^{-q\beta\varphi_s} + q\beta\varphi_s - 1), \qquad \text{where} \quad c = \frac{2\varepsilon_0\varepsilon_r}{\beta}, \tag{2.52}$$

for example using Brent's root finding algorithm described in Sec. 3.2. The electron and hole densities, $n = n_0 + \Delta n$ and $p = p_0 + \Delta p$, respectively, are referred to in the quasi-neutral region at the location z_{SCR} where $\Delta n = \Delta p$. n_0 and p_0 denote the carrier densities in the quasi-neutral region at thermal equilibrium. The concentrations of electrons and holes at the interface can be calculated by [e.g. Sze81]

$$n_s \;=\; n\,\mathrm{e}^{q\beta\varphi_s}, \qquad p_s \;=\; p\,\mathrm{e}^{-q\beta\varphi_s}. \tag{2.53}$$

Note that Eq. (2.52), and thus Eq. (2.53), holds only if both quasi-Fermi levels, E_{fn} and E_{fp}, are constant in the depletion region (between z_{SCR} and the silicon surface). This is the case except for very high R_{surf} values, where a large number of carriers must be supplied from the quasi-neutral region, which causes a considerable gradient in the quasi-Fermi levels. In this case, R_{surf} may be limited by the supply of carriers instead of by S_{n} and S_{p} and is called diffusion-limited recombination.

According to Eq. (2.49), essentially two quantities influence the surface recombination rate significantly: (i) the surface recombination velocity parameters $S_{\mathrm{n}}, S_{\mathrm{p}}$ which are directly proportional to the surface defect density N_{s}, and (ii) the concentrations of electrons n_{s} and holes p_{s} at the surface. Hence, a decrease of both N_{s} and the product $p_{\mathrm{s}}n_{\mathrm{s}}$ reduce S_{eff}. In technology, the first issue is typically accounted for by saturating the DBs with hydrogen or oxygen. To account for the second matter, the product $n_{\mathrm{s}}p_{\mathrm{s}}$ can be efficiently reduced by the implementation of a doping profile below the silicon surface by interface charges in an overlying insulator, for example SiN_x, or on a gate electrode [Abe00].

2.3 Defects and recombination in amorphous silicon

One technique to passivate DBs by hydrogen is the deposition of hydrogenated amorphous silicon (a-Si:H) layers at temperatures around 200 °C. Gap states in a-Si:H can be separated into conduction-band tail-states, valence-band tail-states and deep-level states. The conduction-band tail-states originate in thermal disorder [Don98], and are strongly temperature dependent due to modulation by transverse acoustic phonons [Dra91]. The valence-band tail states arise to almost equal parts from structural disorder [Dra91], which is assumed to originate from weak Si–Si bonds [Pow93, Smi87], and from thermal disorder [Dra91]. The temperature dependence of the valence-band tails is less pronounced than for the conduction-band tails, because they are influenced by optical phonons rather than by acoustic phonons [Dra91]. The deep-level states in a-Si:H originate mainly from the DBs [Pow93, Smi87].

During formation of the a-Si:H network, the breaking of a neutral, covalent Si–Si bond results either in a pair of neutral silicon atoms, each keeping one electron and forming a neutral DB, denoted as D_{z}; or in a pair comprising a negatively charged and a positively charged silicon atom, forming a D_{e} and a D_{h} DB, respectively [Pow93]. Due to the inherent disorder of the amorphous lattice, DBs can be created at various energy levels which can be modeled as a continuum of defect states. The creation of a large pool of defects is possible. But provided that the defect formation is a chemical equilibrium process, only defects are realized which lower the overall free energy of the system [Alt02a, Pow93, Pow96] (cf. Sec. 2.3.1). In experiments, diverse distributions of the defect states are found, which are often successfully approximated using defect-pool models (DPM) [Pow93, Pow96], for example in a-Si:H [Bal93, Fef95, Mer01, N9́7, Pow93, Pow96] or at grain boundaries [Alt02a, Kaz04, Pap08].

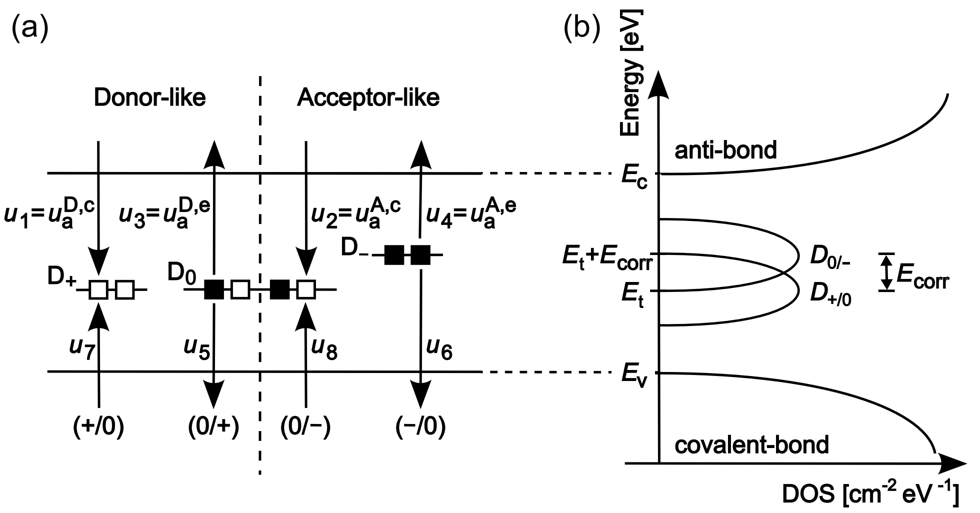

Figure 2.8: (a) Eight possible carrier transitions u_i for amphoteric recombination statistics (for details, see Sec. 2.3.2). (b) Typical defect distribution over energy for the transition from positive to neutral charge state, $D_{+/0}$ (donor-like defect distribution), and from zero to negative charge state, $D_{+/0}$ (acceptor-like defect distribution). These two transitions differ by the correlation energy E_{corr}.

The DB defects can be occupied by zero, one or two electrons. Hence, the DBs may either be in a positive, a neutral, or a negative charge state, indicated by D_+, D_0, and D_-, respectively. Since three charge states are possible for each DB defect, the recombination centers are amphoteric, i.e. they behave in either a donor-like or an acceptor-like manner. A charge transition from the positive to the neutral states ((+/0)-transition) may occur at the donor-like defect distribution $D_{+/0}$ if an electron from the conduction band is captured by the defect, as sketched in Fig. 2.8. Similarly, a charge transition from the neutral to the negative states ((0/−)-transition) may occur at the acceptor-like defect distribution $D_{0/-}$ if the defect captures a second electron from the conduction band. In total, eight charge transitions are possible, denoted by [Li08, Vai86]:

$$D_+ + e^- \rightleftharpoons D_0, \quad \text{with transition rates } u_1, u_3, u_5, u_7, \tag{2.54a}$$

$$D_0 + e^- \rightleftharpoons D_-, \quad \text{with transition rates } u_2, u_4, u_6, u_8, \tag{2.54b}$$

where Eq. (2.54a) denotes the (+/0)-transitions and Eq. (2.54b) denotes the (0/−)-transitions. The eight transition rates u_i between the DBs and the valence band or the conduction band are indicated in Fig. 2.8, and will be discussed in Sec. 2.3.
The energy level of a DB defect depends on both the configuration of the surrounding silicon atoms and on the charge state of the DB [BY87]. The charge dependence of the energy level is mainly due to Coulomb interaction. This results in a characteristic energy shift, denoted as the correlation energy E_{corr}, of the acceptor-like defects $D_{0/-}$ to higher energies with respect to the donor-like defects $D_{+/0}$, as indi-

cated in Fig. 2.8. Besides the Coulomb repulsion depending on the charge state of the DBs, E_{corr} depends on several further effects: possible lowering by lattice relaxation at the defect-site [de 09, Jac82, Nor89, Str91b], electron-phonon interactions, and the re-hybridization of DB orbitals [Tan99]. It is generally accepted that E_{corr} is positive in a-Si:H [Nor89, Str91b, Win90], and in the range of $0.2 - 0.45\,\mathrm{eV}$ [de 09, Jac82, Nor89].

In Sec. 2.3.1 we review the DPM developed by Powell and Deane [Pow93] to describe the defect density in a-Si:H. It will be applied in an extended form, described in Sec. 5.1.1, to model the defect density in a-Si:H passivation layers in Secs. 5.2.4.2 and 5.2.4.3. Section 2.3.2 introduces a model, derived by Vaillant and Jousse [Vai86], to accurately describe the recombination rate via amphoteric defects. Unfortunately, amphoteric recombination cannot be expressed by a closed-form solution which causes problems in numerical device simulations. Therefore, an approximation to the exact model is derived in Chapter 5.

2.3.1 The defect-pool model (DPM) by Powell and Deane

This section reviews the derivation of the DPM suggested by Powell and Deane [Pow93]. The fundamental ideas of the DPM were already published by Bar-Yam and Joannopoulos [BY87] who stated (i) that the formation energy of a defect depends on its charge state, (ii) that the differences in the formation energies depend on the Fermi level E_{f}, and (iii) on the energy level E_{d} of the defect. The DPM is a thermodynamic model which considers chemical equilibrium reactions between deep-level states and e.g. distorted Si–Si bonds or Si–H bonds [Alt02a]. The defect-pool describes an energy distribution of sites in a disordered system which possibly form defects. Each site will form a defect only if the corresponding chemical reaction minimizes the free energy of the system. It was shown that hydrogen is important for defect equilibration [Jac90, Jac92, Kak87, Str91a]. For example, the breaking of a weak Si–Si bond (WB) into DBs and its inverse process may be supported by swapping Si-H bonds. There are several different DPMs reported in the literature [e.g. Bal93, Mer01, Sch94b, Sch96] which differ mainly in the considered chemical reactions. In this work, we use the DPM of Ref. [Pow93], which assumes that hydrogen is not part of the defect-pool itself. By mediating defect reactions, hydrogen yields sufficient entropy to lower the defects chemical potential, and thereby allows to explain the measured DOS [Pow93, Str89].

Powell and Deane [Pow93] and Street and Winer [Str89] consider essentially three possible defect reactions, where i Si–H bonds mediate the WB-breaking reaction

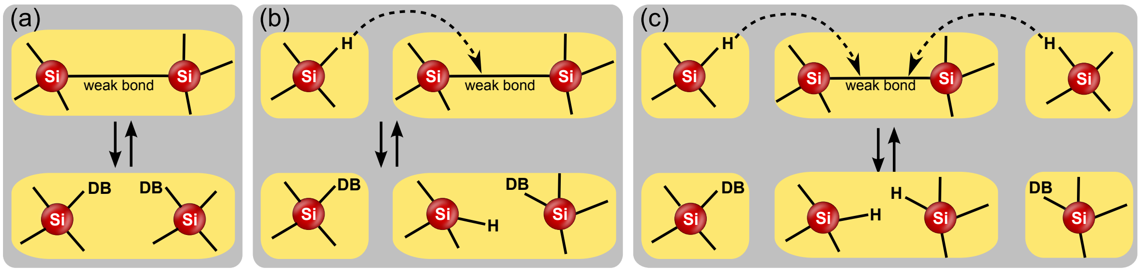

Figure 2.9: Schematics of the defect reactions in the defect-pool model (DPM) in Eqs. (2.55a)–(2.55c).

and lead to the formation of DB defects:

$$\text{WB} \rightleftharpoons (\text{2DB})_{\text{pair}}, \qquad i = 0 \tag{2.55a}$$

$$(\text{Si–H}) + \text{WB} \rightleftharpoons (\text{DB} + \text{Si–H}) + \text{DB}, \qquad i = 1 \tag{2.55b}$$

$$2(\text{Si–H}) + \text{WB} \rightleftharpoons (\text{Si–HH–Si}) + \text{2DB}, \qquad i = 2. \tag{2.55c}$$

Figure 2.9(a) illustrates the reaction (2.55a) which describes the conversion of a WB into a pair of DBs which do not diffuse apart. A weak bonding orbital is likely to break apart, and it is commonly assumed that the WBs can be associated with the valence-band tail-states [Smi87]. Reaction (2.55b) considers the case where an H-atom is released from an H-site (an a-Si:H bond), and breaks a WB, as sketched in Fig. 2.9(b). Here, one defect remains on an isolated a-Si:H bond from which the H-atom is removed and the other defect remains in a singly occupied WB [Pow93]. In the last reaction (2.55c), illustrated in Fig. 2.9(c), a second H is released from a Si–H bond and a doubly hydrogenated WB as well as two isolated DB defects remain [Pow93].

To find an expression for the defect density, first the chemical potential of the defects needs to be specified. Note that for constant volume V and constant temperature T, the free energy density $\mathcal{F} = \mathcal{E} - T\mathcal{S}$ is minimized in equilibrium. Here, $\mathcal{E}$ is the internal energy, defined by the sum of all energy contributions to the thermodynamic system and $\mathcal{S}$ is the conventional entropy.[6] The chemical potential μ_d is defined as the change in free energy when adding a defect to the system [Dea93, Pow93]:

$$\mu_\text{d}(E_\text{d}) = \langle e(E_\text{d})\rangle - T\mathcal{S}_\text{d}^\text{e}(E_\text{d}) - T\mathcal{S}_\text{d}^\text{H}(E_\text{d}). \tag{2.56}$$

Three terms contribute to μ_d of amphoteric DBs:

(i) the mean energy $\langle e(E_\text{d})\rangle$ of the electron(s) of the defect,

(ii) the entropy $\mathcal{S}_\text{d}^\text{e}(E_\text{d})$ corresponding to the occupancy of the defect by electrons,

---

[6] Note the conventional entropy $\mathcal{S}$ is related to the fundamental entropy s used in Ref. [Pow93] via $\mathcal{S} = k_\text{B}s$.

(iii) additional entropy $\mathcal{S}_{\mathrm{d}}^{\mathrm{H}}(E_{\mathrm{d}})$ of H motion if defect separation due to H motion is allowed.

To begin with (i), the electrons of the defect can be in each of the three charge states:

- *positive*: the electron has been removed to the Fermi level E_{f}
- *neutral*: the energy of the electron is that of the defect E_{d}
- *negative*: an additional electron must be transferred from E_{f} to the defect. Thereby, the additional energy E_{corr} is required to place a second electron on the singly occupied defect. The total energy is therefore $2E_{\mathrm{d}} - E_{\mathrm{f}} + E_{\mathrm{corr}}$.

The mean electron energy $\langle e(E_{\mathrm{d}})\rangle$ is determined by the occupied fractions of the energies contributing to these charge states:

$$\langle e(E_{\mathrm{d}})\rangle = E_{\mathrm{f}} f^{+}(E_{\mathrm{d}}) + E_{\mathrm{d}} f^{0}(E_{\mathrm{d}}) + (2E_{\mathrm{d}} - E_{\mathrm{f}} + E_{\mathrm{corr}}) f^{-}(E_{\mathrm{d}}). \tag{2.57}$$

The occupation fractions f^{+}, f^{0} and f^{-} are obtained by applying the principle of detailed balance and by determining the grand partition function [Vai86]:

$$\begin{aligned} f^{+}(E_{\mathrm{d}}) &= \frac{1}{1 + 2\,\mathrm{e}^{\beta(E_{\mathrm{f}}-E_{\mathrm{d}})} + \mathrm{e}^{\beta(2(E_{\mathrm{f}}-E_{\mathrm{d}})-U)}} && (2.58\mathrm{a}) \\ f^{0}(E_{\mathrm{d}}) &= 2\,\mathrm{e}^{\beta(E_{\mathrm{f}}-E_{\mathrm{d}})} f^{+}(E_{\mathrm{d}}) && (2.58\mathrm{b}) \\ f^{-}(E_{\mathrm{d}}) &= \mathrm{e}^{\beta(2(E_{\mathrm{f}}-E_{\mathrm{d}})-U)} f^{+}(E_{\mathrm{d}}), && (2.58\mathrm{c}) \end{aligned}$$

with $f^{+}(E_{\mathrm{d}}) + f^{0}(E_{\mathrm{d}}) + f^{-}(E_{\mathrm{d}}) = 1$. E_{d} is the energy of the (+/0)-transition and $E_{\mathrm{d}} + E_{\mathrm{corr}}$ is the energy of the (0/−)-transition.
According to the Boltzmann definition [Kit01], the entropy due to the electron occupancy (issue (ii)) is given by $\mathcal{S}_{\mathrm{d}}^{\mathrm{e}} = -k_{\mathrm{B}} \sum p_j \ln(p_j)$. Here, p_j is the probability of the system to be in state j and the summation is done over all accessible states. For the DB defects, this yields [Pow93]:

$$\mathcal{S}_{\mathrm{d}}^{\mathrm{e}} = -k_{\mathrm{B}} \left[f^{+}(E_{\mathrm{d}}) \ln(f^{+}(E_{\mathrm{d}})) + 2\frac{f^{0}(E_{\mathrm{d}})}{2} \ln\left(\frac{f^{0}(E_{\mathrm{d}})}{2}\right) + f^{-}(E_{\mathrm{d}}) \ln(f^{-}(E_{\mathrm{d}}))\right]. \tag{2.59}$$

The additional factor 2 in the middle term of Eq. (2.59) is due to the spin degeneracy of the neutral state. For the cases of positively charged ($f^{+} = 1$) or negatively charged ($f^{-} = 1$) defects, we find $\mathcal{S}_{\mathrm{d}}^{\mathrm{e}} = 0$, whereas $\mathcal{S}_{\mathrm{d}}^{\mathrm{e}} = -k_{\mathrm{B}} \ln(1/2)$ for neutral defects. This means that neutral defects are formed twice as likely than one would expect when considering only energetic reasons [Pow93].
Using $f^{+}(E_{\mathrm{d}}) + f^{0}(E_{\mathrm{d}}) + f^{-}(E_{\mathrm{d}}) = 1$, and neglecting the hydrogen entropy for the moment, the chemical defect potential becomes [Pow93]:

$$\mu_{\mathrm{d}} = 2E_{\mathrm{d}} - E_{\mathrm{f}} + E_{\mathrm{corr}} + \frac{\ln(f^{-}(E_{\mathrm{d}}))}{\beta}. \tag{2.60}$$

The entropy $\mathcal{S}_\mathrm{d}^\mathrm{e}$ is too small to explain measured defect distributions. Thus, an additional effect needs to be accounted for: a defect can be transferred away from its origin, the broken WB, to a distant hydrogen site if H-atoms are allowed to swap from Si–H bonds. During this process, the defect gains extra entropy. The number of defects that can swap is $i = 0, 1$ or 2, depending on the reaction (2.55a)–(2.55c). We remark that due to the successive supply of H-atoms compared to the defect density, a huge amount of entropy $\mathcal{S}_\mathrm{d}^\mathrm{H}$ is available. However, defects at energy E_d are only able to gain energy from hydrogen sites that would form a defect at the same energy [Pow93]. Consider, as an example, the formation of a DB at energy E_d from a Si–H site by removal of the H-atom. If N_H is the total H concentration and $P(E_\mathrm{d})$ is the energy distribution of sites that would arise at E_d, the number of these sites is $N_\mathrm{H}P(E_\mathrm{d})$. One calls $P(E_\mathrm{d})$ the defect-pool function. The probability that a defect exists at one of the Si–H sites is [Pow93]

$$p_\mathrm{d} = \frac{iD^\mathrm{DB}(E_\mathrm{d})}{2N_\mathrm{H}P(E_\mathrm{d})}, \tag{2.61}$$

where $D^\mathrm{DB}(E_\mathrm{d})$ is the DB defect density at E_d. As required by the equilibrium reactions (2.55a)–(2.55c), for every two defects that are created, only i defects may swap to distant sites. This is why the factor $i/2$ appears in Eq. (2.61).

The corresponding entropy $\mathcal{S}_\mathrm{d,H} = -k_\mathrm{B}\sum p_d \ln p_d$, where the summation goes over all $N_\mathrm{H}P(E_\mathrm{d})$ hydrogen sites with equal values of p_d. It reads per defect at E_d [Pow93]:

$$\mathcal{S}_\mathrm{d}^\mathrm{H} = -\frac{i}{2}k_\mathrm{B}\ln\left(\frac{iD^\mathrm{DB}(E_\mathrm{d})}{2N_\mathrm{H}P(E_\mathrm{d})}\right). \tag{2.62}$$

Inserting Eqs. (2.59) and (2.62) into Eq. (2.56), we obtain for the total defect chemical potential [Pow93]:

$$\mu_\mathrm{d}(E_\mathrm{d}) = E_\mathrm{d} + \frac{1}{\beta}\left[\ln\left(\frac{f^0(E_\mathrm{d})}{2}\right) + \frac{iD^\mathrm{DB}(E_\mathrm{d})}{2}\ln\left(\frac{i}{2N_\mathrm{H}P(E_\mathrm{d})}\right)\right]. \tag{2.63}$$

To finally calculate the DB defect density $D^\mathrm{DB}(E_\mathrm{d})$, the probability of converting a WB state at energy E_WB is required. Thereby, one must take the depletion of the WBs and the formation of two DBs from one WB into account. We denote the WB states by D_WB, and assume that the WBs are the valence-band tails [Smi87] which can be described by $D_\mathrm{WB}(E_\mathrm{WB}) = N_\mathrm{v0}\exp\left((E_v^\text{a-Si} - E_\mathrm{WB})/E_\mathrm{v0}\right)$. Here, N_v0 is the density of tails states and $E_v^\text{a-Si}$ is the energy of the valence-band mobility-edge in a-Si:H. The so called Urbach energy E_v0 has been measured to increase with increasing disorder [Stu89].

The density of WBs at the energy E_WB, which lead to potential defect sites at the energy E_d, is given by $P(E_\mathrm{d})D_\mathrm{WB}(E_\mathrm{WB})$. Accounting for the depletion of a WB by the two formed DB defects, it follows for the defect density:

$$D^\mathrm{DB}(E_\mathrm{d}) = \frac{P(E_\mathrm{d})D_\mathrm{WB}(E_\mathrm{WB})}{1 + \mathrm{e}^{2\beta(\mu_\mathrm{d}(E_\mathrm{d}) - E_\mathrm{WB})}}. \tag{2.64}$$

In Eq. (2.64), it was assumed that the energy difference between a WB and a DB can be described in a one-electron picture, meaning that the energy difference is approximated by the difference in electronic energy [Pow93, Smi87]. This approach neglects ionic relaxation energies and multielectron contributions, which seems to be a reasonable approximation [Hei80, Pow93, Smi87]. We emphasize that according to Eq. (2.64), the energy of both DBs (each WB forms two DB defects) is E_d because the two defects minimize their free energy independently and thus, have on average the same energy [Pow93].

So far, we considered only one WB at a distinct energy E_WB. To account for all WBs, which are typically distributed in energy, we must integrate Eq. (2.64) over the WB-energies:

$$D^\mathrm{DB}(E_\mathrm{d}) = \int \mathrm{d}E_\mathrm{WB}\, \frac{P(E_\mathrm{d}) D_\mathrm{WB}(E_\mathrm{WB})}{1 + \mathrm{e}^{2\beta(\mu_\mathrm{d}(E_\mathrm{d}) - E_\mathrm{WB})}}. \tag{2.65}$$

The DPM [Pow93] uses an approximation of the integral in Eq. (2.65). It assumes that:

(i) for $\mu_\mathrm{d} < E_\mathrm{WB}$, all WB states are converted into DBs, and

(ii) for $\mu_\mathrm{d} \geq E_\mathrm{WB}$, a Boltzmann fraction of the WB states are converted into DBs.

Using Eq. (2.63), this leads to:

$$D^\mathrm{DB}(E_\mathrm{d}) = \kappa P\left(E_\mathrm{d} + \frac{\rho\sigma_\mathrm{DP}^2}{E_\mathrm{v0}}\right)\left(\frac{2}{f^0(E_\mathrm{d})}\right)^{\rho/\beta E_\mathrm{v0}}, \tag{2.66a}$$

$$P(E_\mathrm{d}) = \frac{1}{\sigma_\mathrm{DP}\sqrt{2\pi}}\,\mathrm{e}^{\frac{(E_\mathrm{d}-E_\mathrm{p})^2}{2\sigma_\mathrm{DP}^2}}, \tag{2.66b}$$

$$\kappa = \left(\frac{2\beta N_\mathrm{v0}E_\mathrm{v0}^2}{2E_\mathrm{v0}\beta - 1}\right)^{\rho}\left(\frac{i}{2N_\mathrm{H}}\right)^{\rho-1}\mathrm{e}^{-\frac{\rho}{E_\mathrm{v0}}\left(E_\mathrm{p} - E_\mathrm{v} - \frac{\rho\sigma_\mathrm{DP}}{2E_\mathrm{v0}}\right)}, \tag{2.66c}$$

where σ_DP is the width of the Gaussian distributed defect-pool, $f^0(E)$ is the occupation fraction of neutral DBs, and $\rho = 2E_\mathrm{v0}/(2E_\mathrm{v0} + i/\beta)$. Note that this leads to a vanishing DB density $D^\mathrm{DB}(E_\mathrm{d}) = 0$ for $i = 0$ because $\kappa \longrightarrow 0$, i.e. for the reaction (2.55a). E_p in Eqs. (2.66b) and (2.66c) is the most probable energy for defect formation, given by $E_\mathrm{p} = E_\mathrm{f}^\mathrm{eq} + \rho\sigma_\mathrm{DP}^2/E_{v0} - E_\mathrm{corr}/2$, where E_f^eq is the Fermi level during defect formation.

Care must be taken for temperatures below the equilibration temperature $T^\mathrm{eq} \approx 500\,\mathrm{K}$, because then all states are frozen in and, hence, the parameter values of E_v0, T and $E_\mathrm{f} = E_\mathrm{f}^\mathrm{eq}$ at the equilibration temperature must be used.

In measurements, typically only the *effective* density of states $g(E_\mathrm{d})$ in the *one-electron* picture can be determined. Thus, it is convenient to introduce an analytical

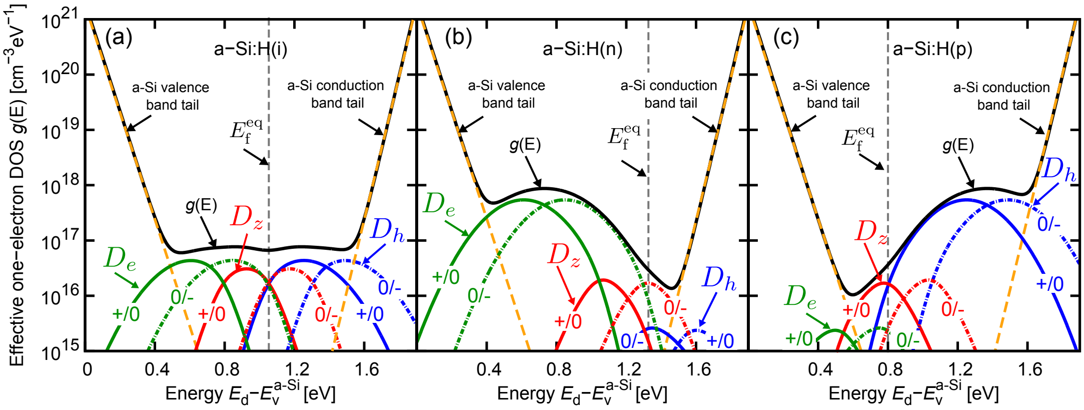

Figure 2.10: Effective one-electron DOS $g(E_\mathrm{d})$ with the contributions of the tail states and the DB states (Eq. (2.67)). The DB states $D^\mathrm{DB}(E_\mathrm{d})$ calculated with Eq. (2.66a) are resolved and separated depending on their charge state during formation into D_e (red lines), D_z (green lines), and D_h states (blue lines) [Pow93], and split up into $(+/0)$ (continuous lines) and $(0/-)$ (dashed lines) transitions. Here, $i = 2$, $E_\mathrm{v0} = 36\,\mathrm{meV}$, $E_\mathrm{corr} = 200\,\mathrm{meV}$, $\sigma_\mathrm{DP} = 178\,\mathrm{meV}$, $N_\mathrm{v0} = 2 \times 10^{21}\,\mathrm{cm}^{-3}\mathrm{eV}^{-1}$. The equilibration Fermi level $E_\mathrm{f}^\mathrm{eq} := E_\mathrm{f,i}^\mathrm{eq} + E_\mathrm{f,sh}$ (cf. Eq. (2.69)) is indicated with arrows and is $E_\mathrm{f,sh} = 0\,\mathrm{eV}$ for a-Si:H(i) in (a), $E_\mathrm{f,sh} = 0.25\,\mathrm{eV}$ for a-Si:H(n) in (b), and $E_\mathrm{f,sh} = -0.25\,\mathrm{eV}$ for a-Si:H(p) in (c). $E_v^\text{a-Si}$ denotes the mobility edge of a-Si:H. All parameters are taken from Ref. [Pow93].

approximation for the effective DB-DOS $g_\mathrm{DB}(E_\mathrm{d})$ [Pow93]:

$$\begin{aligned} g_\mathrm{DB}(E_\mathrm{d}) &\approx D^\mathrm{DB}\left(E_\mathrm{d} + \frac{\ln(2)}{\beta}\right) + D^\mathrm{DB}\left(E_\mathrm{d} - E_\mathrm{corr} - \frac{\ln(2)}{\beta}\right) && \text{(2.67a)} \\ &=: D_{+/0}(E_\mathrm{d}) + D_{0/-}(E_\mathrm{d}), && \text{(2.67b)} \end{aligned}$$

where the term $\ln(2)/\beta$ is due to the degeneracy of the neutral state.
We remark that the free energy of the system depends on the energy of the defects and on the Fermi E_f^eq during defect formation. While the defect density D^DB is small for energies near E_f^eq, it is large far away from E_f^eq if the defect-pool is distributed relatively wide within the bandgap [Alt02a, Pow93]. This dependency on E_f^eq is demonstrated in Fig. 2.10. Here, the *effective* density of states $g(E_\mathrm{d})$, consisting of both the DB contributions g_DB in Eq. (2.67) and the tail-state contributions, is displayed for intrinsic a-Si:H (a-Si:H(i)), n-type a-Si:H (a-Si:H(n)), and p-type a-Si:H (a-Si:H(p)). In addition, g_DB, separated into the $D_{+/0}$ and $D_{0/-}$ states of the D_e, D_z, and D_h distributions according to Eq. (2.67), is shown. The distributions D_e, D_z, and D_h are obtained by:

$$D_\mathrm{e}(E_\mathrm{d}) = f^-(E_\mathrm{d})\,D(E_\mathrm{d}), \quad D_\mathrm{z}(E_\mathrm{d}) = f^0(E_\mathrm{d})\,D(E_\mathrm{d}), \quad D_\mathrm{h}(E_\mathrm{d}) = f^+(E_\mathrm{d})\,D(E_\mathrm{d}), \tag{2.68}$$

where the occupation functions f^+, f^0 and f^- are specified in Eq. (2.58). For a-Si:H(i), shown in Fig. 2.10(a), the total effective DOS $g(E_\mathrm{d})$ (black line) forms a plateau of almost constant defect density and is symmetric to the intrinsic equilibration Fermi level $E_\mathrm{f,i}^\mathrm{eq}$. Figure 2.10(b) shows that in a-Si:H(n), E_f^eq is shifted from $E_\mathrm{f,i}^\mathrm{eq}$ towards the conduction band by

$$E_\mathrm{f,sh} := E_\mathrm{f}^\mathrm{eq} - E_\mathrm{f,i}^\mathrm{eq}. \tag{2.69}$$

As a consequence, the acceptor-like defects above midgap become negatively charged. In turn, this results in an enhanced formation of defects below midgap, see the maximum in $g(E_\mathrm{d})$ in Fig. 2.10(b). For sufficiently high disorder, the defect distribution is well approximated by a Gaussian function. The maximum observed in $g(E_\mathrm{d})$ in a-Si:H(p) (cf. Fig. 2.10(c)) is explained analogously by considering that E_f^eq is shifted by $E_\mathrm{f,sh}$ from $E_\mathrm{f,i}^\mathrm{eq}$ towards the valence band.

2.3.2 Recombination via amphoteric defects

In Sec. 2.2.4, we considered recombination via non-correlated defects. In amorphous silicon, this statistics can be applied to model the recombination rate of free charge carriers via the conduction-band and the valence-band tail states, [e.g. Lee10b, Sak86, Vai86] (Secs. 5.2.3 and 5.2.4.3). Thereby, tail recombination is typically negligible because these defects are relatively shallow, and the rate equations (2.27) are dominated by the emission terms (cf. Sec. 2.2.4 and Fig. 2.4). The dominant recombination path in a-Si:H is recombination of free charge carriers via deep-level DB defect states [Vai86]. A mathematical representation for quantifying the recombination in a-Si:H must take into account both the amphoteric nature and the energy shift E_corr between the states corresponding to the transitions from the positive to the neutral charge state ($D_{+/0}$) and from the neutral to the negative charge state ($D_{0/-}$).

In the following, we derive the recombination model proposed by Vaillant and Jousse [Vai86]. The eight possible carrier transition rates u_i, the three charge states D_+, D_0, and D_-, and the two energy levels E_t and $E_\mathrm{t} + E_\mathrm{corr}$ are sketched in Fig. 2.8. For means of clarity, this representation shows the transition rates for discrete defect levels at E_t and $E_\mathrm{t} + E_\mathrm{corr}$, but the equations given in the following apply to arbitrary defect distributions [Li08, Vai86].

The recombination rate is derived for the case of steady-state conditions and non-coupled defects, where the latter is valid for typically measured defect densities [Vai86] (cf. Chapter 6). The system is fully characterized by the following three independent equations of charge conservation [Vai86]:

$$\begin{aligned}\frac{\mathrm{d}n}{\mathrm{d}t} &= u_1 - u_3 + u_2 - u_4 - g = 0, &\quad (2.70a)\\ \frac{\mathrm{d}p}{\mathrm{d}t} &= u_7 - u_5 + u_8 - u_6 - g = 0, &\quad (2.70b)\\ \frac{\mathrm{d}D_+}{\mathrm{d}t} &= u_1 + u_7 - u_3 - u_5 = 0, &\quad (2.70c)\end{aligned}$$

where g is the generation rate of free charge carriers which is zero in thermal equilibrium. The carrier transition rates for electrons (as illustrated in Fig. 2.8) can be expressed as [Vai86]:

$$\begin{aligned} u_{\mathrm{a}}^{\mathrm{D,c}}(E_{\mathrm{d}}) &:= u_1(E_{\mathrm{d}}) = c_{\mathrm{n}}^{+} f^{+}(E_{\mathrm{d}}) D_{+/0}(E_{\mathrm{d}}),\\ u_{\mathrm{a}}^{\mathrm{A,c}}(E_{\mathrm{d}}) &:= u_2(E_{\mathrm{d}}) = c_{\mathrm{n}}^{0} f^{0}(E_{\mathrm{d}}) D_{+/0}(E_{\mathrm{d}}),\\ u_{\mathrm{a}}^{\mathrm{D,e}}(E_{\mathrm{d}}) &:= u_3(E_{\mathrm{d}}) = e_{\mathrm{n,a}}^{0}(E_{\mathrm{d}}) f^{0}(E_{\mathrm{d}}) D_{+/0}(E_{\mathrm{d}}),\\ u_{\mathrm{a}}^{\mathrm{A,e}}(E_{\mathrm{d}}) &:= u_4(E_{\mathrm{d}}) = e_{\mathrm{n,a}}^{-}(E_{\mathrm{d}}) f^{-}(E_{\mathrm{d}}) D_{+/0}(E_{\mathrm{d}}).\end{aligned} \qquad (2.71)$$

In the following, we use the notation for the carrier transition rates given on the left-hand side of Eq. (2.71) to distinguish between acceptor like (index "A") and donor like (index "D") defects. The lower index "a" refers to amphoteric recombination statistics, and the upper indices "c" and "e" refer to electron capture and emission, respectively. The carrier transition rates for holes are:

$$\begin{aligned} u_5(E_{\mathrm{d}}) &= c_{\mathrm{p}}^{0} f^{0}(E_{\mathrm{d}}) D_{+/0}(E_{\mathrm{d}}), & u_6(E_{\mathrm{d}}) &= c_{\mathrm{p}}^{-} f^{-}(E_{\mathrm{d}}) D_{+/0}(E_{\mathrm{d}}),\\ u_7(E_{\mathrm{d}}) &= e_{\mathrm{p,a}}^{+}(E_{\mathrm{d}}) f^{+}(E_{\mathrm{d}}) D_{+/0}(E_{\mathrm{d}}), & u_8(E_{\mathrm{d}}) &= e_{\mathrm{p,a}}^{0}(E_{\mathrm{d}}) f^{0}(E_{\mathrm{d}}) D_{+/0}(E_{\mathrm{d}}).\end{aligned} \qquad (2.72)$$

Different from the SRH statistics for uncorrelated defects (cf. Sec. 2.2.4), the principle of detailed balance imposes certain restrictions to the emission rates of these correlated defects: each DB has to be in equilibrium with the band states [Sah58, Vai86]. Whereas in the uncorrelated approach the emission rates e are determined solely by the capture rates c and the initial conditions, in the correlated approach they are in addition determined by the requirements $u_1 = u_3$, $u_2 = u_4$, $u_5 = u_7$, and $u_6 = u_8$ for each defect level E_{d} [Vai86]. Thus, it follows for the (+/0)-transition of the donor-like defect state at arbitrary defect energy E_{d}:

$$c_{\mathrm{n}}^{+} = v_{\mathrm{th,n}} n \sigma_{\mathrm{n}}^{+}, \qquad c_{\mathrm{p}}^{0} = v_{\mathrm{th,p}} p \sigma_{\mathrm{p}}^{0}, \qquad (2.73a)$$

$$e_{\mathrm{n,a}}^{0}(E_{\mathrm{d}}) = \frac{c_{\mathrm{n},0}^{+}}{2}\, \mathrm{e}^{\beta(E_{\mathrm{d}}-E_{\mathrm{f}})}, \qquad e_{\mathrm{p,a}}^{+}(E_{\mathrm{d}}) = 2 c_{\mathrm{p},0}^{0}\, \mathrm{e}^{\beta(E_{\mathrm{f}}-E_{\mathrm{d}})}, \qquad (2.73b)$$

with

$$c^{+}_{\mathrm{n},0} \;=\; v_{\mathrm{th,n}} n_0 \sigma^{+}_{\mathrm{n}}, \qquad c^{0}_{\mathrm{p},0} \;=\; v_{\mathrm{th,p}} p_0 \sigma^{0}_{\mathrm{p}}. \tag{2.73c}$$

σ^{+}_{n} and σ^{0}_{p} are the CCS for donor-like defect states, and those for acceptor-like states are σ^{0}_{n} and σ^{-}_{p} (see below). All other parameters and quantities have the same meaning as in Eq. (2.29).

For the acceptor-like defect distribution, the capture and emission coefficients are:

$$c^{0}_{\mathrm{n}} = v_{\mathrm{th,n}} n \sigma^{0}_{\mathrm{n}}, \qquad c^{-}_{\mathrm{p}} = v_{\mathrm{th,p}} p \sigma^{-}_{\mathrm{p}}, \tag{2.74a}$$

$$e^{-}_{\mathrm{n,a}}(E_{\mathrm{d}}) = 2c^{0}_{\mathrm{n},0}\, \mathrm{e}^{\beta(E_{\mathrm{d}}+E_{\mathrm{corr}}-E_{\mathrm{f}})}, \qquad e^{0}_{\mathrm{p,a}}(E_{\mathrm{d}}) = \frac{c^{-}_{\mathrm{p},0}}{2}\, \mathrm{e}^{\beta(E_{\mathrm{f}}-E_{\mathrm{d}})}, \tag{2.74b}$$

with

$$c^{0}_{\mathrm{n},0} \;=\; v_{\mathrm{th,n}} n_0 \sigma^{0}_{\mathrm{n}}, \qquad c^{-}_{\mathrm{p},0} \;=\; v_{\mathrm{th,p}} p_0 \sigma^{-}_{\mathrm{p}}. \tag{2.74c}$$

At thermal equilibrium, the occupation fractions f^{+}, f^{0} and f^{-} are given by Eq. (2.58). Out of equilibrium, they are derived by inserting the definitions of the carrier transitions (2.71) and (2.72) into the conservation equations in Eq. (2.70) [Vai86]:

$$f^{+}(E_{\mathrm{d}}) \;=\; \frac{1}{1+\frac{e^{+}_{\mathrm{p,a}}(E_{\mathrm{d}})+c^{+}_{\mathrm{n}}}{e^{0}_{\mathrm{n,a}}(E_{\mathrm{d}})+c^{0}_{\mathrm{p}}}\left(1+\frac{e^{0}_{\mathrm{p,a}}(E_{\mathrm{d}})+c^{0}_{\mathrm{n}}}{e^{-}_{\mathrm{n,a}}(E_{\mathrm{d}})+c^{-}_{\mathrm{p}}}\right)} \tag{2.75a}$$

$$f^{0}(E_{\mathrm{d}}) \;=\; \frac{e^{+}_{\mathrm{p,a}}(E_{\mathrm{d}})+c^{+}_{\mathrm{n}}}{e^{0}_{\mathrm{n,a}}(E_{\mathrm{d}})+c^{0}_{\mathrm{p}}} f^{+}(E_{\mathrm{d}}) \tag{2.75b}$$

$$f^{-}(E_{\mathrm{d}}) \;=\; \frac{e^{0}_{\mathrm{p,a}}(E_{\mathrm{d}})+c^{0}_{\mathrm{n}}}{e^{-}_{\mathrm{n,a}}(E_{\mathrm{d}})+c^{-}_{\mathrm{p}}} f^{0}(E_{\mathrm{d}}), \tag{2.75c}$$

with $f^{+}(E_{\mathrm{d}}) + f^{0}(E_{\mathrm{d}}) + f^{-}(E_{\mathrm{d}}) = 1$. The dynamics of the occupation fractions is shown in Fig. 2.11.

Equation (2.70c) implies that the total carrier transition rates of electrons and holes are equal [Vai86]. This is due to the assumption of steady-state conditions and thus, it suffices to evaluate the recombination rate for electrons only. Hence, we find for the recombination rates at donor- and acceptor-like defect states:

$$\begin{aligned} U^{D}_{\mathrm{a}}(E_{\mathrm{d}}) &= u^{\mathrm{D,c}}_{\mathrm{a}}(E_{\mathrm{d}}) - u^{\mathrm{D,e}}_{\mathrm{a}}(E_{\mathrm{d}}) \\ &= v_{\mathrm{th,n}} D_{+/0}(E_{\mathrm{d}}) \sigma^{+}_{\mathrm{n}} \left(n f^{+}(E_{\mathrm{d}}) - \frac{1}{2} n_0 e^{\beta(E_{\mathrm{d}}-E_{\mathrm{f}})} f^{0}(E_{\mathrm{d}}) \right) \end{aligned} \tag{2.76a}$$

$$\begin{aligned} U^{A}_{\mathrm{a}}(E_{\mathrm{d}}) &= u^{\mathrm{A,c}}_{\mathrm{a}}(E_{\mathrm{d}}) - u^{\mathrm{A,e}}_{\mathrm{a}}(E_{\mathrm{d}}) \\ &= v_{\mathrm{th,n}} D_{+/0}(E_{\mathrm{d}}) \sigma^{0}_{\mathrm{n}} \left(n f^{0}(E_{\mathrm{d}}) - 2 n_0 e^{\beta(E_{\mathrm{d}}-E_{\mathrm{f}})} f^{-}(E_{\mathrm{d}}) \right). \end{aligned} \tag{2.76b}$$

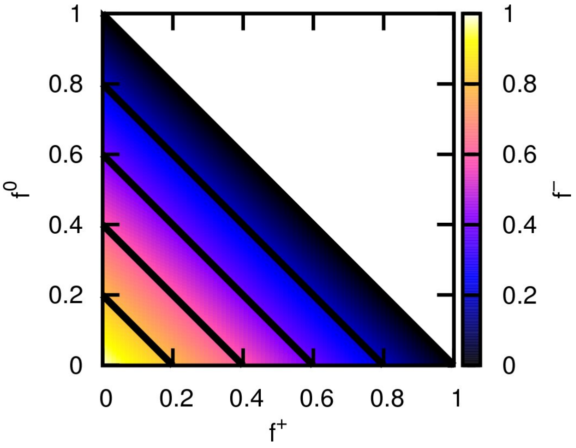

Figure 2.11: Dependence between the occupation probabilities f^+, f^0, and f^- of amphoteric recombination statistics, calculated with Eq. (2.75). The diagonal lines indicate the linear relationship between the probabilities.

The total recombination rate in dependence on the defect energy E_d follows from a superposition of the rates via both defect distributions:

$$U_\mathrm{a}(E_\mathrm{d}) = U^D(E_\mathrm{d}) + U^A(E_\mathrm{d}). \tag{2.77}$$

The amphoteric recombination statistics cannot be solved in a closed form and thus, approximations to this model are desirable. In Chapter 5, we suggest an approximate SRH-model which imitates the amphoteric character for certain prerequisites, and investigate the differences between the correlated amphoteric and the uncorrelated amphoteric approach.

2.4 Solar cell characteristics

The current-voltage characteristics (I-V curve) contains the relevant properties of a solar cell. One distinguishes between the I-V curve measured in the dark and under illumination.

2.4.1 The *I*-*V* curve without illumination

2.4.1.1 Shockley equation and ideality factor

The dark I-V curve coincides with the diode characteristics of the solar cell, and the measured current is equal to the recombination current. The recombination current in semiconductors is usually quantified using the SRH recombination statistics via a single defect level [Hal52, Sho52], discussed in Sec. 2.2.4. When this model is applied to recombination in the SCR of p-n junction diodes, it influences the diode ideality factor n_D of the current-voltage (I-V) curve, described by the Shockley equation [Sho49]:

$$j(V) = j_0 \left(\mathrm{e}^{\frac{q\beta V}{n_\mathrm{D}}} - 1 \right), \tag{2.78}$$

where j_0 is the saturation current-density and j is the diode current density I/A (current per area). Usually, the bias-dependent ideality factor n_D is approximated from Eq. (2.78) as:

$$n_\mathrm{D}(V_i) = \frac{q\beta(V_i - V_{i-1})}{\ln\left(j(V_i)/j(V_{i-1})\right)}, \tag{2.79}$$

where the subscripts i and $i-1$ of V denote neighboring voltage points of the measured *I*-*V* curve, and $j(V_i)$, $j(V_{i-1})$ are the corresponding current densities. This equation is only valid at $V > 3/q\beta$. Therefore, we use the more accurate method proposed by Rhoderick and Williams [Rho88]:

$$n_\mathrm{D}(V_i) = \frac{q\beta(V_i - V_{i-1})}{\ln\left(\frac{j(V_i)\left(1-\mathrm{e}^{-q\beta V_{i-1}}\right)}{j(V_{i-1})\left(1-\mathrm{e}^{-q\beta V_i}\right)}\right)}. \tag{2.80}$$

Equation (2.80) is also valid near 0 V and for reverse bias.

2.4.1.2 Limitations to the ideality factor by SRH statistics

The ideality factor n_D cannot increase above 2, if SRH theory is used exclusively for modeling the defect recombination [And77, Cho86, Cor96, Lee80, McI00a, Nus73, Pal97, Sah57]. In the following, we give an explanation similar to that of Ref. [McI00a] to show that SRH theory yields $n_\mathrm{D} = 2$ as an upper limit for the ideality factor n_D. We assume a symmetric p-n junction, extended in the z-direction, where the center position is at z_0. A sufficiently high junction voltage ($V \gtrsim 300\,\mathrm{mV}$) is required such that there is $n(z) \gg n_\mathrm{i,eff}$ and $p(z) \gg n_\mathrm{i,eff}$ in the whole depletion region. In this case, there holds $n(z)p(z) \gg n^2_\mathrm{i,eff}$. We further assume that E_d is equal to E_i in the whole depletion region, and consequently $n_1(z) = p_1(z) = n_\mathrm{i,eff}$ (Eqs. (2.13),(2.14) and (2.17)). If, in addition, the lifetime parameters of electrons and holes are equal ($\tau_0 := \tau_\mathrm{n} = \tau_\mathrm{p}$) and uniform in the depletion region, the SRH recombination rate simplifies to:

$$R_\mathrm{SRH} = \frac{n(z)p(z)}{\tau_0\left(n(z) + p(z)\right)}, \tag{2.81}$$

which is maximal at the position z_0, where $n(z) = p(z)$. Assuming further that the quasi-Fermi levels of electrons and holes are constant in the whole depletion region and that they are separated by V, yields:

$$n(z_0) = p(z_0) = n_\mathrm{i}\,\mathrm{e}^{\left(\frac{q\beta V}{2}\right)}. \tag{2.82}$$

Hence, $R_\mathrm{SRH}(z_0) \propto \exp\left(q\beta V/2\right)$ and thus, $n_\mathrm{D} = 2$ (cf. Eq. (2.78)). However, contributions from other regions (e.g. the bulk with $n_\mathrm{D} = 1$) reduce n_D such that $n_\mathrm{D} = 2$ remains as the upper limit that can be obtained by SRH recombination.

In contrast to these theoretical findings, it has been well-known for more than 40 years [Que62] that the forward-characteristics may show n_D values larger than 2, up to values of about 5, over an extended voltage range. This is observed in most industrially fabricated silicon solar cells and frequently also in cell designs under development. Moreover, the reverse characteristics are in these cases typically non-saturating but often increase nearly Ohmic or slightly super-linear with the reverse bias voltage. This effect cannot be described within the SRH model either: it predicts a saturation behavior (cf. Eq. (2.78)).
In Chapter 6, we investigate in detail what kind of effects may explain $n_\mathrm{D} > 2$. We find two likely candidates for this: deep-level DAP recombination (cf. Secs. 2.2.7 and 6.2.1), and p-n junctions bordering on surfaces containing a density of fixed charges (cf. Sec. 6.3.2).

2.4.2 The *I*-*V* curve under illumination

If the contacts of an illuminated solar cell are short-circuit, the photo current is discharged via the contacts, and the short circuit current density j_sc can be measured. In the current-less case, the open circuit voltage V_oc is accessible at the contacts. The optimal working condition for a solar cell is the maximum power point (MPP). It corresponds to the voltage V_mpp, at which the extracted power density P_mpp is maximal. The MPP is determined from the maximum of the current-voltage product. The current density measured at V_mpp is denoted as j_mpp. One defines the fraction of P_mpp and the product $j_\mathrm{sc}V_\mathrm{oc}$ as the fill factor FF of a solar cell:

$$FF = \frac{j_\mathrm{mpp}\,V_\mathrm{mpp}}{j_\mathrm{sc}\,V_\mathrm{oc}}. \tag{2.83}$$

The cell efficiency η is given by the ratio of P_mpp and the power density of the illuminated light P_light:

$$\eta = \frac{j_\mathrm{mpp}\,V_\mathrm{mpp}}{P_\mathrm{light}}. \tag{2.84}$$

These definitions are required for the analysis of *I*-*V* characteristics in Chapter 7.

Chapter 3

Numerical Methods

3.1 Data fitting using genetic algorithms

Microscopic phenomena or quantum mechanical properties are commonly implemented into device simulators by means of parametrized models. The reason is that the accuracy of these models is often sufficient to describe device characteristics, while strongly reduced computation times are provided. The development of such parametric models may contribute significantly to the improvement of solar cells if it relies on physically meaningful parameters, ideally obtained from independent experimental data. However, typically a large number of parameters remains undetermined. These parameters are then adapted by fitting the model to experimental data. Thereby, the reliability of data fitting increases with the number of available data sets N_s, and with the number of parameters that can be determined via independent experiments. During fitting, these parameters have to be carefully restricted to a reasonable range. Nevertheless, the number of local minima in the $N_\mathrm{p} \times N_\mathrm{p}$ parameter space increases rapidly with the number of free parameters N_p, which makes deterministic optimization procedures unsuitable.

Genetic algorithms (GA) meet the challenge of being insensitive to local minima and yet to converge relatively quickly. The first evolutionary algorithm (EA) was applied by Barricelli [Bar54]. One subclass of EAs are GAs, the simplest of which was published in a pioneer work by Holland [Hol75]. Since then, GAs have been established for optimization tasks in diverse applications. Such algorithms mirror biological evolution in which the fitness of a population is increased by the processes of selection, crossover, and mutation [Sch08c]. The typical procedure is sketched in Fig. 3.1. The fitting algorithm is initialized by setting a seed population (generation 0). One or more parents are generated with an initial set of reliable parameter values (*propagation*) by adding a Gaussian random number to every parameter value of the set (*mutation*). During each simulation step, a part of the population is replaced by newly generated children. In each iteration, the members of the current

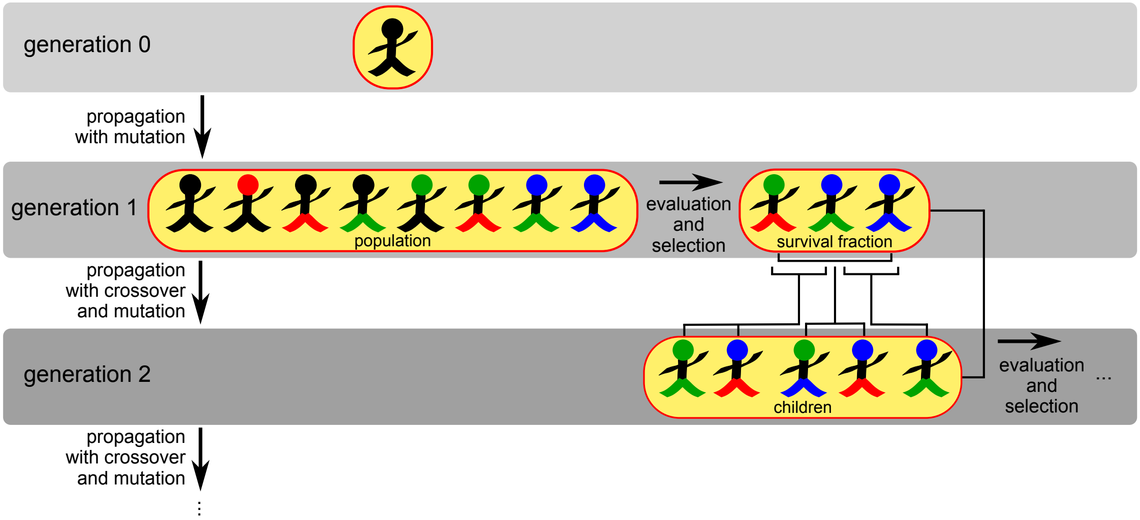

Figure 3.1: Principle of the genetic algorithm (see text for details).

population are evaluated using a fitness function that is based on the least-square-method (*evaluation*, see below). The *selection* is made proportional to the member's fitness [Hol75]. Only the “fittest” fraction of the population survives, and is able to propagate during the next iteration. During propagation, children are generated (generation 1) by mixing the parameter values of two arbitrarily chosen parents (*crossover*), and adding a Gaussian noise to these parameter values (*mutation*). This procedure is repeated until the terminating condition, e.g. a lower bound of the fitness function or a maximal number of generations, is reached. GAs are good in finding global maxima, but are not very efficient in finding the precise location of the absolute maximum [Ako10, Reb96]. To improve the fit and to optimize the convergence behavior, we make use of *annealing*. If the fitness of the fittest member of the population does not improve over several generations, the amplitude of the Gaussian noise is reduced gradually to refine the fitting procedure close to the currently optimal parameter sets. Simulated annealing in combination with GAs [Dju97, Gan05] has been used before. These authors apply annealing to the probability of accepting newly generated children having a fitness smaller than the best fitness. To the best of our knowledge, the noise-annealing approach suggested here has not been published before.

To give a concrete example, we apply this algorithm in the current work to model the injection dependence of the effective surface recombination velocity S_{eff} at SiN_x and $\mathrm{Al_2O_3}$ passivated n-Si and p-Si substrates of various resistivities. Fitting several samples simultaneously is important for the development of a consistent model. This is done as follows: several parameters can be assumed to be independent of the bulk resistivity and the passivating layer, and therefore, need to be optimized globally for all samples (*global parameters*). Some parameters, however, depend on the bulk-

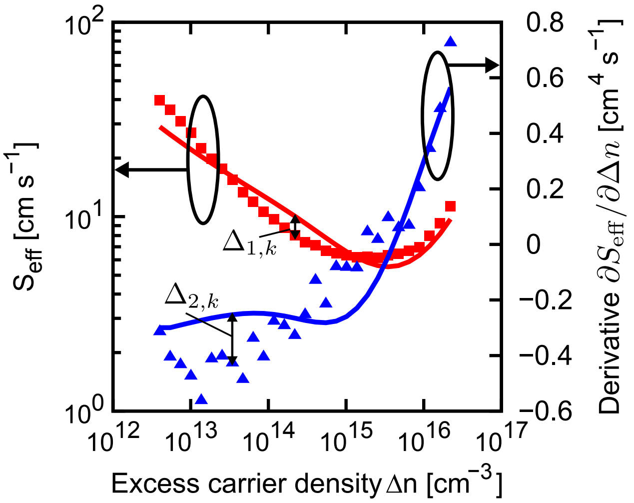

Figure 3.2: Example of the error functions Δ_1 and Δ_2 used for the genetic algorithm. The injection dependent effective recombination velocity is shown on the left axis and its derivative is displayed on the right axis. Continuous lines correspond to the simulation and symbols to measurements [Ker02b]. The error in data points $\Delta_{1,k}$ and the error in the first derivative $\Delta_{2,k}$ are indicated.

doping or the deposited material, and thus, have to be varied individually for each sample (*local parameters*). We developed a special fitting algorithm, which allows to adjust global and local optimization parameters simultaneously, automatically, and reliably for an almost arbitrary large set of measurements, as introduced in the following.

The fitness function used to evaluate a parameter set for the genetic optimization algorithm is defined as the weighted sum of several square errors Δ^2_{jk}. The index j goes over all N_{e} error functions and the index k goes over all N_{m} data points of one data set.

In general, the fitness function f_ℓ for the local parameters reads:

$$f_\ell = \frac{1}{N_{\mathrm{m}} \sum\limits_{j=1}^{N_{\mathrm{e}}} \omega^{\mathrm{e}}_j} \left(\sum_{j=1}^{N_{\mathrm{e}}} \omega^{\mathrm{e}}_j \underbrace{\sum_{k=1}^{N_{\mathrm{m}}} \omega^{\mathrm{m}}_{jk} \left(\Delta_{jk}\right)^2}_{=:\Delta_j} \right), \tag{3.1}$$

where each data point of a measurement is weighted by ω^{m}_{jk}, and the N_{e} error functions Δ_j are weighted by ω^{e}_j. When applying the GA to several data sets simultaneously, the global fitness function f_{g} is defined as

$$f_{\mathrm{g}} = \frac{1}{N_{\mathrm{s}}} \sum_{i=1}^{N_{\mathrm{s}}} \omega^{\mathrm{s}}_i f_{\ell,i}, \tag{3.2}$$

where N_{s} is the number of data sets weighted by ω^{s}_i. For all simulations in this work, we use $\omega^{\mathrm{s}}_i = 1$. We further use two error functions, the difference between measured data points and simulated points, Δ_1, and the differences in the corresponding first derivative, Δ_2, as shown exemplarily in Fig. 3.2. Thereby, we typically choose the weight of the derivative error function to be $\omega^{\mathrm{e}}_2 = 0.2\,\omega^{\mathrm{e}}_1$. The weights of the data points $\omega^{\mathrm{m}}_{1k} = \omega^{\mathrm{m}}_{2k}$ are set to $\omega^{\mathrm{m}}_{jk} = 1$ in the intermediate injection range $\Delta n \simeq 10^{13} \ldots 10^{16}\,\mathrm{cm}^{-3}$, and are decreased gradually outside these bounds. This is done because for very low or very high injection densities Δn, the measured data is often noisy or even erroneous. To improve the convergence behavior, it is useful to smooth noisy data before fitting. The convergence speed is enhanced by interpolating large measured data sets and evaluating them at equally distributed positions on a linear or logarithmic scale.

3.2 Brent's root-finding algorithm

If charges are present at the interface of a semiconductor, charge neutrality must hold. For this reason, the energy bands in the system are bent towards the surface. Note that in the models presented in this work (Chapters 4 and 5), we assume that only the energy bands in the semiconductor bulk material are allowed to bend. The condition of charge neutrality is a root-finding problem that needs to be solved numerically. We solve Eq. (2.52) (and the slightly modified version in Eq. (5.16)) using Brent's algorithm [Bre73, Dek69]. This algorithm is an advanced root-finding method which combines the secant method [Jee58], the bisection method [e.g. Sik82] and the method of inverse quadratic interpolation [Mar74]. If possible, the faster of both the secant method or inverse quadratic interpolation is used. In case of convergence problems, the algorithm switches to the more reliable and more robust bisection method. Thus, the algorithm has the reliability of the bisection method, while it may perform as quick as the less reliable methods.

The algorithm is sketched in Fig. 3.3. Initially, two values a_1 and b_1 are chosen such that $f(a_1) \cdot f(b_1) < 0$, where the function f is continuous between a_1 and b_1. The intermediate value theorem [proofed by Bol80] then guarantees that a root of f lies between a_1 and b_1. Before each iteration step k, it is ensured that b_k is closer to the root than (or equally close as) a_k. Otherwise, a_k and b_k are swapped.

In the first step of each iteration, either the method of inverse quadratic interpolation or the secant method is chosen. The secant rule determines a new value s by:

$$s := f_{\mathrm{sec}}(a_k, b_k, f(a_k), f(b_k)) = b_k - f(b_k)\frac{b_k - a_k}{f(b_k) - f(a_k)}, \tag{3.3}$$

and the inverse quadratic interpolation yields s according to:

$$\begin{aligned} s := f_{\mathrm{quad}}(a_k, b_k, f(a_k), f(b_k)) &= \frac{a f(b_k) f(b_{k-1})}{(f(a_k) - f(b_k))(f(a_k) - f(b_{k-1}))} \\ &+ \frac{b_k f(a_k) f(b_{k-1})}{(f(b_k) - f(a_k))(f(b_k) - f(b_{k-1}))} \\ &+ \frac{b_{k-1} f(a_k) f(b_k)}{(f(b_{k-1}) - f(a_k))(f(b_{k-1}) - f(b_k))}. \end{aligned} \tag{3.4}$$

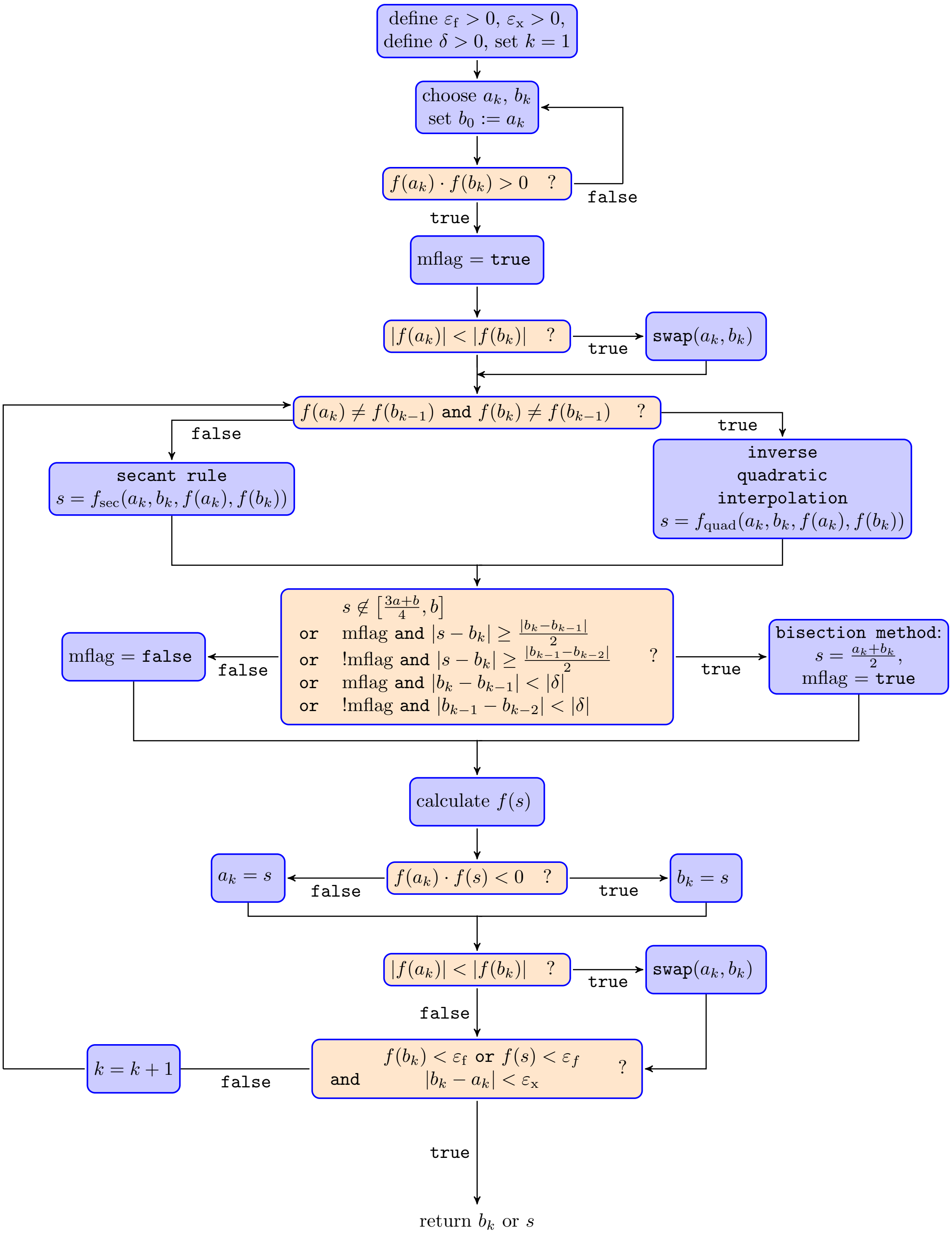

Figure 3.3: Brent's root finding algorithm as described in Refs. [Bre73, Wik11]. See the text for details.

The efficiency of the inverse quadratic interpolation is slightly improved compared to the linear interpolation used in the secant method, however, it can only be applied if f_{a_k}, f_{b_k} and $f_{b_{k-1}}$ are distinct.
Using the secant rule or inverse quadratic interpolation alone may cause long iteration times if f is not sufficiently well-behaved [Wik11]. Therefore, in case of convergence problems, the bisection method is used to determine s:

$$s := f_{\mathrm{bis}}(a_k, b_k) = \frac{a_k + b_k}{2}. \tag{3.5}$$

This iteration is repeated until the root is determined sufficiently accurate. Finally, b_k or s are returned as the root, i.e. in our application the value for the band bending φ_s.
In this work, we implemented a conditional convergence criteria: in addition to the requirement that $f(s)$ or $f(b_k)$ are sufficiently close to zero ($f(s) < \varepsilon_f$ or $f(b_k) < \varepsilon_f$, where $\varepsilon_f > 0$), we require that the difference in $|a_k - b_k|$ or $|a_k - s|$ is sufficiently small as well ($|a_k - b_k| < \varepsilon_x$ or$|a_k - s| < \varepsilon_x$, where $\varepsilon_x > 0$).
The charge neutrality conditions (Eq. (2.52) or Eq. (5.16)) may have more than one root. However, typically only one root is physically meaningful. In addition, it is not straightforward to find an initial pair a_1 and b_1 such that $f(a_1) \cdot f(b_1) < 0$. Therefore, we do three things: first, the range of values the band bending φ_s can take is restricted to a physically meaningful range. Second, both a_1 and b_1 are initialized to zero (in the first simulation step). Then b_1 is ramped in relatively small steps until $f(b_1)$ changes its sign. Note that to improve convergence speed it is convenient to adapt the step size for ramping b_1 in dependence on the interface charge density. In case one may decide beforehand whether the band bending is positive or negative, we automatically set the direction into which b_1 is initially ramped. For example, in p-Si, the energy bands bend downwards for positive interface charges, whereas they bend upwards for negative charges at an n-Si interface. Third, when determining S_eff or τ_eff in dependence on the injection density Δn (cf. Eqs. (2.51) and (2.41)), for each value of Δn, a_1 and b_1 are initialized to the solution at the preceding value of Δn. This approach is efficient, since φ_s changes smoothly with Δn.

Chapter 4

Defects Close to Charged Interfaces

Recombination of excess charge carriers at the surfaces of silicon solar cells can be reduced by deposition of charged dielectrics, such as positively charged amorphous silicon nitride SiN_x [Hez89] or negatively charged aluminum oxide $\mathrm{Al_2O_3}$ [Sch08a, Sch08b]. This property is called (electronic) passivation, and was intensively investigated in the photovoltaics community in the 1990ies [Abe97, Elm97, Leg96]. It was noted, that passivation depends on both the dopant density [Che94] and the density of the excess carriers (injection density) [Abe95b]. In particular, the passivation has to be effective also at low illumination levels, where the excess carrier density is small ($\Delta n \lesssim 10^{14}\,\mathrm{cm}^{-3}$). However, the passivation performance of commonly used SiN_x layers is rather weak at low illumination levels if the silicon material is p-type with $N_\mathrm{A} < 10^{17}\,\mathrm{cm}^{-3}$ [Abe95b, Elm97, Ker02b, Leg96]. For such dopant densities, measurements show a strong increase of the effective surface recombination velocity S_eff with decreasing excess carrier density $\Delta n < 10^{15}\,\mathrm{cm}^{-3}$ [Abe95b, Elm97, Ker02b, Leg96]. If such an interface is incorporated into silicon solar cells, it causes their performance to deteriorate under low-injection conditions, as will be demonstrated in Chapter 7. This has implications on present solar cell designs: as most silicon solar cells are fabricated on p-Si wafers with $N_\mathrm{A} < 10^{17}\,\mathrm{cm}^{-3}$, their surface parts must usually be diffused with dopants to achieve a good performance under weak illumination conditions. A qualitatively similar effect – though less pronounced – has recently been observed for $\mathrm{Al_2O_3}$ layers on n-Si. This phenomenon is not well understood and, accordingly, cannot be avoided up to date. We develop a model which reproduces S_eff in both p-Si and n-Si, passivated using SiN_x or $\mathrm{Al_2O_3}$ layers, respectively, at all relevant Δn and all relevant dopant densities. The model presented in this chapter was published in Refs. [Ste10a, Ste10b, Ste10c].

We begin in Sec. 4.1 with theoretical considerations to motivate that the reduced performance of SiN_x and Al_2O_3 layers at low illumination densities cannot be explained by SRH theory at the surface alone. Based on this observation, in Sec. 4.2 we suggest a model that explains the measured recombination on a microscopic level by assuming recombination active defects in the silicon bulk underneath the interface. This model will be used to reproduce a large set of experimental data. Further, predictions shall be made regarding the cases where surface-near defects have a detrimental influence on the passivation quality, and regarding the improvement that is necessary to significantly improve the passivation at low excess carrier densities.

Since the injection dependence of S_{eff} at SiN_x passivated surfaces is much stronger pronounced compared to Al_2O_3 passivation, this chapter will focus mainly on SiN_x. We will show further that the proposed model is also well suitable to describe the behavior of S_{eff} at the Al_2O_3/c-Si interface.

4.1 Theoretical considerations

We model the recombination rate R_{surf} at the interface between crystalline silicon and the passivation layer using the SRH formalism [Hal52, Sho52] (Eqs. (2.49)–(2.51) in Sec. 2.2.8). SiN_x layers usually contain a high density of positive fixed charges Q_{f}, typically near $2 \times 10^{12}\,\text{q/cm}^2$ (unless additional manipulation is applied [Web94]). Charge neutrality in the whole device is obtained by taking the band bending in the c-Si substrate according to Eq. (2.52) into account. The resulting concentrations of electrons and holes at the surface are determined using Eq. (2.53).

The symbols in Fig. 4.1 show S_{eff} in dependence of Δn exemplarily for three p-Si and three n-Si substrates with different resistivities, measured by Kerr and Cuevas [Ker02b][1] using the quasi-steady-state photoconductance (QSSPC) method [Sin96]. We calculate the acceptor density N_{A} and the donor density N_{D} of the samples from their resistivities according to Ref. [Thu80a] for p-Si and according to Ref. [Thu80b] for n-Si. The S_{eff} values increase with Δn at intermediate injection conditions where $\Delta n > N_{\text{dop}}$, because the product $n_{\text{s}}p_{\text{s}}$ in Eq. (2.49) increases. However, in p-type material (with an acceptor density N_{A}), the S_{eff} values increase also towards lower Δn at low-injection conditions where $\Delta n < N_{\text{A}}$. This implies that passivation deteriorates at low excess carrier densities in p-Si solar cells. In the following, we demonstrate that this feature cannot be explained alone by means of the SRH formalism at the surface.

To understand the dynamics of S_{eff}, we underline that p-Si with $N_{\text{A}} < 10^{17}\,\text{cm}^{-3}$ is

---

[1] Note that in contrast to the original publication [Ker02b], S_{eff} is extracted from the original lifetime measurements by taking an injection dependence of τ_{SRH} into account (see below and Ref. [Ste10b]).

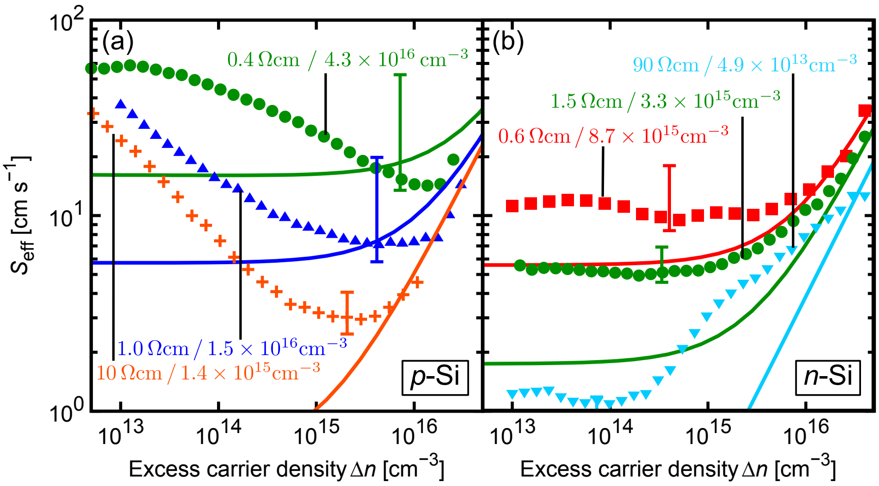

Figure 4.1: Effective recombination velocity S_{eff} in dependence on the excess carrier density Δn in the quasi-neutral region of silicon (symbols) [Ker02b] in (a) p-Si and (b) n-Si wafers with the denoted resistivity and the related acceptor density N_{A} [Thu80a] and the donor density N_{D} [Thu80b] in p-Si and n-Si, respectively. The calculations (lines) are not a fit to the data, but show the contribution solely from surface recombination taking a fixed charge density of $Q_{\text{f}} = 2.21 \times 10^{12}$ q/cm^2 into account (Eqs. (2.49), (2.51), and (4.1)). $S_{\text{p}} = S_{\text{n}}$ is given by the symbols in Figs. 4.5(c) and 4.5(d).

strongly inverted[2] underneath SiN$_x$ layers at typical injection conditions. Note that in pioneering work [Sch99a], it was assumed that electron injection under illumination reduces Q_{f} to an extent that strong inversion does not prevail, but this was revoked later [Dau02c]. In n-Si, electrons are attracted by the positive Q_{f} in the nitride layer and are the dominant carrier species at the surface, leading to accumulation conditions.[2] This behavior is explained in terms of the band bending at the surface φ_{s}, induced by Q_{f} via Poisson's equation (2.1). The equation for the band bending was introduced in Sec. 2.2.8 in Eq. (2.52) and is recapitulated here:

$$\begin{aligned}\frac{Q_{\text{f}}^2}{c} &= p(\,\mathrm{e}^{-q\beta\varphi_{\text{s}}} + q\beta\varphi_{\text{s}} - 1) + n(\,\mathrm{e}^{q\beta\varphi_{\text{s}}} - q\beta\varphi_{\text{s}} - 1)\\ &\overset{Eq.\ (2.53)}{=} p_{\text{s}} + p(q\beta\varphi_{\text{s}} - 1) + n_{\text{s}} - n(q\beta\varphi_{\text{s}} + 1), \qquad \text{where} \quad c = \frac{2\varepsilon_0\varepsilon_{\text{r}}}{\beta}.\end{aligned} \tag{4.1}$$

The band bending φ_{s} is obtained from the implicit Eq. (4.1) and is shown in Fig. 4.2 as a function of Δn for different acceptor densities N_{A}. In case of accumulation conditions, φ_{s} stays below the dashed line. Here, the charges Q_{f} are compensated mainly by the depletion of holes, whose density does not significantly change with Δn.

---

[2] Inversion conditions in a p-type (n-type) semiconductor denote the situation where electrons (holes) are in excess to holes (electrons). Accumulation conditions mean that holes (electrons) are in excess to electrons (holes).

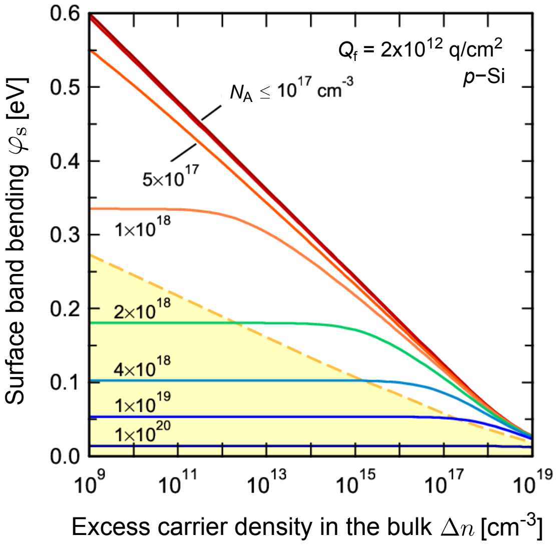

Figure 4.2: Band bending φ_s at the Si surface underneath the SiN$_x$ layer as a function of the injection density Δn in the quasi-neutral region of Si, for various acceptor densities N_A according to Eq. (4.1). The fixed charge Q_f has a density of $2 \times 10^{12}\,\mathrm{q/cm^2}$. The regions under (above) the dashed curve denote accumulation (inversion) conditions.

Therefore, φ_s is insensitive to Δn. Between accumulation and strong inversion, weak inversion prevails, were Q_f is compensated to a similar extent by the accumulation of electrons and by the depletion of holes. For $N_\mathrm{A} \lesssim 10^{17}\,\mathrm{cm^{-3}}$, the substrate is strongly inverted underneath the surface. Consequently, there is a sufficient number of electrons available to compensate for the positive Q_f of the SiN$_x$ layer and φ_s is almost independent of N_A in Fig. 4.2. In addition, φ_s decreases linearly as a function of $\ln(\Delta n)$. This is explained as follows. In the case of strong inversion in p-Si, and in the case of accumulation in n-Si, there is $p \ll n$ below the silicon surface and, consequently, the right-hand side of Eq. (4.1) is dominated by the term $n \exp(q\beta\varphi_\mathrm{s})$. Hence, it holds that:

$$\varphi_\mathrm{s} \approx \frac{1}{q\beta} \ln\left(\frac{Q_\mathrm{f}^2}{cn}\right) \overset{n \gg n_0}{\approx} -\frac{1}{q\beta} \ln\left(\frac{c\Delta n}{Q_\mathrm{f}^2}\right). \tag{4.2}$$

Thus, analytical expressions can be applied to quantify the band parameters in case of strong inversion. By inserting this equation into the relations for the surface concentrations in Eq. (2.53), both p_s and n_s can be written in the simple form:

$$p_\mathrm{s} \approx c\frac{pn}{Q_\mathrm{f}^2}, \qquad n_\mathrm{s} \approx \frac{Q_\mathrm{f}^2}{c}. \tag{4.3}$$

When inserting these two expressions into the equation for the surface recombination rate (2.49), S_eff can be explicitly computed as a function of Δn. Approximating Eq. (2.49) further for low-injection conditions [Kuh95], yields:

$$S_\mathrm{eff} \approx S_\mathrm{p}\frac{c}{Q_\mathrm{f}^2}N_\mathrm{dop}, \tag{4.4}$$

with $N_\mathrm{dop} = N_\mathrm{A}$ in p-Si and $N_\mathrm{dop} = N_\mathrm{D}$ in n-Si, respectively. The substrates used for the measurements in Fig. 4.1 are fabricated on substrates with $N_\mathrm{dop} < 10^{17}\,\mathrm{cm^{-3}}$

and hence, the approximations made above are valid. The calculated S_{eff} values, obtained from Eq. (2.51), are shown as lines in Fig. 4.1. They are indeed independent of Δn for all acceptor levels N_{A} and for all donor levels N_{D}, as expected from Eq. (4.4).[3] The measured curves follow the constancy in S_{eff} for n-Si substrates, but for p-Si an increase of the measured S_{eff} towards low Δn is observed. Consequently, SRH surface recombination alone cannot explain the surface recombination at the SiN_x/p-Si interface.

To conclude, by approximating the charge neutrality condition for the cases of strong inversion in p-Si, we showed that an injection independent behavior of $S_{\text{eff}}(\Delta n)$ is expected for SiN_x passivated p-Si surfaces in low-injection according to the SRH theory for surfaces. This is in contradiction with measurements showing a strong increase of S_{eff} towards low Δn. In the following Sec. 4.2, we develop a model that allows to explain these measurements.

4.2 Interpretation of reduced passivation by surface damage

The straightforward extension [Bra53, Sim71] of the SRH formalism in Eq. (2.32) allows to account for the distribution of defect states $D(E_{\text{d}})$ within the bandgap of silicon at the SiN_x/c-Si interface. Measured defect distributions were reported by Elmiger *et al.* [Elm97] and Schmidt *et al.* [Sch97]. The overall density of the distributions seems to vary with the quality of the nitride layer: both the defect density and the S_{eff} values in Ref. [Elm97] are about ten times larger than in Ref. [Sch97]. However, the qualitative shape of $D(E_{\text{d}})$ does not seem to vary greatly, although the relative proportion between the observed peaks in $D(E_{\text{d}})$ may vary to some extent. Taking $D(E_{\text{d}})$ into account, the SRH surface recombination theory cannot explain the increase in S_{eff} with decreasing Δn, for the following reasons (see also Sec. 4.2.5). It is a general feature of SRH recombination that only defects within a limited range of E_{d} in the bandgap can effectively contribute to R_{surf}, see Fig. 2.4 in Sec. 2.1.3. This range becomes smaller with decreasing Δn, implying that S_{eff} would decrease rather than increase with decreasing Δn, regardless of the E_{d} dependencies of the cross sections for electron and hole capture, σ_{n} and σ_{p}, respectively. This contradiction necessitated further assumptions [Sch99a]. In particular, one must distinguish between acceptor- and donor-like defects, and include their charge occupation Q_{it}^{A} and Q_{it}^{D}, respectively, in the electrostatic condition at the interface. A comparison of

---

[3] Note that the parameters for the computed S_{eff} curves are not fitted to the measurements. Instead, they are chosen from the extended recombination model described in Sec. 4.2 to show the contributions of the surface in this extended model.

Eq. (4.1) and Eq. (4.4) with the experimental values in Fig. 4.1 reveals that a value of $Q_{\mathrm{it}}^{\mathrm{A}}+Q_{\mathrm{it}}^{\mathrm{D}}$ below $-1.4 \times 10^{12}\,\mathrm{q/cm^2}$ ($-2 \times 10^{12}\,\mathrm{q/cm^2}$) in $1\,\Omega\mathrm{cm}$ ($10\,\Omega\mathrm{cm}$) p-Si material would be required to compensate the fixed charge Q_{f} and to increase S_{eff} sufficiently strongly (cf. Sec. 4.2.5). The total defect density in Ref. [Sch97] is definitely too small to host this large amount of charge, ruling it out as a cause of the increasing S_{eff} values.

A further way to obtain the desired S_{eff} values is to exploit the fact that a smaller Q_{f} can be more easily compensated by $Q_{\mathrm{it}}^{\mathrm{A}}$ and $Q_{\mathrm{it}}^{\mathrm{D}}$. In pioneering work [Sch99a], the behavior of S_{eff} was indeed interpreted by an injection dependence of Q_{f} on Δn. Thereby, significantly lower Q_{f} values ($\approx 10^{11}\,\mathrm{q/cm^2}$) at low Δn were assumed, causing accumulation conditions in low-injection. However, such low Q_{f} values were revoked later when detailed measurements became available [Dau02c]. Other authors [Elm97] reported very high defect densities, even higher than those measured in the pioneering work by Hezel and Jaeger [Hez89]. Assuming that Q_{f} is rather low ($1 \times 10^{12}\,\mathrm{q/cm^2}$), that all defect states below midgap are donor-like, and that states above midgap are acceptor-like, $Q_{\mathrm{it}}^{\mathrm{A}}$ and $Q_{\mathrm{it}}^{\mathrm{D}}$ can indeed influence S_{eff} in the desired way. However, the samples shown in Fig. 4.1 have low values of S_{eff}, and are thus well passivated. This is most probably due to a higher $Q_{\mathrm{f}} \gtrsim 2 \times 10^{12}\,\mathrm{q/cm^2}$ and a low density of interface states similar to that reported by Schmidt *et al.* [Sch97] rather than that reported by Elmiger *et al.* [Elm97]. Such low defect densities cannot compensate Q_{f} sufficiently, as will be shown quantitatively in Sec. 4.2.5. Hence, the behavior of S_{eff} cannot be caused by the defect charges alone.

Furthermore, the model for field-effect passivation at $\mathrm{SiO_2}$/c-Si interfaces [Glu99a] was adapted to SiN_x/c-Si interfaces [Dau02c]. This model suggests that enhanced SRH recombination in the SCR causes the reduced values of S_{eff} at low-injection conditions. Hence, a diode equation was added to Eq. (2.49) and fitted to the observed S_{eff} values by choosing a saturation current density $j_{02} = 800\,\mathrm{pA/cm^2}$ [Dau02c]. While such a model and data fit is plausible, it does not reveal the underlying causes, making it difficult to draw conclusions for improvements in surface passivation. We therefore give a more detailed analysis of recombination in the SCR in the following [Ste10b, Ste10c, Ste10d].

4.2.1 The surface damage model

High-quality float zone (FZ) wafers were used for the measurements shown in Fig. 4.1. Their measured bulk excess carrier lifetimes τ_{b} are high and cannot cause a sufficient amount of recombination near the interface. Consequently, we assume that – caused by an enhanced defect density – τ_{b} is degraded near the silicon surface. The origin of this *surface-damage region* (SDR) is not yet clear, and will be discussed in Sec. 4.2.7. As a motivation for our model, we outline only one hypothesis: an excessive density of hydrogen present below the silicon surface. It was shown that during the deposition and annealing of the SiN_x layer, up to 2×10^{22} hydrogen atoms per cm^3 are released into the silicon [Kot95]. This density comes close to the density of silicon atoms ($4.9 \times 10^{22}\,\mathrm{cm}^{-3}$) and may weaken the covalent bonds of silicon to the extent that it causes a considerable number of lattice defects and hence, a reduction of τ_b near the interface. This is in agreement with the observation that hydrogenation, e.g. during SiN_x processing, induces electrically active defects near the middle of the silicon bandgap up to $0.8\,\mu\mathrm{m}$ away from the interface [Joh87]. For high-quality FZ wafers with a low inherent defect density, hydrogen may interact mainly with dopant impurities by forming stationary defects in the form of complexes [Sop02]. Deeper in the silicon, the hydrogen density drops and is well known to improve τ_b, e.g. in multicrystalline silicon materials [Bäh04, Wen85]. Measurements of the hydrogen-density profile near the interface by means of secondary ion mass spectroscopy (SIMS) indicate that there is a high hydrogen density present to a depth of $z \approx 0.1 \ldots 0.2\,\mu\mathrm{m}$ from the interface [Sop05].

In our microscopic model, we assume that there is a damaged region in the bulk near the interface, possibly caused by hydrogen. We model this by a volume density N_d of defect states which is maximal at the interface ($z = 0$) and decreases exponentially into the bulk:

$$N_\mathrm{d} = N_\mathrm{d,dam}\,\mathrm{e}^{-z/z_\mathrm{deg}} + N_\mathrm{d,bulk}, \tag{4.5}$$

where z_deg determines the slope of the exponential decrease of the defect density $N_\mathrm{d,dam}$ and $N_\mathrm{d,bulk}$ is the inherent density of bulk defects. This is in agreement with the assumption that the defects may result from a high hydrogen density, because most of the measured hydrogen profiles in silicon [Sop05] can be approximated by an exponential function. We model recombination in the SDR using the SRH formalism in the bulk [Hal52, Sho52] according to Eq. (2.35). The lifetime parameters $\tau_\mathrm{n} = 1/N_\mathrm{d}\sigma_\mathrm{n}v_\mathrm{th,n}$ and $\tau_\mathrm{p} = 1/N_\mathrm{d}\sigma_\mathrm{p}v_\mathrm{th,p}$ (Eq. (2.33)) are inversely proportional to N_d. Hence, assuming that the CCS σ_n and σ_p do neither depend on depth z nor on the defect's energy E_d, we describe $\tau_\mathrm{n}(z)$ and $\tau_\mathrm{p}(z)$ by an exponential depth-profile. We implement this by an exponentially increasing function that is truncated at the value of the non-degraded bulk lifetime parameter $\tau_0 := \tau_{n0} = \tau_{p0}$, as shown in Fig. 4.3(a):

$$\begin{aligned} \tau_\mathrm{n}(z) &= \min(\tau_\mathrm{surf,n}\,\mathrm{e}^{z/z_\mathrm{deg}}, \tau_0) \\ \tau_\mathrm{p}(z) &= \min(\tau_\mathrm{surf,p}\,\mathrm{e}^{z/z_\mathrm{deg}}, \tau_0). \end{aligned} \tag{4.6}$$

This causes a reduction of the charge carrier lifetime τ_b near the SiN_x/c-Si interface, because $\tau_\mathrm{b} = \Delta n/R_\mathrm{SRH}$ where the recombination rate R_SRH is defined in Eq. (2.35). Note that the exact shape of this profile is rather irrelevant, but with higher-order exponentials, like e.g. a Gaussian function, or with the extreme case of an abrupt

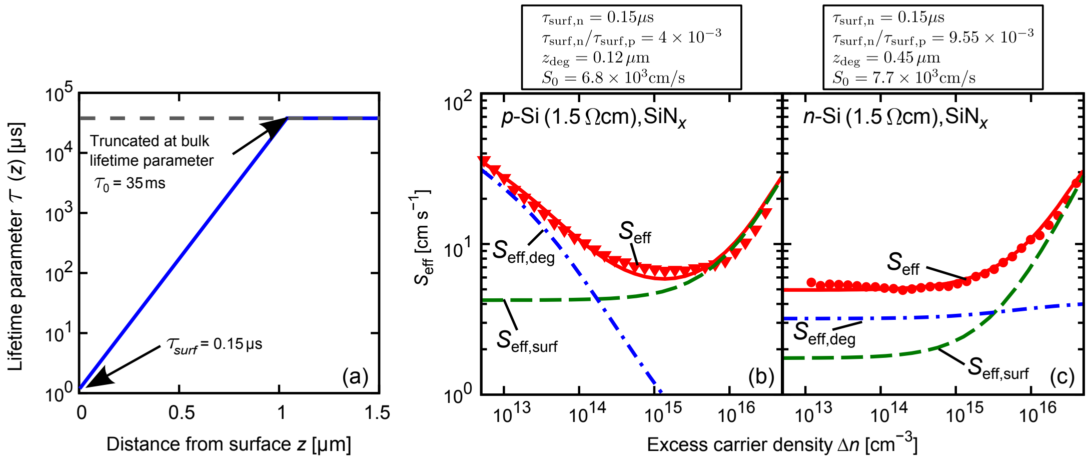

Figure 4.3: (a) The lifetime parameters $\tau_{\mathrm{n}}(z)$ and $\tau_{\mathrm{p}}(z)$ of the silicon bulk increase exponentially from the lifetime parameter at the interface, τ_{surf}, to the bulk lifetime parameter τ_0. (b), (c) Measured [Ker02b] (symbols) and calculated $S_{\mathrm{eff}}(\Delta n)$ dependence (lines) according to Eqs. (2.49), (2.51), (4.6), (4.7), and (4.8) for (b) a p-Si and (c) an n-Si substrate. For small Δn, the calculated S_{eff} (continuous red lines, Eq. (4.8)) is dominated by recombination in the SDR $S_{\mathrm{eff,deg}}$ (blue dashed-dotted lines) calculated using Eq. (4.7), and for high Δn by the surface contribution $S_{\mathrm{eff,surf}}$ (green dashed lines) given by Eq. (2.51).

step-function, we were unable to obtain satisfactory fits to the experimental S_{eff} values of Fig. 4.1 in the whole range of N_{dop} and Δn.

The lifetime reduction enhances S_{eff}, described by Eq. (2.51), by the following additive term:

$$S_{\mathrm{eff,deg}} = \int_0^{z_{\mathrm{deg}}} \mathrm{d}z \; \frac{R_{\mathrm{SRH}}(z)}{\Delta n}. \tag{4.7}$$

In essence, S_{eff} has two main contributions: the usual interface recombination rate, described by $S_{\mathrm{eff,surf}}$ (Eq. (2.51)), and the recombination rate in the SDR, described by $S_{\mathrm{eff,deg}}$ (Eq. (4.7)):

$$S_{\mathrm{eff}} = S_{\mathrm{eff,surf}} + S_{\mathrm{eff,deg}}. \tag{4.8}$$

These two contributions are shown in Fig. 4.3(b) for a p-Si substrate and in Fig. 4.3(c) for an n-Si substrate (both 1.5 Ωcm), passivated by a SiN$_x$ layer. It is obvious, that recombination in the damaged region $S_{\mathrm{eff,deg}}$ (Eq. (4.7)) contributes significantly to S_{eff} at low injection densities. The contributions from the surface, $S_{\mathrm{eff,surf}}$ (Eq. (2.51)), are situated significantly below the measured S_{eff} values for both p-Si and n-Si substrates. This implies that recombination in the SDR is also important in n-Si materials (Fig. 4.3(c)), although it does not lead to an increasing S_{eff} towards low Δn.

In order to determine $R_{\mathrm{SRH}}(z)$ in Eq. (4.7) according to Eq. (2.35), the electron and hole concentrations at the distance z from the interface must be known. They are derived as follows. Analogously to Eq. (2.53), n and p depend on the band bending φ_z at a depth z away from the surface via:

$$n(\varphi_z) \;=\; n\,\mathrm{e}^{q\varphi_z}, \qquad p(\varphi_z) \;=\; p\,\mathrm{e}^{-q\varphi_z}. \tag{4.9}$$

With increasing distance z from the surface, $|\varphi_z|$ decreases and becomes zero beyond the SCR. Similarly to Eq. (2.52), we define a charge density in dependence of φ_z:

$$Q(\varphi_z) = \pm\sqrt{c\;(p(\,\mathrm{e}^{-\beta\varphi_z} + \beta\varphi_z - 1) + n(\,\mathrm{e}^{\beta\varphi_z} - \beta\varphi_z - 1))}, \tag{4.10}$$

where c is defined as in Eq. (4.1). The sign in Eq. (4.10) depends on the sign of Q_f and is positive if $Q_\mathrm{f} < 0$ and negative if $Q_\mathrm{f} > 0$. Note that $Q(\varphi_z) \longrightarrow 0$ as $\varphi_z \longrightarrow 0$. The distance z from the surface, where the band bending takes a given value φ_z, is given by the integral [Dau04, Gro66, Man65, Mön01]:

$$z(\varphi_z) = \int_{\varphi_\mathrm{s}}^{\varphi_z} \mathrm{d}\varphi\;\frac{\varepsilon_\mathrm{r}\varepsilon_0}{Q(\varphi)}. \tag{4.11}$$

Hence, using the relations (4.9)–(4.11), n and p can be determined in dependence on z.

We remark that the integration in Eq. (4.7) is performed until the damage depth z_deg. This is different from previous approaches [Dau02c, Dau04], which restrict the enhanced recombination rate to the extension of the SCR. The authors use constant SRH lifetime parameters $\tau_\mathrm{n} = \tau_\mathrm{p} = 1/N_\mathrm{d}\sigma v_\mathrm{th}$ in the SCR, which are reduced compared to the τ_0 value of the bulk. This approach is a strong simplification. On the one hand, neither the defect density nor the CCS are expected to change abruptly. On the other hand, the extension of the SCR depends on Δn and thus, also $N_\mathrm{d,dam}$ would depend on Δn, which is physically not plausible.

Before proceeding to adjust the parameters in Eq. (4.6), we comment on the procedure Kerr and Cuevas [Ker02b] used to obtain their S_eff-data. The authors measured the effective lifetime τ_eff and decomposed the contributions from the bulk and the surface. For the contribution from bulk SRH recombination, they choose an injection-independent but doping-dependent lifetime by using an equation proposed by Kendall [Ker02b]. We adapt the interpretation of their measured τ_eff-values by using Eq. (2.35) instead of the Kendall expression to take account of the injection dependence of τ_b, and because τ_SRH is independent of the dopant density in modern silicon wafer material. The resulting S_eff-curves are similar to the original publication, but are more consistent [Ste10b].

In summary, the surface-damage model includes an additional contribution to the effective surface recombination velocity S_eff which results from a highly defective region underneath the surface in the silicon. Thereby, it is assumed that the defect density is maximal at the interface and decreases exponentially into the silicon substrate.

4.2.2 Experiments and methods

We apply the surface damage model to a total number of 24 measurements of $S_{\text{eff}}(\Delta n)$ for various resistivities on n-Si and p-Si substrates. We consider both SiN_x passivated substrates measured by Kerr and Cuevas [Ker02b], and measurements made on Al_2O_3 passivated samples at the Institute for Solar Energy Research Hamelin (ISFH) [Ste10c, Zie10a, Zie10b].

The investigated SiN_x films have a thickness of $\approx 70\,\text{nm}$ [Ker02b]. They were deposited on both sides of the wafers in a high-frequency (13.56 MHz) direct plasma-enhanced chemical vapor deposition (PECVD) reactor, with ammonia and dilute silane (4.5 % in nitrogen) used as the process gases [Ker02b]. The aluminum oxide films were fabricated via plasma-assisted atomic layer deposition (PA-ALD, 20 nm) in an Oxford Instruments FlexAL$^{\text{TM}}$ reactor, or thermal ALD (th-ALD, 30 nm). The process temperature of the SiN_x deposition is close to 400 °C, while the th-ALD layers are grown at 260 °C, and the PA-ALD layers are deposited at 200 °C. The as-deposited ALD-layers contain only a low density of fixed charges. During a subsequent annealing process at temperatures between 350 °C and 450 °C, a highly negative charge density is formed, which leads to the outstanding field-effect passivation properties of the Al_2O_3 layers [Sch08a, Sch08b, Wer10]. The negative fixed charge density of the Al_2O_3 layers is determined by gradually depositing positive corona charges Q_{C} onto both sides of the samples, which partly compensate the fixed charges of the dielectrics. The deposited charges Q_{C} were quantified via Kelvin probe measurements [Dau03] assuming $\varepsilon_{\text{r}} = 7.7$ for the relative permittivity of Al_2O_3. Transient lifetime measurements [Ber98a, Nag99] were performed after each Corona deposition. Assuming symmetric CCS for electrons and holes, flat-band conditions (i.e. full charge compensation) are achieved if the product $n_{\text{s}}p_{\text{s}}$ in Eq. (2.49) is maximized and hence, τ_{eff} is minimal. Thus, plotting τ_{eff} vs. Q_{C} at $\Delta n = 10^{15}\,\text{cm}^{-3}$ and determining the minimum of τ_{eff} yields $Q_{\text{f}} = -Q_{\text{C}}$ of the Al_2O_3 layer. We obtain $Q_{\text{f}} = -5.2(6) \times 10^{12}\,\text{q/cm}^2$ on p-Si, and $Q_{\text{f}} = -6.2(2) \times 10^{12}\,\text{q/cm}^2$ on n-Si, as shown in Fig. 4.4. This is in agreement with the literature where negative values of the fixed charge densities with absolute values up to $Q_{\text{f}} \approx 10^{13}\,\text{cm}^{-3}$ after annealing are reported [Hoe08a, Hoe08b, Sch08b].

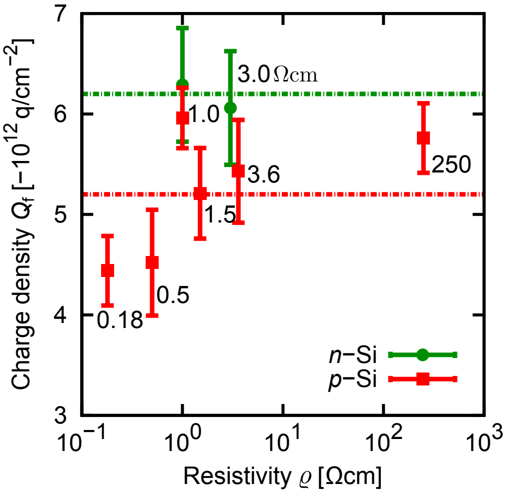

Figure 4.4: Negative fixed charge density Q_f at the Al_2O_3/c-Si interface, determined from injection dependent lifetime measurements of Corona charged surfaces (see text for details). The dashed lines indicate the average values used in the simulations ($Q_\mathrm{f} = -5.2 \times 10^{12}\,\mathrm{q/cm^2}$ for p-Si, and $Q_\mathrm{f} = -6.2 \times 10^{12}\,\mathrm{q/cm^2}$ for n-Si.

4.2.3 Reproduction of experimental data

The measured $S_\mathrm{eff}(\Delta n)$ data of eleven SiN_x passivated n-Si and p-Si substrates of different resistivities [Ker02b] (cf. Sec. 4.2.2) are plotted in Figs. 4.5(a) and 4.5(b). Figures 4.6(a)–4.6(c) show the S_eff measurements of thirteen Al_2O_3 passivated samples [Ste10c, Zie10a] (cf. Sec. 4.2.2).

We fit the measured data using the genetic algorithm, described in Sec. 3.1 with a set of parameters in Eqs. (2.49), (2.35), and (4.6). Considering the large set of free parameters, namely $\tau_\mathrm{surf,n}, \tau_\mathrm{surf,p}, z_\mathrm{deg}, \tau_0, S_\mathrm{n}, S_\mathrm{p}$, and Q_f, the most precise data fitting may be obtained when all parameters are allowed to vary with the dopant density N_dop. In this case, however, the fitted parameters are not necessarily physically meaningful. Therefore, we reduce the number of free parameters as much as possible and emphasize the behavior of the few parameters that remain free. In particular, we denote those parameters, which are expected to be independent of the dopant density N_dop, as *global*, because they need to be optimized for all data sets at once. In addition, those quantities, which are likely to vary with the dopant density, are considered as *local* parameters and are optimized for each data set separately.

In case of Al_2O_3, we determined the charge density Q_f from the measurements in Sec. 4.2.2 and thus, Q_f can be eliminated as a fit parameter. For SiN_x passivated surfaces we use external S_eff data [Ker02b] for which no measured Q_f is available. To the best of our knowledge, it is reasonable to assume that the dependence of Q_f on the deposition process is much stronger than its dependence on the wafer resistivity. Hence, Q_f is used as a global fit parameter (cf. Sec. 3.1) for all SiN_x samples and the range of Q_f is restricted to $1.5 \times 10^{12} \ldots 3 \times 10^{12}\,\mathrm{q/cm^2}$ in agreement with measured values reported in the literature [Dau02c, Sch08b].

The magnitude of τ_0 is obtained from the extraction of S_eff from the τ_eff data by considering that a too high (too low) τ_0-value would cause too low (too high) S_eff values in the intermediate Δn range. Hence, τ_0 is optimized globally for all 24 data sets, i.e.

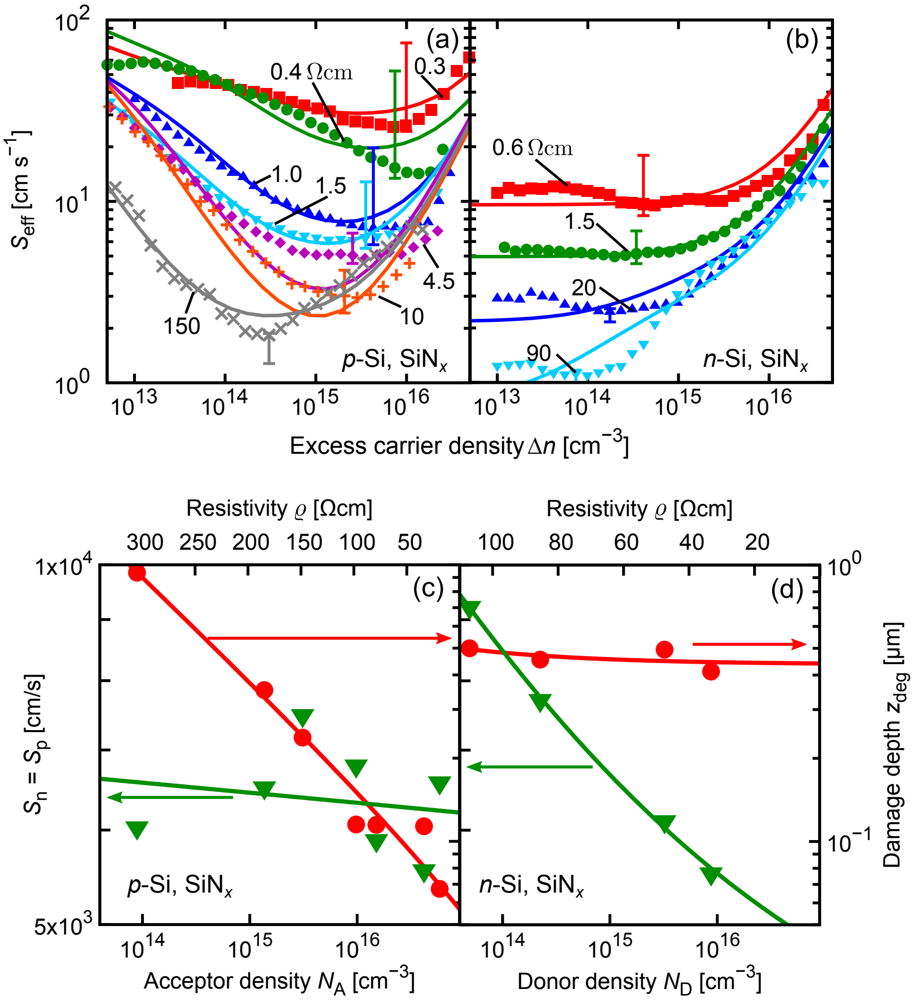

Figure 4.5: Fits to measurements [Ker02b] of SiN$_x$ passivated substrates including recombination in the SDR. (a) and (b) Effective recombination velocity S_{eff} (symbols) as obtained using a slightly revised procedure from the measurements by Kerr and Cuevas [Ker02b] (cf. Sec. 4.2.1). The lines are calculated by means of Eqs. (2.49) – (2.52) and (4.6), with the parameter values given in Table 4.1 and by the symbols in the lower two panels. (c) and (d) $S_{\mathrm{n}} = S_{\mathrm{p}}$ of Eq. (2.49) (green triangles, left axes) and the degradation depth z_{deg} of Eq. (4.6) (red circles, right axes) dependent on the dopant density for p-Si and n-Si substrates. The dependence of z_{deg} on N_{dop} is fitted (red lines) according to (4.12), with the parameters in Table 4.1. The green lines are guides to the eye.

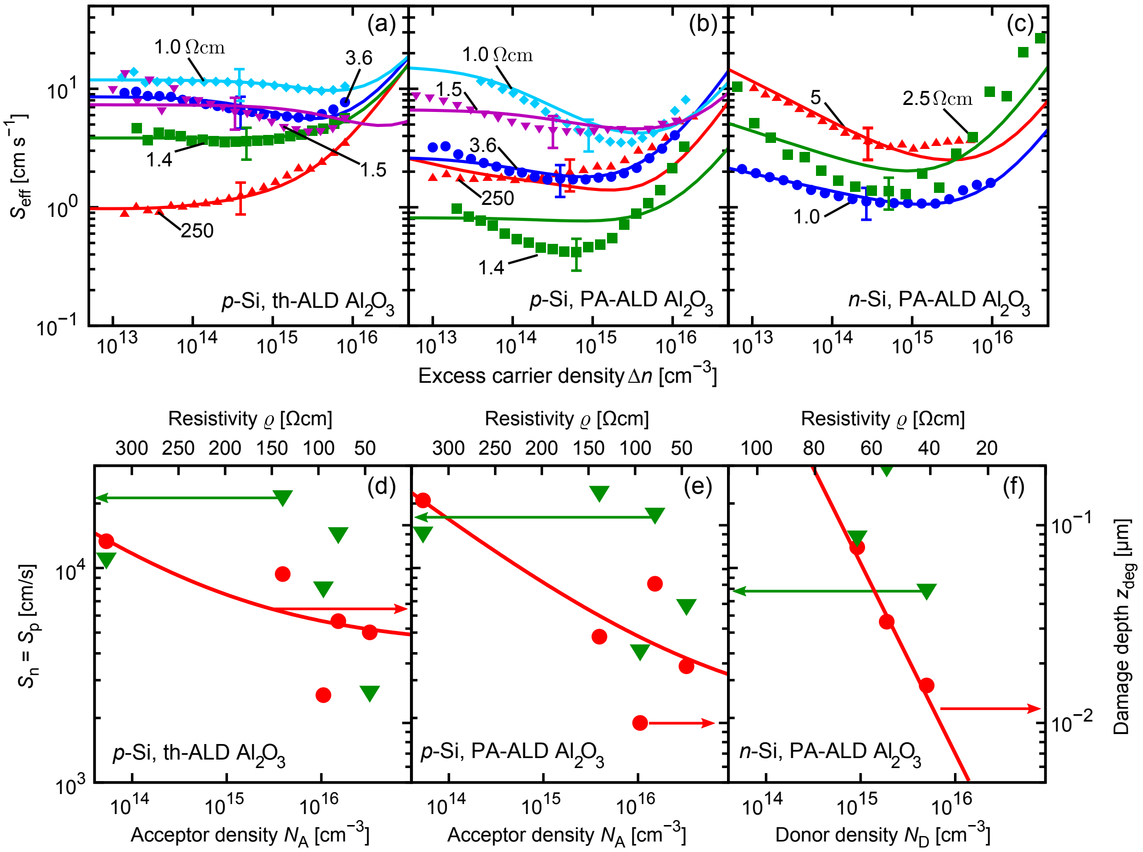

Figure 4.6: Fits to measurements of Al_2O_3 passivated substrates [Ste10c, Zie10a] including recombination in the SDR. (a)–(c) Effective recombination velocity S_{eff} (symbols) of (a) p-Si passivated by thermal ALD, and (b)–(c) p-Si and n-Si passivated by plasma assisted ALD. The lines are calculated by means of Eqs. (2.49) – (2.52) and (4.6), with the parameter values given in Table 4.1 and by the symbols in the lower two panels. (d)–(f) Fit parameters $S_{\mathrm{n}} = S_{\mathrm{p}}$ (green triangles, left axes) and the degradation depth z_{deg} (red circles, right axes) in dependence on the dopant density for p-Si and n-Si substrates. The dependence of z_{deg} on N_{dop} (lines) is fitted according to Eq. (4.12), with the parameters in Table 4.1.

treated as being independent of N_{dop}. Due to the high quality of the FZ substrates, we restrict the fit to $\tau_0 > 1\,\mathrm{ms}$. It is established, that the surface recombination velocity parameters S_{n} and S_{p} depend on the deposition conditions, on the wafer pretreatment and – at least for high dopant densities $N_{\mathrm{dop}} > 10^{17}\,\mathrm{cm}^{-3}$ [Alt02a, Alt06b, Che94] – on the dopant type and on the dopant density.

Moreover, R_{surf} is limited by holes for the investigated SiN_x samples due to the large n_{s}. Similarly, the electrons dominate R_{surf} for $\mathrm{Al_2O_3}$ layers. Hence, S_{n} in case of SiN_x and S_{p} in case of $\mathrm{Al_2O_3}$ have a negligible influence on data fitting, and we choose $S_{\mathrm{n}} = S_{\mathrm{p}}$ and use S_{p} as a local fit parameter for both SiN_x and $\mathrm{Al_2O_3}$. Assuming further that hydrogen is a possible cause of the SDR, the penetration behavior of hydrogen during the deposition process and hence, z_{deg} is likely to depend on the dopant density N_{dop} and on the dopant species in the silicon wafer. This is due to the fact that the diffusivity of hydrogen was found to depend strongly on various parameters, such as material quality, process conditions, annealing, firing etc. [Sop02, Sop05]. Also, the hydrogen solubility depends on the dopant species and on N_{dop}, especially if B-H or P-H complexes are formed [Sop02]. Therefore, we treat z_{deg} as a local fit parameter. Also, it may be assumed that the ratio of the CCS for electrons and holes differs for n-Si and p-Si substrates. Such a behavior may be explained by different kinds of defects formed in presence of boron or phosphorus atoms. Hence, a discrimination between dopant type is made. We take $\tau_{\mathrm{surf,n}}$ as a global fit parameter, but allow the ratio $\tau_{\mathrm{surf,n}}/\tau_{\mathrm{surf,p}}$ to be different for n-Si and p-Si substrates. Therefore, S_{p} and z_{deg} remain as the sole local fit parameters which are allowed to vary with N_{dop}.

The fitted curves are displayed as lines in comparison to the measured data points in Figs. 4.5(a) and 4.5(b) for SiN_x, and in Figs. 4.6(a)–4.6(c) for $\mathrm{Al_2O_3}$. Obviously, the S_{eff} measurements of both passivation materials are reproduced well over the extended range of substrate resistivities between $0.4\,\Omega\mathrm{cm}$ and $250\,\Omega\mathrm{cm}$ on both n-Si and p-Si.

The resulting global fit parameters are listed in Table 4.1. Indeed, the magnitude of the global parameters (τ_0, Q_{f}, $\tau_{\mathrm{surf,n}}$, and $\tau_{\mathrm{surf,p}}$) are plausible. We find $\tau_{\mathrm{surf,n}}/\tau_{\mathrm{surf,p}} = 4 \times 10^{-3}$ on p-Si, and $\tau_{\mathrm{surf,n}}/\tau_{\mathrm{surf,p}} = 9.55 \times 10^{-3}$ on n-Si. Q_{f} of the $\mathrm{Al_2O_3}$ layers is taken from measurements (cf. Sec. 4.2.2), and for the SiN_x layers we obtain $Q_{\mathrm{f}} = 2.21 \times 10^{12}\,\mathrm{q/cm^2}$ [Ste10a, Ste10b, Ste10c] which agrees well with values between $Q_{\mathrm{f}} = 2 \times 10^{12}\,\mathrm{q/cm^2}$ and $Q_{\mathrm{f}} = 2.5 \times 10^{12}\,\mathrm{q/cm^2}$ reported in the literature [Dau02c, Sch08b]. Further, we determine $\tau_0 = 35\,\mathrm{ms}$, indicating that bulk losses are negligible. The fit results of the local parameters $S_{\mathrm{n}} = S_{\mathrm{p}}$ and z_{deg} for SiN_x passivated samples are displayed in Figs. 4.5(c) and 4.5(d) and for $\mathrm{Al_2O_3}$ passivated samples in Figs. 4.6(d)–4.6(f) as lines. The surface recombination velocities parameters $S_{\mathrm{n}} = S_{\mathrm{p}}$ scatter slightly in a range of approximately half an order of magnitude for SiN_x and somewhat stronger for $\mathrm{Al_2O_3}$. For SiN_x layers, we obtain an aver-

abbreviation	**value**	**description**
global fit parameters		
τ_b	$3.5 \times 10^{-2}\,\mathrm{s}$	bulk lifetime parameter
$\tau_\mathrm{surf,n}$	$0.15\,\mathrm{\mu s}$	electron lifetime parameter at the interface
$\tau_\mathrm{surf,n}/\tau_\mathrm{surf,p}$ (p-Si)	4×10^{-3}	ratio of τ_surf between electrons and holes on p-Si
$\tau_\mathrm{surf,n}/\tau_\mathrm{surf,p}$ (n-Si)	9.55×10^{-3}	ratio of τ_surf between electrons and holes on n-Si
$S_\mathrm{n}/S_\mathrm{p}$	1	ratio of the surface recombination velocity parameters for electrons and holes
E_d	E_i	energy of defect level
parameterization of fit results (Eqs. (4.1) and (4.12))		
N_ref	$1 \times 10^{14}\,\mathrm{cm^{-3}}$	reference dopant density
p-Si, SiN$_x$		
$Q_\mathrm{f,1}$	$2.21 \times 10^{12}\,\mathrm{q/cm^{-2}}$	fixed positive charge density
$z_\mathrm{ref,1}$	$0.8986\,\mathrm{\mu m}$	degradation depth for $N_\mathrm{A} = N_\mathrm{ref}$
α_1	$-0.9158\,\mathrm{\mu m}$	prefactor for decrease of z_deg with N_A
ξ_1	-3.699×10^{-1}	exponent for decrease of z_deg with N_A
n-Si, SiN$_x$		
$Q_\mathrm{f,2}$	$2.21 \times 10^{12}\,\mathrm{q/cm^{-2}}$	fixed positive charge density
$z_\mathrm{ref,2}$	$0.4822\,\mathrm{\mu m}$	degradation depth for $N_\mathrm{D} = N_\mathrm{ref}$
α_2	$-0.04531\,\mathrm{\mu m}$	prefactor for decrease of z_deg with N_D
ξ_2	-3.699×10^{-1}	exponent for decrease of z_deg with N_D
p-Si, th-ALD		
$Q^*_\mathrm{f,3}$	$-5.2 \times 10^{12}\,\mathrm{q/cm^{-2}}$	fixed positive charge density
$z_\mathrm{ref,3}$	$0.07193\,\mathrm{\mu m}$	degradation depth for $N_\mathrm{A} = N_\mathrm{ref}$
α_3	$-0.04782\,\mathrm{\mu m}$	prefactor for decrease of z_deg with N_A
ξ_3	-3.699×10^{-1}	exponent for decrease of z_deg with N_A
p-Si, PA-ALD		
$Q^*_\mathrm{f,4}$	$-5.2 \times 10^{12}\,\mathrm{q/cm^{-2}}$	fixed positive charge density
$z_\mathrm{ref,4}$	$0.1071\,\mathrm{\mu m}$	degradation depth for $N_\mathrm{A} = N_\mathrm{ref}$
α_4	$-0.09729\,\mathrm{\mu m}$	prefactor for decrease of z_deg with N_A
ξ_4	-3.699×10^{-1}	exponent for decrease of z_deg with N_A
n-Si, PA-ALD		
$Q^*_\mathrm{f,5}$	$-6.2 \times 10^{12}\,\mathrm{q/cm^{-2}}$	fixed positive charge density
$z_\mathrm{ref,5}$	$0.6942\,\mathrm{\mu m}$	degradation depth for $N_\mathrm{D} = N_\mathrm{ref}$
α_5	6.945×10^{-7}	prefactor for decrease of z_deg with N_D
ξ_5	-1.0	exponent for decrease of z_deg with N_D
$S_\mathrm{p}^{\mathrm{SiN}_x}$	$6.40 \times 10^{3}\,\mathrm{cm/s}$	av. surface recombination velocity parameter for holes at SiN$_x$/c-Si interfaces
$S_\mathrm{p}^{\mathrm{Al_2O_3}}$	$1.36 \times 10^{4}\,\mathrm{cm/s}$	av. surface recombination velocity parameter for holes at Al$_2$O$_3$/c-Si interfaces

Table 4.1: Globally optimized simulation parameters and parametrizations of z_deg for the fitted $S_\mathrm{eff}(\Delta n)$ dependence at the SiN$_x$/c-Si interface in Fig. 4.5 and at the Al$_2$O$_3$/c-Si interfaces in Fig. 4.6. The Q_f^* values marked with a star are taken from measurements.

age value of $(6.40 \pm 0.65) \times 10^3$ cm/s, and for Al_2O_3 we find $(13.6 \pm 7.9) \times 10^3$ cm/s. The scattering of the surface recombination velocity parameters $S_\mathrm{n} = S_\mathrm{p}$ can be explained by their sensitivity against the deposition conditions. Slight differences, e.g. in the wafer pretreatment may cause a considerable scattering in the defect density N_d, and accordingly in S_n and S_p (Eq. (2.50)). Moreover, it is difficult to determine S_n and S_p accurately from the measurements, because in low-injection S_eff is dominated by the recombination in the SDR $S_\mathrm{eff,deg}$ (Eq. (4.7)) rather than by surface recombination $S_\mathrm{eff,surf}$ (Eq. (2.51)), as illustrated in Fig. 4.3. For high-injection conditions, the choice of the Auger model used to extract S_eff from the τ_eff measurements sensitively influences the values of the fit parameters S_n and S_p. Thus, the considerable increase in S_n or S_p with N_dop as observed by Chen and Altermatt [Alt02a, Alt06b, Che94] is expected to become relevant only for $N_\mathrm{dop} > 10^{17}\,\mathrm{cm}^{-3}$, where surface damage becomes negligible. Figures 4.5(c), 4.5(d) and 4.6(d)–4.6(f) show that z_deg decreases with N_dop in both n-Si and p-Si substrates and for both SiN_x and Al_2O_3.

In order to arrive at a description suitable for numerical device simulators, we parametrize the observed dependence of z_deg on N_dop in Figs. 4.5(c)–4.5(d) and 4.6(d)–4.6(f) using the equation:

$$z_{\mathrm{deg},i} = z_{\mathrm{ref},i} + \alpha_i \left(1 - \left(\frac{N_\mathrm{dop}}{N_\mathrm{ref}} \right)^{\xi_i} \right), \tag{4.12}$$

where the index $i = 1, \ldots, 5$ stand for the five investigated data sets, the SiN_x passivated samples on p-Si (i=1) and n-Si (i=2), the th-ALD passivated p-Si substrates (i=3) and the PA-ALD passivated p-Si (i=4) and n-Si (i=5) wafers. All parameters are specified in Table 4.1. The resulting damage depths $z_{\mathrm{deg},i}$ are shown as lines in Figs. 4.5(c), 4.5(d) and 4.6(d)–4.6(f).

In conclusion, the parametrization of the surface damage model was obtained by precisely reproducing measurements of the injection dependent effective surface recombination velocity $S_\mathrm{eff}(\Delta n)$. Both SiN_x and Al_2O_3 passivated c-Si wafers were investigated. Due to the large set of reference samples used for the parametrization, the model reliably predicts the $S_\mathrm{eff}(\Delta n)$ behavior of wafers with arbitrary resistivity and is thus useful for device simulations. Choosing all parameters according to Table 4.1 and applying Eq. (4.12) for the dependence of z_deg on the substrate doping, allows us to predict, for example, the influence of surface damage on SiN_x passivated solar cells, even if no detailed measurements are available, as will be shown in Chapter 7.

4.2.4 Recombination dynamics

In the following, we discuss the recombination dynamics. As mentioned in Sec. 4.1, the interface of SiN_x-passivated p-Si is strongly inverted for typical injection conditions as a consequence of non-compensated positive fixed charges Q_f. Figure 4.7(a) shows the spatially resolved carrier densities $n(z)$ and $p(z)$ at three different Δn, determined according to Eqs. (4.9)–(4.11). With increasing Δn, the position z where n equals p shifts towards the interface. This is indicated by the dashed-dotted line and the background color, where the latter indicates the positions where $p < n$ (blue) and $p > n$ (red). In general, the SRH recombination rate is maximal when $\tau_\mathrm{p}(z)n(z)/\tau_\mathrm{n}(z)p(z) = 1$. Apart from the ratio $n(z)/p(z)$, the recombination rate depends on $\tau_\mathrm{n}(z)$ and $\tau_\mathrm{p}(z)$, as shown in Fig. 4.7(b). For the regions very close to the interface, it holds $\tau_\mathrm{p}(z)n(z)/\tau_\mathrm{n}(z)p(z) > 1$ and recombination is limited by the density of holes $p(z)$. Deeper within the wafer, there is $\tau_\mathrm{p}(z)n(z)/\tau_\mathrm{n}(z)p(z) < 1$ and recombination is limited by the density of electrons $n(z)$. The corresponding recombination rates for the three values of Δn are shown in Fig. 4.7(c). With increasing z_deg, the maximum of R_SRH is shifted deeper into the wafer and, accordingly, $S_\mathrm{eff,deg}$ increases and so does the total surface recombination velocity S_eff (Eq. (4.8)). Hence, the fit to the experiment depends rather sensitively on z_deg, $\tau_\mathrm{surf,n}$, and $\tau_\mathrm{surf,p}$.

We remark that according to SRH theory (Eq. (2.49)), S_eff is expected to decrease with the dopant density N_dop of the bulk, when assuming that S_n and S_p do not depend on N_dop. The decrease of z_deg with N_dop according to Eq. (4.12) may cause this relation to be violated. This implies that substrates with a certain dopant density N_dop may have lower S_eff values than slightly lower doped substrates.

4.2.5 Continuous defect distributions

So far, we have modeled the interface recombination without considering a distribution of interface states $D(E_\mathrm{d})$ within the bandgap, and without considering the injection dependent contribution to the interface charge density Q_it that results from the occupation of $D(E_\mathrm{d})$ by electrons and holes. In the following, we investigate how the modeled S_eff is influenced by $D(E_\mathrm{d})$ and Q_it by replacing S_n and S_p with $D(E_\mathrm{d})$, σ_n, and σ_p according to Eq. (2.50). The remaining parameters are chosen as above. We assume that the defect distribution $D(E_\mathrm{d})$ consists of a donor-like distribution $D^\mathrm{D}(E_\mathrm{d})$ and an acceptor-like distribution $D^\mathrm{A}(E_\mathrm{d})$. The contribution to the interface charge density Q_it of D^A and D^D follows from the definition of acceptor-like defect states (negatively charged if occupied and neutral if unoccupied) and donor-like defect states (positively charged if unoccupied and neutral if

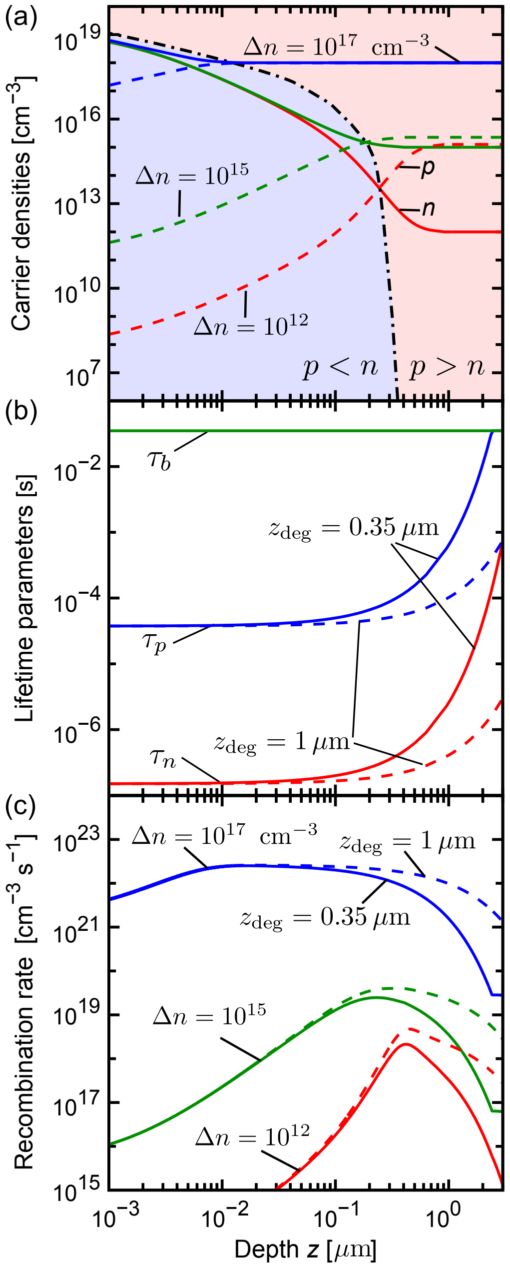

Figure 4.7: (a) Electron and hole densities, (b) lifetime parameters, and (c) recombination rates as a function of depth from the SiN$_x$/c-Si interface in 10 Ωcm p-Si material, for three different excess carrier densities Δn in the quasi-neutral region, and for two different values of the degradation depth $z_{\rm deg}$ of Eq. (4.6). The remaining parameters are chosen according to [Ste10b].

occupied), respectively, and is given by:

$$Q_{\rm it}^{\rm A} \;=\; -q \int_{E_{\rm v}}^{E_{\rm c}} {\rm d}E_{\rm d}\; f(E_{\rm d}) D^{\rm A}(E_{\rm d}), \qquad Q_{\rm it}^{\rm D} \;=\; q \int_{E_{\rm v}}^{E_{\rm c}} {\rm d}E_{\rm d}\; (1 - f(E_{\rm d})) D^{\rm D}(E_{\rm d}). \tag{4.13}$$

Assuming the thermal velocity of electrons and holes to be equal, the occupation fraction $f(E_{\rm d})$ is calculated as (cf. Eq. (2.30)):

$$f(E_{\rm d}) = \frac{\sigma_{\rm n}(E_{\rm d}) n_{\rm s} + \sigma_{\rm p}(E_{\rm d}) p_1(E_{\rm d})}{\sigma_{\rm n}(E_{\rm d})[n_{\rm s} + n_1(E_{\rm d})] + \sigma_{\rm p}(E_{\rm d})[p_{\rm s} + p_1(E_{\rm d})]}, \tag{4.14}$$

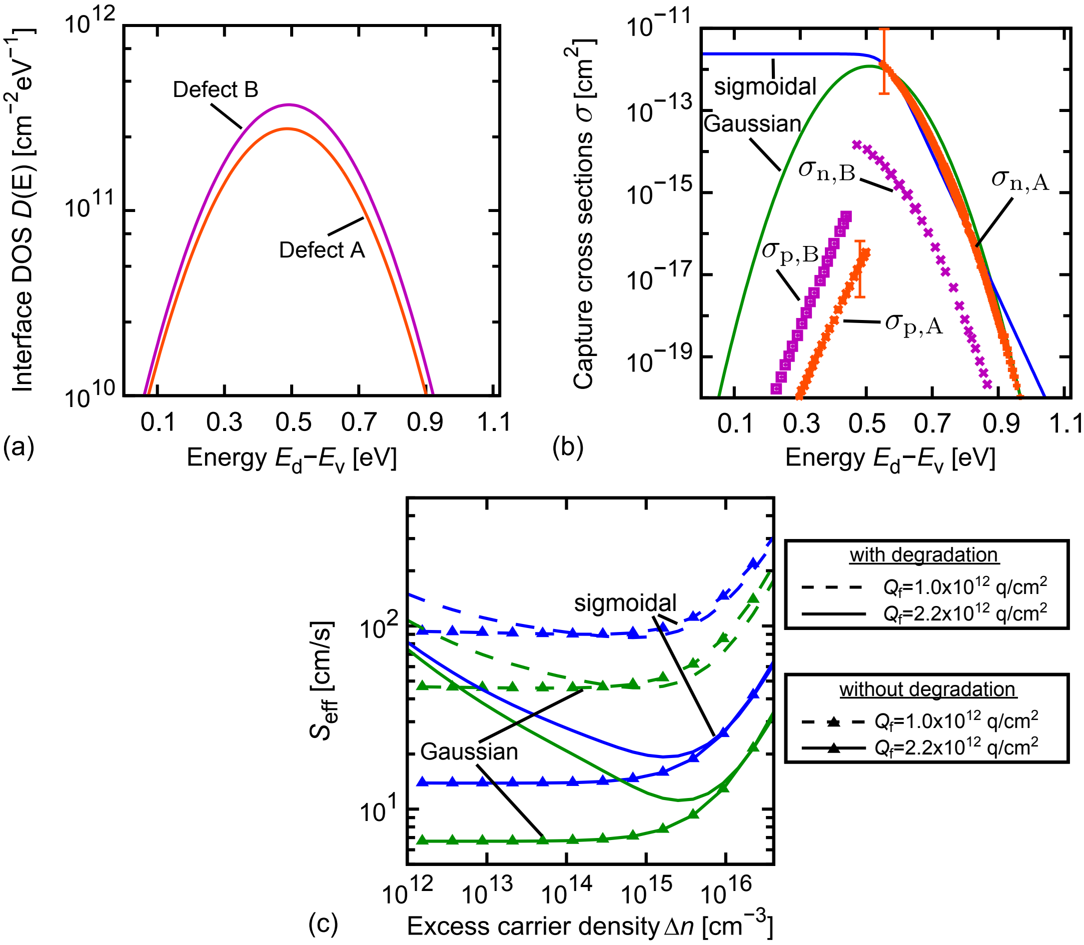

Figure 4.8: Application of the extended SRH formalism to a continuous distribution of defect states. (a) Measured [Sch97] densities of interface defect states, parametrized via Eq. (4.15a) and the parameters in Table 4.2. (b) Measured [Sch97] cross sections for electron capture σ_n and hole capture σ_p at the SiN$_x$/c-Si interface, as a function of energy E_d from the valence band edge E_v within the silicon bandgap (symbols) with an extrapolation (lines) using either a Gaussian or a sigmoidal function (Eqs. (4.15b), (4.15c), and Table 4.2). (c) The resulting calculated S_eff values without bulk degradation (triangles) and with bulk degradation (lines) at two different fixed charge densities Q_f.

where $n_1(E_\mathrm{d})$ and $p_1(E_\mathrm{d})$ are defined in Eq. (2.34), and n_s and p_s are given by Eq. (2.53). To obtain the band bending φ_s, Q_f in Eq. (4.1), is replaced by $Q_\mathrm{it} = Q_\mathrm{f} + Q_\mathrm{it}^\mathrm{A} + Q_\mathrm{it}^\mathrm{D}$.

Schmidt *et al.* [Sch97] measured the defect distribution $D(E_\mathrm{d})$ at samples prepared by direct PECVD at low frequency. The resulting distribution $D(E_\mathrm{d})$ has three distinct peaks labeled A, B, and C, cf. Ref. [Sch97]. The peak C is probably caused by the ion bombardment occurring in low-frequency direct PECVD [Sch99a]. Because

abbreviation	**defect A**		**defect B**		unit
	Gaussian defect distribution (Eq. (4.15a))				
σ_0		2.77×10^{11}		3.73×10^{11}	cm
E_0		-0.073		-0.069	eV
χ		0.161		0.160	eV
	capture cross sections (CCS) - gaussian (Eq. (4.15b))				
	electrons	holes	electrons	holes	
σ_0	1.213×10^{-12}	3.951×10^{-17}	1.396×10^{-14}	3.399×10^{-16}	cm
E_0	-0.06	-0.01	-0.195	-0.06	eV
ϑ_j	0.075	0.06	0.075	0.06	eV
	capture cross sections (CCS) - sigmoid (Eq. (4.15c))				
	electrons	holes	electrons	holes	
σ_0	1.196×10^{-12}	2.17×10^{-16}	5.77×10^{-15}	1.585×10^{-14}	cm
E_0	0	0	0	0	eV
ζ_j	40	-40	40	-40	1/eV

Table 4.2: Parameters for Eqs. (4.15a)–(4.15c) used for the simulations in Fig. 4.8.

the SiN$_x$ films considered in this work were prepared at high-frequency [Ker02b], we must neglect this peak. The remaining two peaks are shown in Fig. 4.8(a). Their $\sigma_\mathrm{n}(E_\mathrm{d})$ and $\sigma_\mathrm{p}(E_\mathrm{d})$ dependencies were measured in the same samples using small-pulse deep-level transient spectroscopy (DLTS) [Sch97], shown as symbols in Fig. 4.8(b). With this technique, one can only determine σ_p in the lower half of the bandgap and σ_n in the upper half of the bandgap. Therefore, the measured values must be extrapolated to the other unknown half of the bandgap. We do this either by means of a Gaussian function Eq. (4.15b) or using a sigmoidal function Eq. (4.15c), similarly to Schmidt and Aberle [Sch99a]:

$$
\begin{aligned}
D(E_\mathrm{d}) &= N_0\,\mathrm{e}^{-\frac{(E_\mathrm{i}+E_0-E_\mathrm{d})^2}{2\chi^2}} && \text{gaussian defect distribution,} \quad (4.15\mathrm{a})\\
\sigma_j(E_\mathrm{d}) &= \sigma_{0,j}\,\mathrm{e}^{-\frac{(E_\mathrm{i}+E_{0,j}-E_\mathrm{d})^2}{2\vartheta_j^2}} && \text{gaussian CCS,} \quad (4.15\mathrm{b})\\
\sigma_j(E_\mathrm{d}) &= \frac{2\sigma_{0,j}}{1+\,\mathrm{e}^{-\zeta_j(E_i+E_{0,j}-E_\mathrm{d})}} && \text{sigmoidal CCS.} \quad (4.15\mathrm{c})
\end{aligned}
$$

Here the index j =n, p refers to free electrons and free holes, respectively. The functions (4.15b) and (4.15c) are exemplarily shown in Fig. 4.8(b) for $\sigma_{\mathrm{A,n}}$ (lines). Note that an exponential extrapolation of the measured $\sigma_j(E_\mathrm{d})$ dependence as a third possible scenario would lead to S_eff values that exceed the measured values tremendously. We assign donor-like (acceptor-like) properties to defect states having $\sigma_\mathrm{n} > \sigma_\mathrm{p}$ ($\sigma_\mathrm{n} < \sigma_\mathrm{p}$), based on the assumption that the Coulomb interaction dominates the ratio between σ_n and σ_p [Mac04a].

The calculated S_{eff} values are displayed in Fig. 4.8(c) with and without surface damage for both scenarios for σ_j (Eqs. (4.15b) and (4.15c)). Using the Gaussian model (Eq. (4.15b) for the CCS results in lower S_{eff} values than the sigmoidal dependence of the CCS on defect energy (Eq. (4.15c)). Hence, the injection dependence obtained with degradation is stronger pronounced in case of the Gaussian scenario. Since smaller Q_{f} can be more easily compensated by Q_{it}, we also show calculations with $Q_{\text{f}} = 1 \times 10^{12}\,\text{q/cm}^2$. It is apparent that Q_{it} has no noticeable influence on S_{eff}. Consequently, the rise in S_{eff} towards low Δn can only be achieved with local degradation.

We do not perform a fit of the entire data with this extended model, because the measured samples [Sch97] had an intentionally high $D(E_{\text{d}})$ in order to obtain sufficiently large DLTS signals [Abe99]. Hence, a reduction of $D(E_{\text{d}})$ by about one order of magnitude may be assumed for well-passivated wafers. In such samples, the influence of Q_{it} is definitely negligible, and we see no need to include Eqs. (4.13) and (4.14) into a device model.

In summary, we demonstrated the influence of charges Q_{it} trapped in the interface defects by employing measured defect distributions and capture cross sections [Sch97]. It was shown that Q_{it} cannot cause an injection dependence of S_{eff} in low-injection if the defect density and capture cross sections are chosen in ranges that are typical for SiN_x passivation layers. Hence, Q_{it} can be neglected in a recombination model.

4.2.6 Understanding and reducing the surface damage

In the previous sections, we have shown that an SDR, characterized by a strongly reduced excess carrier lifetime τ_{b} in the bulk, leads to the pronounced $S_{\text{eff}}(\Delta n)$ dependence which is experimentally observed on SiN_x passivated p-Si wafers [Ker02b]. An important practical consequence of the pronounced $S_{\text{eff}}(\Delta n)$ dependence is that at excess carrier densities Δn, which are typical for solar cell operation conditions, the surface passivation quality is strongly deteriorated compared to higher injection densities.

In Fig. 4.9, we investigate the injection dependence of S_{eff} for low Δn with and without SDR in dependence on the fixed charge density Q_{f} at the interface for a $1.5\,\Omega\text{cm}$ p-Si substrate. The injection dependence is characterized by the fraction $\delta_i = S_{\text{eff}}(\Delta n = 10^{12}\,\text{cm}^{-3})/S_{\text{eff}}(\Delta n = 10^{15}\,\text{cm}^{-3})$, where $i = \text{dam}$ denotes the injection dependence with surface damage and $i = \text{ideal}$ stands for the injection dependence of the non-damaged surface. We find a significant influence of the SDR only for $Q_{\text{f}} \gtrsim 3 \times 10^{11}\,\text{q/cm}^2$ (cf. Fig. 4.9). For $Q_{\text{f}} \lesssim 3 \times 10^{11}\,\text{q/cm}^2$, the injection dependencies with and without SDR are approximately equal ($\delta_{\text{dam}} \approx \delta_{\text{ideal}}$). Be-

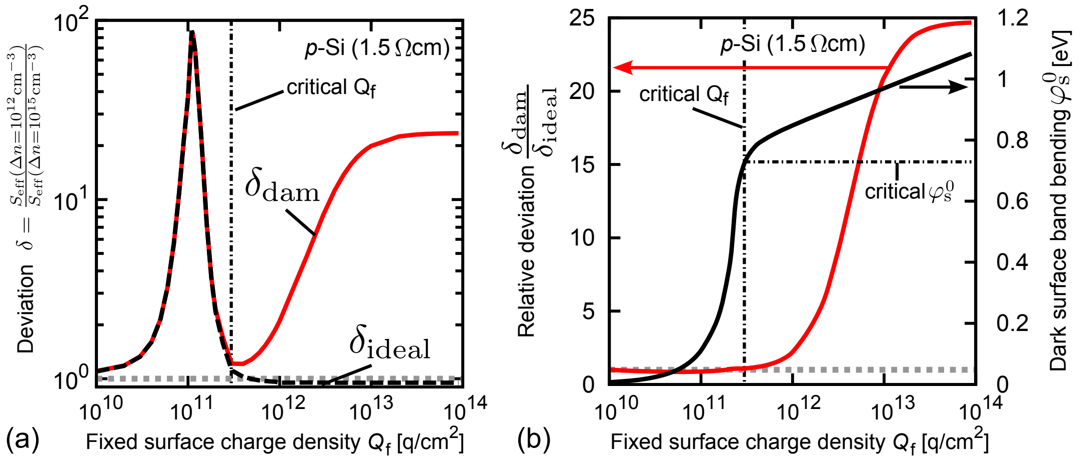

Figure 4.9: (a) Injection dependence of S_{eff} vs. Q_{f} for a p-Si substrate of 1.5 Ωcm resistivity, characterized via $\delta_i = S_{\mathrm{eff}}(\Delta n = 10^{12}\,\mathrm{cm}^{-3})/S_{\mathrm{eff}}(\Delta n = 10^{15}\,\mathrm{cm}^{-3})$. The injection dependence is evaluated with SDR (δ_{dam}, red line) and without SDR (δ_{ideal}, black line). For $Q_{\mathrm{f}} \lesssim 3 \times 10^{11}\,\mathrm{q/cm}^2$ (dashed black line), the injection dependence is independent of the SDR, i.e. $\delta_{\mathrm{dam}} \approx \delta_{\mathrm{ideal}}$. In contrast, $Q_{\mathrm{f}} \gtrsim 3 \times 10^{11}\,\mathrm{q/cm}^2$ leads to a dramatic increase of δ_{dam}, while $\delta_{\mathrm{ideal}} \approx 1$, as expected according to Eq. (4.4). (b) Relative deviation $\delta_{\mathrm{dam}}/\delta_{\mathrm{ideal}}$ (red line, left axis) and the dark surface band-bending φ_{s}^0 (black line, right axis) versus Q_{f}. The critical value of Q_{f} and φ_{s}^0 are indicated by dashed black lines. All parameters apart from Q_{f} are chosen according to the fit in Fig. 4.5 and Table 4.1. The dashed gray lines indicate $\delta = 1$.

tween $Q_{\mathrm{f}} \approx 3 \times 10^{11}\,\mathrm{q/cm}^2$ and $Q_{\mathrm{f}} \approx 2 \times 10^{13}\,\mathrm{q/cm}^2$, δ_{dam} increases with a maximum slope at $Q_{\mathrm{f}} \approx 4 \times 10^{12}\,\mathrm{q/cm}^2$. For higher values of Q_{f}, δ_{dam} saturates and finally becomes independent of Q_{f} above $Q_{\mathrm{f}} \approx 8 \times 10^{13}\,\mathrm{q/cm}^2$. Note that the strong peak in the injection dependence of S_{eff} at $Q_{\mathrm{f}} \approx 1.1 \times 10^{11}\,\mathrm{q/cm}^2$ is due to the transition from accumulation to inversion conditions with increasing Δn at the surface. For $Q_{\mathrm{f}} \ll 1.1 \times 10^{11}\,\mathrm{q/cm}^2$, the silicon wafer below the surface is in accumulation condition for both $\Delta n = 10^{12}\,\mathrm{cm}^{-3}$ and $\Delta n = 10^{15}\,\mathrm{cm}^{-3}$. Thus, no injection dependence of S_{eff} is expected (cf. Sec. 4.1). Similarly, for $Q_{\mathrm{f}} \gg 1.1 \times 10^{11}\,\mathrm{q/cm}^2$, the silicon wafer below the surface is inverted for both injection densities, and no injection dependence is observed either if surface damage is neglected. For $Q_{\mathrm{f}} \approx 1.1 \times 10^{11}\,\mathrm{q/cm}^2$ and $\Delta n = 10^{12}\,\mathrm{cm}^{-3}$, there is $n_{\mathrm{s}} \approx p_{\mathrm{s}}$. Thus, the product $n_{\mathrm{s}}p_{\mathrm{s}}$ is maximized which causes S_{eff} to be maximal (Eq. (2.49)).[4] With increasing Δn, the surface becomes inverted and at $\Delta n = 10^{15}\,\mathrm{cm}^{-3}$, there is $n_{\mathrm{s}}/p_{\mathrm{s}} \approx 40$. Consequently, at $\Delta n = 10^{15}\,\mathrm{cm}^{-3}$, S_{eff} is strongly reduced compared to the value at $\Delta n = 10^{12}\,\mathrm{cm}^{-3}$. This results in the peak in the injection depen-

---

[4] In the general case, recombination is maximal for $S_{\mathrm{n}}n_{\mathrm{s}} = S_{\mathrm{p}}p_{\mathrm{s}}$. In Fig. 4.9, we choose $S_{\mathrm{n}} = S_{\mathrm{p}}$ and thus, the surface recombination velocity parameter cancels out, leading to the simple condition $n_{\mathrm{s}} = p_{\mathrm{s}}$.

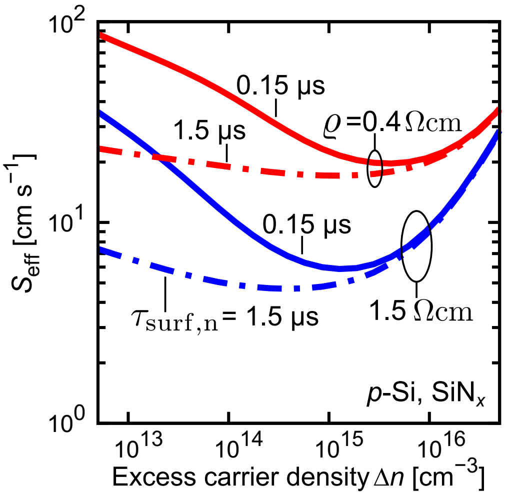

Figure 4.10: Influence of the defect density in the surface-damage region (SDR) on the injection dependence of S_{eff}. Calculated S_{eff} in the SiN$_x$ passivated p-Si samples with 0.4 Ωcm and 1.5 Ωcm resistivity. The continuous lines are determined using the values of $\tau_{\text{surf,n}}$ and $\tau_{\text{surf,p}}$ obtained from the fit in Fig. 4.5. The dashed curves are obtained using enhanced values of τ_{surf}, multiplied by one order of magnitude. This shows that a strong improvement of S_{eff} towards low Δn can be achieved if the degradation lifetime parameters are increased by only a factor of ten.

dence $\delta_i = S_{\text{eff}}(\Delta n = 10^{12}\,\text{cm}^{-3})/S_{\text{eff}}(\Delta n = 10^{15}\,\text{cm}^{-3})$ in Fig. 4.9(a). In Fig. 4.9(b), the dark surface band-bending φ_{s}^{0} is plotted in addition to the relative deviation $\delta_{\text{dam}}/\delta_{\text{ideal}}$. This is done to estimate a critical value of φ_{s}^{0}, above which surface damage becomes significant.

Our microscopic interpretation of surface damage allows us to predict which improvement of the lifetime in the degraded volume is necessary to maintain the high performance of a p-Si solar cell also at low illumination levels, even though it contains non-diffused surfaces passivated with SiN$_x$. Note that for non-diffused n-Si solar cells passivated with Al$_2$O$_3$ layers, the detrimental effect caused by the SDR is less pronounced, since the damage depth is by one order of magnitude smaller than for SiN$_x$. Figure 4.10 shows the simulated S_{eff} values of a 0.4 Ωcm and of a 1.5 Ωcm sample passivated by SiN$_x$ (continuous lines), calculated using the $\tau_{\text{surf,n}}$ and $\tau_{\text{surf,p}}$ values that reproduce the experiments in Fig. 4.5(a) (cf. Table 4.1). For comparison, S_{eff} calculated with τ_{surf} values multiplied by a factor of ten are shown (dashed curves). Surprisingly, an improvement of τ_{surf} by a factor of mere 10 already avoids the reduced S_{eff} values at low Δn. In Chapter 7, we will show by means of SENTAURUS-DEVICE simulations that this prediction holds also for the efficiency improvement of solar cells containing SiN$_x$ layers. A detailed understanding of the cause for the deteriorated region may help to achieve this improvement.

To conclude, we found that surface damage significantly influences surface recombination only if the surface charge density exceeds a doping-dependent critical value, e.g. $Q_\mathrm{f} \gtrsim 3 \times 10^{11}\,\mathrm{cm}^{-3}$ for a 1.5 Ωcm p-Si substrate. In addition, we predicted that for this material a reduction of the defect density in the SDR by a factor of 10 is sufficient to reduce S_eff in low-injection to an amount that surface damage becomes negligible.

4.2.7 Possible causes of the SDR and implications on experiment

As discussed in the previous section, a relatively small reduction of the surface damage may help to reduce the surface recombination velocity at SiN_x passivated samples in low-injection. Therefore, we suggest here possible causes of the SDR. Our high resolution transmission electron micrographs (HRTEM images) [Ste10c] of the surface-near region underneath PECVD-SiN_x layers fabricated at ISFH [Har09] show defect-like contrasts reaching up to 30 nm into the silicon substrate (Fig. 4.11).[5] This sample was deposited in a remote-plasma chamber (Oxford Instruments Plasmalab 80^+) using silane and ammonia as process gases. A main cause for the formation of such an SDR underneath SiN_x layers might be the extremely high density of hydrogen (up to $10^{22}\,\mathrm{cm}^{-3}$) observed in silicon substrates close to the SiN_x layer [Sop05]. Such high densities of hydrogen in silicon are known to lead to the formation of platelets, and recombination-active deep-level defects [Joh87, New91, Web08]. A possible source of hydrogen are the H-atoms stored in the SiN_x layers (typically $10-15$ at. %). However, the H-content in the ALD-layers is only approximately 1 at. %. Therefore, we suggest that H-termination during wafer-pretreatment provides an additional, non-negligible source of hydrogen. H-termination during wet chemical etching is known to induce hydrogen in high concentrations into the silicon wafer. This has been experimentally validated via acceptor deactivation close to the interface [Web08]. Further indications of hydrogen-related defects are obtained by comparing the penetration depth of hydrogen to the determined damage depth z_deg. The effective diffusion coefficient D_eff of hydrogen in silicon was experimentally determined by several groups (for an overview see [e.g. Riz91, Sop02]) and is known to decrease from $D_\mathrm{eff} \approx 10^{-11}\,\mathrm{cm}^2/\mathrm{s}$ at typical deposition temperatures of SiN_x (400 °C) down to $D_\mathrm{eff} \gtrsim 5 \times 10^{-13}\,\mathrm{cm}^2/\mathrm{s}$ at deposition temperatures of PA-ALD (200 °C). Assuming deposition times that are commonly reported in the literature ($t = 1.5$–$10\,\mathrm{min}$), the penetration depth $d = \sqrt{D_\mathrm{eff} t}$ is roughly approximated to be $0.3-0.8\,\mu\mathrm{m}$ for SiN_x and $0.060-0.17\,\mu\mathrm{m}$ in case of PA-ALD. This estimation of the H-diffusion depth is of the same order of magnitude as the depth of the SDR modeled in Sec. 4.2.3, which is $0.1-1\,\mu\mathrm{m}$ in case of SiN_x and $0.01-0.1\,\mu\mathrm{m}$ for $\mathrm{Al_2O_3}$. In addition to a smaller diffusion coefficient, the out-diffusion of hydrogen during annealing of the

---

[5] Note that for reference samples, passivated by thermal $\mathrm{SiO_2}$, no such defect-rich contrasts in the HRTEM micrographs are observed.

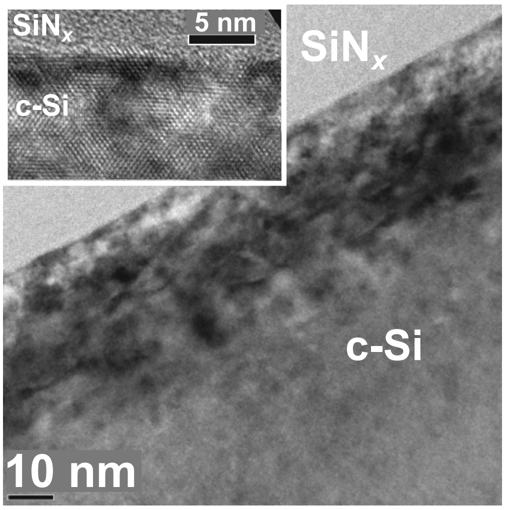

Figure 4.11: HRTEM images of a 30 nm thick defect-rich region in the silicon substrate underneath a SiN$_x$ passivating layer. Short, non-connected defect-like contrasts are observed that are aligned almost parallel to the interface. The micrographs were provided by Seibt [Sei10].

Al_2O_3 layers may reduce the extent of the SDR further. Our simulations predict that already a moderate reduction of the H-content will help to decrease recombination at low injection densities, while the good passivation properties at high illumination levels are maintained (cf. Sec. 4.2.6).

From these considerations, we may derive some rules of thumb for experimenters to further improve the passivation quality of SiN$_x$ on p-Si surfaces at low injection densities. One direction for avoiding the SDR would be to strongly reduce the hydrogen concentration in the SiN$_x$ films. In fact, there are deposition techniques, such as low-pressure chemical vapor deposition (LPCVD), that lead to a strongly reduced hydrogen content compared to PECVD films. However, these hydrogen-lean films do not provide as good passivation properties as PECVD-SiN$_x$ does, due to the lack of hydrogen at the SiN$_x$/c-Si interface, where the hydrogen passivation of interface states effectively reduces interface recombination. Hence, a reduction in the hydrogen content might not be the best approach for avoiding the SDR, as the interface passivation is deteriorated at the same time.

If the surface damage cannot be eliminated in experiment, a promising idea would be to strongly reduce or even invert the interface charge of the SiN$_x$ layers (cf. Fig. 4.10 in Sec. 4.2.6). This would reduce the impact of the SDR on S_{eff}, and could thereby significantly improve the passivation quality of SiN$_x$ on p-Si at low injection densities Δn. In addition, this would help to reduce the effect of parasitic shunting, where the inversion layer couples to the p-contacts and causes strongly reduced short circuit currents [Dau02a]. The fixed charge density in SiN$_x$ can be manipulated by charge injection [Kri88] which is exploited in memory devices [Fuj85]. It has recently been demonstrated experimentally that Q_{f} in SiN$_x$ films deposited by LPCVD can be permanently switched from large positive to large negative values, leading to a pronounced improvement in the surface passivation of p-Si [Web09]. Hence, the development of negatively charged SiN$_x$ may be a promising approach for improving

SiN_x passivation on p-Si surfaces.
Another approach to reduce Q_f uses double stacks of silicon rich a-SiN_y:H and SiN_x [Gat11a]. Such stacks have been shown to achieve similar S_eff values (after firing) as SiN_x layers at intermediate Δn, whereas the surface passivation in low-injection is enhanced. Since, in addition, no parasitic shunting is observed for these layers, we assume that Q_f is low at the interface.
It might also be worthwhile to study in more detail the impact of the wet chemical etching prior to the SiN_x deposition in more detail. Only little data exists concerning the impact of the chemical pretreatment of the silicon surface on the passivation quality after SiN_x deposition. The effect of the chemical etchant and the duration of the chemical treatment should be studied with regard to the formation of an SDR.
A recent approach suggests a low Fe-contamination of $[\mathrm{Fe}]= 2 - 5 \times 10^{10}\,\mathrm{cm}^{-3}$of the wafer material as a possible cause for the injection dependence of S_eff [Cue11, to be published]. An experimental verification is still missing and could easily be confirmed by carrier lifetime measurements [Mac04b, Rei05b, Rei05a]. We remark, that the existence of Fe-contamination does not exclude H-induced defects as a reason for the injection dependent S_eff, because both defects could exist in parallel.

In conclusion, we suggested H-contamination, e.g. due to the wafer pretreatment as a possible cause for surface damage. Also Fe-contamination was considered as a possible, perhaps additional, reason. To eliminate the influence of surface damage on the injection dependence of the effective surface recombination velocity S_eff, we considered a reduction of the H-content during the deposition and the wafer pretreatment, a switching of the fixed charge density Q_f to negative values [Web09], or a reduction of Q_f, e.g. by using a-SiN_y:H/SiN_x stacks [Gat11a]. We recommend the latter two approaches because a reduction of the H-content may reduce the passivation quality of SiN_x. To trace the underlying causes of the injection dependence of S_eff, a detailed study regarding the exact values of Q_f, the hydrogen content in the substrates, wafer pretreatment, as well as SEM imaging of defect-rich regions and measurements of the hydrogen out-diffusion during annealing is required.

4.3 Conclusion

We have used theoretical considerations and numerical simulations to understand the causes of the passivation behavior of SiN_x/c-Si and $\mathrm{Al_2O_3}$/c-Si interfaces at low illumination levels. A model was derived, based on which suggestions for improvements and further experimental studies have been made. This model quantifies interface recombination by the SRH formalism with the inclusion of lifetime reduction in the bulk of silicon near the surface, called the surface-damage region (SDR) [Ste10a, Ste10b, Ste10c]. The model explains the measured effective surface recombination velocity S_{eff} to a high precision level in a wide range of excess carrier densities Δn and dopant densities N_{dop}, in both p-Si and n-Si. All model parameters are physically meaningful, and predict that a tenfold improvement of the SRH lifetime in the SDR, corresponding to a tenfold reduction of the density of states, eliminates the strong increase of S_{eff} towards low Δn in $1.5\,\Omega$cm p-Si to the extent that non-diffused SiN_x passivated surfaces can be incorporated in silicon solar cells. In addition, it was shown how a reduction in the fixed surface charge density Q_{f} of SiN_x layers could improve the performance of SiN_x in low-injection. The damage region was also observed in HRTEM micrographs and does not necessarily originate from the deposition conditions alone, but possibly also from the wafer pretreatment. We found that the thickness of the SDR is $0.1-1\,\mu$m in case of SiN_x and, almost negligible, $0.01-0.1\,\mu$m for $\mathrm{Al_2O_3}$. With an extension of the model to include measured distributions of the interface states and energy-dependent cross sections for electron and hole capture, respectively, it was confirmed that, at typical values for the fixed charge density Q_{f} at the SiN_x/c-Si interface, the charges stored at the interface defects have a negligible influence on S_{eff}. A parametrization suitable for numerical device modeling was given by Eqs. (2.49), (2.35), (4.6), and (4.12), and in Table 4.1. In Chapter 7, we will include this model into SENTAURUS-DEVICE simulations and demonstrate the influence of the SDR on solar cell performance in dependence on cell design.

Chapter 5

Limits to SRH Statistics for Quantifying Recombination via Amphoteric Defects

Models for quantifying the recombination at a-Si:H/c-Si interfaces must take into account both the amphoteric nature and the energy separation between the donor-like and acceptor-like defect states. Such an amphoteric model was proposed by Vaillant and Jousse [Vai86] (cf. Sec. 2.3.2). This model has only a non-closed-form solution and is thus computationally demanding. Therefore, it is common practice in semiconductor device modeling to approximate recombination via amphoteric defects by simplified models. Various approaches have been applied, including simple SRH statistics [Hal52, Sho52] by Garin *et al.* [Gar05], an extended SRH formalism by Brattain and Bardeen, Simmons and Taylor [Bra53, Sim71] that includes a distribution of defects within the bandgap, and simplified closed-form solutions where the thermal emission is neglected, as proposed by Hubin *et al.* [Hub92] and applied by Olibet *et al.* [Oli07]. Sometimes, a constant density of defect states is chosen [Pla07], with donor-like properties below midgap and acceptor-like behavior above midgap. Recently, we extended the SRH formalism [Ste10d] and demonstrated that our extension is a significantly better estimation of the amphoteric model than was achieved in Refs. [Gar05, Hub92, Oli07, Pla07]. Here, we introduce this SRH approach and investigate the parameter ranges for which it is valid. Based on the results, error bounds for the approximate model are derived which help to decide in which cases it is applicable.

We model the defect distribution in a-Si:H using an extended form of the DPM [Pow93] which takes the dependence of the valence-band tails on the dopant density into account. This model is developed in Sec. 5.1.1. In Sec. 5.2.4, we apply this extended DPM to simulate the defect distribution in 10 nm thin a-Si:H passivation layers. We underline that the applicability of the DPM to thin layers is not yet clear. However, as we are interested in the recombination statistics rather than in the exact defect distributions, we believe that using the DPM is a valid approximation. Section 5.1.2 explains how the defect densities at the a-Si:H/c-Si interface are modeled. In Sec. 5.2 we investigate the differences between our extended SRH model and the amphoteric model [Vai86] in detail and in a mathematically rigorous way. We quantify the systematic error that arises when applying SRH theory instead of the amphoteric statistics. These investigations yield error bounds for the uncorrelated approach that are helpful for device simulations: for a certain, physically relevant parameter range, the use of an easily-implementable and computationally-inexpensive recombination model is valid, whereas it fails outside these bounds. We furthermore demonstrate the importance of using a self-consistent model that takes the interface charges, caused by trapped charge carriers, into account. The model for band bending at the a-Si:H/c-Si interface is implemented following Leendertz *et al.* [Lee10b] and is described in Sec. 5.2.3. Finally, we compare the recombination properties at the SiN_x/c-Si and the a-Si:H/c-Si interface to justify the different approximations used in the two recombination models in Sec. 5.3. Part of the work presented in this chapter is submitted to *physica status solidi* A [Ste11b].

5.1 Defects in amorphous silicon

5.1.1 Extended DPM with dopant dependent Urbach tails

The slope of the valence-band tail in a-Si:H is usually smaller than the slope of the conduction-band tail. This was observed in both experiment [Alj90] and theory [Dra91], and was explained by a strong dependence of the valence-band tail on structural disorder, compared to the insensitivity of the conduction-band tail to structural effects [Don98, Dra91] (cf. Sec. 2.3). Accordingly, the Urbach tail E_{v0}, defined as the inverse slope of the a-Si:H valence-band tail (cf. Sec. 2.3.1), increases with increasing disorder [Dra91, Stu89]. The disorder in a-Si:H is, for example, enhanced when dopants are added. Thus, a close relation between E_{v0} and N_{dop} can be expected. Stutzmann [Stu89] has published a compilation of measurements that correlate the total DB density $D^{\mathrm{DB}}_{\mathrm{tot}} = \int_{E_{\mathrm{v}}^{\mathrm{a\text{-}Si}}}^{E_{\mathrm{c}}^{\mathrm{a\text{-}Si}}} \mathrm{d}E_{\mathrm{d}} D^{\mathrm{DB}}(E_{\mathrm{d}})$ to the Urbach tail E_{v0}, as shown in Fig. 5.1(a). To include this measured relation into the DPM by Powell and Deane [Pow93], we require a dependence of the shift in Fermi energy for doped a-Si:H, $E_{\mathrm{f,sh}} := E_{\mathrm{f}}^{\mathrm{eq}} - E_{\mathrm{f,i}}^{\mathrm{eq}}$ (Eq. (2.69)), and the Urbach tail E_{v0} on the dopant density N_{dop}. To obtain these relations, we proceed as follows:

We insert the measured E_{v0} values [Stu89] into the DPM (cf. Eq. (2.66)). Thereby, we determine for each E_{v0} value a value $E_{\mathrm{f,sh}}$, such that the corresponding measured $D^{\mathrm{DB}}_{\mathrm{tot}}(E_{\mathrm{v0}})$ value shown in Fig. 5.1(a) is obtained. The resulting $E_{\mathrm{f,sh}}(E_{\mathrm{v0}})$

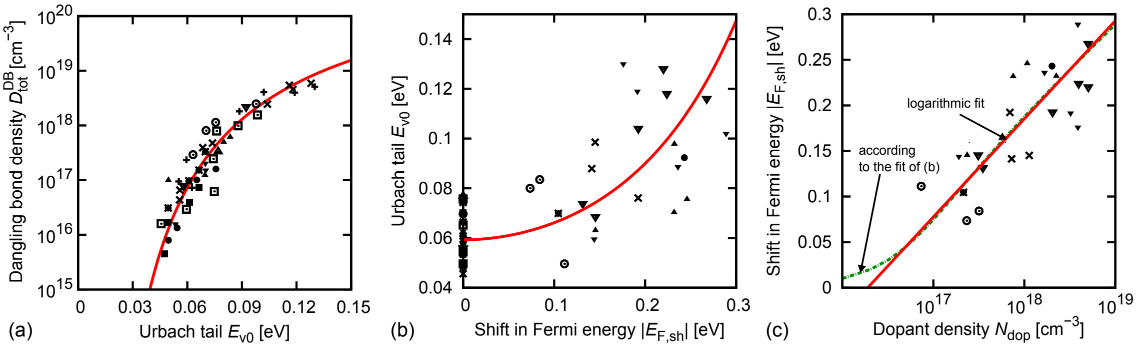

Figure 5.1: Parametrization of the dependencies between E_{v0}, $E_{\mathrm{f,sh}}$ and N_{dop} calculated using the DPM by including a doping dependence of E_{v0} according to a compilation of measured data [Stu89]. (a) Measured $D_{\mathrm{tot}}^{\mathrm{DB}}(E_{\mathrm{v0}})$ dependence compiled by [Stu89]. Different symbols correspond to different data sets, and the red line is a guide to the eye. The symbols for the $E_{\mathrm{v0}}(E_{\mathrm{f,sh}})$ dependence in (b) and the $E_{\mathrm{f,sh}}(N_{\mathrm{dop}})$ dependence in (c) are calculated using the DPM (Eqs. (2.66) and (5.1)) for the data points in (a). The continuous red lines show the parametrizations according to Eq. (5.2a) and Eq. (5.2b), respectively. The dashed-green line in (c) shows in comparison to the fit, the approximated expected dependency according to the parametrization of the DPM shown in (b) and given by Eq. (5.2a). All remaining parameters are chosen as in Fig. 2.10 of Sec. 2.3.1 and Ref. [Pow93].

dependence is displayed by the symbols in Fig. 5.1(b). We find two solutions of $E_{\mathrm{f,sh}}$ for each E_{v0}: a positive one, corresponding to a-Si:H(n), and a negative one, corresponding to a-Si:H(p). Due to the symmetry of the DPM, the absolute values of $E_{\mathrm{f,sh}}$ (cf. Sec. 2.3.1) are equal for n-Si and p-Si material if $D_{\mathrm{tot}}^{\mathrm{DB}}$ is equal for both materials. This is fulfilled, if $N_{\mathrm{A}} = N_{\mathrm{D}} \equiv N_{\mathrm{dop}}$, because the dopant density in the modeled a-Si:H material is identically equal to the net charge density of the DBs [Pow96]:

$$N_{\mathrm{dop}} = \Big| \int_{E_{\mathrm{v}}^{\mathrm{a\text{-}Si}}}^{E_{\mathrm{c}}^{\mathrm{a\text{-}Si}}} \mathrm{d}E_{\mathrm{d}}\, \left(D_{\mathrm{e}}(E_{\mathrm{d}}) - D_{\mathrm{h}}(E_{\mathrm{d}})\right) \Big|. \tag{5.1}$$

The resulting $E_{\mathrm{f,sh}}(N_{\mathrm{dop}})$ dependence is plotted in Fig. 5.1(c). To arrive at a formulation for the relations $E_{\mathrm{v0}}(E_{\mathrm{f,sh}})$ and $E_{\mathrm{f,sh}}(N_{\mathrm{dop}})$, we parametrize the calculated points in Fig. 5.1(b) and Fig. 5.1(c) by the arbitrarily chosen functions:

$$E_{\mathrm{v0}}(E_{\mathrm{f,sh}}) \;=\; a\,\mathrm{e}^{b\left(\frac{|E_{\mathrm{f,sh}}|}{E_{v0,\mathrm{ref}}}\right)^{c}}, \tag{5.2a}$$

$$E_{\mathrm{f,sh}}(N_{\mathrm{dop}}) \;=\; \pm\, E_{\mathrm{dop,0}}\, \ln\left(\frac{N_{\mathrm{dop}}}{N_{\mathrm{dop,0}}}\right), \tag{5.2b}$$

where the fit parameters are specified in Table 5.1, and $E_{\mathrm{f,sh}}$ is positive in a-Si:H(n), and negative in a-Si:H(p).

abbreviation	**value**	**unit**
a	59.25	meV
b	9.257	1
c	1.925	1
$N_{\mathrm{dop},0}$	1.9×10^{16}	cm^{-3}
$E_{\mathrm{dop},0}$	46.75	meV

Table 5.1: Fit parameters used in Eq. (5.2) to parametrize the behavior of $E_{\mathrm{v0}}(E_{\mathrm{f,sh}})$ in Fig. 5.1(b) and the behavior of $E_{\mathrm{f,sh}}(N_{\mathrm{dop}})$ in Fig. 5.1(c).

By inserting Eq. (5.2) into the DPM (Eq. (2.66)), our model now allows to calculate the DB distribution distribution $D^{\mathrm{DB}}(E_{\mathrm{d}})$ in dependence on the dopant density by taking the dependence of disorder on N_{dop} into account. The parametrized dependencies are accurate in the doping range $N_{\mathrm{dop}} = 4 \times 10^{16} \ldots 4 \times 10^{20}\,\mathrm{cm/s}$ as shown by the red line in Fig. 5.1(c). In this range, the relative deviation between the desired value of the dopant density N_{dop} and the value obtained from the DPM remains well below five percent. For $N_{\mathrm{dop}} \ll 4 \times 10^{16}\,\mathrm{cm}^{-3}$, the error between Eq. (5.2b) and the values obtained from the DPM increases as can be seen by comparing the red curve to the dashed green line in Fig. 5.1(c). However, the applications used in this work are restricted to either intrinsic or highly doped material with $4 \times 10^{16}\,\mathrm{cm}^{-3} \ll N_{\mathrm{dop}} \ll 4 \times 10^{20}\,\mathrm{cm}^{-3}$. Thus, we define $E_{\mathrm{f,sh}} = 0\,\mathrm{eV}$ for intrinsic material as expected from the DPM, and apply Eq. (5.2b) for the doped samples.

The E_{v0} values in Fig. 5.1 and Table 5.1 refer to 300 K. We take account of the temperature dependence of E_{v0} via $E_{\mathrm{v0}}(T)^2 = E_{\mathrm{v0}}(0)^2 + (k_B T)^2$ [Stu92]. The parametrization of $E_{\mathrm{v0}}(E_{\mathrm{f,sh}})$ yields a room temperature value of E_{v0} for intrinsic a-Si:H of 59 meV, compared to $E_{\mathrm{v0}} \approx 45\,\mathrm{meV}$ used by Powell and Deane [Pow93]. This is in agreement with the measured value of $E_{\mathrm{v0}} \approx 60\,\mathrm{meV}$ by Korte [Kor06a]. However, the quality of the a-Si:H layers used by this author is relatively poor (see also the discussion in Sec. 5.3), and for a given value of E_{v0}, they feature a higher defect density compared to the defect densities compiled by Stutzmann [Stu89]. Consequently, Eq. (5.2b) does not apply to the samples of Ref. [Kor06a]. Therefore, we emphasize that the suggested parametrizations in Eq. (5.2) and Table 5.1 are only valid for high-quality, low-defective a-Si:H layers. This is no restriction here, since for applications to solar cells, defect-lean a-Si:H material is required. Figure 5.2 shows an example of the doping dependence of the DB distribution $D^{\mathrm{DB}}(E_{\mathrm{d}})$. For highly doped material, a near-Gaussian distribution is formed, which is shifted from the equilibrium Fermi level $E_{\mathrm{f}}^{\mathrm{eq}} = 1.05$ eV by $E_{\mathrm{f,sh}}$ towards higher energies in a-Si:H(p), and towards lower energies in a-Si:H(n) [Pow93] (cf. Sec. 2.3.1). This originates from the suppression of defect states near $E_{\mathrm{f}}^{\mathrm{eq}}$, which occurs for sufficiently high lattice disorder.

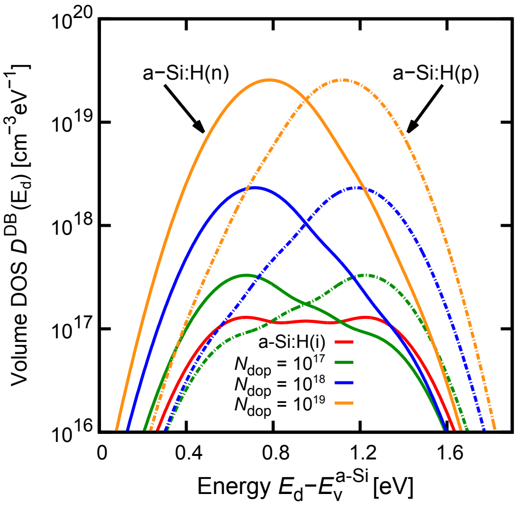

Figure 5.2: Doping dependence of the DB distribution $D^{\mathrm{DB}}(E_{\mathrm{d}})$ in a-Si, obtained using the extended DPM [Pow93], where a doping dependence of the Urbach tail is taken into account according to Eq. (5.2), with the parameters specified in Table 5.1. The remaining parameters are chosen as in Fig. 2.10 of Sec. 2.3.1 and Ref. [Pow93].

In summary, we suggested an extension of the DPM of Ref. [Pow93], which takes the measured dependence of the Urbach tail on the defect density into account.

5.1.2 Defect distributions at the a-Si:H/c-Si interface

The majority of the deep-level defect states at the a-Si:H/c-Si interface are DB states [Kor06a, Lee10b, Li08, Oli07]. In the following, we consider the distribution of these DB defect states at the a-Si:H/c-Si interface. Defects in thick hydrogenated a-Si:H layers are well described by DPMs (cf. Secs. 2.3.1 and 5.1.1). Also, the defects at the a-Si:H/c-Si interface have been modeled using the DPM [Ste10d]. However, it is not clear whether the DPM also applies to interface states. For example, there is no agreement in the literature [e.g. Lee10b] whether the shift of the defect distribution from midgap in doped a-Si:H is transferred to the interface or if the defect distribution remains close to midgap [Lee10b]. In analogy to Leendertz *et al.* [Lee10b], we therefore consider two scenarios for the DB interface states $D_{\mathrm{it}}^{\mathrm{DB}}$: either the DB distribution in the volume of the a-Si:H layer is mapped to the interface by multiplying the density of states (DOS) $D^{\mathrm{DB}}(E_{\mathrm{d}})$ in the volume by an effective interface-layer thickness w_{eff}:

$$D_{\mathrm{it}}^{\mathrm{DB}}(E_{\mathrm{d}}) = w_{\mathrm{eff}} D^{\mathrm{DB}}(E_{\mathrm{d}}). \tag{5.3a}$$

Or a Gaussian defect distribution

$$D_{\mathrm{it}}^{\mathrm{DB}}(E_{\mathrm{d}}) = D_{\mathrm{Gauss}} \exp((-0.5\ ((E_{\mathrm{d}} - E_0)\sigma_{\mathrm{Gauss}})^2)), \tag{5.3b}$$

centered at midgap, is used independently of the a-Si:H layer doping. We choose an effective interface-layer thickness of $w_{\mathrm{eff}} = 5\,\mathrm{\mathring{A}}$ as in Ref. [Lee10b], which is in agreement with $w_{\mathrm{eff}} = 7\,\mathrm{\mathring{A}}$ obtained from tight-binding simulations [Ber98b]. In Ref. [Lee10b], a Gaussian defect distribution is assumed for the volume DOS. In

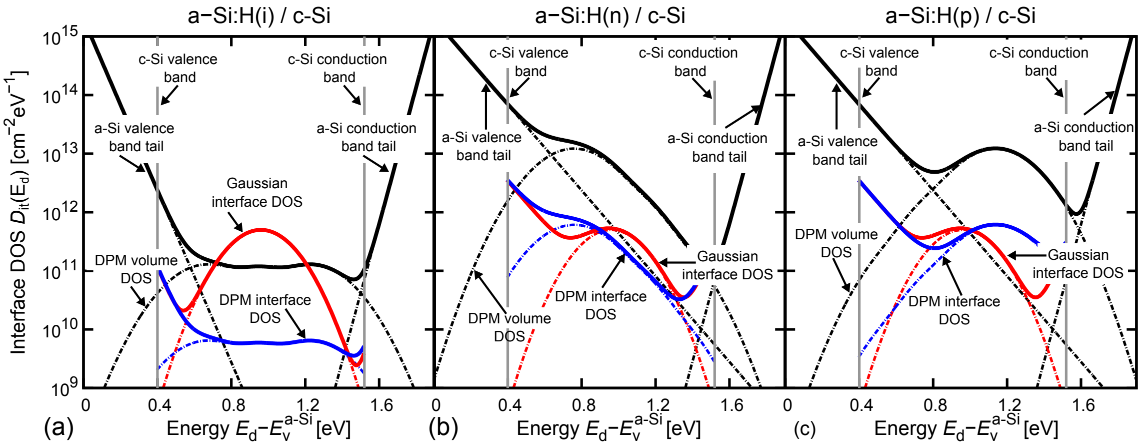

Figure 5.3: Defect distribution at the a-Si:H/c-Si interface for (a) a-Si:H(i), (b) a-Si:H(n), and (c) a-Si:H(p) capping layers. The defect distribution in the volume of a-Si:H is integrated over the layer thickness of $w_{\text{a-Si}} = 10\,\text{nm}$. The interface defect distribution is either modeled using the Gaussian defect distribution in Eq. (5.3b) with $D_{\text{Gauss}} = 5 \times 10^{11}\,\text{cm}^{-2}\text{eV}^{-1}$, $\sigma_{\text{Gauss}} = 0.2\,\text{eV}$, and $E_0 = E_{\text{g}}^{\text{a-Si}}/2$ (red lines), where $E_{\text{g}}^{\text{a-Si}}$ is the bandgap of a-Si:H. Or, the DPM is mapped to the interface according to Eq. (5.3a), where an effective interface-layer thickness of $w_{\text{eff}} = 5\,\text{Å}$ is assumed [Lee10b] (blue lines). The room temperature value of the Urbach tail is (a) 59 meV for a-Si:H(i) and (b), (c) 120 meV for doped a-Si:H ($N_{\text{dop}} = 5 \times 10^{18}\,\text{cm}^{-3}$). Further parameters are $E_{\text{g}}^{\text{a-Si}} = 1.9\,\text{eV}$, $\Delta E_{\text{v}} = 0.4\,\text{eV}$ and $E_{\text{c0}} = 30\,\text{meV}$. $E_{v}^{\text{a-Si}}$ denotes the mobility edge of a-Si:H.

contrast, we model the volume DOS $D^{\text{DB}}(E_{\text{d}})$ in the a-Si layer by the modified DPM [Pow93] developed in Sec. 5.1.1 (cf. Eqs. (2.66) and (5.2)). This is done because the DPM is experimentally motivated, and takes the measured dependence of the valence-band tail-slope (Urbach tail E_{v0}) on the defect density into account [Stu89].

In essence, the interface-DOS D_{it} has two contributions: the relatively shallow tail states $D_{\text{it}}^{\text{tail}}$ and the deep-level DB states $D_{\text{it}}^{\text{DB}}$. Figure 5.3 shows the total a-Si:H/c-Si interface defect distribution D_{it}, including the tail-state contribution $D_{\text{it}}^{\text{tail}}$, for a-Si:H(i), a-Si:H(n), and a-Si:H(p), where $N_{\text{dop}} = 5 \times 10^{18}\,\text{cm}^{-3}$ is chosen for the doped layers. Both scenarios for $D_{\text{it}}^{\text{DB}}$ are displayed. The volume DOS, multiplied by the a-Si:H layer thickness $w_{\text{a-Si}}$ is shown in addition by black lines.

For the a-Si:H(i)/c-Si interface in Fig. 5.3(a), the DB $D_{\text{it}}^{\text{DB}}$ calculated with the DPM-DOS in Eq. (5.3a) is almost constant at $D_{\text{it}} \approx 6 \times 10^{9}\,\text{cm}^{-3}$ over an energy range extending approximately from $E_{\text{v}}^{\text{c-Si}} + 0.2\,\text{eV}$ to $E_{\text{c}}^{\text{c-Si}} - 0.22\,\text{eV}$, as indicated by the dashed blue lines. For the doped layers ($N_{\text{dop}} = 5 \times 10^{18}\,\text{cm}^{-3}$), a nearly Gaussian distribution is formed below the c-Si midgap for a-Si:H(n) and above midgap for a-Si:H(p), as shown in Figs. 5.3(b) and 5.3(c), respectively. The peak

density of these distributions for the a-Si:H(i)/c-Si interface in Fig. 5.3(a) lies about two orders of magnitude above the plateau of $D_{\mathrm{it}}^{\mathrm{DB}}$.
The Gaussian $D_{\mathrm{it}}^{\mathrm{DB}}$ in Eq. (5.3b) is independent of N_{dop}, and is shown by the dashed red lines in Figs. 5.3(a)–(c).
Further, it is apparent that the Urbach tails E_{v0}, calculated via Eq. (5.2), are larger in doped a-Si:H than in a-Si:H(i). Thus, $D_{\mathrm{it}}^{\mathrm{tail}}$ affects the total D_{it} considerably if N_{dop} is large. Due to the insensitivity of E_{c0} on the disorder [Alj90, Dra91], we assume a room temperature value $E_{\mathrm{c0}} = 30\,\mathrm{meV}$ independently of the dopant density N_{dop}.

As discussed above, it is not yet clear which of the described models for the interface-DOS is more suitable for describing the defect distributions at the a-Si:H/c-Si interfaces and in thin a-Si:H layers. It was observed both in simulation [Sta03] and experiment [Kon08, Tag00, Tan92, vC97] that the a-Si:H/c-Si cell-performance is improved by the incorporation of an a-Si:H(i) layer at the a-Si:H/c-Si hetero-interface. This improvement was attributed to reduced recombination at the a-Si:H(i)/c-Si interface compared to an a-Si:H(doped)/c-Si interface. These observations indicate, that the interface-DOS $D_{\mathrm{it}}^{\mathrm{DB}}$ at a-Si:H(n)/c-Si or a-Si:H(p)/c-Si interfaces is higher than at the a-Si:H(i)/c-Si interface. Consequently, a Gaussian distributed interface-DOS $D_{\mathrm{it}}^{\mathrm{DB}}$, whose amplitude is independent of the dopant density N_{dop}, as in Eq. (5.3b), does probably not describe the real defect distributions, correctly. The extended DPM in Eqs. (2.66) and (5.2), mapped to the interface according to (5.3a), in contrast, incorporates the expected enhanced amplitudes of $D_{\mathrm{it}}^{\mathrm{DB}}$ with increasing dopant density N_{dop}, as was shown in Fig. 5.2. However, the applicability of the DPM of Ref. [Pow93] to extremely thin a-Si:H layers or a-Si:H/c-Si interfaces has not been confirmed, yet. Therefore, we apply both scenarios for $D_{\mathrm{it}}^{\mathrm{DB}}$ in Eq. (5.3) to model the recombination rate at a-Si:H/c-Si interfaces in Sec. 5.2.

5.2 Recombination at the a-Si:H/c-Si interface

In this section, we describe an approximate model to amphoteric recombination statistics based on SRH theory. We compare this uncorrelated approach to the correct statistics in a mathematical rigorous way by considering the quasi-Fermi levels for traps and quantify the systematic error of the approximate model.

5.2.1 SRH recombination statistics for donor- and acceptor-like defects

Recombination at the a-Si:H/c-Si interface cannot be generally modeled using simple SRH theory, which considers only a single defect state E_{d} (see Sec. 2.2.4). Rather the extended SRH formalism, allowing for a distribution of defect states, has to be applied [Bra53, Sim71]. However, SRH statistics does not account for the amphoteric nature of the defects. Therefore, we approximate the amphoteric behavior by considering two defect distributions: one for donor-like defects $D^{\mathrm{D}}(E_{\mathrm{d}})$ and the other for acceptor-like defects $D^{\mathrm{A}}(E_{\mathrm{d}})$. Assuming an identical correlation energy E_{corr} for all defects, the amphoteric nature of the DBs requires that the shapes of the defect distributions $D_{+/0}(E_{\mathrm{d}})$ and $D_{0/-}(E_{\mathrm{d}})$ (cf. Sec. 2.3.2) are equal. Hence, in the SRH model both $D^{\mathrm{D}}(E_{\mathrm{d}})$ and $D^{\mathrm{A}}(E_{\mathrm{d}})$ are modeled by equally-shaped distributions which are separated in energy by the effective correlation energy E_{corr}: $D^{\mathrm{D}}(E_{\mathrm{d}}) = D^{\mathrm{A}}(E_{\mathrm{d}} + E_{\mathrm{corr}})$.

The recombination rates $U^{\mathrm{D}}(E_{\mathrm{d}})$ of the distribution $D^{\mathrm{D}}(E_{\mathrm{d}})$ and $U^{\mathrm{A}}(E_{\mathrm{d}})$ of the distribution $D^{\mathrm{A}}(E_{\mathrm{d}})$ distribution are calculated independently and summed up to $U_{\mathrm{SRH}} = U^{\mathrm{A}} + U^{\mathrm{D}}$. This yields the total recombination rate $R_{\mathrm{SRH}} = \int_{E_{\mathrm{v}}^{\mathrm{c\text{-}Si}}}^{E_{\mathrm{c}}^{\mathrm{c\text{-}Si}}} \mathrm{d}E \, U_{\mathrm{SRH}}(E_{\mathrm{d}})$ according to Eq. (2.32).[1] The capture rates c_{n}^{+}, c_{p}^{0}, c_{n}^{0} and c_{p}^{-} are defined as in the amphoteric statistics [Vai86] according to Eqs. (2.73) and (2.74) in Sec. 2.3.2. The emission rates in this uncorrelated model are, in contrast to the amphoteric theory, solely restricted by the initial conditions and the rate equations (2.27) [Li08]. Hence, the emission rates $e_{\mathrm{n,SRH}}^{0}$, $e_{\mathrm{p,SRH}}^{+}$, $e_{\mathrm{n,SRH}}^{-}$ and $e_{\mathrm{p,SRH}}^{0}$ are given in analogy to Eqs. (2.29a) and (2.29b) in Sec. 2.2.4. They read for a donor-like defect state at energy E_{d}:

$$e_{\mathrm{n,SRH}}^{0}(E_{\mathrm{d}}) = c_{\mathrm{n,0}}^{+} \, \mathrm{e}^{\beta(E_{\mathrm{d}}-E_{\mathrm{f}})}, \qquad e_{\mathrm{p,SRH}}^{+}(E_{\mathrm{d}}) = c_{\mathrm{p,0}}^{0} \, \mathrm{e}^{\beta(E_{\mathrm{f}}-E_{\mathrm{d}})}, \tag{5.4a}$$

and for an acceptor-like defect state:

$$e_{\mathrm{n,SRH}}^{-}(E_{\mathrm{d}}) = c_{\mathrm{n,0}}^{0} \, \mathrm{e}^{\beta(E_{\mathrm{d}}-E_{\mathrm{f}})}, \qquad e_{\mathrm{p,SRH}}^{0}(E_{\mathrm{d}}) = c_{\mathrm{p,0}}^{-} \, \mathrm{e}^{\beta(E_{\mathrm{f}}-E_{\mathrm{d}})}. \tag{5.4b}$$

The electron occupation fractions f^{D} and f^{A} can be written according to Eq. (2.30) in Sec. 2.2.4 as:

$$f^{\mathrm{D}}(E_{\mathrm{d}}) = \frac{c_{\mathrm{n}}^{+} + e_{\mathrm{p,SRH}}^{+}(E_{\mathrm{d}})}{c_{\mathrm{p}}^{0} + e_{\mathrm{n,SRH}}^{0}(E_{\mathrm{d}}) + c_{\mathrm{n}}^{+} + e_{\mathrm{p,SRH}}^{+}(E_{\mathrm{d}})} \tag{5.5a}$$

$$f^{\mathrm{A}}(E_{\mathrm{d}}) = \frac{c_{\mathrm{n}}^{0} + e_{\mathrm{p,SRH}}^{0}(E_{\mathrm{d}})}{c_{\mathrm{p}}^{-} + e_{\mathrm{n,SRH}}^{-}(E_{\mathrm{d}}) + c_{\mathrm{n}}^{0} + e_{\mathrm{p,SRH}}^{0}(E_{\mathrm{d}})}, \tag{5.5b}$$

and the carrier transition rates become (cf. the definitions of $u_{\mathrm{n}}^{\mathrm{c}}$ and $u_{\mathrm{n}}^{\mathrm{e}}$ in Eq. (2.28)

---

[1] Note that this formulation holds also for surfaces and interfaces, where $D(E_{\mathrm{d}})$ is in units of $\mathrm{cm}^{-2}\mathrm{eV}^{-1}$ and R_{SRH} has the units of $\mathrm{cm}^{-2}\mathrm{s}^{-1}$.

in Sec. 2.2.4):

$$\begin{aligned} u^{\mathrm{D,c}}_{\mathrm{SRH}}(E_{\mathrm{d}}) &:= u_1(E_{\mathrm{d}}) = c_{\mathrm{n}}^{+}\,(1-f^{\mathrm{D}}(E_{\mathrm{d}}))\,D^{\mathrm{D}}(E_{\mathrm{d}}),\\ u^{\mathrm{A,c}}_{\mathrm{SRH}}(E_{\mathrm{d}}) &:= u_2(E_{\mathrm{d}}) = c_{\mathrm{n}}^{0}\,(1-f^{\mathrm{A}}(E_{\mathrm{d}}))\,D^{\mathrm{A}}(E_{\mathrm{d}}),\\ u^{\mathrm{D,e}}_{\mathrm{SRH}}(E_{\mathrm{d}}) &:= u_3(E_{\mathrm{d}}) = e^{0}_{\mathrm{n,SRH}}(E_{\mathrm{d}})\,f^{\mathrm{D}}(E_{\mathrm{d}})\,D^{\mathrm{D}}(E_{\mathrm{d}}),\\ u^{\mathrm{A,e}}_{\mathrm{SRH}}(E_{\mathrm{d}}) &:= u_4(E_{\mathrm{d}}) = e^{-}_{\mathrm{n,SRH}}(E_{\mathrm{d}})\,f^{\mathrm{A}}(E_{\mathrm{d}})\,D^{\mathrm{A}}(E_{\mathrm{d}}). \end{aligned} \tag{5.6}$$

As discussed in Sec. 2.3.2, for steady-state conditions it suffices to determine the recombination rate for electrons only. The recombination rates of electrons via the two defect distributions read:

$$\begin{aligned} U^{\mathrm{D}}_{\mathrm{SRH}}(E_{\mathrm{d}}) &= u^{\mathrm{D,c}}_{\mathrm{SRH}}(E_{\mathrm{d}}) - u^{\mathrm{D,e}}_{\mathrm{SRH}}(E_{\mathrm{d}})\\ &= D^{\mathrm{D}}(E_{\mathrm{d}})\frac{np-n_{\mathrm{i}}^2}{\frac{n+N_{\mathrm{c}}\,\mathrm{e}^{-\beta(E_{\mathrm{c}}-E_{\mathrm{d}})}}{v_{\mathrm{th,p}}\sigma_{\mathrm{p}}^{0}}+\frac{p+N_{\mathrm{v}}\,\mathrm{e}^{\beta(E_{\mathrm{v}}-E_{\mathrm{d}})}}{v_{\mathrm{th,n}}\sigma_{\mathrm{n}}^{+}}}, \end{aligned} \tag{5.7a}$$

and

$$\begin{aligned} U^{\mathrm{A}}_{\mathrm{SRH}}(E_{\mathrm{d}}) &= u^{\mathrm{A,c}}_{\mathrm{SRH}}(E_{\mathrm{d}}) - u^{\mathrm{A,e}}_{\mathrm{SRH}}(E_{\mathrm{d}})\\ &= D^{\mathrm{A}}(E_{\mathrm{d}})\frac{np-n_{\mathrm{i}}^2}{\frac{n+N_{\mathrm{c}}\,\mathrm{e}^{-\beta(E_{\mathrm{c}}-E_{\mathrm{d}})}}{v_{\mathrm{th,p}}\sigma_{\mathrm{p}}^{-}}+\frac{p+N_{\mathrm{v}}\,\mathrm{e}^{\beta(E_{\mathrm{v}}-E_{\mathrm{d}})}}{v_{\mathrm{th,n}}\sigma_{\mathrm{n}}^{0}}}. \end{aligned} \tag{5.7b}$$

Finally, the total recombination rate is given by the superposition of $U^{\mathrm{D}}(E_{\mathrm{d}})$ and $U^{\mathrm{A}}(E_{\mathrm{d}})$:

$$U_{\mathrm{SRH}}(E_{\mathrm{d}}) = U^{\mathrm{D}}(E_{\mathrm{d}}) + U^{\mathrm{A}}(E_{\mathrm{d}}). \tag{5.8}$$

5.2.1.1 Quasi-Fermi levels for traps (TQFLs)

In this section, we discuss the properties of the characteristic energies E_{D} and E_{T} introduced in Sec. 2.2.5, as well as the differences between them.

The demarcation levels (DLs) (Eq. (2.37)) applied to the defect distributions introduced in Sec. 5.2.1 read for the donor-like defects according to SRH theory:

$$\begin{aligned} E^{0,\mathrm{SRH}}_{\mathrm{Dn}} &= E_{\mathrm{c}} - (E_{\mathrm{fp}} - E_{\mathrm{v}}) + \frac{1}{\beta}\ln\left(\frac{\sigma_{\mathrm{p}}^{0} N_{\mathrm{v}}}{\sigma_{\mathrm{n}}^{+} N_{\mathrm{c}}}\right),\\ E^{+,\mathrm{SRH}}_{\mathrm{Dp}} &= E_{\mathrm{v}} + (E_{\mathrm{c}} - E_{\mathrm{fn}}) - \frac{1}{\beta}\ln\left(\frac{\sigma_{\mathrm{p}}^{0} N_{\mathrm{v}}}{\sigma_{\mathrm{n}}^{+} N_{\mathrm{c}}}\right), \end{aligned} \tag{5.9}$$

and for the acceptor-like defects:

$$\begin{aligned} E^{-,\mathrm{SRH}}_{\mathrm{Dn}} &= E_{\mathrm{c}} - (E_{\mathrm{fp}} - E_{\mathrm{v}}) + \frac{1}{\beta}\ln\left(\frac{\sigma_{\mathrm{p}}^{-} N_{\mathrm{v}}}{\sigma_{\mathrm{n}}^{0} N_{\mathrm{c}}}\right),\\ E^{0,\mathrm{SRH}}_{\mathrm{Dp}} &= E_{\mathrm{v}} + (E_{\mathrm{c}} - E_{\mathrm{fn}}) - \frac{1}{\beta}\ln\left(\frac{\sigma_{\mathrm{p}}^{-} N_{\mathrm{v}}}{\sigma_{\mathrm{n}}^{0} N_{\mathrm{c}}}\right). \end{aligned} \tag{5.10}$$

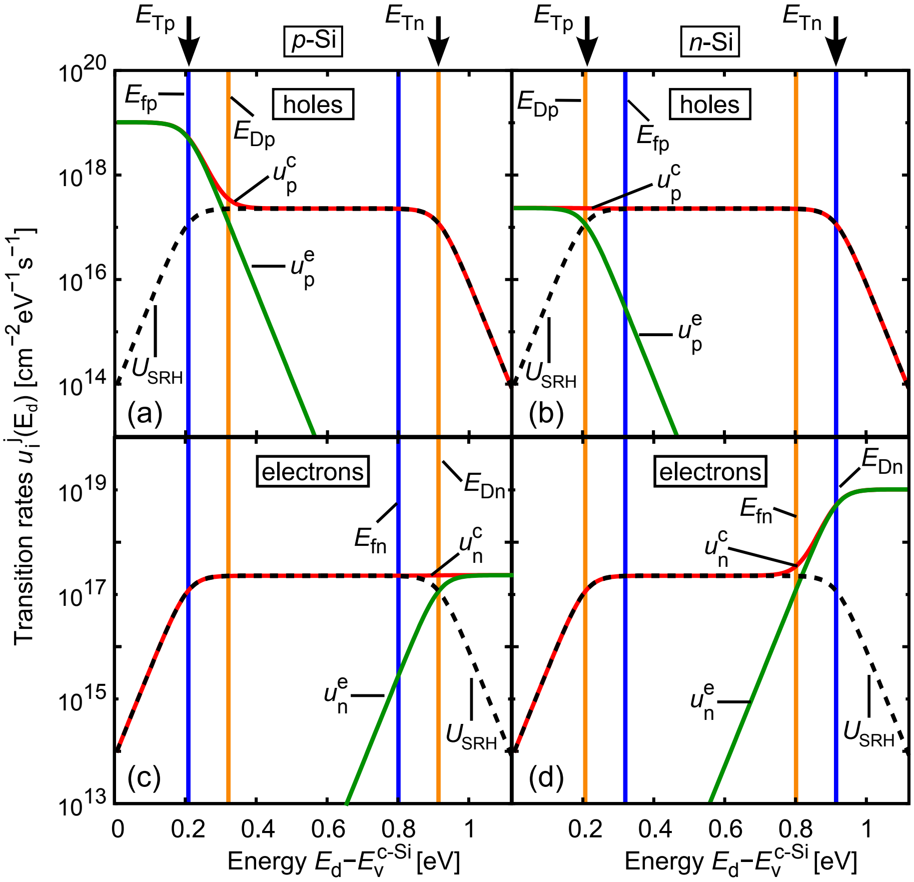

Figure 5.4: Emission rates and capture rates of electrons and holes, respectively, calculated using Eq. (5.6) as a function of the defect's energy level E_d with respect to $E_\mathrm{v}^\text{c-Si}$ in lowly-injected p-Si in (a) and (c) and in n-Si in (b) and (d). We choose $N_\mathrm{A} = N_\mathrm{D} = 10^{16}\,\mathrm{cm}^{-3}$, $\Delta n = 1.3 \times 10^{14}\,\mathrm{cm}^{-3}$, a constant defect density of $10^{12}\,\mathrm{cm}^{-3}$, and $\sigma_\mathrm{p} = \sigma_\mathrm{n} = 10^{-16}\,\mathrm{cm}^2$. (a) and (b) hole transitions, and (c) and (d) electron transitions, dashed lines: total recombination rate U in Eq. (2.32). The vertical lines indicate the quasi-Fermi levels (QFLs) for free charges, E_f in Eq. (2.36) (blue lines), and the demarcation levels (DLs) E_D in Eq. (2.37) (orange lines). The quasi-Fermi levels for the trapped charges (TQFLs) E_T in Eq. (2.38), are indicated by arrows.

The quasi-Fermi levels for traps (TQFLs) (Eq. (2.38)) read for donor-like defects according to SRH statistics:

$$E_\mathrm{Tn}^{0,\mathrm{SRH}} = E_\mathrm{f} + \frac{1}{\beta}\ln\left(\frac{c_\mathrm{n}^+ + c_\mathrm{p}^0}{c_\mathrm{n,0}^+}\right), \qquad E_\mathrm{Tp}^{+,\mathrm{SRH}} = E_\mathrm{f} - \frac{1}{\beta}\ln\left(\frac{c_\mathrm{n}^+ + c_\mathrm{p}^0}{c_\mathrm{p,0}^0}\right), \tag{5.11}$$

and for the acceptor-like defects:

$$E_\mathrm{Tn}^{-,\mathrm{SRH}} = E_\mathrm{f} + \frac{1}{\beta}\ln\left(\frac{c_\mathrm{n}^0 + c_\mathrm{p}^-}{c_\mathrm{n,0}^0}\right), \qquad E_\mathrm{Tp}^{0,\mathrm{SRH}} = E_\mathrm{f} - \frac{1}{\beta}\ln\left(\frac{c_\mathrm{n}^0 + c_\mathrm{p}^-}{c_\mathrm{p,0}^-}\right). \tag{5.12}$$

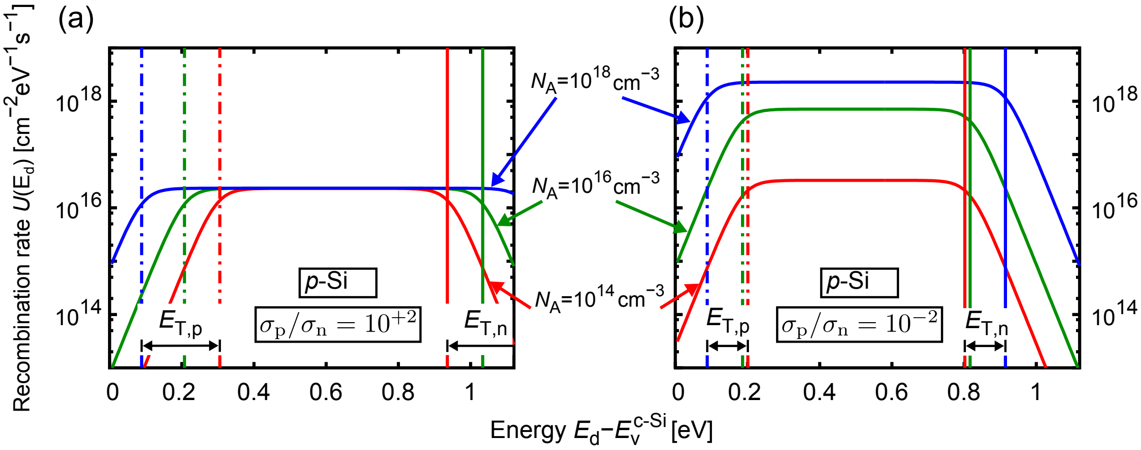

Figure 5.5: The total recombination rate in p-Si, calculated using Eq. (5.7) as a function of the defect's energy level E_d with respect to $E_\mathrm{v}^\text{c-Si}$, for various dopant densities and for different ratios of the cross sections for electrons and holes. (a) $\sigma_\mathrm{p}/\sigma_\mathrm{n} = 100$ and (b) $\sigma_\mathrm{p}/\sigma_\mathrm{n} = 0.01$. The vertical lines indicate the quasi-Fermi levels for the trapped charges, E_Tp and E_Tn, for different N_A.

Note that the discussion still applies only to SRH theory and no amphoteric character is considered. For a better readability, we neglect the index SRH for the characteristic energies in this section.

We consider p-Si and n-Si substrates with a dopant density $N_\mathrm{dop} = 10^{16}\,\mathrm{cm}^{-3}$ and an injection density in the quasi-neutral region of $\Delta n = 1.3 \times 10^{14}\,\mathrm{cm}^{-3}$. Figure 5.4 shows the emission rates and capture rates of electrons and holes, respectively, calculated using Eq. (5.6), as a function of the defect's energy level E_d. The DLs E_D (orange lines), the QFLs E_f (blue lines), and the TQFLs (arrows on top of the graph) are shown in addition. It is apparent, that there is a plateau of approximately constant capture and emission rates between a pair of DLs (E_Dp and E_Dn). However, for many cases, the total recombination rate U_SRH, indicated by the black dashed lines in Fig. 5.4, rather than the capture and emission rates, is relevant, and it shows a plateau between a pair of TQFLs (E_Tp and E_Tn) rather than between a pair of DLs. Nevertheless, the plateau of U_SRH is commonly thought to extend between the majority QFL and the minority DL. Considering the limiting cases $\sigma_\mathrm{n} n \ll \sigma_\mathrm{p} p$, $\sigma_\mathrm{n} n \gg \sigma_\mathrm{p} p$, and inserting them into Eqs. (2.36)–(2.38) shows that indeed, the minority TQFL converges to the minority DL, and the majority TQFL converges to the majority QFL. These limits are only reached in case of both low injection conditions and rather symmetrical CCS, whereas for all other cases, the TQFLs coincide with the boundaries of the plateau.

Further features of the plateau of the approximately constant recombination rate U_SRH are displayed in Fig. 5.5:

- With increasing dopant density, the TQFLs move further apart and the recombination plateau is extended towards the band edges.

- Outside the plateau, U_{SRH} decreases exponentially with increasing distance from the edges of the plateau and thus, the TQFLs are characteristic for the distinction between defect levels that are recombination-active or -inactive.
- U_{SRH} is maximal if $n/\sigma_{\mathrm{p}} = p/\sigma_{\mathrm{n}}$. Otherwise, U_{SRH} is limited by the smaller one of the factors n/σ_{p} and p/σ_{n}.
- The plateau is centered around $E_0 = E_i - \ln(\sigma_{\mathrm{p}}/\sigma_{\mathrm{n}})/2\beta$. Consequently, when switching the dopant type, the $\sigma_{\mathrm{p}}/\sigma_{\mathrm{n}}$ ratio must be inverted to obtain an identical U_{SRH} characteristics.

5.2.2 Amphoteric recombination statistics

For DBs, three charge states and two energy levels exist, as described in Sec. 2.3.2 (cf. Fig. 2.8). A model for quantifying the recombination in a-Si:H that takes into account both the amphoteric nature and the energy separation between the $D_{+/0}$ and the $D_{0/-}$ states [Vai86] was derived in Sec. 2.3.2. The derivation was made based on the observation that, compared to the one-level model, the principle of detailed balance [Sah58] applied to correlated defects imposes additional restrictions on the emission rates. Consequently, the emission rates differ from those derived for the SRH model in Sec. 5.2.1. Nevertheless, we find close similarities between the amphoteric recombination statistics and the SRH formalism: the emission rates of the amphoteric statistics [Vai86] in Eqs. (2.73b) and (2.74b) can be directly related to those of the SRH formalism in Eq. (5.4) according to:

$$\begin{aligned} e^0_{\mathrm{n,a}} &= \frac{1}{2} e^0_{\mathrm{n,SRH}}, & e^-_{\mathrm{n,a}} &= 2 e^-_{\mathrm{n,SRH}} e^{\beta E_{\mathrm{corr,eff}}}, \\ e^0_{\mathrm{p,a}} &= \frac{1}{2} e^0_{\mathrm{p,SRH}} e^{-\beta E_{\mathrm{corr,eff}}}, & e^+_{\mathrm{p,a}} &= 2 e^+_{\mathrm{p,SRH}}. \end{aligned} \tag{5.13}$$

Here, the factor 2 results from the differences in the occupation fractions. The DLs, E_{D}, and the TQFLs, E_{T}, for amphoteric recombination statistics are derived analogously to Eqs. (2.38)–(5.12). They can be related to those of the SRH theory according to:

$$E^{+,\mathrm{a}}_{\mathrm{Dp}} = E^{+,\mathrm{SRH}}_{\mathrm{Dp}} + \frac{\ln 2}{\beta}, \qquad E^{0,\mathrm{a}}_{\mathrm{Dn}} = E^{0,\mathrm{SRH}}_{\mathrm{Dn}} + \frac{\ln 2}{\beta}, \tag{5.14a}$$

$$E^{+,\mathrm{a}}_{\mathrm{Tp}} = E^{+,\mathrm{SRH}}_{\mathrm{Tp}} + \frac{\ln 2}{\beta}, \qquad E^{0,\mathrm{a}}_{\mathrm{Tn}} = E^{0,\mathrm{SRH}}_{\mathrm{Tn}} + \frac{\ln 2}{\beta} \tag{5.14b}$$

for donor-like defects, and

$$E^{0,\mathrm{a}}_{\mathrm{Dp}} = E^{0,\mathrm{SRH}}_{\mathrm{Dp}} - E_{\mathrm{corr,eff}} - \frac{\ln 2}{\beta}, \qquad E^{-,\mathrm{a}}_{\mathrm{Dn}} = E^{-,\mathrm{SRH}}_{\mathrm{Dn}} - E_{\mathrm{corr,eff}} - \frac{\ln 2}{\beta}, \tag{5.15a}$$

(a) Donor-like defects

Quantity	**SRH**	**amphoteric**
Donor-like defect		
electrons		
occupation probability of D_+	$1 - f^{\mathrm{D}}$	f^+
occupation probability of D_0	f^{D}	f^0
emission coefficient	$e^0_{\mathrm{n,SRH}}$	$e^0_{\mathrm{n,a}} = e^0_{\mathrm{n,SRH}}/2$
demarcation level	$E^{0,\mathrm{SRH}}_{\mathrm{Dn}}$	$E^{0,\mathrm{a}}_{\mathrm{Dn}} = E^{0,\mathrm{SRH}}_{\mathrm{Dn}} + \ln(2)/\beta$
TQFL	$E^{0,\mathrm{SRH}}_{\mathrm{Tn}}$	$E^{0,\mathrm{a}}_{\mathrm{Tn}} = E^{0,\mathrm{SRH}}_{\mathrm{Tn}} + \ln(2)/\beta$
holes		
occupation probability of D_-	f^{D}	f^0
occupation probability of D_0	$1 - f^{\mathrm{D}}$	f^+
emission coefficient	$e^+_{\mathrm{p,SRH}}$	$e^+_{\mathrm{p,a}} = 2e^+_{\mathrm{p,SRH}}$
demarcation level	$E^{+,\mathrm{SRH}}_{\mathrm{Dp}}$	$E^{+,\mathrm{a}}_{\mathrm{Dp}} = E^{+,\mathrm{SRH}}_{\mathrm{Dp}} + \ln(2)/\beta$
TQFL	$E^{+,\mathrm{SRH}}_{\mathrm{Tp}}$	$E^{+,\mathrm{a}}_{\mathrm{Tp}} = E^{+,\mathrm{SRH}}_{\mathrm{Tp}} + \ln(2)/\beta$

(b) Acceptor-like defects

Quantity	**SRH**	**amphoteric**
Acceptor-like defect		
electrons		
occupation probability of D_0	$1 - f^{\mathrm{A}}$	f^0
occupation probability of D_-	f^{A}	f^-
emission coefficient	$e^-_{\mathrm{n,SRH}}$	$e^-_{\mathrm{n,a}} = 2e^{\beta E_{\mathrm{corr,eff}}} e^-_{\mathrm{n,SRH}}$
demarcation level	$E^{-,\mathrm{SRH}}_{\mathrm{Dn}}$	$E^{-,\mathrm{a}}_{\mathrm{Dn}} = E^{-,\mathrm{SRH}}_{\mathrm{Dn}} - E_{\mathrm{corr,eff}} - \ln(2)/\beta$
TQFL	$E^{-,\mathrm{SRH}}_{\mathrm{Tn}}$	$E^{-,\mathrm{a}}_{\mathrm{Tn}} = E^{-,\mathrm{SRH}}_{\mathrm{Tn}} - E_{\mathrm{corr,eff}} - \ln(2)/\beta$
holes		
occupation probability of D_0	f^{A}	f^-
occupation probability of D_-	$1 - f^{\mathrm{A}}$	f^0
emission coefficient	$e^0_{\mathrm{p,a}}$	$e^0_{\mathrm{p,a}} = e^{-\beta E_{\mathrm{corr,eff}}} e^0_{\mathrm{p,SRH}}/2$
demarcation level	$E^{0,\mathrm{SRH}}_{\mathrm{Dp}}$	$E^{0,\mathrm{a}}_{\mathrm{Dp}} = E^{0,\mathrm{SRH}}_{\mathrm{Dp}} - E_{\mathrm{corr,eff}} - \ln(2)/\beta$
TQFL	$E^{0,\mathrm{SRH}}_{\mathrm{Tp}}$	$E^{0,\mathrm{a}}_{\mathrm{Tp}} = E^{0,\mathrm{SRH}}_{\mathrm{Tp}} - E_{\mathrm{corr,eff}} - \ln(2)/\beta$

Table 5.2: Relations between entities of the SRH theory and the amphoteric statistics.

$$E^{0,\mathrm{a}}_{\mathrm{Tp}} = E^{0,\mathrm{SRH}}_{\mathrm{Tp}} - E_{\mathrm{corr,eff}} - \frac{\ln 2}{\beta}, \qquad E^{-,\mathrm{a}}_{\mathrm{Tn}} = E^{-,\mathrm{SRH}}_{\mathrm{Tn}} - E_{\mathrm{corr,eff}} - \frac{\ln 2}{\beta} \tag{5.15b}$$

for acceptor-like defects. These and further useful relations between amphoteric and SRH theory are summarized in Table 5.2.

5.2.3 Model for surface band-bending caused by trapped charges

Measurements of the injection dependent lifetime [e.g. Dau02b, Pla07] indicate that there is no considerable amount of fixed charges Q_{f} at the a-Si:H(i)/c-Si interface. Other authors, who consider interfaces with doped a-Si:H, including a-Si:H(n)/a-Si:H(i) or a-Si:H(p)/a-Si:H(i) stacks, use a fixed charge density in the range $Q_\mathrm{f} = -1.5 \times 10^{11} \ldots 7 \times 10^{10}\,\mathrm{q/cm^2}$ to reproduce their lifetime measurements [Oli07]. The authors need a negative charge density to reproduce the surface recombination at samples passivated with a-Si:H(n), and a positive charge density in case of a-Si:H(p). Garin *et al.* [Gar05] present a model that includes the charges in the doped a-Si:H layer of a-Si:H(n)/a-Si:H(i) or a-Si:H(p)/a-Si:H(i) stacks. However, the authors neglect the charge contributions from the a-Si:H(i) layer as well as all injection dependent trapped charges that are stored in the defects. None of the publications mentioned here [Dau02b, Gar05, Oli07, Pla07] applies the fully correlated amphoteric recombination model [Vai86].

As already discussed in Sec. 2.3, depending on their occupation by zero, one or two electrons, the DB defect states in a-Si:H are in either a neutral, a negative or a positive charge state. Thus, an injection dependent charge density at the a-Si:H(i)/c-Si interface has to be expected. Recently, the effect of approximating the injection dependent interface charge density Q_it by a fixed charge density Q_f was investigated [Lee10a]. It was shown that this approach is restricted to a limited range of the injection density and fails dramatically when estimating the dark band-bending. Therefore, we apply the model of injection dependent charges proposed by Leendertz *et al.* [Lee10b] to determine the charge density at the a-Si:H(i)/c-Si interface. The requirement for charge neutrality demands that the total interface charge Q_it, given by the sum of the charges in the a-Si:H layer $Q_\mathrm{a-Si}$ and at the interface Q_it^*, is compensated by an equal amount of charges $Q_\mathrm{c-Si}$ with opposite polarity in the c-Si substrate:

$$Q_\mathrm{it} := Q_\mathrm{it}^*(\Delta n, \varphi_\mathrm{s}) + Q_\mathrm{a-Si}(\Delta n, \varphi_\mathrm{s}) = -Q_\mathrm{c-Si}(\Delta n, \varphi_\mathrm{s}). \tag{5.16}$$

The charge contribution from the interface Q_it^* can be separated into four parts, one contribution from the acceptor-like states Q_it^A, one from the donor-like states Q_it^A, one from the charges stored in the correlated defects $Q_\mathrm{it}^\mathrm{corr}$, and an additional fixed charge density Q_f, which is commonly assumed to be zero [Lee10b, Pla07]:

$$Q_\mathrm{it}^* = Q_\mathrm{it}^\mathrm{A} + Q_\mathrm{it}^\mathrm{D} + Q_\mathrm{it}^\mathrm{corr} + Q_\mathrm{f}. \tag{5.17}$$

In the model, derived in the following, flat quasi-Fermi levels are assumed throughout the whole structure. A justification for this assumption is given below. The band bending towards the interface in the c-Si substrate is calculated according to Eq. (2.52). Thereby, Q_it (Eq. (5.16)) is used instead of Q_f in Eq. (2.52).

When applying amphoteric recombination statistics to the DBs, the charge contribution of the correlated DB defects is [Lee10b]:

$$Q_{\mathrm{it}}^{\mathrm{corr}} = q \int_{E_{\mathrm{v}}^{\text{c-Si}}}^{E_{\mathrm{c}}^{\text{c-Si}}} \mathrm{d}E_{\mathrm{d}}\; D_{+/0}(E_{\mathrm{d}})\,(f^{+}(E_{\mathrm{d}}) - f^{-}(E_{\mathrm{d}})). \tag{5.18}$$

We approximate the recombination of free charge carriers via the acceptor-like conduction-band tail-states and the donor-like valence-band tail-states using SRH statistics [e.g. Lee10b, Sak86, Vai86]. Hence, the charge density stored in these defects is evaluated by (cf. Eq. (4.13)):

$$Q_{\mathrm{it}}^{\mathrm{A}} = -q \int_{E_{\mathrm{v}}^{\text{c-Si}}}^{E_{\mathrm{c}}^{\text{c-Si}}} \mathrm{d}E_{\mathrm{d}}\; f^{\mathrm{A}}(E_{\mathrm{d}})\, D_{\mathrm{it}}^{\mathrm{A}}(E_{\mathrm{d}}), \tag{5.19}$$

$$Q_{\mathrm{it}}^{\mathrm{D}} = +q \int_{E_{\mathrm{v}}^{\text{c-Si}}}^{E_{\mathrm{c}}^{\text{c-Si}}} \mathrm{d}E_{\mathrm{d}}\; (1 - f^{\mathrm{D}}(E_{\mathrm{d}}))\, D_{\mathrm{it}}^{\mathrm{D}}(E_{\mathrm{d}}). \tag{5.20}$$

The integrations in Eqs. (5.18)–(5.20) are performed over the energy gap of c-Si, because only states in the c-Si bandgap contribute to the a-Si:H/c-Si interface charge. When approximating recombination via DB defects by the uncorrelated SRH model, introduced in Sec. 5.2.2, the contribution of the correlated defects $Q_{\mathrm{it}}^{\mathrm{corr}}$ according to Eq. (5.18) vanishes. Instead, the charges of the deep-level acceptor-like and donor-like defect distributions are added to the acceptor-like conduction-band tail-state contribution $Q_{\mathrm{it}}^{\mathrm{A}}$ (Eq. (5.19)) and to the donor-like valence-band tail contribution $Q_{\mathrm{it}}^{\mathrm{D}}$ (Eq. (5.20)), respectively.

The charge in an a-Si:H layer of thickness $w_{\text{a-Si}}$ is given by:

$$Q_{\mathrm{a-Si}} = w_{\text{a-Si}} \left[q\,(p_{\mathrm{a-Si}} - n_{\mathrm{a-Si}} + N_{\mathrm{D,a-Si}} - N_{\mathrm{A,a-Si}}) + Q_{\mathrm{a-Si}}^{\mathrm{A}} + Q_{\mathrm{a-Si}}^{\mathrm{D}} + Q_{\mathrm{a-Si}}^{\mathrm{corr}} \right], \tag{5.21}$$

where $N_{\mathrm{D,a-Si}}$ and $N_{\mathrm{A,a-Si}}$ are the densities of ionized donors and acceptors in the amorphous layer, respectively. Further, $Q_{\mathrm{a-Si}}^{\mathrm{D}}$, $Q_{\mathrm{a-Si}}^{\mathrm{A}}$ and $Q_{\mathrm{a-Si}}^{\mathrm{corr}}$ are the charges of donor-like, acceptor-like and correlated defect states in the a-Si:H layer, respectively. The free charge carrier densities in the a-Si:H layer can be related to those at the c-Si interface [Lee10b]:

$$n_{\mathrm{a-Si}} = n_{\mathrm{s}} \frac{N_{\mathrm{c}}^{\mathrm{a-Si}}}{N_{\mathrm{c}}^{\mathrm{c-Si}}}\, \mathrm{e}^{-\beta \Delta E_{\mathrm{c}}}, \tag{5.22a}$$

$$p_{\mathrm{a-Si}} = p_{\mathrm{s}} \frac{N_{\mathrm{v}}^{\mathrm{a-Si}}}{N_{\mathrm{v}}^{\mathrm{c-Si}}}\, \mathrm{e}^{+\beta \Delta E_{\mathrm{v}}}, \tag{5.22b}$$

where $\Delta E_{\mathrm{c}} := E_{\mathrm{c}}^{\text{a-Si}} - E_{\mathrm{c}}^{\text{a-Si}}$ is the (positive) conduction band offset, $\Delta E_{\mathrm{v}} := E_{\mathrm{v}}^{\text{c-Si}} - E_{\mathrm{v}}^{\text{a-Si}}$ is the (positive) valence band offset, and the surface

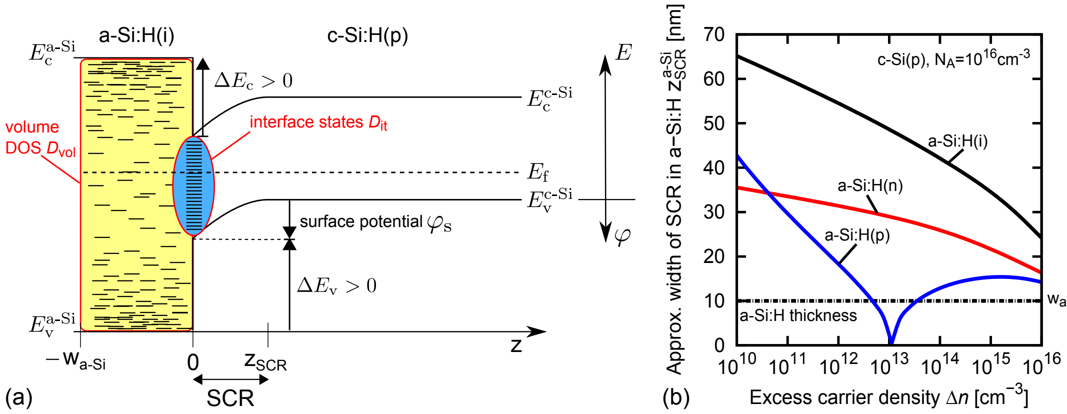

Figure 5.6: (a) Schematics of the amorphous-crystalline heterojunction with flat-band behavior in the a-Si:H layer after Ref. [Kor06a]; not drawn to scale. (b) Width of the space-charge region (SCR) in the a-Si:H layer at the a-Si:H/c-Si(p) heterojunction, estimated using Eq. (5.23). Different dopant densities in the 10 nm thick a-Si:H layer are used: a-Si:H(i) (black line), a-Si:H(n) with $N_D = 5 \times 10^{18}\,\text{cm}^{-3}$ (red line), and a-Si:H(p) with $N_A = 5 \times 10^{18}\,\text{cm}^{-3}$ (blue line). The interface charge is calculated using a Gaussian defect distribution according to Eq. (5.3b), centered at midgap with $D_{\text{Gauss}} = 5 \times 10^{11}\,\text{cm}^{-2}\text{eV}^{-1}$ and $\sigma_{\text{Gauss}} = 0.15\,\text{eV}$. The valence band edge $E_v^{\text{c-Si}}$ and conduction band edge $E_c^{\text{c-Si}}$ of c-Si and the mobility edges $E_v^{\text{a-Si}}$ and $E_c^{\text{a-Si}}$ of a-Si are indicated.

concentrations of electrons n_s and holes p_s are given by Eq. (2.53). Following Leendertz *et al.* [Lee10b], we approximate the interface contribution of the charge in the a-Si:H layer by mapping $Q_{\text{a-Si}}$ to the interface. The charge contribution due to acceptor-like states, donor-like states and correlated states is calculated analogously to Eqs. (5.18)–(5.20) by calculating the occupation functions using the carrier concentrations $n_{\text{a}-\text{Si}}$ and $p_{\text{a}-\text{Si}}$ in Eq. (5.22) [Lee10b].

Before proceeding, we shortly comment on the assumption of flat quasi-Fermi levels. Apart from the requirement that there is negligible generation and recombination in the SCR, it must be ensured that the width of the SCR in the a-Si:H layer $z_{\text{SCR}}^{\text{a-Si}}$ is larger than $w_{\text{a-Si}}$. If this assumption is fulfilled, the whole amorphous layer is recharged homogeneously, and we may assume flat band behavior in the a-Si:H layer [Kor06a], as sketched in Fig. 5.6(a).
To obtain a rough estimate for $z_{\text{SCR}}^{\text{a-Si}}$, we assume an abrupt p-n junction. In this case, the width of the SCR in the c-Si substrate is given by [Sze81]:

$$z_{\text{SCR}}^{\text{c-Si}} = L_D\sqrt{2(q\beta\varphi_s - 1)}, \qquad L_D = \sqrt{\frac{\varepsilon_0\varepsilon_r}{q^2\beta N_{\text{dop}}}}, \tag{5.23}$$

where L_D is the Debye-length. To determine the extension of the SCR in the a-Si:H layer, we replace N_{dop} in Eq. (5.23) by the number of recharged defect states and use the dielectric constant of the crystalline material (cf. Ref. [Kor06a] for a justification). We model the a-Si:H/c-Si interface with the parameters employed for the simulations further below in Sec. 5.2.4.2. In particular, we assume $w_{\text{a-Si}} = 10\,\mathrm{nm}$. Figure 5.6(b) shows the estimated width of the SCR $z_{\mathrm{SCR}}^{\text{a-Si}}$ in dependence of the excess carrier density Δn for the cases of a-Si:H(i), a-Si:H(n) and a-Si:H(p). Whereas for the a-Si:H(i)/c-Si(p) and a-Si:H(n)/c-Si(p) interfaces the requirement $z_{\mathrm{SCR}}^{\text{a-Si}} > w_{\text{a-Si}}$ is well satisfied, care must be taken in case of a-Si:H(p)/c-Si(p). At low-injection densities around $\Delta n \approx 10^{13}\,\mathrm{cm}^{-3}$, the trapped charge density changes from positive to negative values, and hence, the extension of the SCR vanishes. The critical excess carrier density Δn, where this transition occurs, depends on several factors, such as on the dopant densities N_{dop} in both c-Si and a-Si:H, on the interface and volume distribution of defect states, D_{it} and D^{DB}, and on the valence-band and conduction-band offset ΔE_{v} and ΔE_{c}, respectively. Throughout this chapter, we use $\Delta E_{\mathrm{v}} = 0.4\,\mathrm{eV}$ [Kor06a], $E_{\mathrm{g}}^{\text{a-Si}} = 1.9\,\mathrm{eV}$ for the bandgap of a-Si:H [Pow93, Pow96], and use $N_{\mathrm{dop,c-Si}} = 10^{16}\,\mathrm{cm}^{-3}$ as the dopant density in c-Si and $N_{\mathrm{dop,a-Si}} = 5 \times 10^{18}\,\mathrm{cm}^{-3}$ for doped a-Si. Thus, the critical range of excess carrier densities in the quasi-neutral region in c-Si, where $z_{\mathrm{SCR}}^{\text{a-Si}} < w_{\text{a-Si}}$ (cf. Fig. 5.6(b)), is small ($4.6 \times 10^{12}\,\mathrm{cm}^{-3} < \Delta n < 3.5 \times 10^{13}\,\mathrm{cm}^{-3}$) and lies below values which are typically relevant for applications to solar cells.

5.2.4 Comparison between SRH and amphoteric recombination statistics

A comparison between SRH theory and amphoteric recombination statistics has already been treated to some extent in literature. Willemen [Wil98] found that amphoteric recombination statistics is well approximated by SRH theory if (i) the ratio of the CCS of charged and neutral states is large compared to unity and if (ii) the correlation energy E_{corr} is positive and considerably larger than β^{-1}. The author obtained his results by considering the ratios: $U_{\mathrm{SRH}}/U_{\mathrm{a}}$, where U_{SRH} and U_{a} are the SRH and amphoteric recombination rates, respectively. He concluded that the error equals the ratio of the CCS of the minority charge carriers. Halpern [Hal86] and Suntharalingam and Branz [Sun94] reason that, provided that (i) and (ii) are fulfilled, the net charge under non-equilibrium conditions is always well approximated by SRH theory. Willemen already doubts the general validity of this assumption by showing that the absolute deviation in the electron occupation function $\Delta f^{Q} = (f^{0} + 2f^{-}) - (f^{\mathrm{D}} + f^{\mathrm{A}})$ is negligible for strongly doped material, but that it is significant for the intrinsic case. Moreover, he notes that the deviations in case of thermal generation are generally low for positive E_{corr}, whereas the SRH approximation is not applicable in case of negative E_{corr}.

Klimkovsky *et al.* [Kli02] evaluate the deviations between the uncorrelated SRH statistics and the amphoteric recombination statistics by modeling transport properties in a p-i-n structure consisting of a-Si:H layers. The electronic properties of such a device strongly depend on the electric field which is influenced mostly by the majority carriers. Therefore, the observed large deviations in the trapped minority carrier densities influence the deviation between both statistics significantly only for high excess carrier densities at which the device becomes more intrinsic. For surface passivation of non-diffused c-Si surfaces, in contrast, the influence of an electric field is much lower and hence, the deviations in the trapped charge densities are not negligible under low to medium injection conditions.

The requirements that $E_{\mathrm{corr}} > \beta^{-1}$ and that the CCS for electrons and holes are asymmetric [Ste10d, Wil98] are typically met. The origin of E_{corr} was discussed in Sec. 2.3, and it was noted that there is agreement in literature that E_{corr} is positive in a-Si:H and significantly larger than β^{-1} [Nor89, Str91b, Win90]. The cross sections of the donor-like or acceptor-like defect states for electron and hole capture, respectively, depend mainly on three factors: firstly, on the extent to which the wave function of the defect state overlaps with the wave function of the free carriers in the valence or conduction band; secondly, on the Coulomb interaction between the captured carrier and the defect state; and thirdly, on the disorder of the amorphous network. Street [Str84] has shown that the radius of the Coulomb potential of the charged defects is so large that, at the distance of this radius, the disorder potential is stronger than the Coulomb potential. Hence, it is assumed that the Coulomb potential causes the formation of additional tail states from which captured carriers can tunnel to the charged defect states [Str84]. Thereby, the CCS of the charged defects are enhanced and the ratio of the CCS between electrons and holes is $\sigma_{\mathrm{n}}^{+}/\sigma_{\mathrm{p}}^{0} \gg 1$ at donor-like defects and $\sigma_{\mathrm{n}}^{0}/\sigma_{\mathrm{p}}^{-} \ll 1$ at acceptor-like defects [Str84].

In the following, we compare SRH theory with the amphoteric statistics by means of some concrete examples. The main effects are discussed in Sec. 5.2.4.1 by assuming a homogeneous distribution of defect states $D^{\mathrm{D}}(E_{\mathrm{d}})$ over the entire bandgap,[2] which is sometimes used as a rough approximation [Oli07, Pla07]. In Sec. 5.2.4.2, we use more realistic defect distributions to model the DBs at the a-Si:H/c-Si interface. Finally, in Sec. 5.2.4.3 both recombination statistics are applied to fit experimental data.

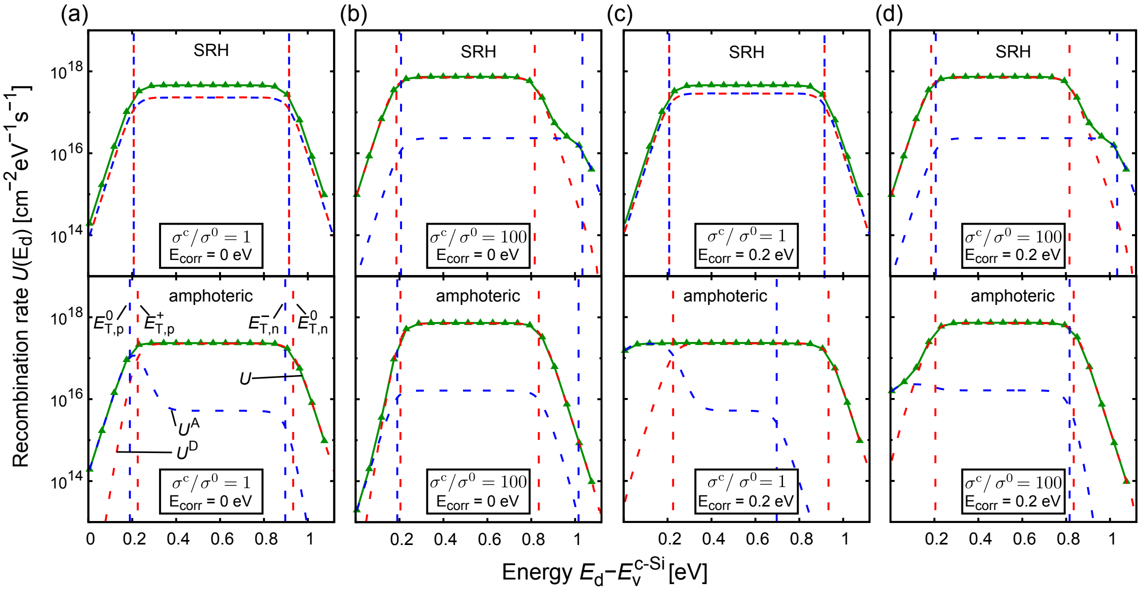

Figure 5.7: The recombination rates for SRH statistics (upper graphs) and amphoteric statistics (lower graphs), distinguished between contributions via donor-like states (blue lines) and via acceptor-like states (red lines), as a function of the defect's energy level E_d with respect to $E_\mathrm{v}^\text{c-Si}$. The total recombination rate is indicated by solid lines with symbols, and the quasi-Fermi levels for trapped charges are plotted as vertical lines. The c-Si material is p-type with $N_\mathrm{A} = 10^{16}\,\mathrm{cm}^{-3}$ and $\Delta n = 1.3 \times 10^{14}\,\mathrm{cm}^{-3}$. Two values of the ratio $\sigma^\mathrm{c}/\sigma^0$ between the CCS of the charged and the neutral defect states and two correlation energies E_corr are chosen.

5.2.4.1 Major differences

The main difference between the two recombination statistics is that the amphoteric theory treats donor-like and acceptor-like defects as being correlated, whereas SRH theory treats them as being independent of each other. In particular, amphoteric recombination statistics includes two competing processes at a single defect distribution D with $f^+ + f^0 + f^- = 1$. In SRH theory, in contrast, there holds for each defect type $f_h + f_e = 1$, separately.

As outlined above, the CCS of amphoteric defects depend on the charge state and it can be assumed that $\sigma_\mathrm{n}^+ > \sigma_\mathrm{p}^0$ for donor-like defect states, and $\sigma_\mathrm{n}^0 < \sigma_\mathrm{p}^-$ for acceptor-like states.

Figure 5.7 shows both the influence of this asymmetry and the influence of E_corr on the recombination rate $U(E_\mathrm{d})$. The differences between the two recombination statistics can be evaluated by means of two characteristics: (i) the height of the recombination plateaus (cf. Sec. 5.2.1.1), and (ii) the width and position of the re-

---

[2] Note that as a result, $D^\mathrm{A}(E_\mathrm{d})$ is shifted to higher energies if $E_\mathrm{corr} > 0$ and does not fill the whole bandgap.

combination plateaus within the bandgap. Differences between these characteristics originate from the fact that in the SRH theory, the recombination rates $U^{\mathrm{D}}(E_{\mathrm{d}})$ and $U^{\mathrm{A}}(E_{\mathrm{d}})$ of the two defect types are independent of each other, whereas in amphoteric statistics, $U^{\mathrm{D}}(E_{\mathrm{d}})$ and $U^{\mathrm{A}}(E_{\mathrm{d}})$ are determined by competing processes. Regarding the first issue (i), the height of the plateaus of $U^{\mathrm{D}}(E_{\mathrm{d}})$ and $U^{\mathrm{A}}(E_{\mathrm{d}})$ is strongly affected by the CCS-ratio between charged (c) and neutral (0) defect states $\sigma^{\mathrm{c}}/\sigma^{0}$. For the case of equal CCS, as in Figs. 5.7(a) and 5.7(c), both plateaus in the SRH statistics are equal, while they are different in amphoteric statistics, causing the total recombination rate $U(E_{\mathrm{d}})$ to differ by a factor of approximately two. This difference diminishes if the CCS are strongly asymmetrical: donor-like defects with $\sigma_{\sigma_{\mathrm{n}}^{+}} \gg \sigma_{\mathrm{p}}^{0}$ cause a high recombination $U^{\mathrm{D}}(E_{\mathrm{d}})$ rate in p-Si, whereas the recombination via acceptor-like states $U^{\mathrm{A}}(E_{\mathrm{d}})$ is suppressed for $\sigma_{\mathrm{n}}^{0} \ll \sigma_{\mathrm{p}}^{-}$ (see the discussion of Fig. 5.5 in Sec. 5.2.1.1). Hence, both statistics yield similar total recombination rates in the case of unequal CCS (cf. Figs. 5.7(b) and 5.7(d)). Since the majority of CCS for DBs reported in literature is asymmetrical [Bec96, Hat95, Lee10b, Oli07, Str84, Wyr91], the recombination can be closely approximated by SRH theory if care is taken that the distribution of the two defect types is separated by a positive value of E_{corr}.

Concerning the second issue (ii), the energetic extension of the plateau within the bandgap is assessed with respect to the TQFLs. According to Eqs. (5.14)(b) and (5.15)(b), the TQFLs of donor-like defects differ only slightly by $\ln(2)/\beta$ between both statistics, while the TQFLs of acceptor-like defects differ additionally by E_{corr}. The SRH recombination rate U_{SRH} has a plateau between a pair of TQFLs. In the case of amphoteric recombination statistics, the relation between the recombination rate U_{a} and the TQFLs is more complex. Consider the example with $\sigma^{\mathrm{c}}/\sigma^{0} = 100$ and $E_{\mathrm{corr}} = 0.2\,\mathrm{eV}$ in Fig. 5.7(d). With amphoteric recombination statistics, the recombination plateau of the acceptor-like defect U^{A} does not extend up to $E_{\mathrm{d}} = E_{\mathrm{Tn}}^{-}$, as in the case of SRH theory, but rather decreases already at energies above E_{Tn}^{0}. This is again attributed to the concurrent recombination paths via the two defect types in amphoteric recombination statistics: f^{+} increases at $E_{\mathrm{d}} > E_{\mathrm{Tn}}^{0,\mathrm{a}}$, which necessarily causes f^{0} to decrease since any state can be occupied by only one electron ($f^{+} + f^{0} + f^{-} = 1$, cf. Fig. 2.11).

To conclude, our results show that, for recombination plateaus lying between the *innermost pair* of TQFLs *from both* statistics, the amphoteric recombination statistics is well approximated by the proposed SRH model if (and only if) the CCS-ratio $\sigma^{\mathrm{c}}/\sigma^{0} \gg 1$. This finding restricts, in particular, the position and shape of those defect distributions which can be approximated using the extended SRH model.

5.2.4.2 Defect distributions

In the previous section, we concluded that the two recombination statistics yield different recombination rates if two conditions are met: firstly, if the $\sigma^{\mathrm{c}}/\sigma^{0}$ ratio is near unity and secondly, if the defect states are situated outside the innermost pair of TQFLs. In the following, we consider a distribution of the DB defect states at the a-Si:H/c-Si interface. As detailed in Sec. 5.1.2, we compare two scenarios: either the a-Si:H defect distribution is mapped to the interface (Eq. (5.3a)), or a Gaussian defect distribution centered at midgap (Eq. (5.3b)) is used, as shown in Fig. 5.3. Note that the band tail contributions, displayed in Fig. 5.3, are neglected in this section in order to focus on the differences between both recombination theories. Furthermore, we follow the common assumption that the fixed charge density Q_{f} at the interface is negligible [Pla07] and use $Q_{\mathrm{f}} = 0$ in Eq. (5.17).

Apart from the position of the defect distribution and its $\sigma^{\mathrm{c}}/\sigma^{0}$ ratio, the precision of the SRH approximation depends considerably on E_{corr} which causes differences in the TQFLs between the two recombination statistics according to Eqs. (5.14) and (5.15). However, it is insufficient to compare solely the recombination rates and the occupation fractions between the two statistics. The trapped charges in the DBs must be considered as well, as they depend on the density of excess charge carriers Δn and cause an interface charge Q_{it}. Thus, we require a self-consistent model that includes band bending at the interface [Lee10b] (cf. Sec. 5.2.3) to investigate the interactions between the recombination rate and the occupation fractions. To demonstrate this effect, we compare both the deviation in charge occupation[3] $\Delta f^{Q} = (f^{+} - f^{-}) - ((1 - f^{\mathrm{D}}) - f^{\mathrm{A}})$ in Fig. 5.8, and the ratio $U_{\mathrm{SRH}}/U_{\mathrm{a}}$ in Fig. 5.10 as a function of energy. We do this for the cases with and without surface band-bending and different dopant densities in the a-Si:H layer. In addition, in Fig. 5.8 the deviation in charge occupation Δf^{Q} is shown for different values of Δn and two values of E_{corr}. Note that we plot Δf^{Q} only for the case of the DPM $D_{\mathrm{it}}^{\mathrm{DB}}$ (Eq. (5.3a)), since the Gaussian $D_{\mathrm{it}}^{\mathrm{DB}}$ (Eq. (5.3b)) causes only marginal differences in the amplitudes of Δf^{Q}. Comparing the top panels 5.8(a)–5.8(d) with the bottom panels 5.8(e)–5.8(h), it becomes apparent that, with decreasing ratio $\sigma^{\mathrm{c}}/\sigma^{0}$, $|\Delta f^{Q}|$ increases near midgap. Near the band edges two distinct maxima of $|\Delta f^{Q}|$ are found, whose amplitudes are influenced mostly by E_{corr}. The amplitudes are large for $E_{\mathrm{corr}} = 0.2\,\mathrm{eV}$ (continuous lines) and much smaller for $E_{\mathrm{corr}} = 0\,\mathrm{eV}$ (dotted lines). The exact position of the maxima are determined by the position of the innermost pair of TQFLs, which are shown in Figs. 5.10(a)–5.10(c) for comparison. With increasing Δn, the TQFLs move closer to the band edges, and so do also the maxima of $|\Delta f^{Q}|$ in Fig. 5.8.

---

[3] Note that Δf^{Q} equals $\Delta f^{Q} = f^{0} + 2f^{-} - (f^{\mathrm{D}} + d^{\mathrm{A}})$ used in Ref. [Wil98], which is obtained by considering $f^{+} + f^{-} + f^{0} = 1$.

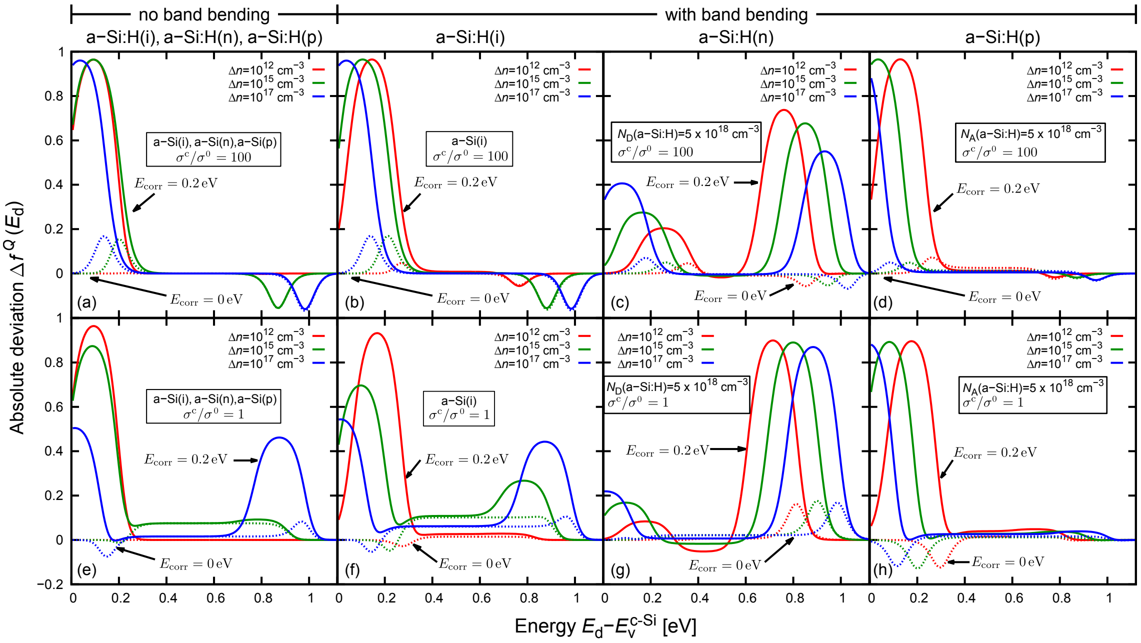

Figure 5.8: Deviation in charge occupation $\Delta f^Q = (f^+ - f^-) - ((1 - f^{\mathrm{D}}) - f^{\mathrm{A}})$ versus the defect's energy level for $\sigma^{\mathrm{c}}/\sigma^0 = 100$ (top row) and $\sigma^{\mathrm{c}}/\sigma^0 = 1$ (bottom row). Band bending is neglected ($Q_{\mathrm{it}} = 0$) in (a) and (e), and determined following Leendertz *et al.* [Lee10b] in the remaining graphs in which the dopant density of a-Si:H is varied. The continuous lines are calculated with $E_{\mathrm{corr}} = 0.2\,\mathrm{eV}$ and dotted lines with $E_{\mathrm{corr}} = 0\,\mathrm{eV}$. An effective interface-layer thickness of $w_{\mathrm{eff}} = 5\,\text{Å}$ is assumed [Lee10b]. The c-Si base dopant density is $N_{\mathrm{A}} = 10^{16}\,\mathrm{cm}^{-3}$.

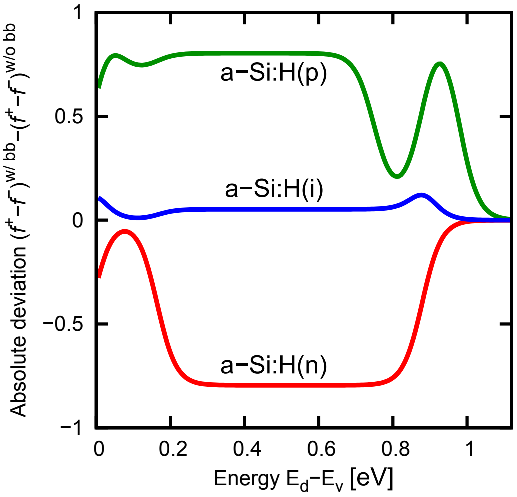

Figure 5.9: Deviation in charge occupation $(f^+ - f^-)^{\text{w/ bb}} - (f^+ - f^-)^{\text{w/o bb}}$ for the cases with band bending ($Q_{\mathrm{it}} \neq 0$) and without band bending ($Q_{\mathrm{it}} = 0$) for a-Si:H(i) (blue lines), a-Si:H(n) (red lines), and a-Si:H(p) (green lines) and amphoteric recombination theory. The c-Si base dopant density is $N_{\mathrm{A}} = 10^{16}\,\mathrm{cm}^{-3}$, $\Delta n = 10^{15}\,\mathrm{cm}^{-3}$, $E_{\mathrm{corr}} = 0.2\,\mathrm{eV}$, and $\sigma^{\mathrm{c}}/\sigma^0 = 100$.

With band bending (Figs. 5.8(b)–5.8(d) and 5.8(f)–5.8(h)), Δf^Q depends sensitively on the a-Si:H doping. In contrast, when neglecting band bending (i.e. $Q_{\mathrm{it}} = 0$), the deviation Δf^Q becomes independent of the dopant density, as shown in Figs. 5.8(a) and 5.8(e). This can be explained as follows. The occupation fractions in Eqs. (2.58) and (5.5) depend on the charge carrier concentrations at the interface, which are influenced by the band bending. The band bending, in turn, depends on the dopant density in the a-Si:H layer and on the interface-DOS due to the trapped charges. Hence, also the occupation fractions change when going from intrinsic to doped a-Si:H. When band bending is neglected in the simulation, the occupation fractions become independent of the defect densities and thus, Δf^{Q} is equal for a-Si:H(i), a-Si:H(n), and a-Si:H(p). Figure 5.9 shows the deviations in charge occupation $(f^{+}-f^{-})^{\mathrm{w/\ bb}}-(f^{+}-f^{-})^{\mathrm{w/o\ bb}}$ for the cases with band bending (w/ bb) and without band bending (w/o bb) for a-Si:H(i), a-Si:H(n), and a-Si:H(p), calculated with amphoteric recombination theory. It is apparent, that the deviations are smallest for a-Si:H(i), whereas they are large for doped a-Si:H. This is because for a-Si:H(i), band bending is typically smaller than for doped a-Si:H due to the low interface charge densities Q_{it} (which are below $10^{10}\,\mathrm{q/cm^2}$ for the parameters investigated here).

Figures 5.10(a)–5.10(c) present examples for $U(E_{\mathrm{d}})$ for the DPM $D_{\mathrm{it}}^{\mathrm{DB}}$ and three different a-Si:H dopant densities. Because the defect distributions for doped a-Si:H do not peak at midgap (cf. Fig. 5.3), strong differences between the correlated and uncorrelated approach are observed when the splitting of the TQFLs is small as for a-Si:H(n) in Fig. 5.10(b). On the contrary, the differences are small in case of a large splitting as for a-Si:H(p) in Fig. 5.10(c).

The ratio $U_{\mathrm{SRH}}/U_{\mathrm{a}}$ for different a-Si:H dopant densities and a CCS-ratio $\sigma^{\mathrm{c}}/\sigma^{0}=100$ is shown in Figs. 5.10(d)–5.10(f) and for $\sigma^{\mathrm{c}}/\sigma^{0}=1$ in Figs. 5.10(g)–5.10(i). As expected from the previous section 5.2.4.1, SRH statistics overestimates the recombination rate in case of equal CCS for both charged and non-charged defects ($\sigma^{\mathrm{c}}/\sigma^{0}=1$) over a wide energy range, as shown in the bottom row of Fig. 5.10 for $E_{\mathrm{corr}}=0.2\,\mathrm{eV}$. In case $\sigma^{\mathrm{c}}/\sigma^{0}\gg 1$, the deviations near midgap are significantly reduced (cf. Figs. 5.10(d)–5.10(f)). In agreement with the discussion above, strong deviations are observed for a-Si:H(n) due to the small splitting of the TQFLs, whereas the deviations are small for a-Si:H(p) where the splitting of the TQFLs is large.

For the characterization of solar cells, the effective surface recombination velocity

$$S_{\mathrm{eff}}^{i}(\Delta n):=\int_{E_{\mathrm{v}}^{\mathrm{c\text{-}Si}}}^{E_{\mathrm{c}}^{\mathrm{c\text{-}Si}}}\mathrm{d}E_{\mathrm{d}}\,\frac{U_i(E_{\mathrm{d}})}{\Delta n},\quad i=\mathrm{SRH\ or\ a}\tag{5.24}$$

is often used, where Δn is referred to at a distance from the interface where band bending is negligible (cf. Sec. 2.2.8 and Chapter 4). The ratio $S_{\mathrm{eff}}^{\mathrm{SRH}}/S_{\mathrm{eff}}^{\mathrm{a}}$ is displayed in Figs. 5.11(a)–5.11(e) for different parameter sets and defect distributions in dependence on Δn. With increasing Δn, also the TQFLs move further apart from

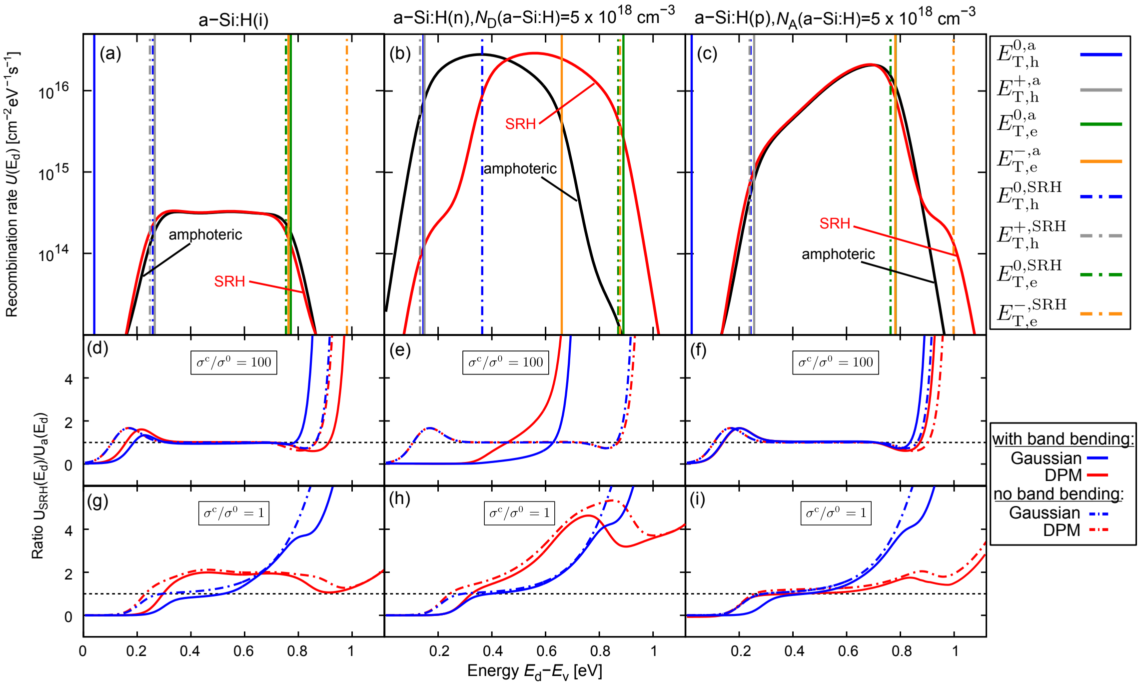

Figure 5.10: (a)–(c) Examples of recombination rates obtained using the DPM $D_{\text{it}}^{\text{DB}}$ for SRH statistics (red lines) and amphoteric statistics (black lines) with band bending for $\sigma^c/\sigma^0 = 100$. (d)–(i) Ratio $U_{\text{SRH}}/U_{\text{a}}$ for $\sigma^c/\sigma^0 = 100$ (top row) and $\sigma^c/\sigma^0 = 1$ (bottom row). Results obtained using the DPM $D_{\text{it}}^{\text{DB}}$ (Eq. (5.3a), red lines) and the Gaussian $D_{\text{it}}^{\text{DB}}$ (Eq. (5.3b), blue lines) are compared for the cases with band bending (continuous lines) and without band bending (dashed lines). The horizontal dashed lines are guides to the eye and indicate the case where $U_{\text{SRH}} = U_{\text{a}}$. The injection density is $\Delta n = 10^{12}\,\text{cm}^{-3}$, $E_{\text{corr}} = 0.2\,\text{eV}$, $D_{\text{Gauss}} = 5 \times 10^{11}\,\text{cm}^{-2}\text{eV}^{-1}$, and $\sigma_{\text{Gauss}} = 0.15\,\text{eV}$. The remaining parameters are chosen according to Fig. 5.8.

each other and hence, $S_{\text{eff}}^{\text{SRH}}/S_{\text{eff}}^{\text{a}}$ becomes smaller. In a similar manner, a low dopant density N_{dop} of the c-Si base enhances the relative deviations, whereas a high N_{dop} reduces the deviations (cf. to the TQFLs in Fig. 5.5). Figure 5.11(a) demonstrates that when band bending is neglected, $S_{\text{eff}}^{\text{SRH}}/S_{\text{eff}}^{\text{a}}$ is smallest for the Gaussian $D_{\text{it}}^{\text{DB}}$. However, when charges are considered, we obtain best consistency between the two statistics for the physically relevant cases, where $\text{E}_{\text{corr}} > 0$ and $\sigma^c/\sigma^0 \gg 0$, if the DOS is described with the DPM model: in Fig. 5.11(c), the relative error is $< 3\,\%$. Using the Gaussian DOS model, a slightly larger deviation between the two statistics is obtained: in Fig. 5.11(b), the relative error is $< 10\,\%$. This confirms the results presented by Leendertz *et al.* [Lee10b]. Apparently, in these cases, the amphoteric statistics can be well approximated using SRH theory at all relevant injection densities. In contrast, the SRH model becomes too approximate in the case of $E_{\text{corr}} \leq 0$, in particular, for symmetric ratios of the CCS σ^c/σ^0 for charged and non-charged defects, as shown in Figs. 5.11(c) and 5.11(d). Figure 5.11(f)

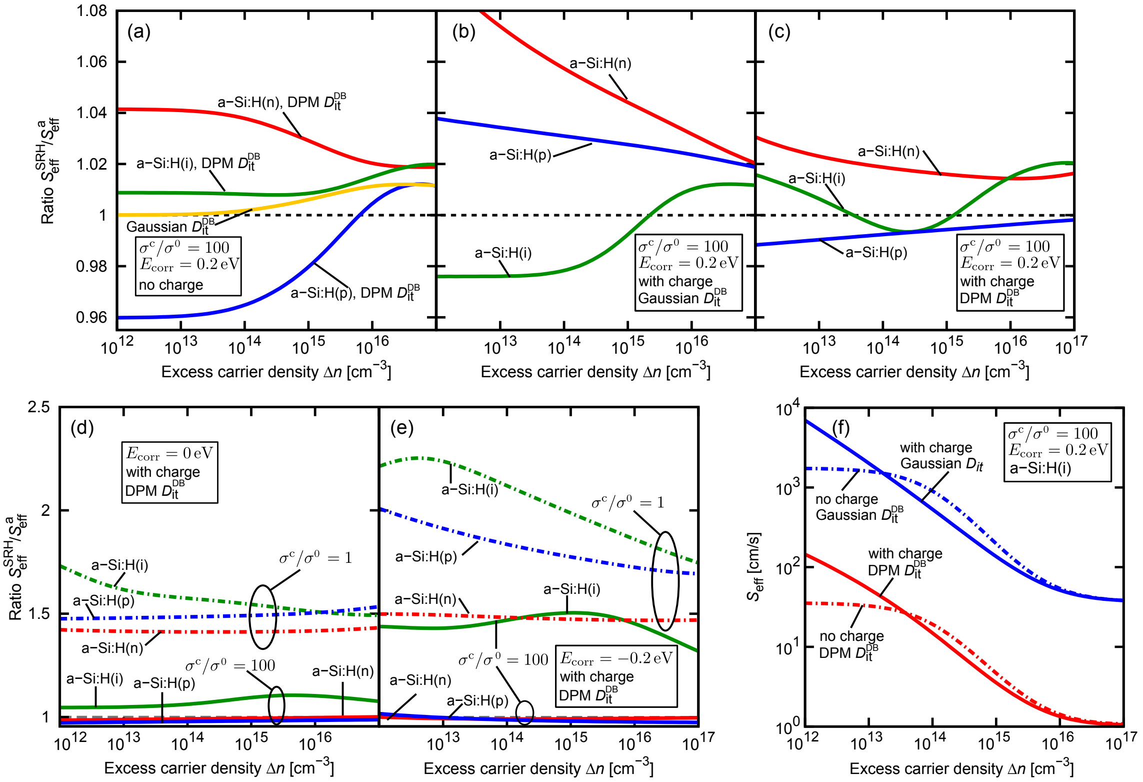

Figure 5.11: (a)–(e) Ratio $S_{\mathrm{eff}}^{\mathrm{SRH}}/S_{\mathrm{eff}}^{\mathrm{a}}$ of the effective surface recombination velocities calculated using the SRH statistics and amphoteric statistics, respectively, for different parameter sets and defect distributions. Note the different scaling of (a)–(c) compared to (d) and (e). The horizontal dashed lines are guides to the eye and indicate the case where $S_{\mathrm{eff}}^{\mathrm{SRH}} = S_{\mathrm{eff}}^{\mathrm{a}}$. (f) Comparison of S_{eff} calculated with the amphoteric recombination model with band bending (continuous lines) and without band bending (dashed lines) for the DPM $D_{\mathrm{it}}^{\mathrm{DB}}$ (Eq. (5.3a), red lines) and the Gaussian $D_{\mathrm{it}}^{\mathrm{DB}}$ (Eq. (5.3b), blue lines). Continuous lines: with interface charges, dashed lines: without interface charges. All parameters are chosen according to Fig. 5.10. Results from SRH statistics are not plotted because they yield almost equal results as the amphoteric statistics.

shows the influence of Q_{it}, obtained from the DPM $D_{\mathrm{it}}^{\mathrm{DB}}$ (Eq. (5.3a)), on S_{eff} for an a-Si:H(i)/a-Si:H(p) interface. Strong deviations compared to the calculations neglecting band bending are found for low Δn, whereas they are negligible for high-injection conditions. This is because the surface band-bending decreases with increasing Δn, and hence, the influence of the charges decreases. Consequently, care must be taken when neglecting the interface charges in simulations at low-injection conditions, for example at the p-n junction of an a-Si:H/c-Si heterojunction solar cell or at low illumination levels.

In conclusion, we confirmed that the results of Sec. 5.2.4.1 also hold for defect

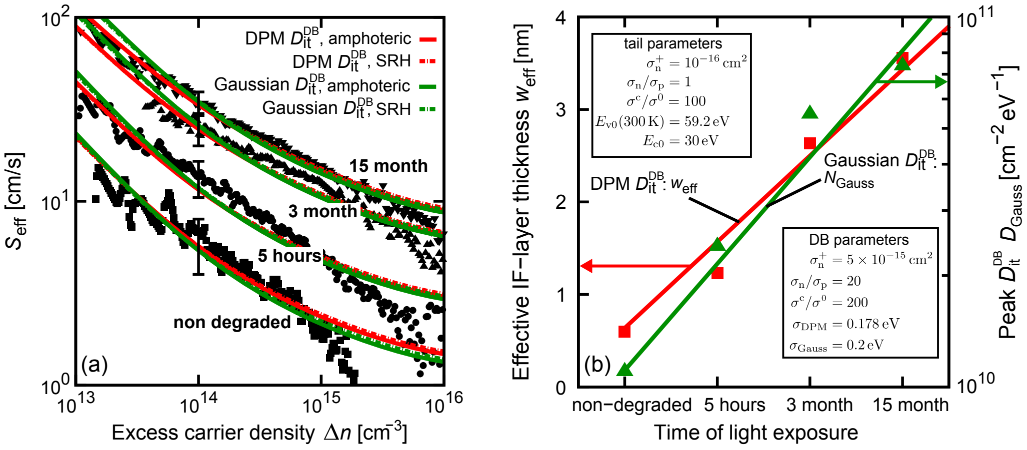

Figure 5.12: (a) The experimentally-determined effective recombination velocity S_{eff} at the a-Si:H(i)/c-Si interface as a function of injection density [Pla07] (symbols) increases for various light-exposure times due to the Staebler-Wronski effect. The numerical fit to the experimental data is performed using SRH statistics (dashed lines) or amphoteric statistics (solid lines) for both the DPM $D_{\text{it}}^{\text{DB}}$ (Eq. (5.3a), red lines) and the Gaussian $D_{\text{it}}^{\text{DB}}$ (Eq. (5.3b), green lines). (b) During fitting, N_t is varied in case of the Gaussian $D_{\text{it}}^{\text{DB}}$, and the effective interface-layer thickness w_{eff} is varied in case of the DPM $D_{\text{it}}^{\text{DB}}$. The lines are guides to the eye. All other parameters are fixed to the values noted in the graph.

distributions D^{DB}. The SRH model can only approximate the amphoteric statistics sufficiently precise in case of $\sigma^{\text{c}}/\sigma^{0} \gg 1$ and $E_{\text{corr}} > 0$. In addition, the splitting of the TQFLs must be sufficiently large, such that the main part of the defect distribution lies within the innermost pair of TQFLs. At the example of the effective surface recombination recombination S_{eff} of a-Si:H/c-Si passivated wafers, we showed that for small splitting, as in the case of a-Si:H(n) or at low Δn, large deviation between SRH theory and the amphoteric statistics arise. On the other hand, the deviations are small in case of a large splitting of the TQFLs, e.g. for a-Si:H(i), a-Si:H(p) or high Δn.

5.2.4.3 Reproduction of recent experimental data

In the following, we test the SRH approximation of describing recombination via amphoteric defects by reproducing experimentally determined $S_{\text{eff}}(\Delta n)$ data at the a-Si:H(i)/c-Si interface of a $1.5\,\Omega$cm p-Si substrate [Pla07, Pla08], shown in Fig. 5.12. The data were extracted from quasi-steady-state photoconductance (QSSPC) measurements [Sin96] of the effective lifetime, using the procedure outlined by Sproul [Spr94], and using the Auger parametrization according to Kerr and Cuevas [Ker02a]. Note that the S_{eff} values increase with the duration of light-exposure of the specimen, due to the creation of light-induced defects (the Staebler-Wronski effect [Pla08, Sta77, Stu85, Stu86]). We calculate S_{eff} with both the Gaussian $D_{\text{it}}^{\text{DB}}$ (Eq. (5.3b)) and the DPM $D_{\text{it}}^{\text{DB}}$ (Eq. (5.3a)) using the correlated amphoteric and uncorrelated SRH approach, and take the surface band-bending into account. We make the simple assumption that the Staebler-Wronski effect only causes changes in the defect density. Hence, during fitting with the genetic algorithm described in Sec. 3.1, only a single parameter is varied in dependence on the light-exposure time. In case of the Gaussian $D_{\text{it}}^{\text{DB}}$, the defect density is adjusted by changing D_{Gauss} in Eq. (5.3b), and for the DPM $D_{\text{it}}^{\text{DB}}$, the effective interface-layer thickness w_{eff} in Eq. (5.3a) is adapted. The lines in Fig. 5.12(a) show the calculated S_{eff} curves. It is apparent that first, the deviations obtained using the SRH formalism are small compared to the measurement error, and second, both models reproduce the data well. The resulting fit parameters displayed in Fig. 5.12(b) are physically plausible: for non-degraded a-Si:H, the DPM yields an effective interface thickness of $w_{\text{eff}} = 6\,\text{Å}$ which corresponds well to $w_{\text{eff}} = 7\,\text{Å}$ predicted by tight-binding simulations [Ber98b]. With increasing light exposure times, a-Si:H degrades and, accordingly, w_{eff} increases which results in an enhanced total DB density $D_{\text{tot}}^{\text{DB}}$. In case of the Gaussian $D_{\text{it}}^{\text{DB}}$, the peak density D_{Gauss} increases with increasing light exposure time which has a similar effect on $D_{\text{tot}}^{\text{DB}}$ as the variations of w_{eff} in the DPM.

In summary, both the SRH model and the amphoteric statistics reproduce the measured $S_{\text{eff}}(\Delta n)$ characteristics of a-Si:H(i)/c-Si passivated interfaces well. The varied parameters (w_{eff} in case of the DPM $D_{\text{it}}^{\text{DB}}$ and D_{Gauss} in case of the Gaussian $D_{\text{it}}^{\text{DB}}$) show a physically plausible increase with the light-exposure time of the sample (Staebler-Wronski effect). The results show that for a-Si:H(i)/c-Si interfaces, the SRH approximation yields very accurate results for all injection densities Δn if $\sigma^{\text{c}}/\sigma^{0} \gg 1$ and $E_{\text{corr}} > 0$.

5.2.4.4 Discussion

In our study, we considered experimentally relevant cases, such as the injection dependent error in the recombination rate integrated over energy. We investigated the error in the integrated recombination rate on the distribution of defect states which has not been taken into account in previous studies [Wil98]. It was shown that amphoteric theory can be approximated closely by SRH theory, if the following requirements are met: (i) the defect distributions lies in between a pair of TQFLs, (ii) the ratio of the CCS between charged and non-charged defects is large, and (iii) the correlation energy E_{corr} is positive. We further showed that the proposed equivalence between the error in the recombination rates and the CCS-ratio of the minorities [Wil98] is not valid in general, but depends e.g. on the illumination conditions and the dopant densities.

Using the example of passivating c-Si surfaces with a-Si:H, we showed that the error in the trapped charge density is not negligible in general. We demonstrated further that a separate analysis of the error in the occupation functions and the recombination rate is not sufficient: an error in the trapped charge density influences the carrier concentration and thereby the recombination rate, and vice versa. Therefore, a self-consistent model is required to consider the influence of all errors simultaneously.

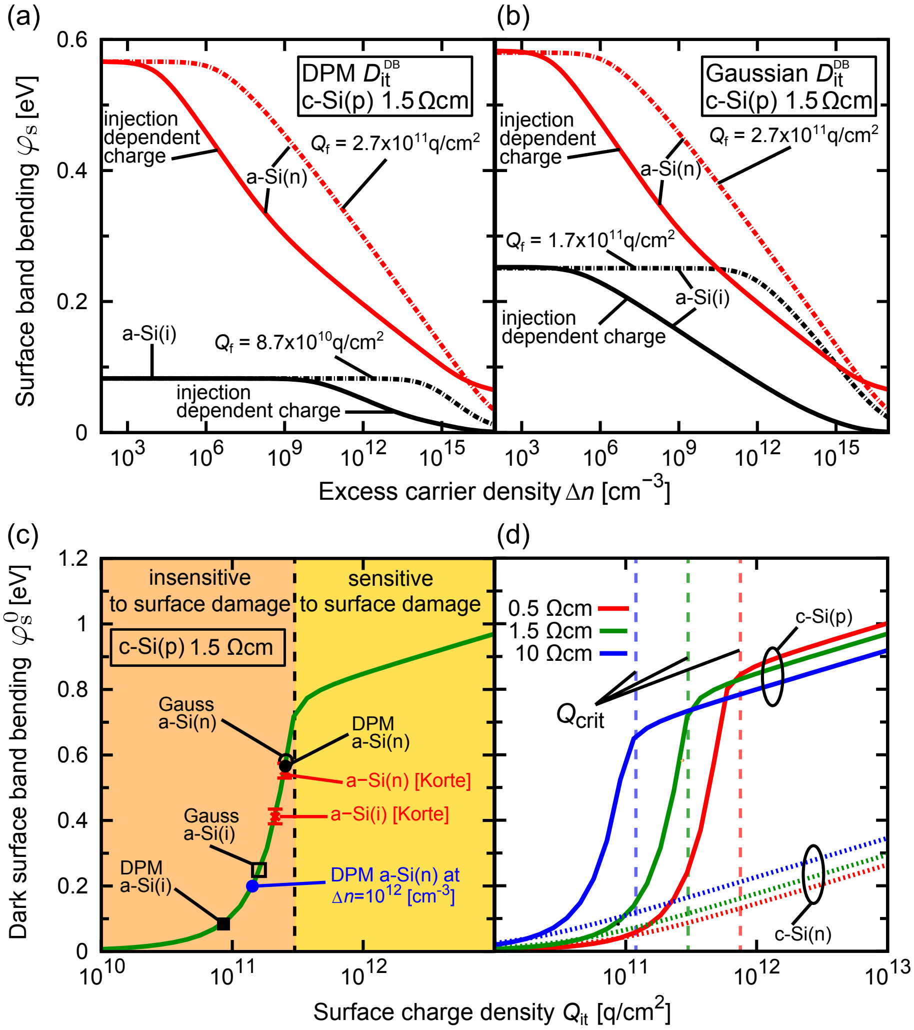

Figure 5.13: (a) and (b) Surface band-bending φ_s for a-Si:H(i)/c-Si(p) (black lines) and a-Si:H(n)/c-Si(p) (red lines, $N_{dop}^{a-Si} = 10^{18}\,cm^{-3}$) as a function of Δn. Continuous lines show $\varphi_s(\Delta n)$ evaluated using an injection dependent interface charge density Q_{it} (Eqs. (5.18)–(5.20)). For comparison, a fixed charge density Q_f is used (dashed lines) that yields an equal dark band-bending φ_s^0 as Q_{it}. D_{it}^{DB} is modeled using the extended DPM model (Eqs. (2.66) and (5.3a)) in (a) and using the Gaussian function (Eq. (5.3b)) in (b). (c) Measured φ_s^0 at a-Si:H-deposition temperatures around 200 °C [Kor06b] (red crosses) and values obtained from the simulations in (a) for a 1.5 Ωcm p-Si substrate are included. The blue symbol indicates the reduction of Q_{it} when going from thermal equilibrium to an injection density of $\Delta n = 10^{12}\,cm^{-3}$. (d) Dark surface band-bending φ_s^0 versus Q_{it} for c-Si(n) (dotted lines) and c-Si(p) (continuous lines) of different resistivity. The critical values of the charge density Q_{crit} for c-Si(p) are indicated by transparent dashed lines behind the data. The recombination parameters in the simulations are $\sigma_n^+ = 10^{-15}\,cm^2$, $\sigma_n^+ = \sigma_p^-$, $\sigma^0/\sigma^p = 100$, and $E_{corr} = 0.2\,eV$. The defect parameters are $w_{eff} = 5\,Å$ for the DPM D_{it}^{DB}, and $N_d = 5 \times 10^{11}\,cm^{-2}eV^{-1}$, and $\sigma_{Gauss} = 0.15\,eV$ for the Gaussian D_{it}^{DB}.

5.3 Comparison of the recombination models for a-Si:H/c-Si interfaces and SiN$_x$/c-Si interfaces

In Sec. 4, we discussed the influence of a surface-near damage layer on measurements of the effective surface recombination velocity S_{eff}. As a possible cause for the damage, we considered an excessive amount of hydrogen in the silicon underneath the surface. Consequently, also when depositing a-Si:H a large amount of hydrogen close to the surface should be expected. The damage depth underneath an a-Si:H layer may be assumed to be similar to that observed close to the Al$_2$O$_3$/c-Si interface ($0.01 \ldots 0.1\,\mu$m) rather than being similar to that underneath the SiN$_x$/c-Si interface ($0.1 \ldots 1\,\mu$m). This assumption originates from the relatively low deposition temperatures ($T \approx 200\,^\circ$C) of a-Si:H layers which are close to the fabrication temperatures of Al$_2$O$_3$ and significantly lower than the deposition temperatures of SiN$_x$ ($T \approx 400\,^\circ$C). In addition, the deposition times of the widely used 10 nm thick a-Si:H layers of ~ 1 min [e.g. Riz91, Sop02] are considerably shorter compared to the deposition times $t > 2$ min used for SiN$_x$ fabrication. This yields $z_{\text{deg}} \approx 0.055\,\mu$m for the a-Si:H/c-Si interface. However, the damage might be more severe due to the high hydrogen density of $10 - 15$ at. % [Kor06a] which is comparable to that of SiN$_x$ layers. As was show in Fig. 4.9 in Sec. 4.2.6, surface damage influences the injection dependence of S_{eff} significantly only above a total critical interface charge density $Q_{\text{crit}} = 3 \times 10^{11}\,\text{cm}^{-3}$ on p-Si with a resistivity of 1.5 Ωcm. For lower values of the charge density, the carrier concentrations in silicon are not inverted underneath the surface and recombination is dominated by recombination at the actual surface. The charge density at the a-Si:H/c-Si interface is far below Q_{crit}, as investigated in Fig. 5.13. In Fig. 5.13(a) and Fig. 5.13(b), the injection dependence of the surface band-bending φ_{s}, obtained using the model of injection dependent charge densities Q_{it} (Eqs. (5.18)–(5.20)), is compared to the band bending obtained when using a fixed charge density Q_{f} that yields the same dark band-bending φ_{s}^0. Both scenarios of the interface defect distributions, the DPM model in Fig. 5.13(a) and the Gaussian model in Fig. 5.13(b), are investigated. The chosen value of the fixed charge density Q_{f} strongly overestimates the band bending in both cases for all relevant injection densities up to $\Delta n \approx 10^{16}\,\text{cm}^{-3}$. This is because the injection dependent interface charge density Q_{it} decreases with increasing illumination level. Therefore, we may take the charge density Q_{it} obtained from φ_{s}^0 at thermal equilibrium as an upper limit to estimate whether surface damage may have an influence on S_{eff} at the a-Si:H/c-Si(p) interface. We find that both measured [Kor06a] and simulated values of φ_{s}^0 lead to charge densities below the critical value as demonstrated in Fig. 5.13(c). Using the example of the a-Si:H(n)/c-Si interface, we show in Fig. 5.13(c) that the charge density is shifted considerably further below the critical value (blue symbol) if Δn is increased. Comparing the simulated values of φ_s^0 with the measured ones [Kor06a] shows that the simulations match the experiment well for a-Si:H(n), whereas the measured values for a-Si:H(i) are considerably larger than the simulated ones (cf. Fig. 5.13(c)). The main reason for this discrepancy is that the measured samples are only *nominal* intrinsic. Due to relative high basis pressures before the deposition ($p_b \approx 7 \times 10^{-7}$ mbar), a considerable oxygen[4] contamination around $4 \times 10^{19}\,\mathrm{cm}^{-3}$ was determined from SIMS measurements [Kor06a]. In addition, the intrinsic layers were deposited in the same chamber as the n-doped layers, so Korte assumes that the a-Si:H(i) layers contain a non-negligible amount of phosphorus impurities, leading to a shift of the Fermi level well above midgap. The dependence between φ_s^0 and the interface charge Q_{it} is shown in Fig. 5.13(d), and helps to estimate the critical charge density in dependence of the substrate doping. The investigations made here indicate that the surface damage is expected to be rather irrelevant for a-Si:H/c-Si interfaces and can thus be neglected in the simulations. A further verification of this estimation will be given by SENTAURUS DEVICE [SD] simulations in Chapter 7.

The observation that Q_{it} obtained from the simulations is small also supports the common assumption that a-Si:H passivates mainly via the saturation of DBs [Oli07, Vai86] in contrast to the field effect passivation obtained by depositing amorphous silicon nitride (SiN$_x$) layers. Also in SiN$_x$, the dominating defect is known to be the silicon DB defect which lies deep within the c-Si bandgap. For nitrogen-rich films, in addition, the nitrogen DB defect density becomes considerable [Abe99]. Nevertheless, the SiN$_x$/c-Si interface is well described by simple SRH theory [Ste10a, Ste10b, Ste10c]. This is mainly due to the fact that the effect of SiN$_x$ passivation layers originates mainly from the fixed interface charge density Q_{f}, while the trapped charges Q_{it} are negligible, as was demonstrated in Sec. 4.2.5. Therefore the exact distribution of the deep-level defects is not important. In contrast, the relatively small Q_{it} at the a-Si/c-Si interface significantly influences the recombination rate, in particular for doped a-Si:H (cf. Fig. 5.11 in Sec. 5.2.4.2). Therefore, a detailed description of the recombination properties requires that the defect distribution is known and is included in the recombination model. In addition, the requirement to apply a more accurate model for the defect states in a-Si:H – with physically more relevant parameters – is motivated by the wide range of different applications. Whereas SiN$_x$ is used in solar cells only as passivation layer or antireflective coating, a-Si:H may not only be used because of its excellent passivation properties, but also to form a p-n junction or to serve as low-cost bulk material. For example, the sensitivity of the simulated behavior of an a-Si p-i-n structure to the recombination statistics has been demonstrated by Klimkovsky *et al.* [Kli02].

---

[4] Oxygen is a donor in silicon.

In conclusion, we estimated by means of analytical considerations that surface damage is negligible at the a-Si:H/c-Si interface for both intrinsic and strongly doped a-Si:H layers. This was attributed to the relatively small interface charge density Q_{it} which is by more than a magnitude lower than for SiN_x/c-Si interfaces. The influence of surface damage on a-Si:H/c-Si passivated solar cells will be investigated by means of device simulations in Chapter 7. In addition, we discussed whether the consideration of the amphoteric statistics and realistic defect distributions for the DBs could also significantly improve simulation results at SiN_x/c-Si interfaces. It was concluded that because S_{eff} at the SiN_x/c-Si interface is determined to a large extent by the fixed interface charge density Q_{f}, simple SRH statistics yields sufficiently accurate results.

5.4 Conclusion

We have shown that, for a range of conditions, amphoteric recombination statistics can be approximated with the uncorrelated SRH formalism if two equally shaped distributions for donor-like and acceptor-like defect states are used to imitate the amphoteric character. The two distributions must be separated by the effective correlation energy $E_{\mathrm{corr}} > 0$ and, additionally, the following two conditions must be met: (i) the defect distributions peak between the quasi-Fermi levels for trapped charges (TQFLs); and (ii) the ratio between the capture cross sections (CCS) of neutral and charged defects is significantly different from unity. Condition (ii) is usually met, but care must be taken with respect to condition (i): it may not be fulfilled under low to medium injection conditions, for example in the p-n junction of an a-Si:H/c-Si heterojunction solar cell or at low illumination levels. Furthermore, the TQFLs move closer together when going to lowly-doped substrates. This may cause strong deviations between the two statistics, in particular for defect densities that are not centered near midgap.

We have derived equations which relate the characteristic energy levels and the emission coefficients of the SRH model to those of the amphoteric statistics (cf. Table 5.2). These equations allow to estimate physically plausible error bounds directly from simulations performed using SRH theory. This is important for device simulations of c-Si solar cells containing a p-n junction or a high-low junction made with doped a-Si:H layers or when modeling a-Si:H(i)/c-Si passivated interfaces. For such applications, the derived error bounds can be employed to estimate at which injection densities Δn and for which defect distributions, the approximate SRH model agrees sufficiently accurate with the amphoteric statistics.

As discussed above, the typically applied uncorrelated closed-form approach may fail significantly. Nevertheless, by reproducing injection-dependent measurements of the effective surface recombination velocity S_{eff}, we found indications that conditions (i) and (ii) are typically met at the a-Si:H(i)/c-Si interface, and hence SRH statistics approximates the amphoteric model closely.

We have applied a self-consistent model, which includes the band bending in c-Si caused by light-induced trapped charges in the a-Si:H layer and at the a-Si/c-Si interface [Lee10b]. It was demonstrated that these trapped charges significantly influence the surface recombination rate. Neglecting the charges results in an underestimation of the effective surface recombination velocity S_{eff} for low to medium excess carrier densities Δn. The amount of trapped charges is influenced by the defect distribution in the a-Si:H layer and at the interface. Hence, accurate models for the defect distributions are required for a detailed modeling of S_{eff}. The defect-pool model (DPM) by Powell and Deane [Pow93] predicts a dependence of the defect distribution in a-Si:H on the valence-band tail (Urbach tail). To account for the doping dependence of this Urbach tail, we have developed an extension of the DPM which was used to model the defect distribution in the volume of doped a-Si:H passivation layers. By comparing two scenarios for the interface defect distributions, a Gaussian distribution at midgap and the extended DPM, we showed that SRH statistics is a better estimate of amphoteric statistics in case of the DPM. Based on the calculated trapped charge density Q_{it} at the a-Si:H/c-Si interface, we predict that the influence of surface damage is negligible for a-Si:H passivated substrates.

Chapter 6

Shunt Currents in c-Si Solar Cells

Shunt currents in c-Si solar cells are a frequently observed phenomenon. They influence the I-V characteristics of solar cells in a detrimental way, and hence, it is important to identify their underlying reasons.

The dark current-voltage (I-V) characteristics are defined via the Shockley equation (2.78) in Sec. 2.4.1.1. The ideality factor n_D of the Shockley equation is a measure for the increase of the current density j with the voltage V. For $n_\mathrm{D} = 1$, an exponential increase of the recombination current j with applied forward voltage V is observed. A saturation behavior, i.e. a sub-exponential increase of j with V, is obtained if $n_\mathrm{D} > 1$. Recombination in the SCR of p-n junction diodes influences the ideality factor n_D. It was demonstrated in various attempts [And77, Cho86, Cor96, Lee80, McI00a, Nus73, Pal97, Sah57] that n_D can reach but not exceed 2 if it is modeled with SRH theory (cf. Sec. 2.4.1.2). An overview of such attempts is given by McIntosh *et al.* [McI00b]. In contrast to these theoretical findings, it has been well-known for more than 40 years that the forward-characteristics may show an n_D value larger than 2, up to values of about 5, over an extended voltage range [Que62]. This is observed in most industrially fabricated silicon solar cells, and frequently also in cell designs under development [Lan02]. Moreover, the reverse characteristics are in these cases often nearly Ohmic or even slightly super-linear, which cannot be described within the SRH model either: The SRH theory predicts a saturation behavior. Previous attempts to explain large ideality factors were made with various models, including trap-assisted tunneling [Kam96], field-enhanced recombination [Sch95], saturation effects within the SRH-model for donor-like levels [Bei93], resistance-limited action of SRH-type edge recombination currents [McI00a, McI01, vdH05], and bias-dependent band bending that extends the recombination region to the p-type surface [Küh00]. In some of these models [Bei93, Kam96, Sch95], it was assumed that point defects are more or less homogeneously distributed in the whole depletion region. This assumption was proven wrong, because it contradicts measurements of the excess carrier lifetime τ in the order of microseconds in the applied materials. These τ values would lead to SRH recombination currents with $n_\mathrm{D} \leq 2$ that are orders of magnitude lower than the measured ones [Küh00, McI00a, McI01, vdH05]. For this reason, Kaminski *et al.* [Kam96] and Schenk and Krumbein [Sch95] took additional effects like field-enhanced recombination and the accumulation of shallow levels within the depletion region into consideration. Until now, such effects could not be verified experimentally.

As it was suggested already in 1962 [Que62], we assume here that the currents having $n_\mathrm{D} > 2$ do not originate from a homogeneous distribution of defects, but from local sites with a high defect density. This was experimentally confirmed by investigating differently sized samples [Bre94, McI00a, McI01] and by lock-in thermography [Bre01a, Bre01b, Bre03, Hau01]. For example, it was found that an increased recombination current can be observed in the whole edge region, but the edge current-density distinctly peaks at a few sites at the edge, which are called local edge shunts [Bre01b, Hau01]. Ideality-factor mapping performed by lock-in thermography showed that n_D is generally larger than 2 only in these local edge shunts, whereas there is $n_\mathrm{D} \lesssim 2$ in the other edge regions as expected from SRH theory [Bre01b].

In this chapter, we verify the local nature of shunts by disturbing the p-n junction depletion region in the interior part of solar cells in a controlled and reproducible manner by cleaving, laser scribing, or diamond scratching of the front surface above the shallow diffused emitter. We propose that the source of currents with $n_\mathrm{D} > 2$ are defects that are coupled and therefore cannot be described by the SRH theory. Defects with energy levels deep in the forbidden bandgap have a localized wave function and therefore act in general as isolated entities. A remarkable coupling between the defects occurs if their density becomes so high that their wave functions overlap. This is indeed the case in local shunt areas: oxidized surfaces may already show a density of defect states of about $10^{12}\,\mathrm{cm}^{-2}$, corresponding to a mean distance between the defects of 10 nm. A highly disturbed region may easily have a hundredfold higher defect density, corresponding to a mean distance below 10 nm. This makes interaction among deep-level defects likely. We reproduce our measured currents with a model of donor-acceptor-pair (DAP) recombination via deep-level states as opposed to the usually treated shallow levels [Hop63, Tho65]. In a qualitative study, deep-level DAP recombination was proposed to be responsible for large ideality factors already in Refs. [Bre06b, Bre06a]. Here, the deep-level DAP recombination model is further refined and implemented in a realistic device simulation.

To avoid ambiguities, we define a shunt in a diode as any path where carriers flow as an alternative to being fully injected across the p-n junction [McI01]. This implies that not all currents having $n_\mathrm{D} > 2$ are shunts. For example, the recombination rate at oxidized silicon rear surfaces shows a saturation behavior and can cause $n_\mathrm{D} > 2$ if this rate is dominating the cell's total recombination rate [Gha89, Rob95].

Such current paths do not provide an alternative to being injected across the p-n junction since the recombination occurs after the carriers are injected. In contrast, if such a surface is situated in the p-n junction depletion region, recombination may provide a short-cut for carriers through the p-n junction, so they do not need to be thermally excited above the entire potential barrier across the p-n junction. In this work, we deal solely with depletion region recombination currents that are shunts.

This chapter is structured as follows. We present the measured dark current densities j and ideality factors n_{D} of ideal (non-disturbed) solar cells and of cells having a disturbed p-n junction in Sec. 6.1. In Sec. 6.2, we motivate the DAP recombination as a possible cause for the observed shunt currents j and develop a parametrization for the recombination parameters in dependence on the defect density. In Section 6.3, we apply the DAP model to SENTAURUS-DEVICE [SD] simulations which allow to reproduce the measured n_{D}. Further, we implement a second possible cause of high ideality factors, the bias-dependent spatial extension of the recombination area which may cause a resistance limitation of the recombination currents j. The major part of the work presented in this chapter is submitted to *Journal of Applied Physics* [Ste11a].

6.1 Experimental results

For the experiments, seven identical, 1 cm^2 sized, laboratory *passivated emitter with rear locally diffused* (PERL) cells which show no significant shunt currents were selected. The *I*-*V* characteristics of all these cells, obtained at room temperature in the dark, corresponded initially to the "virgin" curve shown in Figs. 6.1(a) and 6.1(c). In order to induce shunt currents, three of these cells were disturbed each in a different way:

(i) cleavage in the (100) direction (after scratching the backside), so that the cleaved surface crosses the p-n junction depletion region over a length of 1 cm;

(ii) laser-cutting through the diffused emitter into the p-n junction depletion region (1 mm along the front surface between two metal fingers);

(iii) diamond scratching through the diffused emitter into the p-n junction depletion region (3 mm long at the front surface between two metal fingers).

These treatments affect the *I*-*V* curves both in forward and reverse direction, as shown in Figs. 6.1(a) and 6.1(c). The ideality factor n_{D}, displayed in Fig. 6.1(b), is extracted from the measured *I*-*V* characteristics according to Eq. (2.80). The virgin cell shows an n_{D} considerably smaller than 2 over the whole measured bias range,

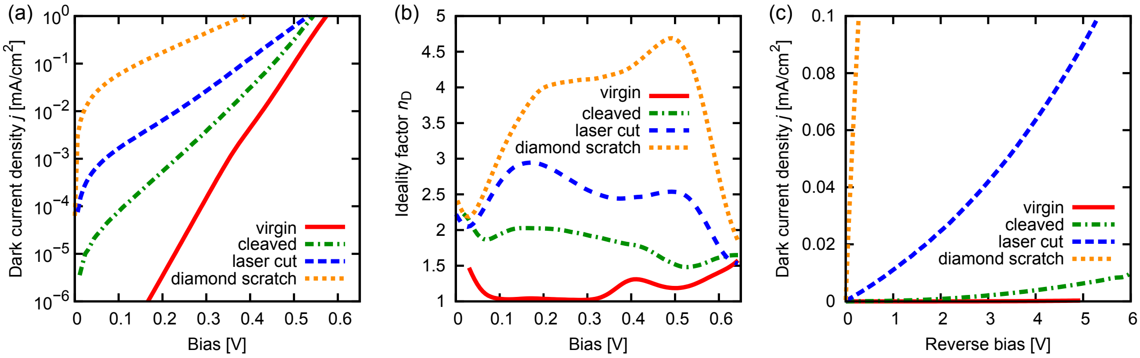

Figure 6.1: Measured dark *I*-*V* characteristics of identical PERL cells except that their p-n junction depletion region was damaged in various ways to generate recombination shunts in a controlled and reproducible manner. (a) the forward *I*-*V* curves in the dark, (b) the ideality factor n_D obtained from (a) using Eq. (2.80), and (c) the reverse *I*-*V* curves.

because there is no significant shunt current contribution. Note that the small peak near 0.41 V is due to recombination saturation at the rear oxidized surface [Abe95a]. The increase towards low voltages is due to SRH recombination in the p-n junction depletion region, which is an unavoidable recombination current. The corresponding lock-in thermography image in Fig. 6.2 shows a homogeneous thermal signal across its whole area.[1] The associated reverse current in Fig. 6.1(b) is low (in the nA range) up to many volts.

After disturbing, the thermography images confirm that additionally created currents arise which are limited to the disturbed regions. In Fig. 6.1, there is a clear correlation between the magnitude of the recombination current j and the ideality factor n_D: the higher the current j, the larger the ideality factor n_D. Cleaving produces the lowest recombination current per length unit and also the lowest n_D, while diamond scratching produces the highest current and the largest n_D. From scanning electron microscopy (SEM) micrographs (not presented), it is apparent that cleaving disturbs the p-n junction depletion region the least, while diamond scratching disturbs it the most. With the assumption that cleaving introduces the smallest density of defects, and scratching the largest, we infer that the higher the defect density, the higher is n_D. In addition, the increase of the reverse *I*-*V* curve is stronger the higher n_D.

In a separate experiment, a Vickers indenter was used to scratch each of the three cells at room temperature along a line of 1 mm with the predefined forces of 0.06 N, 0.09 N, or 0.26 N. The largest force caused a 1 μm deep scratch through the p-n junction depletion region [Bre06b]. In this way, we are able to increase the

---

[1] Note that the dark spots on the right hand side of each figure arise from shadowing by the sample holder.

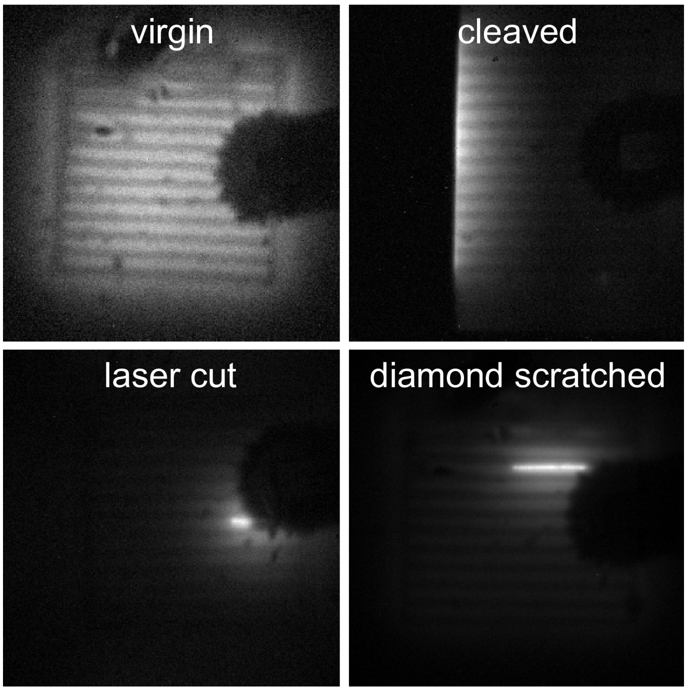

Figure 6.2: Lock-in thermography images of the cells whose *I*-*V* curves are shown in Fig. 6.1. Bright areas are caused by heat due to excessive recombination. Note that the brightness scaling is not the same in the virgin cell (with identical scaling the virgin cell would appear completely black).

damage in a controlled manner. This experiment and its interpretation will be discussed in Sec. 6.3.

6.2 Theoretical description of shunt currents

A correlation between the ideality factor n_D and the magnitude of a local recombination current j, similar to that described in Sec. 6.1, can be explained by resistance-limited recombination [McI00a, McI01], where a larger current j is more resistance-limited. While we acknowledge that this model describes some relevant situations, we found that it does not explain the most commonly observed experimental findings. For example, the resistance-limitation appears only at a forward bias above 0.2 V, where the current j is sufficiently high for this effect to become dominating, while typical measured *I*-*V* curves show $n_\mathrm{D} > 2$ already below 0.1 V, as displayed in Fig. 6.1(a). In addition, the induced shunt locations have a very simple geometry: the scratch lies in parallel to the two neighboring metal fingers and shows a homogeneous recombination activity across its entire length in Fig. 6.2. Hence, its series resistance can be described by a single resistor rather than by a distribution of various resistors, which would be necessary in the resistance-limited model for explaining $n_\mathrm{D} > 2$ over an extended bias range.

6.2.1 Deep-level donor-acceptor-pair (DAP) recombination

As the features in Fig. 6.1 cannot be described by series resistance effects, we need to resort to recombination that increases sub-exponentially with applied bias V, i.e. leads to a “saturation behavior” in the dark current density j. In the SRH formalism, the recombination rate R_{SRH} is proportional to the excess carrier density Δn at low-injection conditions, and there is no saturation behavior possible except in SCRs where n or p saturate with increasing V (e.g. at interfaces to charged dielectrics). However, if two defect states are coupled, there exist additional capture and emission processes as shown in Fig. 2.6 of Sec. 2.2.7. The recombination rate may become limited by the coupling rate from one to the other defect at sufficiently high Δn, which may result in the desired saturation behavior. We model the dark current density j using the coupled-defect level (CDL) recombination model of Schenk and Krumbein [Sch95], described in Sec. 2.2.7 by Eqs. (2.46)–(2.48). While Schenk has assumed the inter-level recombination probability to be infinite, we will introduce a finite probability being dependent on the inter-level distance. Apart from the coupling, these statistics satisfy the assumptions of the SRH theory, e.g. the energy levels are constant and independent of each other, the capture coefficients are also constant and independent of the occupancy of the coupled states, etc. In reality, the energy of one level will depend on the occupancy state of the other level, where the Coulomb interaction energy may be in the order of 100 meV. However, as we will show in Sec. 6.3.1.2, DAPs with energy levels within a broad range allow for the occurrence of ideality factors $n_{\mathrm{D}} > 2$. Hence, the simplification of constant energy levels is a valid approximation.

In the following we deal with the question which properties the capture and emission processes of the two coupled defects must have to cause the observed shunt currents. To answer this, we may restrict ourselves to the type of defects that cause the highest recombination rates. In the SRH formalism, the probability that a defect state captures an electron or hole is determined by its CCS σ_{n} and σ_{p}. These cross sections are influenced by two main factors: the charge residing in the defect state, and the overlap of the defect's wave function with the wave function of the incoming carrier. A literature review [Mac04a] shows that for many deep-level defects it is mainly the charge that controls the CCS. Concretely: a positively charged defect level is more likely to attract electrons than holes, i.e. $\sigma_{\mathrm{n}} > \sigma_{\mathrm{p}}$ [Lax59]. As the capture probability of electrons and holes is given by the CCS, we propose that the recombination rate is dominated by sites where an acceptor-like defect (with $\sigma_{\mathrm{n}} \ll \sigma_{\mathrm{p}}$) is coupled to a donor-like defect (with $\sigma_{\mathrm{n}} \gg \sigma_{\mathrm{p}}$). Due to the asymmetric CCS, the donor-like state captures electrons likely, transfers this electron to the acceptor-like defect, which is then likely to capture a hole. The recombination via this type of coupled defect is described in the literature as donor-acceptor-pair (DAP) recombination [Bin74, Hop63, Tho65]. However, these references consider shallow defects, which have a well extended wave function. We will show below that the experimentally observed shunt currents cannot be reproduced with shallow defects. Instead, we require *deep-level* donor-like and acceptor-like defects, which have constricted wave functions and, accordingly, need to exist both in high densities to couple to each other. Therefore, we need to extend the DAP recombination model with dependencies on the defect density, as described in the following.

6.2.2 Models for the DAP parameters

With an increasing density of defects, the experiments in Sec. 6.1 show a transition from SRH-like recombination via isolated defects ($n_\mathrm{D} \leq 2$) to recombination with $n_\mathrm{D} > 2$. To include this effect in the simulations, we introduce dependencies between the recombination parameters and the defect density. We assume that both the CCS and the coupling parameter c_DA in Eq. (2.45) depend on the distance r between donor and acceptor [Tho65].

6.2.2.1 Capture cross sections (CCS)

The effective charge state of coupled DAPs sensed by free charge carriers is a function of the DAP separation r. For r much larger than the distance r_c between the charge carrier and one of the defects ($r \gg r_c$), the CCS will be that of the isolated defects [Tho65]. For small separations ($r \ll r_\mathrm{c}$), however, the defect pair appears quasi-neutral leading to a much smaller CCS. Note that if a dipole is formed, as in case of Fig. 2.6(a) (an electron tunnels from the donor to the acceptor), "neutral" refers to the fact that the electron senses only the monopole, independent of the orientation of the pair.

Following the empirical relation proposed by Thomas *et al.* [Tho65], we assume the CCS to be proportional to the square of r:

$$\sigma_i(r) = \sigma_i^0 \left(\frac{r}{r_0}\right)^2 := Ar^2, \qquad i = \mathrm{n}, \mathrm{p}. \tag{6.1}$$

The divergence of the CCS for $r \longrightarrow \infty$ is no problem, since Eq. (6.1) only refers to the CCS for electrons and holes of the donor and acceptor in a coupled DAP, where large distances between the defects in a pair are unlikely[2].

So far, we assumed that a free charge carrier is captured by an ionized DAP with the capture probability independent of the orientation of the pair. An ionized DAP forms a dipole because the probability of finding the electron of the pair is highest close to the acceptor and smallest at the donor. Once a free carrier is captured

---

[2] For large distances, the exponent of r/r_0 should be zero instead of two.

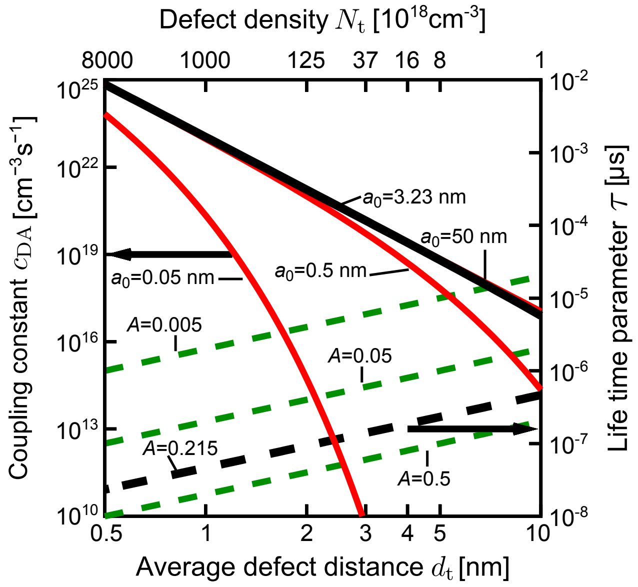

Figure 6.3: Dependence of the coupling constant c_{DA} (Eqs. (2.45) and (6.5), red solid lines) and the carrier lifetime parameter (dashed green lines) on the distance between the coupled defects d_{t}, for various values of the Bohr radius of the defect, a_0 in Eq. (6.3), and the proportionality constant of the CCS, A in Eq. (6.1). $\hat{c}^0_{\mathrm{DA}}$ is fixed to $1.1 \times 10^{-19}\,\mathrm{cm}^3/\mathrm{s}$. The parameters chosen for the simulations in Sec. 6.3 ($A = 0.215$, $a_0 = 3.23\,\mathrm{nm}$) are indicated by bold black lines. The upper x-axis is determined according to $N_{\mathrm{t}} = 1/d_{\mathrm{t}}^3$.

by the pair, it depends on the charge of the free carrier whether it couples to the part of the DAP wave-function located at the position of the donor or to the part located near the acceptor. We model this by assuming an asymmetric ratio $\sigma_{\mathrm{n}}/\sigma_{\mathrm{p}}$ with values ranging from 10^3 to 10^{12} for donors *in a pair*. Inverse ratios are used for the acceptors. Note that these high ratios cannot be measured, because for *isolated* defect levels, the asymmetry of this ratio is $10^{-4} < \sigma_{\mathrm{n}}/\sigma_{\mathrm{p}} < 10^4$.
We express the cross sections as carrier lifetime parameters

$$\tau_i \;=\; \left(N_{\mathrm{DAP}}\sigma_i v_{\mathrm{th},i}\right)^{-1}, \qquad i = \mathrm{n}, \mathrm{p}, \tag{6.2}$$

where $N_{\mathrm{DAP}} = N_t/2$ is the DAP density, and N_{t} is the sum of the defect density of the donor-like and acceptor-like defects.

6.2.2.2 Capture coefficient

We assume that the coupling coefficient c_{DA}, which is related via $c_{\mathrm{DA}} = \hat{c}_{\mathrm{DA}} N_D N_A$ [Sch95] to the reduced capture coefficient $\hat{c}_{\mathrm{DA}}$ (Eq. (2.45) in Sec. 2.2.7), is proportional to the overlap integral of the wave functions. Assuming further H-like radial-symmetric wave functions of equal extension for acceptor- and donor-like defects, the first radial wave-function reads [Gas74]:

$$R_{10}(\varrho) = 2\left(\frac{Z}{a_0}\right)^{3/2} \exp\left(-\frac{Z\varrho}{a_0}\right), \tag{6.3}$$

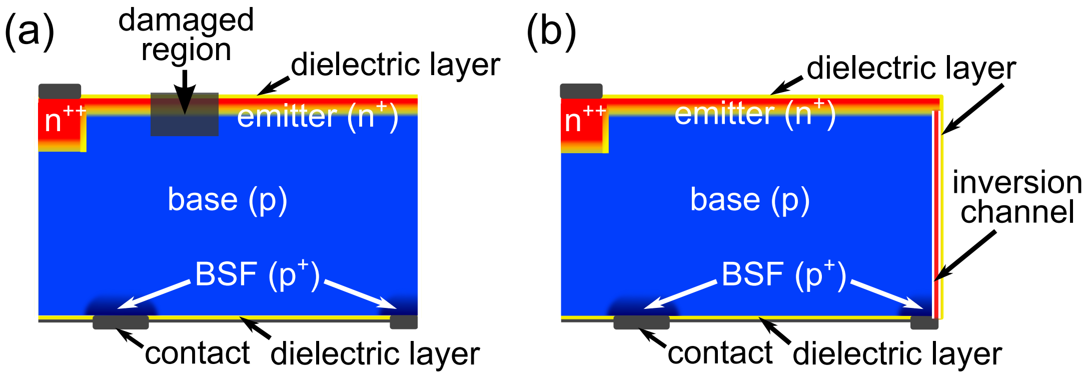

Figure 6.4: Simulation domain of the Passivated Emitter and Rear Locally-diffused (PERL) cells used in Section Sec. 6.1 with either (a) a partly damaged p-n junction depletion region, or (b) a dielectric layer along the edge of the cell, causing an inversion channel between the emitter and the p-contact at the rear. The local rear side diffusions in the sketch are labeled BSF as an abbreviation for back surface field. Not drawn to scale.

where a_0 is the Bohr radius of the donor or acceptor and ϱ is the spherical coordinate of the H-atom. Assuming $Z = 1$ for ionized defects, the overlap integral of the wave functions results in [Gas74]:

$$L(r) = \left[1 + \frac{r}{a_0} + \frac{1}{3}\left(\frac{r}{a_0}\right)^2\right]^2 \exp\left(-\frac{r}{a_0}\right). \tag{6.4}$$

This leads to the following definition of the capture probability $\hat{c}_{\mathrm{DA}}$:

$$\hat{c}_{\mathrm{DA}}(r) = \hat{c}^0_{\mathrm{DA}} L(r) \tag{6.5}$$

Figure 6.3 shows the dependence of the coupling constant c_{DA} and the CCS, expressed as carrier lifetime parameter (Eq. (6.2)), on the distance between the two coupled defects r.

6.3 Device simulations

We use the numerical device simulator SENTAURUS-DEVICE [SD] to model the I-V curves of the solar cell used in the experiments described in Sec. 6.1. Figure 6.4(a) shows the simulation domain. The parameters are taken from Refs. [Alt96, Alt03]. The damaged region covers an adjustable fraction of the entire simulation domain.

6.3.1 DAP recombination

6.3.1.1 Dependencies on the defect density

Figure 6.5(a) shows the simulated dark current densities j in dependence of the applied bias for an increasing density of defect states N_t. $N_\mathrm{t} = 10^{22}\,\mathrm{cm}^{-3}$ is chosen as an upper limit in order not to exceed the density of silicon atoms ($N_\mathrm{Si} \approx 4.9 \times 10^{22}\,\mathrm{cm}^{-3}$). The ideality factors n_D, calculated from the currents j in Fig. 6.5(a) with Eq. (2.80), are displayed in Fig. 6.5(b). In this example, the energy levels are $E_\mathrm{D} = 100\,\mathrm{meV}$ and $E_\mathrm{A} = 0\,\mathrm{meV}$, where we define $0\,\mathrm{eV}$ as midgap. The CCS and the coupling constant c_DA vary with N_t according to Eqs. (6.1)–(6.5). For the lowest defect density, $N_\mathrm{t} = 10^{18}\,\mathrm{cm}^{-3}$, the distance between the defects is as large as at oxidized surfaces (10 nm), and the overlap of the wave function is too small to lead to noticeable coupling. In this limit the CDL model results in vanishing recombination, hence the ideality factor becomes $n_\mathrm{D} = 1$. Note that no additional single-level recombination processes have been taken into account. With higher N_t, the CDL recombination starts to dominate the other recombination mechanisms in the cell (SRH and Auger) and this leads to the desired saturation behavior. Note that $n_\mathrm{D} > 2$ appears already at bias voltages below 0.1 V where the resistance-limited edge recombination does not show any effect [McI00a, McI01]. Both the recombination current j and the maximal ideality factor n_D increase with increasing N_t, mostly caused by the increased coupling coefficient c_DA (Eq. (2.45)). With increasing c_DA also the voltage where n_D becomes maximal increases because higher voltages are required for the inter-defect transition rate to become limiting (see the explanation of the saturation behavior in Sec. 2.2.7).

In conclusion, we showed that both the dark current density j and the ideality factor n_D increase with increasing defect density N_t. Further, the voltage, where n_D has its maximum, increases with increasing N_t. Both effects were attributed to the increased coupling coefficient c_DA.

6.3.1.2 Dependencies on the energy levels

We assume that there are two defect levels E_A and E_D, that are assigned to the acceptor and to the donor, respectively. These energy levels will be different from those of the isolated defects, because, in case of coupling, the Hartree-energy causes a non-negligible energy shift.

We vary the energy levels of the defects from $-200\,\mathrm{meV}$ to $+300\,\mathrm{meV}$ for a fixed defect density of $N_\mathrm{t} = 10^{21}\,\mathrm{cm}^{-3}$. Figure 6.6 displays the corresponding dark current densities j and ideality factors n_D in dependence of the bias. The currents j are largest near $E_\mathrm{A} = E_\mathrm{D} + 100\,\mathrm{meV}$. When E_A is shifted below E_D, the current j at a

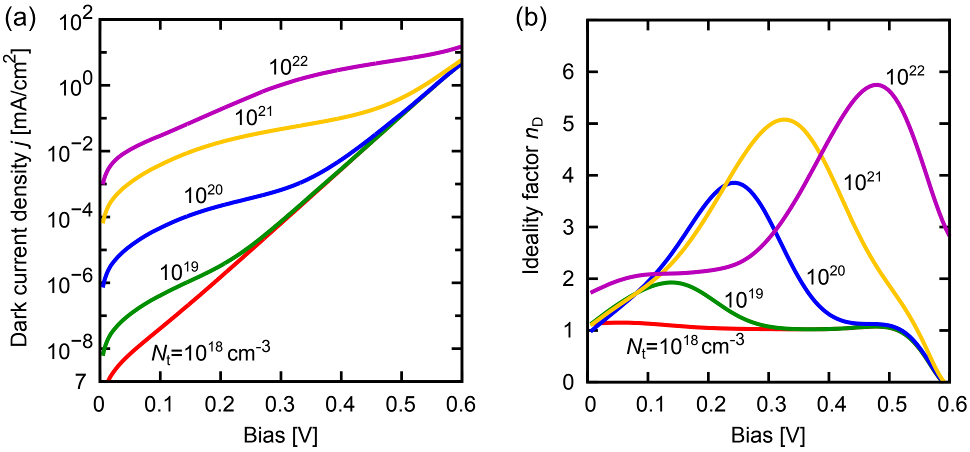

Figure 6.5: (a) Dark current density j and (b) ideality factor n_D in dependence of the bias voltage for various defect densities N_t. The energy levels of the defects are $E_\mathrm{D} = 100\,\mathrm{meV}$, $E_\mathrm{A} = 0\,\mathrm{meV}$, where $E = 0\,\mathrm{eV}$ at midgap. The parameters for the density dependence of the recombination parameters according to Eqs. (6.1)–(6.5) are set to $c^0_\mathrm{DA} = 1.1 \times 10^{-19}\,\mathrm{cm}^3/\mathrm{s}$, $A = 0.215$, $a_0 = 3.23\,\mathrm{nm}$ (cf. Fig. 6.3). An asymmetry of the free-to-bound CCS of $\sigma_\mathrm{n}/\sigma_\mathrm{p} = 10^{12}$ is assumed for the donors, and an inverse ratio is taken for acceptors.

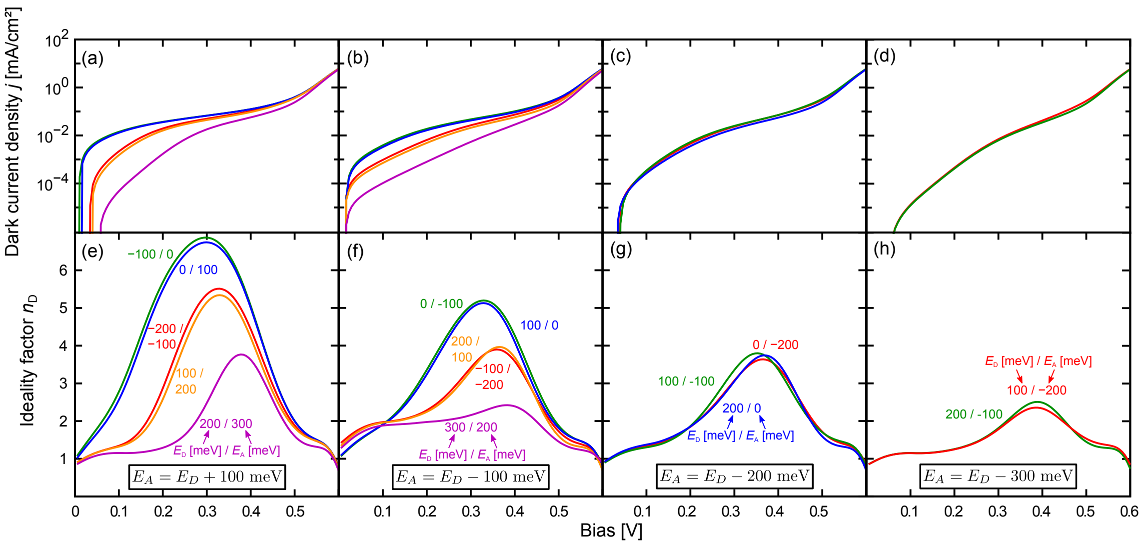

Figure 6.6: (a)–(d) Dark current densities j and (e)–(h) the corresponding ideality factors n_D versus bias for different energy levels E_D and E_A for a defect density of $N_\mathrm{t} = 10^{21}\,\mathrm{cm}^{-3}$. Each column shows, for a given energy separation between E_D and E_A, the n_D and j characteristics for different alignments of E_D and E_A. The energy levels are indicated with respect to midgap.

given voltage decreases slowly with the energy separation between both levels (cf. Figs. 6.6(a)–6.6(d)) and the voltage at which n_D peaks shifts slowly higher (cf.

Figs. 6.6(e)–6.6(h)). However, note that in general the recombination rate depends on the occupancy of the defects. With decreasing recombination current j, also the saturation effect reduces with increasing $|E_D - E_A|$ if recombination via DAPs is the dominating process, so n_D decreases. In addition, the DAP recombination is most effective close to midgap. Hence, for given $E_D - E_A$, j and n_D are maximal for an almost symmetric distribution of E_A and E_D around midgap. Note that the behavior of the curves is symmetric to midgap for symmetric lifetimes $\tau_\mathrm{n}^\mathrm{A} = \tau_\mathrm{p}^\mathrm{D}$ and $\tau_\mathrm{n}^\mathrm{D} = \tau_\mathrm{p}^\mathrm{A}$, where the indices A and D stand for acceptor-like and donor-like defects, respectively. We choose $\sigma_\mathrm{n}^\mathrm{A} = \sigma_\mathrm{p}^\mathrm{D}$ and $\sigma_\mathrm{n}^\mathrm{D} = \sigma_\mathrm{p}^\mathrm{A}$, but the thermal velocities for electrons and holes are slightly different, so a slight asymmetry can be observed, as can be seen for example in Fig. 6.6(e). Finally, for given $E_D - E_A$ and increasing distance of the energy pair from midgap, the DAP limitation, and therewith the saturation behavior, sets in at higher voltages. Hence, also the voltage where n_D peaks is shifted to higher values.

In our studies, we observed that, for equal CCS ($\sigma_\mathrm{n}^A = \sigma_\mathrm{p}^A$ and $\sigma_\mathrm{n}^D = \sigma_\mathrm{p}^D$), the saturation effect is negligible if the carrier densities are equal (not shown). Only in case of $\sigma_\mathrm{n} \neq \sigma_\mathrm{p}$ does the smaller capture coefficient provide a bottleneck for the recombination rate, which – for low voltages – can be bypassed by the CDL recombination rate.

If one of the coupled defects is shallow, free carriers may tunnel into this defect. This effect is called trap-assisted tunneling (TAT) [Sch95]. For our set of parameters, this effect plays a negligible role in forward bias. However, in reverse bias, variations in the lattice relaxation energy $E_\mathrm{LR} = S_\mathrm{HR}\hbar\omega$, where S_HR is the Huang-Rhys factor and $\hbar\omega$ is the effective phonon energy [Sch92], may strongly influence the breakdown-voltage. We also remark that, while TAT is a point defect mechanism, which should be independent of the defect density N_t, both the suggested DAP recombination model and the model of resistance-limited recombination, described below in Sec. 6.3.2, take N_t into account.

In summary, we found that an asymmetric ratio of the CCS ($\sigma_\mathrm{n}^\mathrm{D}/\sigma_\mathrm{p}^\mathrm{D} \gg 1$ and $\sigma_\mathrm{n}^\mathrm{A}/\sigma_\mathrm{p}^\mathrm{A} \ll 1$) is required to obtain a saturation behavior, i.e. $n_\mathrm{D} > 2$, in the dark forward I-V characteristics. In addition, it was shown that DAP recombination is most efficient for coupled energy levels which are symmetric to midgap.

6.3.1.3 Dependencies on the shunted area

Our simulations predict that a second peak in the ideality factor n_D may appear at high voltages ($V_2 \approx 650\,\mathrm{mV}$). As shown in Fig. 6.7, this feature occurs if a large area fraction $A_\mathrm{shunt}/A_\mathrm{tot}$ of the p-n junction depletion region is disturbed. In contrast, it does not appear if DAPs are only present in a small area fraction

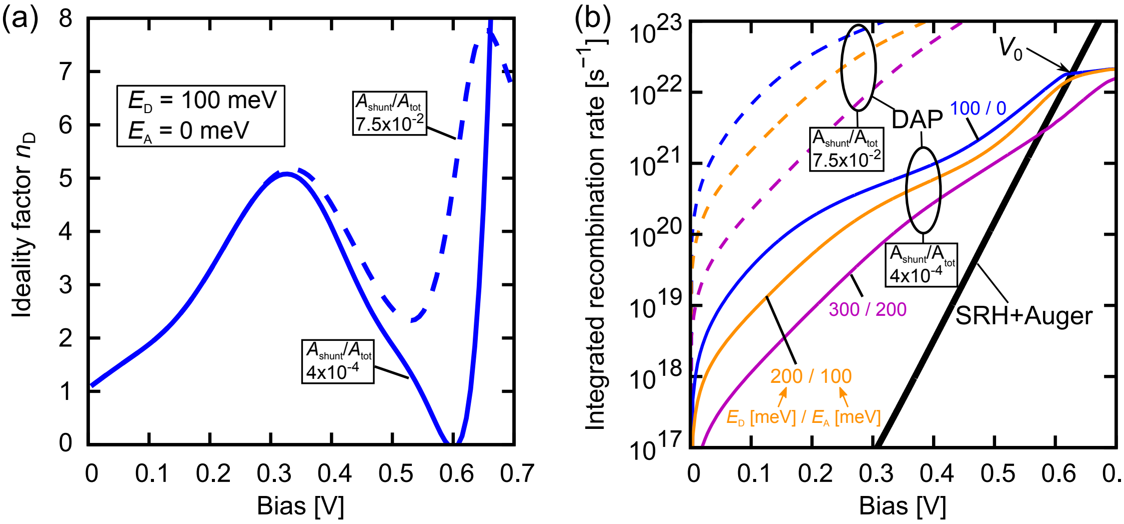

Figure 6.7: Investigation of the influence of the size of the shunted area for $N_t = 10^{21}\,\mathrm{cm}^{-3}$, $E_D = 100\,\mathrm{meV}$, and $E_A = 0\,\mathrm{meV}$. (a) For large disturbed area fractions of the p-n junction $A_{shunt}/A_{tot} = 7.5 \times 10^{-2}$, the n_D-V characteristic shows two peaks (dashed line). For cells with a smaller fraction $A_{shunt}/A_{tot} = 4 \times 10^{-4}$ (continuous line), the second peak at high voltages vanishes, whereas the amplitude and shape of the first peak remains equal. (b) Integrated DAP recombination rate for three different DAPs and the two shunted areas of (a). Large shunted area: dashed lines, small shunted area: continuous lines. For comparison, the sum of the integrated SRH and Auger recombination rates is shown (continuous black line).

similar to that of the experimental cells in Sec. 6.1. Due to the saturation effect, the recombination rate in the damaged region becomes (above some bias V_0), dominated by recombination in other device regions, as illustrated in Fig. 6.7(b). Accordingly, CDL recombination cannot influence n_D considerably above V_0. The values of V_0 and $n_D(V_0)$ depend on N_t in the damaged region, on the size of the damaged region in relation to the whole cell, and on the recombination rates outside the damaged region. In all solar cells we investigated, there is $V_0 > V_2$ as illustrated in Fig. 6.7(b). Consequently, the second peak in n_D does not appear in the dark I-V curve, which is the sum of recombination of all device parts, cf. Fig. 6.7(a).

To conclude, the simulations show a second peak in the ideality factor n_D at high voltages if the shunted area is so large that recombination via the DAPs dominates the total recombination rate for forward bias voltages up V_{oc}.

6.3.1.4 Dependencies on the defect distribution

It is well known that heavily defected semiconductors have a broad distribution of defect levels within the bandgap. Therefore, we use a superposition of various

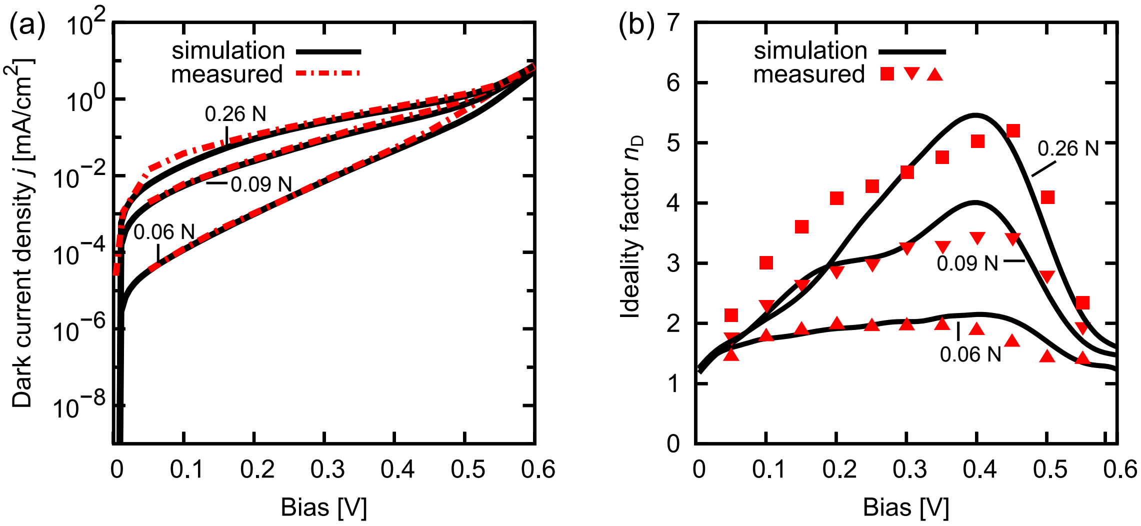

Figure 6.8: (a) Measured *I*-*V* curves and (b) the ideality factor n_D of PERL cells that received a 1 mm long scratch at the front surface with a load of 0.06 N, 0.09 N, or 0.26 N, respectively. The experiment is fitted with simulations (continuous lines) using a combination of three different DAPs specified in Table 6.1.

force [N]	N_t [cm^{-3}]	E_D [meV]	E_A [meV]	fraction %
0.06	1×10^{21}	0	100	41.67
	1×10^{22}	0	-200	8.33
	1×10^{19}	100	0	50
0.09	1×10^{21}	0	100	26
	3×10^{21}	0	-200	42
	1×10^{21}	100	0	32
0.26	1×10^{21}	0	100	36
	3×10^{21}	0	100	29
	1×10^{22}	100	0	36

Table 6.1: Combinations of DAPs used to fit the *I*-*V* curve and the ideality factor n_D in Fig. 6.8.

DAPs to reproduce the measured data. Figure 6.8 shows the measured *I*-*V* curves and n_D-V curves of three PERL cells. The p-n junctions of these cells were disturbed by a 1 mm long scratch at the front surface, made with a Vickers indenter while exerting a load of 0.06 N, 0.09 N, or 0.26 N, respectively. We fitted these curves with simulations using a combination of only three different DAPs and obtain satisfactory agreement with the measurement. The heaviest load caused a 1 µm deep crater, so it is difficult to reproduce the experiment in the entire voltage range. Important is that the fit parameters reflect an increasing N_t with increasing indentation load, as summarized in Table 6.1.

Using only three distinct DAPs is a simplification. In reality, there is a rather

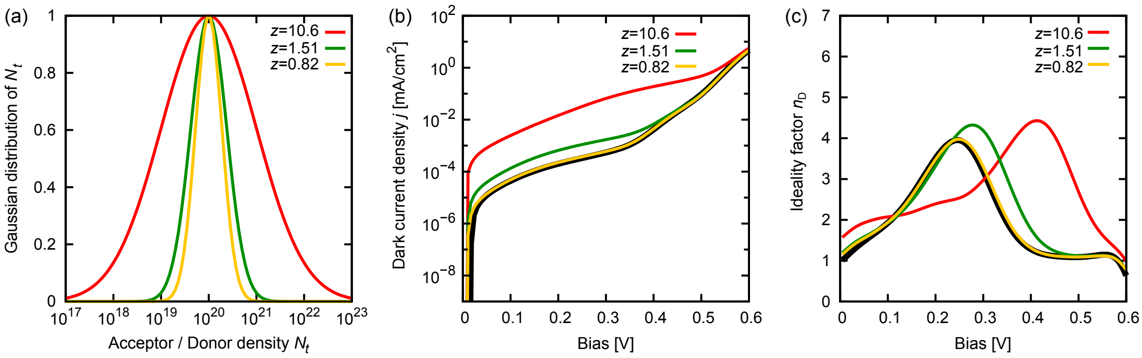

Figure 6.9: (a) Logarithmic Gaussian distributions $\exp(-(\log(N_\mathrm{t}/N_\mathrm{t0}))^2/z)$ around $N_\mathrm{t0} = 10^{20}\,\mathrm{cm}^{-3}$ for different values of z. (b) Simulated dark current density j and (c) ideality factor n_D for the Gaussian distributions from (a). The black curve shows the results for a distinct peak density $N_\mathrm{t} = N_\mathrm{t0}$. The DAP energy levels are $E_\mathrm{D} = 100$ meV and $E_\mathrm{A} = 0$ meV.

broad distribution of DAPs both with respect to N_t and to the position of the DAPs in the bandgap. The effect of the width of a logarithmic Gaussian distribution $\exp(-(\log(N_\mathrm{t}/N_\mathrm{t0}))^2/z)$ on n_D is shown exemplarily in Fig. 6.9. A relatively narrow distribution has small influence on the exact position of n_D. For broad distributions, in contrast, the influence from defects, with $N_\mathrm{t} > N_\mathrm{t0}$, becomes stronger, and the peak value of n_D shifts towards higher voltages (cf. Sec. 6.3.1.1). Heavily defected regions are not expected to have only one specific type of defects, but to have a multitude of defect types extending over a broad range of energies. However, our study predicts that only deep-level DAPs lead to recombination currents j that allow to reproduce the commonly observed shape of n_D as a function of bias voltage. DAPs are characterized by $\sigma_\mathrm{n}^D \gg \sigma_\mathrm{p}^D$ and $\sigma_\mathrm{p}^A \gg \sigma_\mathrm{p}^D$, and hence, are most efficient for recombination compared to other coupled defects having $\sigma_\mathrm{n} \approx \sigma_\mathrm{p}$. Consequently, the DAPs dominate the overall recombination rate and, hence, the dark I-V curve. We like to stress here that also other combinations of defects than listed in Table 6.1 may lead to the same satisfactory fit results. This is an important outcome, because our model yields the commonly observed shape of n_D whenever DAPs are present in an almost arbitrary broad distribution.

To conclude, we reproduced measured dark I-V curves and the corresponding ideality factors n_D of intentionally disturbed PERL cells in forward bias using a combination of three DAPs. Thereby, heavier disturbed cells need to be modeled with higher defect densities N_t in the shunted regions. We remark that the fit results are not restricted to three distinct DAPs. Also different broad DAP distributions may lead to satisfactory fits whenever DAPs are present with a sufficiently high density $N_\mathrm{t} \gtrsim 5 \times 10^{19}\,\mathrm{cm}^{-3}$.

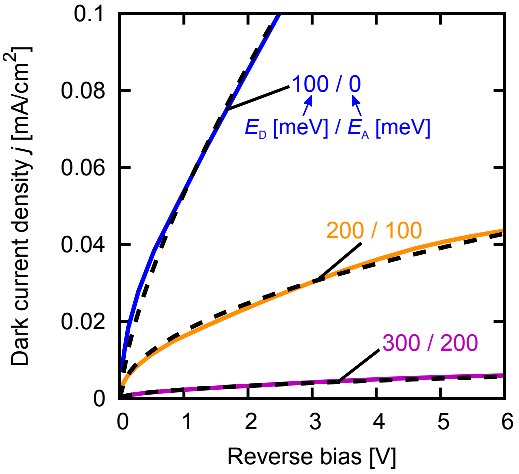

Figure 6.10: Simulated reverse characteristics with $N_\mathrm{t} = 10^{21}\,\mathrm{cm}^{-3}$ and for three different DAPs. The dashed black lines indicate a square-root dependence on the bias.

6.3.1.5 Reverse characteristics

It is commonly observed [Bre06b, Bre06a, Bre09] that the measured reverse characteristics (cf. Fig. 6.1(c)) is influenced by the degree of disturbance. The higher the recombination current j and the ideality factor n_D under forward bias, the stronger is the increase of the reverse I-V characteristics. This effect is also observed in the simulation. Our simulations predict an almost ideal behavior of the reverse characteristics in the investigated voltage range ($I < 0.005\,\mathrm{mA/cm}^2$ at 6 Volt reverse bias) for defect densities $N_\mathrm{t} \leq 10^{20}\,\mathrm{cm}^{-3}$ (not shown). For higher values of N_t, as e.g. $N_\mathrm{t} = 10^{21}\,\mathrm{cm}^{-3}$, the correlation between high ideality factors n_D under forward bias and the increased current j under reverse bias is clearly visible, as displayed in Fig. 6.10 for the examples of Fig. 6.7. According to SRH-theory, j saturates in reverse direction according to the Shockley equation (2.78). In the presence of DAPs, each of the DAPs in the depletion region contributes to the total saturation current. Assuming a Schottky diode with an abrupt p-n junction, the extension of the depletion region z_SCR increases with $z_\mathrm{SCR} \propto \sqrt{V_\mathrm{D} - V}$ for an applied reverse bias $V < 0$, where V_D is the diffusion voltage [Iba02]. Consequently, the number of DAPs contributing to the total current increases with increasing reverse bias. Thus, a square-root dependence of j on $V_\mathrm{D} - V$ in the depletion region can be expected. Indeed, the simulated reverse currents in Fig. 6.10 are well approximated by a square-root dependence on V. The measured scratch-induced reverse currents in Fig. 6.1(c) do not show this behavior: they are Ohmic or slightly super-linear. It was found in Ref. [Bre06b] that the temperature dependence of these reverse currents can be explained by variable range hopping conduction according to Mott's theory [Mot90]. Since this type of conductivity requires charge transfer between many defects, it cannot be explained by our deep-level DAP model. Hence, for correctly describing the reverse characteristics our model had to be extended to include transitions between many levels.

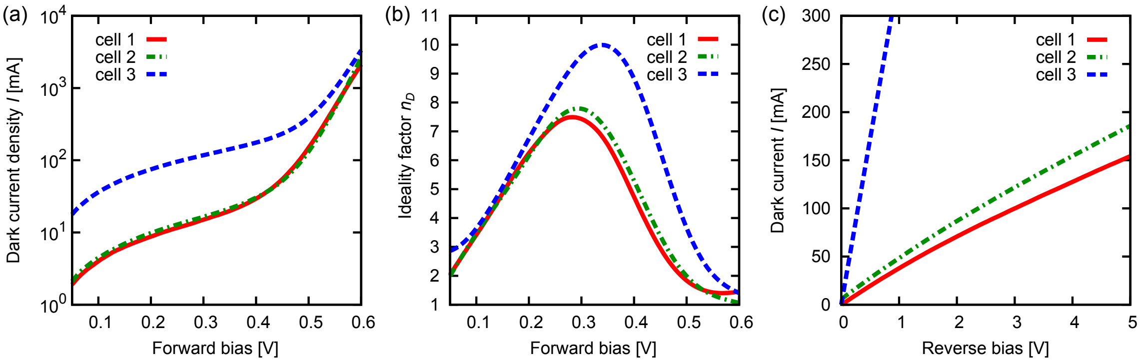

Figure 6.11: Measured *I*-*V* characteristics of industrial-type cells. (a) the forward *I*-*V* curves in the dark, (b) the ideality factor n_D obtained from (a) using Eq. (2.80), and (c) the reverse *I*-*V* curves.

However, for industrial-type cells showing $n_\mathrm{D} > 2$ at forward bias, often a slightly sub-linear behavior of the reverse currents is observed, as plotted in Fig. 6.11 for three examples. It may be assumed that these cells contain a lower defect density than the intentionally disturbed cells we used in our experiments. Hence, we believe that our model describes the reverse currents sufficiently well as long as the defect densities are not too high.

To summarize, the simulated reverse currents of cells showing $n_\mathrm{D} > 2$ under forward bias increase slightly sub-linear with increasing reverse voltage, similar to reverse currents commonly observed for industrial-type cells. Further, higher defect densities N_t result in higher reverse currents, which is also observed for the measured reverse characteristics of the intentionally disturbed PERL cells, shown in Fig. 6.8. To model the super-linear increase of the reverse-currents of these cells, transitions between many defect levels must be included in the DAP model.

6.3.1.6 Summary

We have presented a deep-level DAP recombination model which takes the dependence of the coupling and the CCS on the defect density into account. This model allows to reproduce measured shunt currents with ideality factor $n_\mathrm{D} > 2$ under forward bias, whenever DAPs are present in an almost arbitrary broad distribution. We found a clear correlation between the simulated ideality factor n_D and the defect density in both experiment and simulation: the higher the defect density N_t in the disturbed region, the higher n_D. Moreover, it could be shown that DAPs at energies close to midgap are more efficient for recombination than defect pairs further away from midgap. Finally, we presented simulations of reverse currents of cells which show $n_\mathrm{D} > 2$ under forward bias. The reverse currents yield a slightly sub-linear behavior with increasing reverse voltage, similar to reverse currents commonly observed for industrial-type cells. This behavior was attributed to the dependence of the spatial extension of the p-n junction on the applied bias. In addition, the reverse current increases with increasing defect densities N_t, similar to the measured reverse characteristics of intentionally disturbed PERL cells. To explain the superlinear behavior of the reverse-currents of these cells, our model needs to be extended by allowing for transitions between many defect levels.

6.3.2 Bias-dependent spatial extension of the recombination area

So far, we have treated heavily defected regions that extend into a p-n junction depletion region. This is not the only common source of large shunt currents: they are often observed at the edge of solar cells as well, or possibly at micro-cracks within the cell. It was shown by Altermatt *et al.* [Alt02b] that n_D generally does not increase above 2 at a bias below 0.2 V if the p-n junction borders on the edge of the cell that is passivated with a charged dielectric layer. Kühn *et al.* [Küh00] showed that a maximum possible surface saturation current density[3] of $j_{02,\mathrm{surf}} = 2 \times 10^{-8}$ A/cm can be reached if the edge contains no fixed charges or only a small density of fixed charges Q_f. This value is limited by the thermal velocity v_th of carriers that have to diffuse to the narrow recombination region where the depletion region reaches the surface. This implies that the observed edge recombination currents with surface saturation current densities as large as $j_{02,\mathrm{surf}} = 10^{-5}$ A/cm and $n_\mathrm{D} > 2$ cannot be interpreted by the simple recombination action of a plane crossing the p-n junction. Two major effects may cause such large edge recombination currents: firstly, a strongly reduced lifetime in the bulk close to the edge, or secondly, an inversion layer that extends the p-n junction depletion region at the front along the charged edge [Küh00] or along a charged micro-crack down to the rear metal contact, as shown in Fig. 6.4(b).

The first case of a strongly reduced lifetime is treated in Sec. 4 [Ste10a, Ste10b, Ste10c]. We consider it as unlikely that this can be the source for the observed strong shunt currents, particularly if the edge region was etched. In the following, we investigate the case that the inversion layer extends from the front p-n junction to the rear contact. Surface charging occurs at the surface of bare silicon or native oxide due to carrier capturing of the surface states and may cause a surface depletion region. For surfaces passivated with dielectrics, like e.g. SiN_x, positive fixed charges are present at the interface, which increase the depletion region at the p-Si surface, and may even lead to inversion. For a given surface state concentration, the

---

[3] Note that the surface saturation current density $j_{02,\mathrm{surf}}$ is given in units of A/cm, compared to the well known area related saturation current density j_{02} with units of A/cm^2.

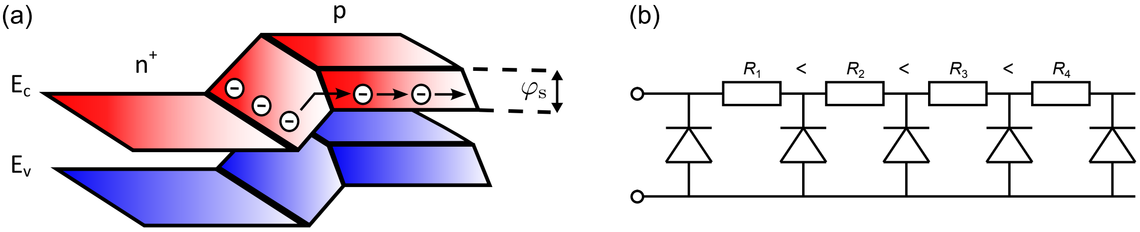

Figure 6.12: (a) Schematic representation of the 2-dimensional band edge diagram of a forward biased p-n junction bordering to a positively charged surface at the front of the drawing. The barrier height across the p-n junction is lowered by the band bending at the surface, φ_s, and hence, forms a shunt-path to the rear contact. The sketch layout is similar to [Bre94]. (b) Equivalent circuit of the device shown in (a).

degree of band bending at the surface reduces with increasing doping concentration. For the highly doped emitter or back surface field (BSF), the band bending may be negligible. In contrast, band bending may lead to inversion conditions in wafer material with $N_\mathrm{dop} \approx 10^{16}\,\mathrm{cm}^{-3}$ (cf. Fig. 4.2 in Sec. 4.1), which is typically used for solar cells.

Under forward bias, electrons from the emitter are injected into the potential groove close to the charged p-type surface as sketched in Fig. 6.12(a). Thereby, the edge recombination current is considerably increased. Kühn *et al.* [Küh00] investigated this situation using 2-D SENTAURUS-DEVICE [SD] simulations in dependence on the surface charge density. For sufficiently high charges, they found a remarkable increase of the surface recombination current. Indeed, also saturation behavior in the *I*-*V* characteristics was observed, leading to regions with $n_\mathrm{D} > 2$. However, the authors considered only a 5 µm thick solar cell and a maximum recombination velocity of $S_\mathrm{n} = S_\mathrm{p} = 1000\,\mathrm{cm/s}$. Under these conditions, the series resistance within the inversion channel plays only a minor role. Here, we perform similar calculations, where we allow higher surface state densities which may well be observed along edges or along micro-cracks, and use a thicker solar cell of 200 µm width, corresponding to a longer traveling path of the electrons.

In Fig. 6.12(b), the chain of diodes represents the recombining p-type surface at different distances to the emitter. With the help of this circuit, the saturation behavior of the *I*-*V* characteristics can be easily understood. For low bias voltages, where the recombination currents are low, the resistances of the diodes are high, and the series resistances R_i play only a minor role. Here, the recombination extends over the largest region. With increasing forward bias, the conductivity of the diodes increases. Thus, for the diodes situated further away from the emitter, the currents decrease, and thereby the region contributing to recombination becomes smaller, causing a saturation behavior. Note that this effect is different from the resistance-limited edge recombination effect considered by McIntosh and Honsberg [McI00a]

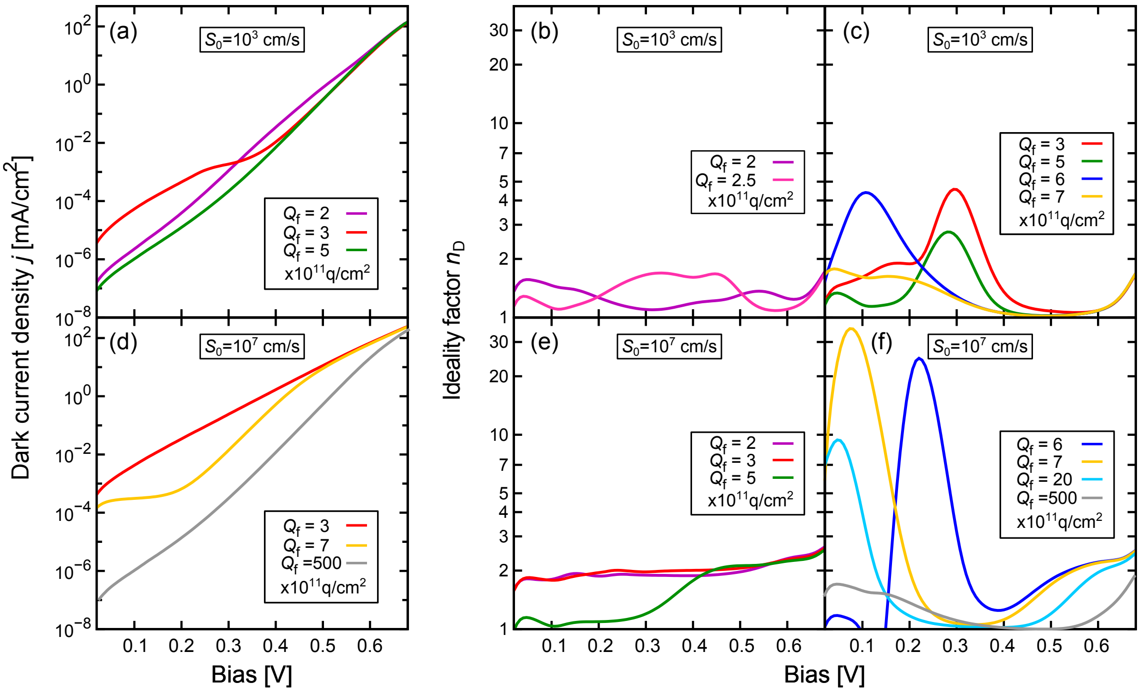

Figure 6.13: (a), (d) Simulated *I*-*V* curves and (b), (c), (e), (f) ideality factors n_D of a PERL cell with an inversion layer along its edge, as shown in Fig. 6.4, for different values of the fixed charge density Q_f. (a)–(c) are obtained with a surface recombination velocity parameter $S_0 = 10^3$ cm/s, and (d)–(f) with $S_0 = 10^7$ cm/s. (a) and (d) show j exemplarily for three different values of Q_f. (b) and (e) show n_D for values of Q_f that do lead not to inversion conditions at the edge and hence $n_D \leq 2$. (c) and (f) show n_D for the cases where inversion occurs. The base doping is $N_A = 2 \times 10^{16}\,\text{cm}^{-3}$.

and McIntosh [McI01]. In these references, only the emitter resistance was considered to limit the surface recombination current, which is independent of the bias.

In the following, we employ the software SENTAURUS-DEVICE [SD] to simulate the PERL cell of Fig. 6.4(b). We do not include DAP recombination, since we wish to model these two effects separately. In the simulations, we vary the SRH surface recombination velocity parameter $S_0 := S_n = S_p$ and the fixed charge density Q_f at the edges. The resulting dark current densities j and ideality factors n_D are shown in Fig. 6.13. Depending on Q_f and S_0, a peak in n_D may be observed, as displayed in Fig. 6.13(c) and Fig. 6.13(f). The voltage, where n_D peaks, depends on the values of Q_f and S_0. In particular, the occurrence of saturation behavior in the dark *I*-*V* curves is limited by two critical values of the charge density, Q_1 and Q_2. Only for $Q_1 \leq Q_f \leq Q_2$, an ideality factor $n_D > 2$ may be obtained, whereas there is $n_D \leq 2$ and for $Q_f < Q_1$ and $Q_f > Q_2$. The exact values of Q_1 and Q_2 depend on several cell parameters, as will be discussed below. For $Q_f < Q_1$ ($Q_1 \approx 2.8 \times 10^{11}$ q/cm² for $S_0 = 10^3$ cm/s), no inversion channel is formed, and thus,

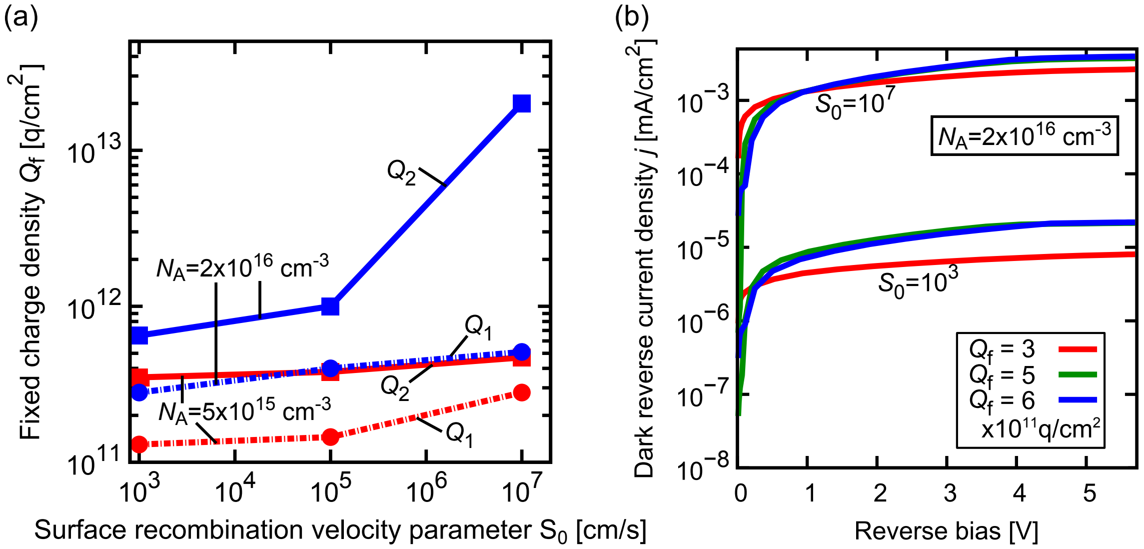

Figure 6.14: (a) Critical charge densities Q_1 (dashed lines) and Q_2 (continuous lines) for two base dopant densities $N_\mathrm{A} = 2 \times 10^{16}\,\mathrm{cm}^{-3}$ (blue lines) and $N_\mathrm{A} = 5 \times 10^{15}\,\mathrm{cm}^{-3}$ (red lines) in dependence on S_0 (see text for details). (b) Reverse characteristics of cells with $N_\mathrm{A} = 2 \times 10^{16}\,\mathrm{cm}^{-3}$ for different values of S_0 and Q_f which yield $n_\mathrm{D} > 2$ under forward bias.

no saturation behavior is observed in the current densities j, as shown in Figs. 6.13(a) and 6.13(d). Consequently, the ideality factors n_D in Figs. 6.13(b) and 6.13(e) may reach but do not exceed 2. This is in agreement with the observations made in Ref. [Alt02b]. Generally, $n_\mathrm{D} > 2$ can only be realized if Q_f is sufficiently high so the surface is close to inversion already at thermal equilibrium. This is observed for charges $Q_\mathrm{f} \geq Q_1$, where the resistance limitation of the current through the inversion layer causes high ideality factors, as shown in Figs. 6.13(c) and 6.13(f). The influence of this series resistance limitation increases with an increasing value of S_0 and hence, the maximum of n_D increases with S_0 (compare e.g. n_D for $Q_\mathrm{f} = 6 \times 10^6\,\mathrm{q/cm}^2$ for both values of S_0). In comparison with the DAP recombination, the peaks of n_D are typically more narrow and may reach very high values ($n_\mathrm{D} \approx 30$). For further increasing charge densities $Q_\mathrm{f} > Q_2$ ($Q_2 \approx 6.5 \times 10^{11}\,\mathrm{q/cm}^2$ for $S_0 = 10^3\,\mathrm{cm/s}$), the series resistance becomes negligible and the saturation behavior of the current density j vanishes. Thus, for $Q_\mathrm{f} > Q_2$, the ideality factor n_D does not exceed a value of 2.

The values of the critical charge densities Q_1 and Q_2 are investigated in dependence on S_0 and N_A in Fig. 6.14(a). It is apparent, that both Q_1 and Q_2 depend on S_0 and N_A. With S_0, the series resistance increases and hence, Q_1 and Q_2 increase. Further, the charge density that causes inversion in thermal equilibrium reduces with decreasing base doping and hence, Q_1 and Q_2 decrease. As the series resistance increases with increasing distance to the emitter, thicker cells require higher charges (or voltages) to achieve a continuous inversion channel from the emitter to the rear contact. Thus, also Q_1 and Q_2 increase with increasing thickness (not presented). It is generally observed that cells with a high ideality factor n_D under forward bias tend to have non-saturating reverse characteristics. Fig. 6.14(b) shows that this effect cannot be explained with the surface charge model, since the band bending is reduced or inverted under reverse bias, such that the depletion or inversion layer vanishes. Thus, the surface model can only explain shunt currents under forward bias. However, as the reverse current densities are low, they also do not hamper the occurrence of the non-saturating effects as obtained from the DAP model. Hence, it is possible that both DAPs and charged edges or micro-cracks, if present simultaneously, may contribute to the high ideality factors under forward bias.

To conclude, we modeled shunt currents by assuming an inversion layer that extends from the front p-n junction to the rear contact via the edge of the cell or along micro-cracks. We found that the occurrence of $n_\mathrm{D} > 2$ depends sensitively on the surface recombination velocity parameter S_0, the fixed charge density Q_f at the surface, the wafer doping N_dop, and the cell thickness. In a cell-specific range of charge densities Q_f, $n_\mathrm{D} > 2$ may occur, whereas for too low or two high charge densities Q_f the saturation behavior vanishes. This surface charge model can explain shunt currents under forward bias. For reverse bias, a saturation behavior is obtained, in contrast to the typically measured non-saturating reverse characteristics. Thus, this model may only yield a contribution to the saturation current in forward bias. To describe the reverse currents, DAPs are required in addition.

6.4 Conclusion and outlook

We have presented direct experimental evidence that the ideality factor n_D of the I-V characteristics of crystalline silicon solar cells increases beyond 2 for an increasing amount of disturbance by cleaving, laser cutting or scratching. We showed that recombination within such locations requires model descriptions that go beyond the Shockley-Read-Hall (SRH) approximation, because the density of defects is so high that recombination does not occur via isolated, but via coupled defect states. We reproduced the experimental findings with Sentaurus-Device [SD] simulations using a variant of coupled-defect level (CDL) recombination, the donor-acceptor-pair (DAP) recombination via deep-level states, in contrast to formerly employed shallow levels. The suggested model explains the experimentally observed transition from ideality factors $n_\mathrm{D} < 2$ to $n_\mathrm{D} > 2$ when going from low to high defect densities. Further, the observation that in experiment both the forward and reverse currents j increase with the defect density can be explained. We do not need a particular set of defects to reproduce the commonly observed shape of n_D as a function of bias. Our model yields the commonly observed shape of n_D whenever there are DAPs present in an almost arbitrary broad distribution with DAP densities $N_\mathrm{DAP} > 5 \times 10^{19}\,\mathrm{cm}^{-3}$. DAPs are most efficient for recombination compared to other coupled defects, and hence, dominate the overall recombination rate. Additionally, our model yields slightly sub-linear reverse-characteristics, as frequently observed for industrial-type cells with $n_\mathrm{D} > 2$ under forward bias. This was explained by an increasing number of DAPs contributing with increasing reverse bias to the current because the spatial extension of the depletion region increases. The sometimes measured slightly super-linear reverse-characteristics are most probably due to variable range hopping conduction [Bre06b], which cannot be explained by our deep-level DAP model. For correctly describing reverse characteristics, the DAP model must be extended by including transitions across many levels.

We also investigated another source of shunt currents: an inversion layer that extends from the front p-n junction to the rear contact via the edge of the cell or along micro-cracks. Generally, $n_\mathrm{D} > 2$ can only be realized if Q_f is sufficiently high such that the surface is close to inversion already at thermal equilibrium. In comparison with the DAP recombination, the peaks of n_D are typically more narrow and may reach very high values $n_\mathrm{D} \approx 30$. This surface charge model can explain shunt currents in forward bias, whereas it fails to explain the commonly observed non-saturating reverse I-V characteristics. Hence it may be possible that in cells where both DAPs and charged edges or micro-cracks exist, the DAPs are responsible for the large reverse currents, while both DAP recombination and an inversion layer extending from the front p-n junction to the rear contact may contribute simultaneously to the high ideality factors under forward bias.

Our simulations explain, possibly for the first time, the observation made with lock-in thermography that the ideality factor n_D increases with increasing disturbance, in both forward and reverse bias.

Until now an experimental verification of the suggested DAP recombination mechanism is still lacking. However, a number of experiments are practicable which may verify these mechanisms. For shallow-level DAP-luminescence, the maximum of the luminescence wavelength decreases with increasing recombination intensity (blue shift reported in [Bin74, Hop63]). If any kind of luminescence showing a blue shift should be observed at the position of recombination-induced shunts, this could be a hint to DAP recombination. Also, a contribution of free-to-bound transitions, e.g. between a charge carrier and a charged surface state, may be visible to a rather weak extent in low-temperature luminescence measurements. Such observations could explain the origin of the second investigated source of shunt currents, an inversion layer that extends from the front p-n junction to the rear contact.

Microscopic electroluminescence imaging of the edge region of solar cells may thus show the real extension of the recombination region. Furthermore, a consideration of deep-level DAPs in the interpretation of lifetime measurements may be reasonable, because DAP recombination could play a role if the lifetime is dominated by localized high densities of surface states.

Chapter 7

Surface damage in Industrial Type Solar Cells

In this chapter, we apply the models presented in Chapters 4 and 5 to industrial type solar cells using 2-D SENTAURUS-DEVICE [SD] simulations (the shunt model was already applied to solar cells in Chapter 6). This application demonstrates the suitability of the models for device simulators. Further, by investigating the influence of the investigated defect types on the illuminated solar cell *I*-*V* characteristics, we show the relevance of the presented models. As an example, we choose the rear-side passivation of PERL[1] solar cells [e.g. Gre94, Wan90] with SiN_x or a-Si:H layers. This is a promising alternative compared to costly high temperature processes, such as thermal oxidation or back-surface-field diffusions. However, often problems arise with SiN_x, such as surface damage (cf. Chapter 4) or parasitic shunting [Dau02a]. Here, we investigate the impact of surface damage on the performance of differently designed PERL cells in dependence on the intensity of illumination. Surface damage at the SiN_x passivated rear side is only expected to have significant influence on the *I*-*V* characteristics if recombination at the rear contributes considerably to the overall recombination rate and thus, limits the cell efficiency. Analyzing the recombination losses in different cell regions separately, enables us to identify those regions of the cell which limit the cell efficiency. We also investigate the influence of surface damage on the performance of a-Si:H passivated solar cells. Thereby, the goal is to support the hypothesis made in Chapter 5 that surface damage has negligible influence on the recombination properties of a-Si:H passivated substrates.
Part of the work presented in this chapter will appear in *Energia Procedia* (Proceedings of the 1st Silicon PV) [Ste11c].

---

[1] PERL: Passivated Emitter and Rear Locally-diffused

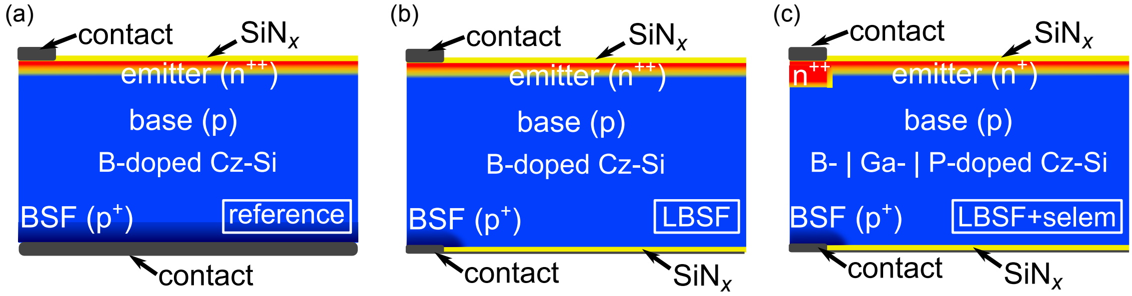

Figure 7.1: Simulated cell designs. (a) The reference cell, (b) the LBSF cell, and (c) the LBSF+selem cell. All simulation parameters are specified in Table 7.1.

7.1 Cell designs

We consider three cell designs. Figure 7.1(a) shows a standard screen-printed, industrial-type solar cell fabricated on a 2.5 Ωcm boron-doped Czochralski (Cz) grown silicon substrate at ISFH [Ste11c]. The textured front side of the cell is diffused by a phosphorus emitter with a sheet resistance[2] of $R_{\mathrm{sh}} \approx 80\,\Omega/\square$, and passivated with SiN$_x$. The fully metalized rear side of the cell contains an aluminum alloyed Al–p^+ back surface field (BSF). The *LBSF cell* (local BSF cell), displayed in Fig. 7.1(b), constitutes a modification of the reference cell into a PERL cell. The wafer is alloyed with aluminum atoms underneath the local rear contacts only, and the remaining surface parts of the rear-side are passivated by SiN$_x$. The *LBSF+selem cell* (local back surface field and selective emitter cell) in Fig. 7.1(c) is an industrial feasible improvement of the LBSF cell. Its rear side is the same as for the LBSF cell, while the front side is optimized using a selective emitter. This emitter is highly doped ($R_{\mathrm{sh}} \approx 19\,\Omega/\square$) only underneath the contacts to account for a low contact resistance, while the remaining part of the emitter is rather lowly-doped ($R_{\mathrm{sh}} \approx 149\,\Omega/\square$) to reduce surface recombination and Auger recombination losses. Three different dopant species of the Cz-Si base are considered: boron (B-Cz-Si), gallium (Ga-Cz-Si) and phosphorus (P-Cz-Si). Using gallium improves the charge carrier lifetimes compared to boron-doped material [Glu01]. Further, Ga-Cz-Si does not suffer from light-induced degradation as it is the case for B-Cz-Si [Glu01] (cf. Sec. 7.2.1.1). When using P-Cz-Si, i.e. changing the substrate doping from p-type to n-type, the dopant species of the BSF and the emitter are exchanged. This leads to changes in the sheet resistances of the diffused layers, because the carrier mobilities change [Kla92a]. In particular, for equal doping profiles, for p-type dopants a higher R_{sh} is obtained than for n-type dopants, cf. Table 7.1.
All simulations parameters are summarized in Tables 7.1 and 7.2.

---

[2] The resistance R of a thin film of a length d_{x}, a width d_{y} and a uniform thickness d_{z}, is given by $R = \varrho/d_{\mathrm{z}} \cdot d_{\mathrm{x}}/d_{\mathrm{y}} = R_{\mathrm{sh}} d_{\mathrm{x}}/d_{\mathrm{y}}$. The sheet resistance R_{sh} denotes the specific resistance ϱ per thickness d_{z}. It is usually given in units of “Ohms per square” ($\Omega/\square$), i.e. for a sheet with $d_{\mathrm{x}} = d_{\mathrm{y}}$.

Property	Parameter / Model		
unit cell	2089 μm × 160 μm		
front contact width	70 μm		
rear contact width	130 μm		
substrate resistivity	2.5 Ωcm		
	reference cell	**LBSF cell**	**LBSF+selem cell**
substrate dopant species	boron	boron	boron | gallium | phosphorus
emitter diffusion (e)	measured (diffused, Fig. 7.2(a))	measured (diffused, Fig. 7.2(a))	simulated (implanted)
$R_{\mathrm{sh,e}}$ [Ω/□]	80	80	149 | 149 | 302
$N_{0,\mathrm{e}}$ [cm^{-3}]	1.6×10^{20}	1.6×10^{20}	2.3×10^{18}
emitter contact diffusion (ec)	—	—	implanted (simulated)
$R_{\mathrm{sh,ec}}$ [Ω/□]	—	—	19 | 19 | 27
$N_{0,\mathrm{ec}}$ [cm^{-3}]	—	—	9.6×10^{20}
BSF profile (BSF)	measured (Fig. 7.2(b))	measured (Fig. 7.2(b))	measured (Fig. 7.2(b))
$R_{\mathrm{sh,BSF}}$ [Ω/□]	23	23	23 | 23 | 11
$N_{0,\mathrm{BSF}}$ [cm^{-3}]	1.5×10^{19}	1.5×10^{19}	1.5×10^{19}
SRH lifetime parameter τ_{n} [μs]	280 (non-degraded) 58 (degraded)	280 (non-degraded) 58 (degraded)	280 | 1000 | 3500 58 (degraded) | — | —
SRH lifetime parameter τ_{p} [μs]	280 (non-degraded) 579 (degraded)	280 (non-degraded) 579 (degraded)	280 | 1000 | 3500 579 (degraded) | — | —
$S_{\mathrm{n,front}}$ [cm/s]	8×10^{6}	8×10^{6}	$2.1{\times}10^{3}$ | $2.1{\times}10^{3}$ | $5.4{\times}10^{3}$
$S_{\mathrm{p,front}}$ [cm/s]	8×10^{5}	8×10^{5}	$2.1{\times}10^{2}$ | $2.1{\times}10^{2}$ | $5.4{\times}10^{2}$
$Q_{f,\mathrm{front}}$, $Q_{f,\mathrm{rear}}$ [q/cm^{2}]	2.21×10^{12}	2.21×10^{12}	2.21×10^{12}
$S_{\mathrm{n,rear}}$, $S_{\mathrm{p,rear}}$ [cm/s]	—	6.8×10^{3}	6.8×10^{3}

Table 7.1: Parameters used in the SENTAURUS-DEVICE solar-cell simulations. The SRH lifetime parameter for the B-Cz-Si wafers in the degraded state is obtained using Eq. (7.1) with $[\mathrm{O_i}] = 7 \times 10^{17}\,\mathrm{cm}^{-3}$ and $G = 2.17$.

7.2 Device simulations

In this section, we employ the software Sentaurus-Device to model the different solar cells introduced in Fig. 7.1. For the device-simulations, we employ a variety of models that has been developed specifically tailored to solar cell device simulations during the last twenty-five years. These models are based on independent experiments and thus, help to perform highly predictive simulations of entire cells without having to adjust many free parameters.
In the Sentaurus-Device simulations presented here, we use the following physical models: Intrinsic density and bandgap narrowing [Alt03], electron and hole masses [Gre90], Auger recombination [Alt97], surface passivation [Alt02c, Alt06b], mobility [Kla92a, Kla92b], and Fermi-Dirac statistics. All models and parameters are listed in Table 7.2 (see also [Ohr11]).

In Sec. 7.2.1, we simulate the reference cell (cf. Fig. 7.1(a)). First, a model for the SRH excess carrier lifetime in B-Cz-Si is introduced. Second, the measured doping profiles used for the emitter and the BSF are discussed. Finally, the accuracy of the simulation is demonstrated by reproducing the measured *I*-*V* curves. In Sec. 7.2.2, we model the PERL cell structures, sketched in Figs. 7.1(b) and 7.1(c).

7.2.1 Reference cell

7.2.1.1 Light-induced degradation of boron-doped Cz-silicon

Boron is the standard dopant of p-Si Cz-Si used for PV applications. In this material, the SRH excess carrier lifetime τ_{SRH} (Eqs. (2.35) and (2.40)) degrades under light-exposure until a stable value is reached. This degradation is due to the formation of boron oxygen (B–O) complexes [Bot05, Rei03, Sch99b], described by the SRH recombination parameters (Eq. (2.35)) [Alt09, Bot05]:

$$\begin{aligned} \tau_{\mathrm{n}} &= 4.402024 \times 10^{39}\,\mathrm{s} \left(\frac{[\mathrm{B_s}]}{1\,\mathrm{cm}^{-3}}\right)^{-0.824} \left(\frac{[\mathrm{O_i}]}{1\,\mathrm{cm}^{-3}}\right)^{-1.748} G && (7.1) \\ \tau_{\mathrm{p}} &= 10\,\tau_{\mathrm{n}} && (7.2) \\ E_{\mathrm{d}} &= E_{\mathrm{c}} - 0.41\,\mathrm{eV}, && (7.3) \end{aligned}$$

where $[\mathrm{B_s}] = N_{\mathrm{A}}$ is the substitutional boron density, and $[\mathrm{O_i}]$ is the interstitial oxygen density. The latter depends on the Cz-process and the position of the wafer in the ingot and takes values between 10^{17}–$10^{18}\,\mathrm{cm}^{-3}$ [Bot05, Lim10]. G denotes a dimensionless improvement factor for τ_{SRH} and is typically in the range $2-3.5$ [Bot05]. It depends on the density of oxygen dimers and on the boron-oxygen complex density $[\mathrm{B_s}]$, which can be reduced e.g. during a phosphorus diffusion. The asymmetric ratio of $\tau_{\mathrm{p}}/\tau_{\mathrm{n}} = 10$ results in an injection-dependent SRH excess carrier lifetime τ_{SRH}.

Property	Parameter / Model
Device simulation	
Equations numerically solved	Semiconductor drift-diffusion equations Eq. (2.5)
Temperature	298.15 K
Free carrier statistics	Fermi-Dirac
Intrinsic carrier density	$n_\mathrm{i} = 9.65 \times 10^{9}\,\mathrm{cm}^{-3}$ [Alt03] Obtained with setting E_g to a lower value in [Gre90]
Bandgap narrowing model	Ref. [Sch98b]
Free carrier mobility	Klaassen's unified mobility model [Kla92a, Kla92b]
Radiative recombination	$B = 4.73 \times 10^{-15}\,\mathrm{cm}^3/\mathrm{s}$ [Tru03]
its doping and injection-dependence	Refs. [Alt05a] and [Alt06a]
Auger recombination	Ref. [Dzi77]
its temperature dependence	Ref. [Alt97] $C_i = (A_i + B_i \cdot (T/T0) + D_i \cdot (T/T0)^2) \times (1 + H_i \exp(-(n,p)/N_{0,i}))$, with $i = \mathrm{n}, \mathrm{p}$ $A_\mathrm{n} = 2.8 \times 10^{-31}\,\mathrm{cm}^6/\mathrm{s}$, $A_\mathrm{p} = 7.91 \times 10^{-32}\,\mathrm{cm}^6/\mathrm{s}$, $B_\mathrm{n} = 0$, $B_\mathrm{p} = -1.239 \times 10^{-32}\,\mathrm{cm}^6/\mathrm{s}$, $D_\mathrm{n} = 0$, $D_\mathrm{p} = 3.231 \times 10^{-32}\,\mathrm{cm}^6/\mathrm{s}$, $H_\mathrm{n} = 8$, $H_\mathrm{p} = 8$, $N_{0,\mathrm{n}} = 2.5 \times 10^{17}\,\mathrm{cm}^{-3}$, $N_{0,\mathrm{p}} = 2.5 \times 10^{17}\,\mathrm{cm}^{-3}$, $T_0 = 300\,\mathrm{K}$
SRH bulk recombination	degraded state: B-Cz-Si: Refs. [Bot05, Rei03, Sch99b] non-degraded state: $\tau_\mathrm{n} = \tau_\mathrm{p}$, $E_\mathrm{d} = E_\mathrm{i}$
SRH surface recombination	phosphorus-diffused surfaces: Ref. [Alt02c] boron-diffused surfaces: Ref. [Alt06b]
Lifetime degradation in Al–p^+	Ref. [Alt09] with $f = 0.007$
Surface damage	Refs. [Ste10a, Ste10b, Ste10c] (Chapter 4)
Recombination at the a-Si:H/c-Si interface	SRH model of Refs. [Ste10d, Ste11b] (Chapter 5)
Optical simulation	
Solar spectrum	Standard AM1.5g
Optical dispersion relations	silicon from Ref. [Gre08], Al from Ref. [Shi80], SiN_x measured at ISFH

Table 7.2: Device simulation models and parameters, developed specifically for the simulation of Si solar cells [Ohr11].

According to SRH theory (Eq. (2.35)), τ_SRH is limited by τ_n in low-injection and by $\tau_\mathrm{n} + \tau_\mathrm{p}$ in high-injection. This causes τ_SRH to increase by a factor of 11 when going from low- to high-injection conditions. In Sec. 7.2.1.3, we will adjust the values for $[\mathrm{O_i}]$ and G to reproduce the measured I-V characteristics of the reference cell

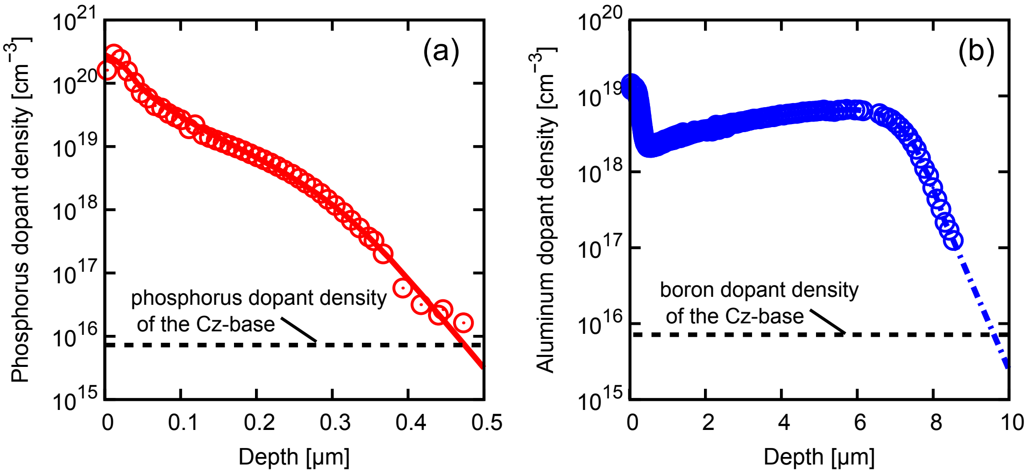

Figure 7.2: (a) ECV measurement (symbols) [Gat11c] and simulation (line) of the phosphorus emitter profile. The sheet resistivity is $R_{\mathrm{sh}} \approx 80\,\Omega/\Box$ (b) ECV measurement of the aluminum alloyed Al–p^+ BSF with $R_{\mathrm{sh}} \approx 23\,\Omega/\Box$. The dashed lines show the profile extrapolated to higher depths, which is used in the simulations.

with device-simulations.

7.2.1.2 Doping profiles

In the following, we will introduce the doping profiles used for the formation of the emitter and the BSF of the reference cell. Both profiles were measured using the electrochemical capacitance-voltage (ECV) technique, and are shown in Fig. 7.2. We characterize the electronic quality of these highly doped layers via the saturation current density $j_{0,i}$, where the index i = e, BSF stands for the emitter and the BSF, respectively. The $j_{0,i}$ values are obtained from Sentaurus-Device simulations of test-structures under steady-state open-circuit conditions according to Refs. [Alt02c, Sch01]. The equation for the emitter saturation current density $j_{0,\mathrm{e}}$ is given by [Alt02c]

$$j_{0,\mathrm{e}} = j_{\mathrm{p}}(z_{\mathrm{e}})\frac{n_{\mathrm{i,eff}}^2}{n(z_{\mathrm{e}})p(z_{\mathrm{e}}) - n_{\mathrm{i,eff}}^2}, \tag{7.4}$$

where z_{e} is a position in the quasi-neutral region of the base near the junction and j_{p} is the hole current across the junction. As long as the recombination inside the emitter layer is not too high, the value of $j_{0,\mathrm{e}}$ sensitively depends on the surface recombination velocity parameters at the strongly doped silicon surface. For the measured profile in Fig. 7.2(a), we use the parametrization of Ref. [Alt02c] to adjust the surface recombination velocity parameters S_{n} and S_{p} in dependence on the phosphorus concentration at the interface. The continuous line in Fig. 7.2(a) shows the emitter profile reproduced with process simulations using the model of Ref. [Dun92].

The BSF is formed by alloying the silicon at the rear side of the cell with aluminum. The resulting highly Al-doped layer is referred to as the Al–p^+ BSF. Its measured saturation current densities $j_{0,\mathrm{BSF}}$ are typically between 600 fA/cm^2 and 900 fA/cm^2 [Alt09]. The simulated BSF saturation current density $j_{0,\mathrm{BSF}}$ is determined from the simulation by [Alt02c]

$$j_{0,\mathrm{BSF}} = j_\mathrm{n}(z_\mathrm{BSF}) \frac{n_\mathrm{i,eff}^2}{n(z_\mathrm{BSF})p(z_\mathrm{BSF}) - n_\mathrm{i,eff}^2}, \tag{7.5}$$

where z_BSF is a position in the quasi-neutral region of the base near the junction and j_n is the electron current across the junction. Applying Eq. (7.5) to the simulation results of a symmetric test structure with the profile shown in Fig. 7.2(b) on both sides, yields $j_{0,\mathrm{BSF}}$ values which are much lower than the measured ones. The measured $j_{0,\mathrm{BSF}}$ values can be explained by a degraded SRH excess carrier lifetime τ_SRH in the bulk-region of the Al-doping, which may be due to the formation of Al–O complexes [Sch09]. In Ref. [Sch09], a parametrization was developed to describe lifetime measurements in Al-doped bulk material with dopant densities in the range $N_\mathrm{A} = 1 \times 10^{15} - 2 \times 10^{16}\,\mathrm{cm}^{-3}$, for which extremely low τ_SRH values were reported. In particular, a dependence of τ_SRH on the aluminum acceptor density N_A was observed. Extrapolation of the parametrization in Ref. [Sch09] to higher acceptor densities N_A yields far too low τ_SRH values to explain the typically measured $j_{0,\mathrm{BSF}}$ values of Al-alloyed BSFs. Thus, we introduced a correction factor $f < 1$ for the application to Al–p^+ layers [Alt09] in the model of Ref. [Sch09]:

$$\frac{1}{\tau_n} = \frac{1}{\tau_p} = 2.8339 \times 10^{-18} \frac{1}{\mathrm{s}} \left(\frac{N_\mathrm{A}}{1\,\mathrm{cm}^{-3}} \right)^{1.5048} f. \tag{7.6}$$

In the simulations, we adjust f to obtain satisfactory agreement of the simulated and measured $j_{0,\mathrm{BSF}}$ values (cf. Sec. 7.2.1.3). The reason for $f < 1$ in Al–p^+ layers can be explained as follows. Wafer doping with Al atoms in the melt is an equilibrium process. The Al-BSF formation, in contrast, is achieved during a short high-temperature step (firing step) at $T \approx 900\,^\circ\mathrm{C}$ for only a few seconds [e.g. Alt09, Gat11c]. It may be assumed that this formation process is a non-equilibrium process, and hence, the formation rate of Al–O complexes may be reduced compared to the equilibrium process.

Note that a very recent approach [Rüd11, to be published] suggests incomplete ionization in combination with a reduced SRH lifetime as an explanation of the saturation current densities in Al-alloyed Cz-Si. We acknowledge that this model provides probably a better approximation to measurements than the model in Eq. (7.6). However, as we do not vary the BSF during our simulations, using solely Eq. (7.6) describes $j_{0,\mathrm{BSF}}$ sufficiently well in our simulations.

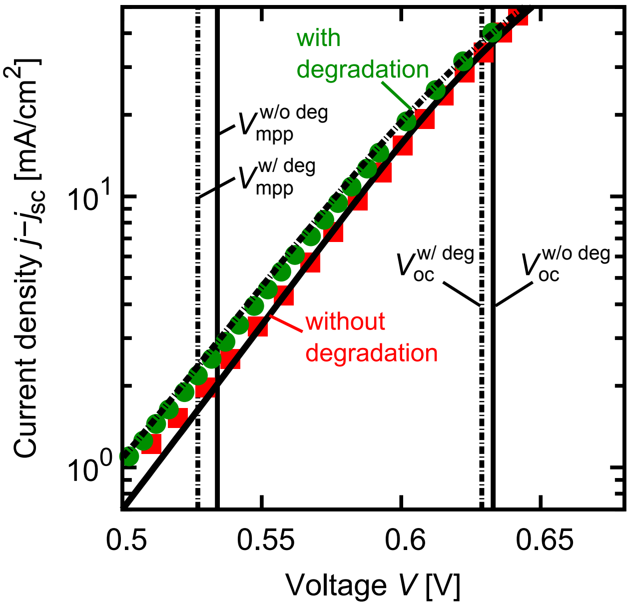

Figure 7.3: I-V characteristics of the reference cell in Fig. 7.1(a) with the parameters given in Table 7.1. The measured (symbols) and simulated (lines) I-V characteristics are shifted by $-j_{\mathrm{sc}}$ to positive current values. The degraded state is indicated with red squares and a continuous line, and for the degraded state green circles and a dashed line are used. The simulation parameters are listed in Tables 7.1 and 7.2.

7.2.1.3 Reproduction of the measured *I*-*V* characteristics

We reproduce the measured I-V characteristics of the reference cell by means of SENTAURUS-DEVICE simulations. The I-V curve of a solar cell is typically characterized by the values of the short-circuit current-density j_{sc}, the open-circuit voltage V_{oc}, the fill factor FF, and the cell efficiency η under 1 sun illumination (cf. Sec. 2.4).[3] These I-V parameters are listed in Table 7.3 for the measured and simulated I-V curves before and after light-degradation,[4] shown in Fig. 7.3. Excellent agreement between the measured and simulated I-V parameters is found.

All cell specific simulation parameters are listed in Table 7.1. The general model parameters are summarized in Table 7.2. For most quantities, parametrized models (see Table 7.2) or measurements exist. Two quantities remain undetermined and need to be adapted in the simulation in order to obtain satisfactory agreement with the measurements: τ_{n} in the base in the degraded state with the parametrization in Eq. (7.1), and τ_{n} in the BSF with the parametrization in Eq. (7.6).

The degraded I-V curves are reproduced best with $\tau_{\mathrm{n}} = 58\,\mu\mathrm{s}$ which can be obtained by using $[\mathrm{O_i}] = 7 \times 10^{17}\,\mathrm{cm}^{-3}$ and $G = 2.17$ in Eq. (7.1) (cf. Table 7.1) in agreement with literature values [Bot05, Lim10]. For the non-degraded base, we choose $\tau_{\mathrm{n}} = \tau_{\mathrm{p}} = 280\,\mu\mathrm{s}$ according to measurements. The degraded lifetime in the Al–p^+ BSF is adjusted by fits to the I-V curve. We obtain best agreement between measurement and simulation for $f = 0.007$ in Eq. (7.6), resulting in $j_{0,\mathrm{BSF}} = 580\,\mathrm{fA/cm^2}$. The emitter saturation current density $j_{0,\mathrm{e}}$ for the

---

[3] 1 sun corresponds to the illumination of an AM1.5G spectrum with an intensity of $100\,\mathrm{mW/cm^2}$.

[4] The degraded cells were illuminated for 24 hours with a halogen lamp.

cell-type and materials		j_{sc} [mA/cm^2]	V_{oc} [mV]	j_{mpp} [mA/cm^2]	V_{mpp} [mV]	η [%]	*FF* [%]
reference*	B-Cz-Si, non-deg.	37.3	633.0	34.9	536.3	18.7	79.4
reference	B-Cz-Si, non-deg	37.1	633.0	35.1	534.1	18.7	79.7
reference*	B-Cz-Si, deg.	37.1	628.8	34.9	527.1	18.3	78.8
reference	B-Cz-Si, deg.	37.0	628.9	34.6	526.9	18.3	78.5
LBSF	B-Cz-Si, sim., non-deg.	38.2	654.8	35.6	529.9	18.9	75.3
LBSF	B-Cz-Si, sim., deg.	37.9	647.8	35.0	510.0	17.8	72.5
LBSF+selem	B-Cz-Si, non-deg.	38.6	677.2	36.1	555.8	20.1	76.8
LBSF+selem	B-Cz-Si, deg.	38.3	669.7	35.4	524.8	18.6	72.4
LBSF+selem	Ga-Cz-Si	38.7	688.1	36.4	571.5	20.8	78.3
LBSF+selem	P-Cz-Si	38.5	676.8	36.0	558.4	20.1	77.0
LBSF+selem	Ga-Cz-Si, a-Si:H(i) pass., as deposited	38.6	691.0	36.2	569.1	20.6	77.3
LBSF+selem	Ga-Cz-Si, a-Si:H(i) pass., after 15 month of light-exposure	38.6	671.4	36.4	549.4	20.0	77.3

Table 7.3: Simulated and measured (*) *I*-*V* parameters for the investigated cell designs without an SDR at an illumination intensity of 1 sun illumination.

phosphorus-diffusion profile in Fig. 7.2(a) is obtained by applying Eq. (7.4) to the simulation results, using S_{n} and S_{p} according to Ref. [Alt02c] and band-gap narrowing according to Ref. [Alt03]. We obtain $j_{0,\mathrm{e}} = 180\,\mathrm{fA/cm^2}$ which is in reasonable agreement with measured values around $j_{0,\mathrm{e}} \approx 200\,\mathrm{fA/cm^2}$.
Note that these adjusted parameters have been confirmed by reproducing additional cells with locally contacted rear side in Ref. [Ste11c].

7.2.2 PERL cells

This section deals with the PERL cell designs shown in Figs. 7.1(b) and 7.1(c). We introduce the parameters and models used for the LBSF+selem cell. The LBSF cell is modeled with the same parameters as the reference cell in Sec. 7.2.1. Finally, the simulated cell results are presented and discussed.

7.2.2.1 Excess carrier lifetimes for different substrate dopant species

For the LBSF+selem cell in Fig. 7.1(c) we use three different dopant species of the Cz-Si base: boron, gallium and phosphorus. In Sec. 7.2.1.1, the degradation of the SRH excess carrier lifetime in B-Cz-Si after light-exposure was discussed. The corresponding injection-dependent τ_{eff} values (according to Eq. (2.41)) are displayed in Fig. 7.4. The strong reduction of τ_{eff} in the degraded state at low excess carrier

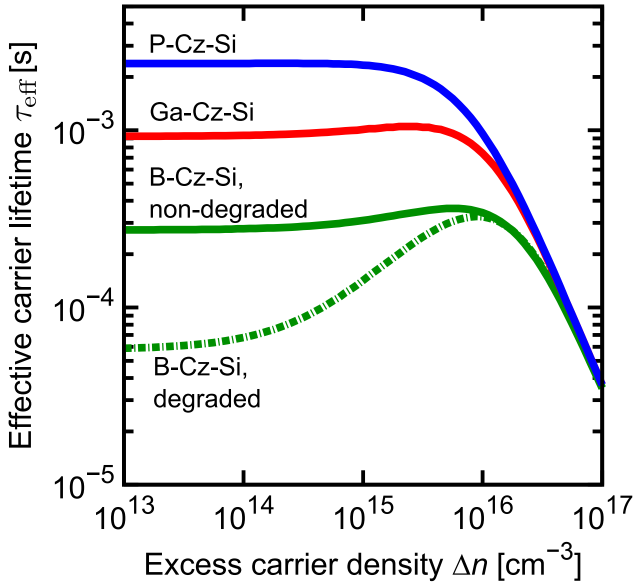

Figure 7.4: Simulated injection dependent effective excess carrier lifetimes for Cz-Si doped with either boron, gallium or phosphorus, cf. Table 7.1. For B-Cz-Si, also the lifetime after light-induced degradation is shown.

densities Δn is clearly visible. Figure 7.4 also shows the simulated $\tau_{\text{eff}}(\Delta n)$ characteristics of Ga-Cz-Si and P-Cz-Si. Although Ga-Cz-Si contains a high concentration of interstitial oxygen $[\text{O}_\text{i}]$, this material has much higher and stable τ_{SRH} values close to 1 ms for similar substrate resistivities than its boron-doped counterpart. This is explained by the fact that in Ga-Cz-Si, oxygen does not form significantly recombination active defects in contrast to the B–O complex formed in B-Cz-Si [Glu99b, Glu01]. This also explains why no significant degradation of τ_{SRH} in Ga-Cz-Si is observed. We further consider a P-Cz-Si base, for which high and stable lifetimes around 3.5 ms have been reported [Sch07a] in agreement with Fig. 7.4.

7.2.2.2 Selective emitter

For the selective emitter of the LBSF+selem cell, we use implanted profiles which were modeled with SENTAURUS-PROCESS [SP], as described in Ref. [Ohr11]. In particular, ion energies of 40 keV and a dose of $5 \times 10^{14}\,\text{cm}^{-2}$ were used for the emitter underneath the non-contacted area, and 10 keV with a dose of $2 \times 10^{16}\,\text{cm}^{-2}$ were employed for the emitter underneath the contacts. The resulting $j_{0,\text{e}}$ values, obtained from Eq. (7.4) with S_n and S_p according to Ref. [Alt02c] and band-gap narrowing [Alt03], are 13 fA/cm^2 and 80 fA/cm^2 for the non-contacted emitter and the contacted emitter, respectively. These very low $j_{0,\text{e}}$ values are used to make the influence of surface damage visible (see Sec. 7.4 below).

7.2.2.3 Cell results

The simulated I-V parameters of the LBSF cell and the LBSF+selem cells (cf. Figs. 7.1(b) and 7.1(c)) are listed in Table 7.3. For all cell designs containing an

LBSF (PERL cells), we observe an improvement in both V_{oc} and j_{sc} compared to the reference cell. Further, V_{oc} and j_{sc} of the LBSF+selem cells are enhanced compared to the LBSF cells. V_{oc} reaches the highest value for a Ga-Cz-Si base, whereas it is similar for B-Cz-Si and P-Cz-Si. However, the fill factor FF for the PERL cells is reduced compared to the reference cell. This effect is strongest for the LBSF cell in the degraded state.

In order to understand the behavior of the I-V characteristics, we perform a loss analysis in the following Section 7.3.

7.3 Loss analysis

The aim of this chapter was to investigate the influence of surface damage on the performance of various cell designs. Before being able to understand the effects of an SDR on the I-V characteristics, it is helpful to understand the behavior of the cells under investigation without an SDR. Therefore, we perform a loss analysis of the I-V curves in the following. In this loss analysis, we carefully separate the resistive losses from the recombination losses. However, as both these losses influence the I-Vcurve, separating them is not a trivial task.

In the following, we begin with the discussion of the reference cell.

7.3.1 Resistive losses

From the I-V curves, the lumped series resistance $R_{\text{s}}(V)$ is commonly extracted as a function of voltage V in two different ways: either by comparing the I-V curve at 1 sun illumination with the j_{sc}-V_{oc} curve [Wol63],[5] or by comparing two I-V curves, illuminated at slightly different light intensities, called the double-light-level (dll) method [Alt96, Han67, Wol63]. These methods are applied to the I-V measurements of the reference cell, as shown in Fig. 7.5. We focus in the following on the behavior of the lumped series resistance R_{s} between the maximum-power-point voltage V_{mpp} and V_{oc} because for these voltages the influence of R_{s} on the I-V parameters is most significant. In this voltage range, the j_{sc}-V_{oc} method and the dll method yield equal R_{s} values for the non-degraded cell (cf. Fig. 7.5(a)). However, in the degraded state (Fig. 7.5(b)), the value of R_{s} at V_{mpp}, extracted using the j_{sc}-V_{oc} method is significantly lower than the value obtained from the dll method. In the following, we explain why the j_{sc}-V_{oc} method underestimates the lumped series resistance R_{s} in the degraded state. The j_{sc}-V_{oc} curve is recorded by ramping the light intensity. Then, the series resistance is obtained by comparing the j_{sc}-V_{oc} curve, shifted by j_{sc} of the I-V curve, at 1 sun illumination with the I-V curve at 1 sun illumination at equal

---

[5] The j_{sc}-V_{oc} curve is obtained by plotting j_{sc} versus V_{oc}, measured at different light intensities.

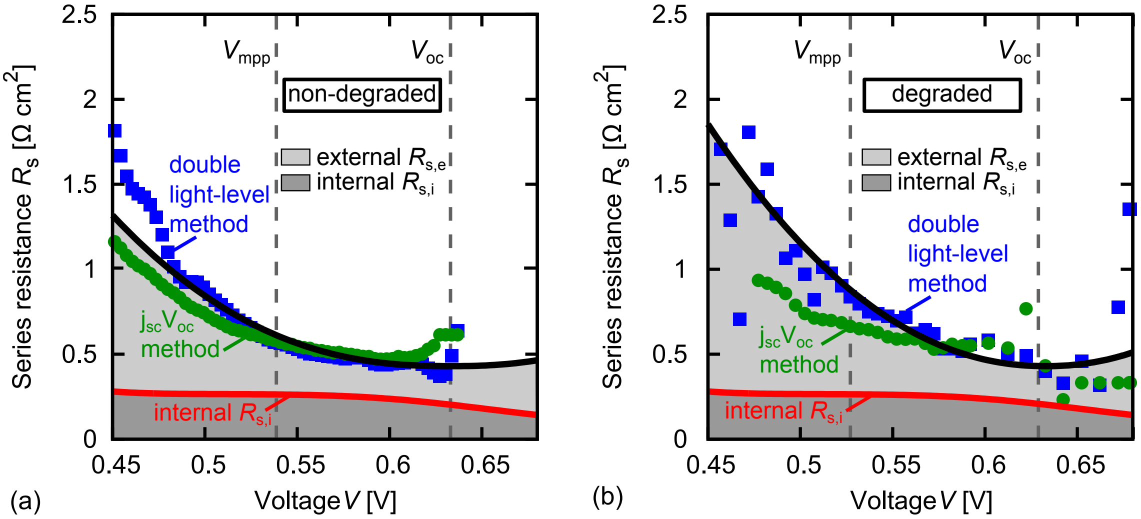

Figure 7.5: The lumped series resistance of the reference cell extracted from the I-V curve at 1 sun illumination using the double-light-level method (blue squares) and the j_{sc}-V_{oc} method (green circles). The blue and green lines are fits to the measurements, and the red line shows the internal series resistance $R_{s,i}$ extracted from the simulation. The contributions of the internal series resistance $R_{s,i}$ are highlighted in dark-gray, and the external series resistance losses $R_{s,e}$ are highlighted in light-gray. The case for the non-degraded B-Cz-Si base is plotted in (a), and for the degraded state in (b).

values of the current densities. For voltages below V_{oc}, the light intensity at which these currents are extracted is lower for the j_{sc}-V_{oc} curve than for the I-V curve at 1 sun illumination. Thereby, the difference in the light intensities increases with decreasing voltage. Because the effective charge carrier lifetime τ_{eff} in degraded B-Cz-Si decreases with decreasing light intensity (cf. Fig. 7.4), the value of R_s obtained by comparing the j_{sc}-V_{oc} curve with the I-V curve underestimates the real series resistance. These observations indicate that in general, care must be taken when applying the j_{sc}-V_{oc} method whenever injection-dependent effects are present.

We extract the *internal* series resistance $R_{s,i}$, which is determined by the contributions of the silicon substrate to the lumped series resistance R_s, from the simulations using the dll method. Therefore, simulations are performed in which the *external* series resistance losses $R_{s,e}$, i.e. series resistance losses in the metalization and at the contacts, are neglected. The obtained $R_{s,e}$-free I-V curves are compared to measurements by correcting the simulated voltage V_{sim} via:

$$V_{corr} = V_{sim} + R_{s,e}(V_{sim})j(V_{sim}). \tag{7.7}$$

The external and the internal contributions to the lumped series resistance, $R_{s,e}$ and $R_{s,i}$, respectively, are shown in Fig. 7.5. While $R_{s,i}$ is rather independent of the applied voltage V, $R_{s,e}$ increases towards lower voltages. This increase is due to changes in the voltage profiles in the metal fingers which are influenced by the voltage applied at the contacts.

Note that for cells with locally contacted rear (e.g. Figs. 7.1(b) and 7.1(c)) both $R_{\mathrm{s,i}}$ and $R_{\mathrm{s,e}}$ increase [Ste11c]. $R_{\mathrm{s,i}}$ is enhanced due to current losses in the substrate, because the (lateral) path length for the charge carriers to the contact increases. Lower substrate resistivities may reduce this problem. $R_{\mathrm{s,e}}$ is enhanced due to losses in the metalization at the rear and higher contact resistivities, due to experimental difficulties with the contact formation [Gat11b]. For the LBSF+selem cell we expect a reduced external series resistance $R_{\mathrm{s,e}}$ compared to the LBSF cell due to an improved contact resistance at the emitter fingers which is caused by the highly doped emitter underneath the contacts.

7.3.2 Recombination losses

We express the series-resistance-free recombination losses as current densities $qR(V)$, as shown for the reference cell in Fig. 7.6(b), where R is the recombination rate in the whole cell or in local regions. Three main features become apparent: (i) In the non-degraded case, the emitter losses and the losses at the rear side dominate the overall losses between V_{mpp} and V_{oc}, whereas the contributions of the base are comparably low. (ii) In the degraded case, the SRH losses in the Cz-base material contribute to a similar amount to the recombination currents as the emitter and the rear side. (iii) The SRH losses in the degraded Cz-Si base increase sub-exponentially between V_{mpp} and V_{oc}. The reason for (iii) is that the excess carrier lifetime in B-Cz-Si strongly increases with higher injection levels [Bot05, Rei03, Sch99b], i.e. toward higher voltages (cf. Fig. 7.4). Note that improving both the emitter and the rear side to an extent that the losses in the base dominate the overall losses, leads to a bent *I*-*V* curve and, accordingly, to a reduced fill factor *FF*. We found in further simulations (not presented) that this saturation effect increases with the wafer resistivity, and hampers efforts to reach efficiency levels significantly higher than about 19.4 % after degradation for standard Cz-material if no further design optimization is applied.

The characteristic *I*-*V* parameters obtained from the simulation of the different cell designs (cf. Sec. 7.1) are summarized in Table 7.3. Here, we explain the observation made in Sec. 7.2.2.3 regarding the influence of the cell design on the *I*-*V* parameters by analyzing both resistive losses and recombination losses. Figure 7.7 shows the recombination currents of the PERL cells, separated into the different device regions. Changing the rear side geometry from fully metalized (reference cell, cf. Fig. 7.6) to locally contacted and rear-side passivated (LBSF cell), strongly reduces the recombination currents at the rear side (cf. Fig. 7.7(a)), which leads to an improved open-circuit voltage V_{oc}. In addition, the enhanced reflectivity of light at the

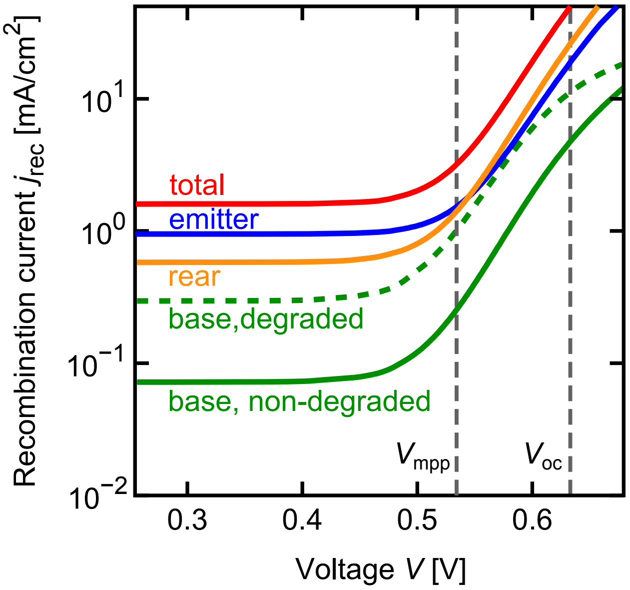

Figure 7.6: Simulated recombination currents, separated in the different device regions, of the non-degraded reference cell in Fig. 7.1(a) with the simulation parameters given in Table 7.1. The loss-currents of the same cell with the base in the degraded state are plotted in addition by dashed lines.

dielectric at the rear side, results in an enhanced short-circuit-current density $j_{\rm sc}$. However, the fill factor FF of the LBSF cell is reduced compared to that of the reference cell. This effect originates mainly from two contributions. First, the enhanced resistive losses (cf. Sec. 7.3.1) cause the fill factor to decrease. Second, for the degraded cell, the recombination current in the base contributes significantly to the total losses. This reduces the fill factor further due to the saturation behavior of the recombination currents in the Cz-base. Due to this small fill factor, only a moderate improvement in the cell efficiency η is achieved in the non-degraded state of the LBSF cell. In the degraded state, the cell efficiency η is even reduced compared to the reference cell.

For the LBSF+selem cells with a p-Si base (B-Cz-Si and Ga-Cz-Si), the emitter loss currents, displayed in Figs. 7.7(b)–7.7(c), are reduced compared to the LBSF cell. This causes both $V_{\rm oc}$ and $j_{\rm sc}$ to improve. The enhanced $j_{\rm sc}$ and $V_{\rm oc}$ are mainly due to the reduced Auger losses in the emitter. In addition, $V_{\rm oc}$ is increased due to the reduced surface recombination velocity resulting from the lower surface dopant density [Alt02c]. In case of B-Cz-Si, shown in Fig. 7.7(b), the base dominates the overall recombination losses. Using Ga-Cz-Si with $\tau_{\rm n} = \tau_{\rm p} = 1\,\text{ms}$ as the wafer material, reduces the recombination contribution from the base, as displayed in Fig. 7.7(c). Consequently, the contributions of all three device regions (emitter, rear and base) contribute to a similar amount to the losses between $V_{\rm mpp}$ and $V_{\rm oc}$. As a consequence, $V_{\rm oc}$ is increased. For the n-Si base (P-Cz-Si), displayed in Fig. 7.7(d), $V_{\rm oc}$ takes values similar to that of the non-degraded B-Cz-Si cell, even though $\tau_{\rm n} = \tau_{\rm p} = 3.5\,\text{ms}$ is improved by more than an order of magnitude compared to the B-Cz-Si base with $\tau_{\rm n} = \tau_{\rm p} = 280\,\mu\text{s}$. These comparably low $V_{\rm oc}$ values result from the enhanced recombination at the boron-doped emitter surface [Alt06b]. Note that for an optimized

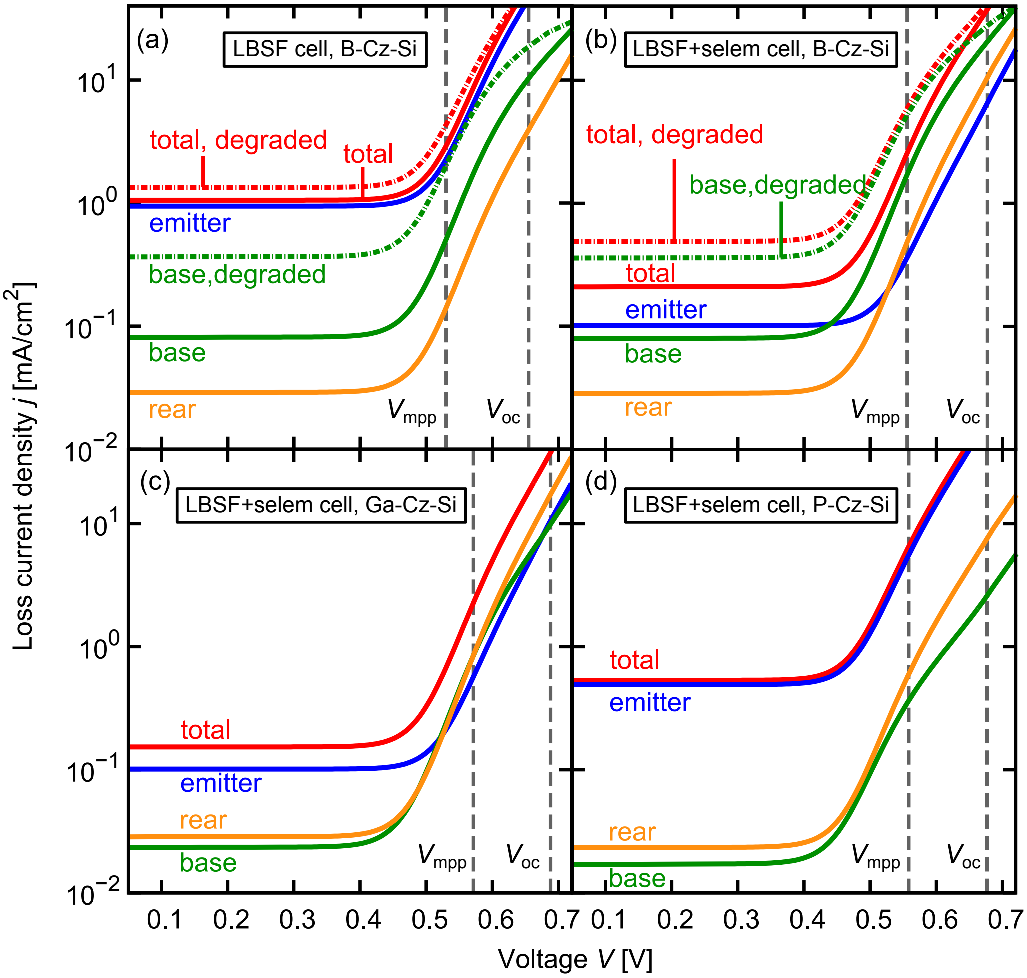

Figure 7.7: Simulated recombination currents of (a) the LBSF cell and (b)–(c) the LBSF+selem cell with (b) a boron-doped base (B-Cz-Si), (c) a gallium-doped base (Ga-Cz-Si), and (d) a phosphorus-doped base (P-Cz-Si). The vertical dashed lines correspond to the values of V_{mpp} and V_{oc} of the non-degraded cells. All parameters are chosen according to Table 7.1.

emitter profile, a strongly improved V_{oc} is expected for P-Cz-Si.
The increase in the fill factor for the LBSF+selem cells compared to the LBSF cell is due to the improved front-contact series resistance at the highly doped emitter, the reduced Auger losses in the emitter and the reduced surface recombination at the emitter surface.

We also investigate a variant of the LBSF+selem cell using a-Si:H(i) instead of SiN$_x$ for the rear side passivation. Therefore, we implement the approximate SRH model for recombination via amphoteric defects at the a-Si:H/c-Si interface (cf. Chapter 5) in the device-modeling tool SENTAURUS-DEVICE. This model is applied to an LBSF+selem cell with a Ga-doped base and an a-Si:H(i) passivated rear. The parameters are chosen according to the parameters used in Sec. 5.2.4.3 to reproduce the measured S_{eff} values of the non-degraded a-Si:H(i)/c-Si(p) interface. For the DB density at the interface, Gaussian distributions (Eq. (5.3b)) are chosen and the volume DOS in a-Si:H is modeled with the extended DPM of Ref. [Pow93] (cf. Sec. 5.1.1).

For the case of a-Si:H passivation, the loss currents at the rear depend on the time of light-exposure of the a-Si:H layers, because the passivation quality reduces due to the Staebler-Wronski [Pla08, Sta77, Stu85, Stu86] effect, treated in Sec. 5.2.4.3. This has impact on the performance of a-Si:H passivated cells. For the as-deposited state of a-Si:H(i), the recombination at the rear side is low and the simulated V_{oc} is enhanced by 3 mV compared to a cell passivated with SiN_x. However, the fill factor FF and the cell efficiency η are slightly lower than the values obtained for SiN_x. This can be explained by the injection dependent trapped charges at the a-Si:H/c-Si interface. After 15 month of light-exposure, the effective surface recombination velocity S_{eff} at the a-Si:H(i)/c-Si interface is strongly increased, as shown in Fig. 5.12(a) of Chapter 5. This leads to a reduction in V_{oc} by 20 mV, causing the cell efficiency to reduce by 0.6 % in total, cf. Table 7.3.

In summary, we have identified the major loss mechanisms in the different PERL cell designs, introduced in Sec. 7.1. Due to the improved rear side, these cells yield both higher V_{oc} and higher j_{sc} values compared to the fully metalized reference cell. When using a selective emitter, we found that the base of B-Cz-Si dominates the total recombination losses. To reach efficiencies larger than 20.1 % in the non-degraded state (18.6 % in the degraded state), the base material needs to be improved. Using, for example, a gallium-doped substrate may increase the efficiency up to approximately 20.8 %. We further identified the series resistance losses as a major loss mechanism which has impact on the fill factor of the PERL cells. Increasing the substrate resistivity and improving the metalization at the rear side may help to reach higher fill factors, and thereby, higher conversion efficiencies.

In addition, we implemented the approximate SRH model for amphoteric defect recombination into SENTAURUS-DEVICE. Thereby, we could show that the Staebler-Wronski effect strongly reduces the V_{oc} and therewith the cell efficiency of a-Si:H passivated solar cells. After 15 month of light exposure, the simulated cell efficiency of a Ga-Cz-Si LBSF+selem cell decreases from 20.6 % to 20.0 %.

Having identified the main loss mechanisms of the PERL cells, allows us to make predictions regarding the influence of an SDR at the rear side of the cells on the cell performance. The strongest influence of the SDR may be expected for the Ga-Cz-Si LBSF+selem cell, because the contribution of the loss currents at the rear side relative to the total recombination current is highest for this cell design. We further

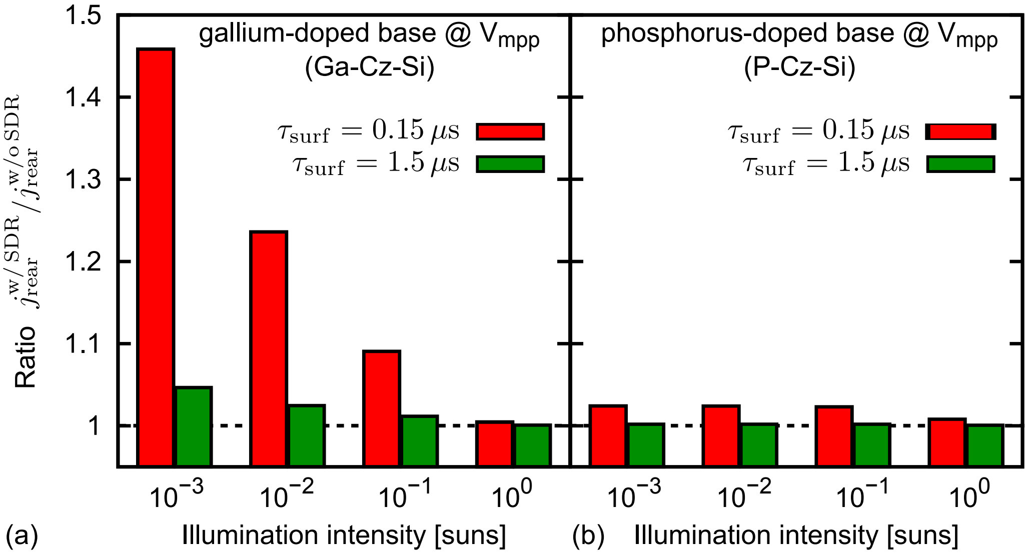

Figure 7.8: Ratio $j_{\mathrm{rear}}^{\mathrm{w/\,SDR}}/j_{\mathrm{rear}}^{\mathrm{w/o\,SDR}}$ of the simulated recombination currents with and without surface damage at the rear side of two LBSF+selem cells. The cells are made on (a) a Ga-Cz-Si and (b) a P-Cz-Si substrate, and the recombination currents are extracted at the V_{mpp} of the cells without an SDR.[6] Red columns correspond to an SDR with $\tau_{\mathrm{surf,n}} = 0.15\,\mu\mathrm{s}$, and green columns represent an SDR with $\tau_{\mathrm{surf,n}} = 1.5\,\mu\mathrm{s}$ ($\tau_{\mathrm{surf,n}}/\tau_{\mathrm{surf,p}} = 4 \times 10^{-3}$). The dashed lines indicate the case where $j_{\mathrm{rear}}^{\mathrm{w/\,SDR}} = j_{\mathrm{rear}}^{\mathrm{w/o\,SDR}}$, i.e. where the SDR has no influence. All parameters are chosen according to Table 7.1.

expect a rather negligible influence of the SDR for B-Cz-Si cells in the degraded state, because here the base dominates strongly. The influence of surface damage on the I-V parameters at different light intensities will be treated quantitatively in the following Section 7.4.

7.4 Influence of surface damage on cell performance

By standard, solar cells are characterized at 1 sun illumination. However, at typical outdoor operation conditions, the light intensity is often weaker than the standard. Here, we investigate the influence of surface damage on the cell performance at reduced illumination levels by means of device-simulations. Therefore, we use the parameters obtained from fitting the SiN$_x$ samples of Ref. [Ker02b], cf. Table 4.1 in Chapter 4. Thereby, degraded SRH lifetime parameters at the interface of $\tau_{\mathrm{surf,n}} = 0.15\,\mu\mathrm{s}$ and $\tau_{\mathrm{surf,n}}/\tau_{\mathrm{surf,p}} = 4 \times 10^{-3}$ were obtained. Here, we consider both $\tau_{\mathrm{surf,n}} = 0.15\,\mu\mathrm{s}$ and a tenfold improved lifetime parameter of $\tau_{\mathrm{surf,n}} = 1.5\,\mu\mathrm{s}$. The ratio $\tau_{\mathrm{surf,n}}/\tau_{\mathrm{surf,p}} = 4 \times 10^{-3}$ is chosen the same for both $\tau_{\mathrm{surf,n}}$ values.

In Fig. 7.8, the influence of the SDR on the simulated recombination currents at the rear side, extracted at V_{mpp},[6] is compared for two LBSF+selem cells, made on a Ga-Cz-Si and a P-Cz-Si substrate, respectively. This influence is quantified by the ratio $j_{\mathrm{rear}}^{\mathrm{w/\,SDR}}/j_{\mathrm{rear}}^{\mathrm{w/o\,SDR}}$ of the recombination currents with and without SDR at the rear side of the cells. At 1 sun illumination, the surface damage does not significantly contribute to the recombination current, because at the MPP there is $\Delta n > 3 \times 10^{14}\,\mathrm{cm}^{-3}$. At this injection density, the differences between the S_{eff} curves with and without SDR are small (cf. Fig. 4.5 in Sec. 4.1). Already at 0.1 sun illumination, the excess carrier density Δn at the MPP is well below $10^{13}\,\mathrm{cm}^{-3}$. For such low Δn, surface damage underneath the SiN_x rear side passivation influences S_{eff} of the rear side of p-Si wafers significantly, as discussed in Chapter 4 (see Fig. 4.5). Thus, a significantly increased recombination current is observed for p-Si cells with surface damage ($\tau_{\mathrm{surf,n}} = 0.15\,\mu\mathrm{s}$) when going to low illumination intensities, as shown in Fig. 7.8(a). In contrast, a negligible influence of surface damage and, in particular, no injection dependence is observed for n-Si wafers in Fig. 7.8(b). This behavior is expected, since no injection dependence of S_{eff} is observed for n-Si in Fig. 4.5 in Sec. 4.1. In addition, it is apparent from the green bars for $\tau_{\mathrm{surf,n}} = 1.5\,\mu\mathrm{s}$ in Fig. 7.8, that an improvement of the lifetime by a factor of mere ten (corresponding to a tenfold reduced defect density at the interface), reduces the influence of the SDR to an extent that it becomes negligible.

The SDR has only major influence on the performance of PERL cells if the rear side contributes significantly to the overall recombination rate. The injection-dependent influence of the SDR on the characteristic I-V parameters (η, FF, $V_{\mathrm{oc}}, j_{\mathrm{sc}}$) for $\tau_{\mathrm{surf,n}} = 0.15\,\mu\mathrm{s}$ is compared for the examples of Fig. 7.7 in the left column of Fig. 7.9. For the LBSF cell – in particular in the degraded state – the losses in the emitter and the base clearly dominate the recombination losses at the rear (cf. Fig. 7.7(a)). The rear side gains of influence when improving the emitter (cf. Fig. 7.7(b)) or, additionally, the SRH lifetime in the wafer material (cf. Fig. 7.7(c)). Thus, for the p-Si substrates investigated in Fig. 7.7, the strongest influence of an SDR on the cell efficiency is observed for the LBSF+selem cell made on a Ga-Cz-Si wafer, as displayed in Fig. 7.9(a). The relative losses in efficiency η are 2.5 % at 0.1 sun and 9.7 % at 0.001 sun. Among the p-Si substrates, the SDR has the smallest impact on the LBSF cell in the degraded state with relative efficiency losses of 0.8 % at 0.1 sun and 2.6 % at 0.001 sun, cf. Fig. 7.9(a). As expected from Fig. 7.8, no significant injection dependence is observed for P-Cz-Si substrates, and the relative loss in η compared to the case without SDR is only 0.35 % for $\tau_{\mathrm{surf,n}} = 0.15\,\mu\mathrm{s}$. We remark that the efficiency losses are mainly due to the reduced V_{oc} caused by the enhanced recombination at the rear side, cf. Fig. 7.9(g). The short circuit current density j_{sc}

---

[6] The V_{mpp} of the cell without SDR is taken as the reference voltage.

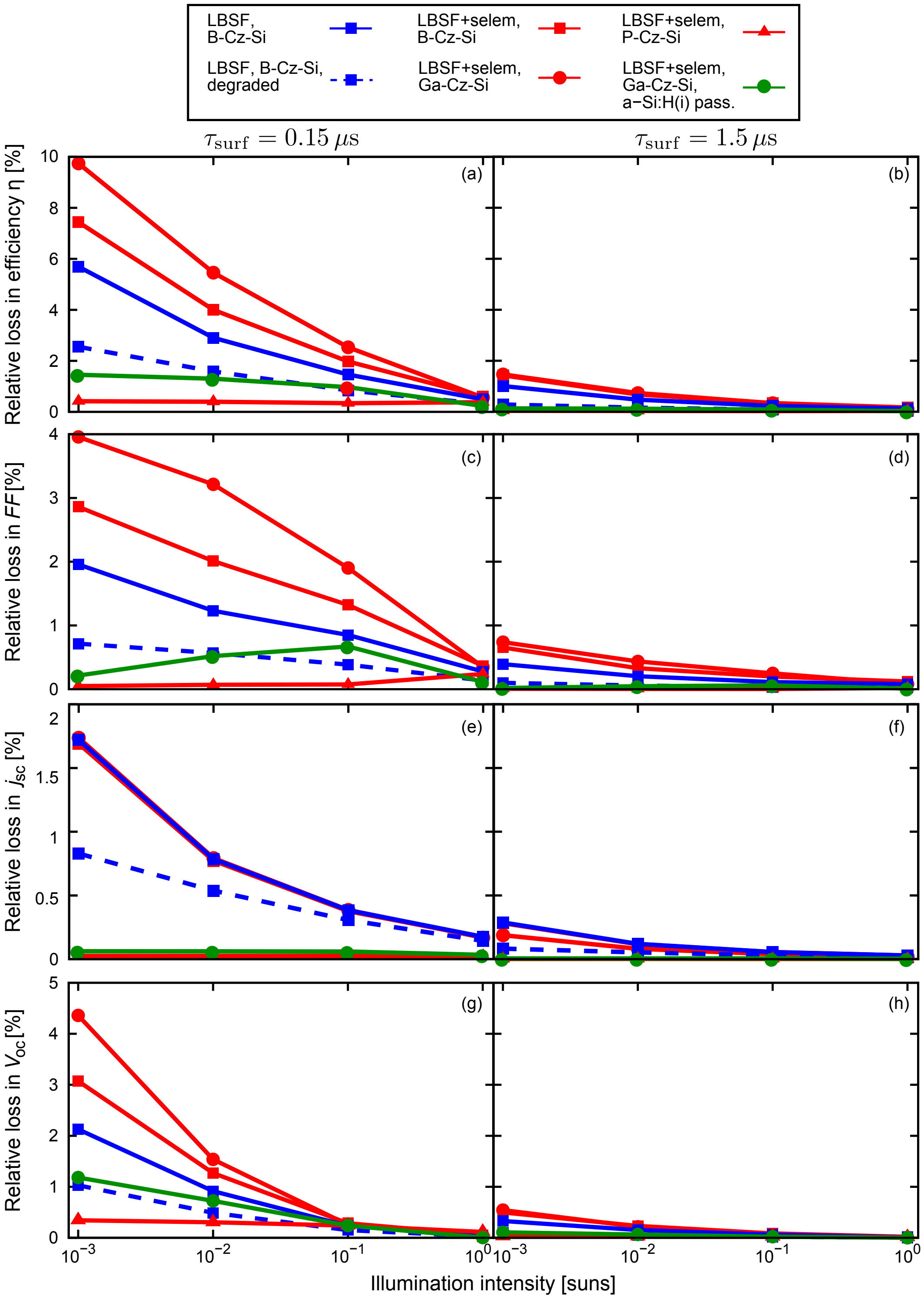

Figure 7.9: Simulated influence of the SDR on (a),(b) η, (c),(d) FF, (e),(f) $j_{\rm sc}$ and (g),(h) $V_{\rm oc}$ relative to the case without SDR for different cell designs (see text and legend) in dependence on the illumination level. Two values of $\tau_{\rm surf,n}$ in Eq. (4.6) are used: $\tau_{\rm surf,n} = 0.15$ µs (left column) and $\tau_{\rm surf,n} = 1.5$ µs (right column). The remaining parameters are chosen according to Table 7.1.

is affected only marginally by the SDR, as displayed in Fig. 7.9(e).
By simulations with an improved lifetime at the interface $\tau_{\mathrm{surf,n}} = 1.5\,\mu\mathrm{s}$, we can confirm the predictions that improving the lifetime at the interface by a factor of 10, reduces the influence of the SDR to an extent that it becomes negligible, as shown in the right column of Fig. 7.9. For all investigated cell-designs, the relative losses in efficiency remain below 1.5 % down to illumination intensities of 0.001 sun. In Sec. 4.2 it was observed that the influence of surface damage increases with decreasing light intensity and increasing substrate resistivity. This was confirmed by device simulations (not presented). While an improvement of $\tau_{\mathrm{surf,n}}$ by a factor of 10 is sufficient to considerably reduce S_{eff} for the $2.5\,\Omega$cm substrate used in the simulations presented here, the same improvement of $\tau_{\mathrm{surf,n}}$ is not enough to reduce recombination in the SDR in a $10\,\Omega$cm substrate. Hence, care must be taken when using SiN_x passivation layers for lowly doped (i.e. highly resistive) substrates.
Finally, we investigate the influence of the SDR on an as-deposited a-Si:H passivated LBSF+selem cell with a Ga-Cz-Si base. Arguing as in Sec. 5.3, we use a damage depth of $z_{\mathrm{deg}} = 0.055\,\mu\mathrm{m}$ in Eq. (4.6). The simulations are made for a Ga-Cz-Si substrate to construct a "worst case scenario". The influence of a possible damage underneath the a-Si:H layer on cell efficiency is shown in Fig. 7.9 along the other curves. The efficiency losses remain for all illumination intensities below 1.5 %, indicating that surface damage is indeed negligible in case of a-Si:H and thus, can be neglected in device simulations. This was explained in Chapter 5 as a consequence of the low interface charge density at the a-Si:H/c-Si interface.

To conclude, by means of device simulations, we were able to support the predictions made in Chapters 4 and 5. We showed that the influence of surface damage on the I-V parameters (j_{sc}, V_{oc}, FF and η) is the more significant the stronger the contribution of the rear side to the total recombination losses. In particular, we found that the influence of an SDR is strongest for an LBSF+selem cell with a Ga-Cz-Si base. The simulations showed further that the influence of surface damage is negligible in case of n-Si substrates which was explained in Chapter 4 by the accumulation conditions close to the surface. Also, for a-Si:H(i) passivated substrates, the simulations reveal no significant influence of the surface damage on the I-V parameters, which we attributed to the low surface charge density at the a-Si:H(i)/c-Si interface in Chapter 5.

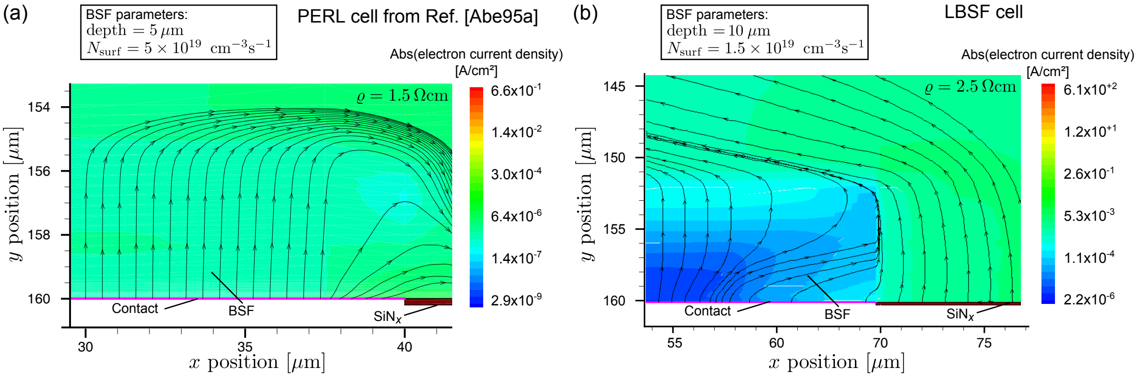

Figure 7.10: Simulated electron current flows between the p-type contact and the inversion region underneath the SiN$_x$ passivation layer in p-Si. (a) PERL cell from Ref. [Abe95a]; the wafer resistivity is $\varrho = 1.5\,\Omega$cm and the BSF modeled using a Gaussian function with $N_{\mathrm{surf}} = 5 \times 10^{19}\,\mathrm{cm}^{-3}$ and a depth of 5 μm. (b) LBSF cell; the wafer resistivity is $\varrho = 2.5\,\Omega$cm and the measured Al-alloyed BSF shown in Fig. 7.2(b) with $N_{\mathrm{surf}} = 1.5 \times 10^{19}\,\mathrm{cm}^{-3}$ and a depth of 10 μm is used. The parameters at the SiN$_x$/c-Si parameters are chosen according to Table 7.1. Note that the electric current density is plotted, so the electrons flow in the direction opposite to the arrows.

7.5 Parasitic shunting

Dauwe *et al.* [Dau02a] observed parasitic shunting on 1.5 Ωcm p-Si, passivated with SiN$_x$. The authors suggest the incorporation of a local BSF as in the LBSF cell or the LBSF+selem cell to repel the electrons from flowing to the p-type contact and thus, to avoid parasitic shunting. To exclude the influence of parasitic shunting in the simulated cell designs, we observed the simulated electron current flowing between the p-type contact and the inverted region underneath the SiN$_x$ passivation layer at short circuit conditions, displayed in Fig. 7.10. It is shown that whether or not a coupling between the contact and the inversion layer is observed, strongly depends on the cell design. Whereas in the PERL cell from Ref. [Abe95a] in Fig. 7.10(a), electrons flow from the inversion layer into the contact, no such parasitic shunting is observed for the LBSF cell in Fig. 7.10(b). In general, we found that both wafer resistivity and the BSF profile influence the occurrence of parasitic shunting. Two issues are important to prevent this shunting. First, a deep BSF, optimally having an extended plateau of a high dopant density as in Fig. 7.2(b), and second, a relatively high wafer resistivity. To conclude, we can exclude parasitic shunting for the LBSF cell and the LBSF+selem cell (cf. Fig. 7.1) which were subject to investigation in the simulations in this chapter.

7.6 Conclusion

By means of Sentaurus-Device [SD] simulations, we demonstrated the influence of surface damage on the performance of different industrial feasible PERL solar cells, passivated with SiN_x or a-Si:H layers.

The simulated cells were designed as a modification of a standard screen-printed, industrial-type solar cell (reference cell) into PERL cells. Therefore, we reproduced the measured I-V characteristics of the reference cell very accurately. All cell designs were investigated by means of a loss analysis, where we distinguished between series resistance and recombination losses. From this loss analysis, predictions regarding the influence of a surface-damage region (SDR) region underneath the passivation layer on the cell performance, were made. These predictions were confirmed by means of device simulations by implementing the SDR model into Sentaurus-Device. It could be shown that the cell efficiency at low illumination levels is strongly affected by surface damage if (i) the recombination rate at the rear side contributes significantly to the total recombination rate, (ii) the substrate is p-type, and (iii) a high density of fixed charges are present at the interface. As a consequence, we found that for a 2.5 Ωcm Ga-doped Cz-Si solar cell with selective emitter at the front, the relative reduction in cell efficiency is 2.5 % for an illumination intensity of 0.1 sun compared to the case without surface damage. For very low illumination intensities of 0.001 sun, the relative efficiency losses increase to 9.7 %. Our simulations predict, that a reduction of the defect density at the interface by a factor of ten reduces the influence of the SDR to an extent that for all investigated cell-designs, the relative losses in efficiency remain below 1.5 % down to illumination intensities of 0.001 sun.

Similarly, it could be shown that the influence of an SDR at a-Si:H/c-Si interfaces as well as for SiN_x passivated n-Si substrates, is negligible. The relative losses in η at 0.1 sun are 0.84 % and 0.34 %, respectively. We found further, that the enhanced surface passivation in low-injection becomes more significant when going to higher substrate resistivities of $\varrho \approx 10\,\Omega$cm. Thus, care must be taken when passivating high-resistive substrates with SiN_x layers.

Our simulation results may have impact on the development of cost-efficient solar cells. Up to date, single SiN_x layers are not used for the passivation of non-diffused surfaces of p-Si solar cells for two main reasons: the occurrence of parasitic shunting and the strong injection dependence of the surface recombination velocity. Our simulations predict that parasitic shunting does not occur when using a suitable local BSF structure. Further, we observed that already a tenfold reduction of the defect density close to the surface improves the cell efficiency in low-injection sufficiently. Hence, focusing in experiments on a (marginal) reduction of surface damage, offers the possibility to use PECVD SiN_x layers, instead of the rather costly thermal SiO_2, for the rear side passivation of PERL cell structures.

Chapter 8

Conclusion and Outlook

Device simulations are capable to accelerate the efficiency optimizations of solar cells. They allow to reproduce measured data precisely, on the one hand because the processing power and the memory capacity of computers have increased continuously, and on the other hand because the physical models have been adapted specifically to photovoltaic demands. Thus, the confidence in predictions regarding design variations is still growing and offers the opportunity to improve the efficiency of experimental optimization methods. This work provides a contribution to the field of solar cell device simulations by developing new models for effects that are detrimental to solar cell performance and have not been explained satisfactorily in the past. With the help of microscopic interpretations of the observed effects, we trace their causes, and are therefore able to suggest strategies to avoid them. The formulations we give for the presented models are suitable for device simulations.

Amorphous silicon nitride (SiN_x) and atomic layer deposited aluminum oxide layers (Al_2O_3) are used for the electrical passivation of crystalline silicon (c-Si) surfaces in solar cells. In Chapter 4, we developed a model to reproduce the measured injection dependence of the effective surface recombination velocity S_{eff} at SiN_x/c-Si and Al_2O_3/c-Si interfaces. The basic assumptions were made based on the observation that a highly defective region, the surface-damage region (SDR), exists underneath the silicon surface. The developed model relies on SRH theory and describes the high density of defects underneath the interface via a reduction of the charge carrier lifetime parameters in this region [Ste10a, Ste10b, Ste10c]. The model explains the measured S_{eff} data to a high precision level for all relevant excess carrier densities Δn and dopant densities N_{dop}, in both p-Si and n-Si. A parametrization suitable for numerical device modeling is given. Since all model parameters are physically meaningful, the model allows to predict what kind of changes are necessary to eliminate the increase of S_{eff} towards low Δn in p-Si. In essence, two parameters could be addressed to reduce this effect. First, we predicted that a tenfold reduction of the density of states in the damage layer would enhance the carrier lifetime parameters in wafers with typically used resistivities around 1.5 Ωcm to an extent that the influence of surface damage on the passivation quality becomes negligible for applications to solar cells. Second, we showed that a reduction in the fixed surface charge density Q_f of SiN_x layers might improve the performance of SiN_x in low-injection. As a possible explanation of surface damage, we suggested a high density of hydrogen underneath the interface. Indications supporting this hypothesis were discussed in detail, and it was concluded that already the H-termination during wafer-pretreatment may provide a non-negligible source of hydrogen. Therefore, it may be helpful to develop strategies to reduce the excessive density of hydrogen during deposition and pretreatment. To address the point of reducing the high fixed interface-charge density, we demonstrated that the charge density trapped by mobile charges at measured defect distributions is not sufficient to compensate the fixed charge density. A promising method may be to permanently switch the sign of the fixed charge density which has recently been shown for LPCVD SiN_x layers [Web09]. An alternative could be the use of silicon rich a-SiN_y:H/SiN_x stacks [Gat11a], which are assumed to have considerably lower charge densities than SiN_x layers.

Similar to SiN_x and $\mathrm{Al_2O_3}$ layers, hydrogenated amorphous silicon (a-Si:H) layers can be used for the electrical passivation of silicon solar cells. In addition, doped a-Si:H layers are applicable as an emitter or a back surface field (BSF). The investigation of the recombination properties at the a-Si:H/c-Si interface was the second major topic of this work and was treated in Chapter 5. Recombination at this interface occurs mainly via defect states, the so called dangling bonds (DBs), which are amphoteric. Thus, the defects are correlated, and recombination cannot be described correctly by SRH theory. Rather, the model for correlated amphoteric defects derived by Vaillant and Jousse [Vai86] has to be applied. For this model, however, no closed-form solution exists, which makes it difficult to implement into device-simulations. Therefore, we suggested an approximate model based on the SRH formalism which imitates the behavior of amphoteric defects. This model uses two equally shaped distributions for donor-like and acceptor-like defect states, which are separated by the effective correlation energy E_corr. We have shown that amphoteric recombination statistics can be approximated using this uncorrelated approach if (i) the defect distribution is situated to a great extent in between the quasi-Fermi levels for trapped charges (TQFLs), (ii) the ratio between the capture cross sections (CCS) of charged and neutral defects is significantly different from unity, and (iii) the correlation energy is positive. We found that condition (ii) and (iii) is typically met, but condition (i) may be violated under low to medium injection conditions, for example at the p-n junction of a solar cell or at low illumination levels. We have derived equations which relate the characteristic energy levels and the emission coefficients of the SRH model to those of the amphoteric statistics. These equations allow to estimate physically plausible error bounds directly from simulations performed using SRH theory. These error bounds have implications on device simulations of solar cells containing a-Si:H layers: they help to decide in which cases the simplified SRH model may be applied to approximate amphoteric recombination with sufficient accuracy. For example, the error of the uncorrelated approach increases with increasing substrate resistivity, because the TQFLs move closer together. This is in particular the case for defect densities that are not centered near midgap, e.g. in doped a-Si:H. In contrast, if a-Si:H(i) is used for passivation purposes of c-Si substrates, the SRH model approximates the amphoteric model closely, as was shown by reproducing the measured injection dependence of S_{eff}.

We apply a self-consistent model, which includes the band bending in c-Si caused by light-induced trapped charges in the a-Si:H layer and at the a-Si/c-Si interface. We show that these trapped charges significantly influence the recombination rate and should not be neglected. Hence, for a detailed description of $S_{\text{eff}}(\Delta n)$, the defect distribution should be known. We further presented calculations which predict that the influence of surface damage is negligible for a-Si:H passivated substrates.

In Chapter 6, we considered the dark forward current-voltage (I-V) characteristics of c-Si solar cells having a diode-ideality factor $n_{\text{D}} > 2$. Such characteristics are observed in most industrially fabricated solar cells and frequently also for cells under development. The microscopic reason for their behavior cannot be explained satisfactorily up to date. Here, we presented experimental results of cells which were intentionally damaged in local regions. The measurements provide evidence that the ideality factor n_{D} increases the further above two the more severe the disturbance is. Motivated by lock-in thermography images, we described these shunts by recombination currents in highly defective, localized regions of the p-n junction depletion region. This high defect density requires to consider a coupling between the defect levels and thus, a suitable model goes beyond the assumptions made in the SRH theory. We reproduced the measured I-V curves by SENTAURUS-DEVICE [SD] simulations using donor-acceptor-pair (DAP) recombination via deep-level states. Thereby, we were able to explain the experimentally observed raise of the ideality factor n_{D} with increasing defect density. We found that many diverse broad distributions of DAPs allow to reproduce the commonly observed shape of n_{D} as a function of bias voltage. This is an important outcome because, in reality, the distribution of DAPs is expected to be rather broad. Heavily defected regions are expected to consist not only of DAPs but rather to consist of a whole class of different types of coupled defect-levels. However, only DAPs allow to explain the commonly observed shape of n_{D}. They are most efficient for recombination compared to other coupled defects and hence, dominate the overall recombination rate. Consequently, our model may reproduce the typical features of I-V curves influenced by nonlinear shunts, whenever DAPs are present in an almost arbitrary broad distribution. The DAP-approach explains both the SRH-limit for decoupled levels at low defect densities ($n_\mathrm{D} \leq 2$), and the case $n_\mathrm{D} > 2$ for coupled defects at high defect densities. Additionally, our model description yields slightly sub-linear reverse-characteristics, as commonly observed for cells with $n_\mathrm{D} > 2$. To explain the sometimes also observed super-linear reverse-characteristics, our DAP model has to be extended by including transitions across many defect levels [Bre06b].

We also investigated a different cause for the occurrence of shunt currents. For sufficiently high fixed charges, an inversion layer that extends from the front p-n junction to the rear contact via the edge of the cell or along micro-cracks may be formed. This model also explains ideality factors $n_\mathrm{D} > 2$, and – compared to the above DAP approach – the peaks of the n_D curves are typically more narrow and may reach very high values $n_\mathrm{D} \approx 30$. However, this effect can only explain shunt currents in forward bias, and hence, it may only be an additional contribution to the shunt currents obtained from DAP recombination.

Our simulations using coupled DAPs explain, possibly for the first time, the observation made with lock-in thermography that the ideality factor n_D increases with increasing disturbance, in both forward and reverse bias. To validate our developed deep-level DAP model, we suggested future experimental studies based on microscopic electroluminescence imaging. Having traced the microscopic causes of $n_\mathrm{D} > 2$ helps to correctly model industrial-type solar cells, and thus, may support the development of improved cell designs. In addition, it provides useful information to experimenters for reducing undesired shunt currents. We further emphasized that a consideration of deep-level DAPs in the interpretation of lifetime measurements may be worthwhile, because DAP recombination could play a role if the lifetime is dominated by localized high densities of surface states.

Finally, we employed SENTAURUS-DEVICE [SD] simulations to demonstrate the influence of surface damage on the performance of industrial feasible PERL solar cells, passivated by SiN_x or a-Si:H layers in Chapter 7. By means of a loss analysis, we separated the series resistance losses from the recombination losses, and made predictions regarding the influence of a surface-damage region (SDR) region underneath the passivation layer on the performance of different cell designs. These predictions were confirmed by means of further device simulations which show that the performance of PERL cells is affected significantly by an SDR if (i) recombination at the rear side contributes significantly to the total recombination rate, (ii) the substrate is p-type, and (iii) a high density of fixed charges is present at the interface.

The maximal influence of the SDR on cell efficiency was found for a 2.5 Ωcm Ga-doped solar cell made on Cz silicon with high excess carrier lifetimes and a selective emitter at the front. At 0.1 sun, the relative reduction in efficiency is 2.5 % compared to the case without surface damage. Such illumination intensities are readily achieved under outdoor operating conditions. When going to even lower illumination intensities, the efficiency reduction is further increased. However, as predicted from the theoretical considerations in Chapter 4, a mere tenfold improvement of the SRH lifetime parameter at the interface reduces the influence of the SDR to an extent that it becomes negligible: the relative efficiency losses reduce to 0.3 % at 0.1 sun illumination. We found that the enhanced surface passivation in low-injection becomes more significant when going to higher substrate resistivities. Further, it was shown that parasitic shunting does not occur for the investigated SiN_x passivated cell designs because the local BSF repels the electrons from the p-type contact, as was already predicted in Ref. [Dau02a]. This is an important finding, because it offers the possibility to use PECVD SiN_x layers, instead of the rather costly thermal SiO_2, for the rear side passivation of PERL cell structures, if the defect density in the SDR could be reduced by a factor of only ten.

By implementing the approximate SRH model for modeling amphoteric recombination statistics [Vai86] developed in Chapter 5, we could show that the influence of an SDR at the a-Si:H/c-Si interface is negligible because the charge at the interface remains below a critical value. Further, the impact of the Staebler-Wronski effect [Pla08, Sta77, Stu85, Stu86] on cell performance was modeled.

An efficiency reduction from $\eta = 20.6\,\%$ in the as-deposited state to $\eta = 20.0\,\%$ after 15 month of light-exposure was obtained in simulations of a PERL cell. This efficiency reduction should be taken into account when developing solar cell designs incorporating a-Si:H layers.

To conclude, we have developed and tested models for different defect types in solar cells. We hope that these model will be applied to improve the reliability of solar cell device-simulations. Further, this work intents to initiate experimental studies which aim at reducing the influence of effects that are detrimental to solar cell performance, such as surface-near damage or nonlinear shunts.

Appendix A

Numerical Solutions of the Stationary Device Problem

A short outline on the numerical solutions of the stationary device problem was outlined in Sec. 2.1.5. Here, the strategies applied in a semiconductor device simulation are explained in more detail.

A.1 Dependent variables and scaling

For non-homogeneously doped semiconductor devices, the carrier densities may change over orders of magnitude within short distances, and their behavior is strongly influenced by the space charge.

One possibility to overcome this problem when solving for the variables (Ψ, n, p), is to apply an appropriate scaling to the semiconductor equations. Such an approach was firstly proposed by DeMari [DeM68],[DeM68]. It was later reformulated in a mathematically more rigorous way by Vasil'eva and Stel'makh [Vas77],[Vas78] and improved by Markowich *et al.* [Mar82],[Mar83].

In the following, we assume steady-state conditions, i.e. the boundary conditions (BSs) for Ψ are time invariant and the partial derivatives of the carrier densities with respect to time are zero. Inserting the current relations (2.5) into the continuity equations (2.3) and applying the scaling leads to the following elliptic set of partial differential equations [Mar82, Mar83, Sel84, Vas77, Vas78]:

$$\begin{aligned} \lambda^2 \Delta\Psi - n + p + N + \frac{\varrho_{\mathrm{t}}}{q} &= 0 \\ \nabla(D_n \vec{\nabla} n - \mu_n n \vec{\nabla}\Psi) - R_{\mathrm{net}}(\Psi, n, p) &= 0 \\ \nabla(D_p \vec{\nabla} p - \mu_p p \vec{\nabla}\Psi) - R_{\mathrm{net}}(\Psi, n, p) &= 0. \end{aligned} \tag{A.1}$$

A different approach makes use of the dependent variables $(\Psi, \varphi_n, \varphi_p)$, which relate to (Ψ, n, p) in the Boltzmann approximation according to Eq. (2.15). If φ_n

and φ_p are interpreted as mathematical quantities rather than as quasi-Fermi potentials, Eq. (2.15) can be seen as a pure mathematical transformation. Hence, the restriction to a Boltzmann-like formulation is no limitation, if the validity of the Boltzmann statistics is accounted for in the derivation of the current relations. Choosing $(\Psi, \varphi_n, \varphi_p)$ for solving the semiconductor equations is advantageous since all variables are of the same order of magnitude. In addition, the carrier densities are positive by definition, whereas negative carrier densities may result when solving for (Ψ, n, p) due to numerical inaccuracies. The set $(\Psi, \varphi_n, \varphi_p)$ has been applied in some device simulations [Hac81b, Hac81a, Lau73a, Lau73b], however one major drawback of this set is the exponential nonlinearity of the current relations and the continuity equations in φ_n, φ_p. Therefore, one may consider instead of φ_n, φ_p, the variables u, v:

$$u = \mathrm{e}^{-q\beta\varphi_n}, \qquad v = \mathrm{e}^{q\beta\varphi_p}. \tag{A.2}$$

The advantage in using this transformation is that in steady state the continuity equations become self-adjoint partial differential equations [Ban83, Sel84]. Today, high standards in solving such equations efficiently are established. Bank *et al.* [Ban83] suggests to preferably use the variables u and v since the range of values u and v can take is much larger then for φ_n, φ_p. However, due to this large range (u and v change over 32 orders of magnitude in the range $\Psi \in [-1, 1]$), care of the numerical accuracy during solving must be taken. Depending on the accuracy of the computer system, the choice of (Ψ, u, v) is restricted to rather low voltages [Sel84]. The numerical solution of such a system is performed in three steps. First, the space domain is partitioned into a distinct number of subdomains by mapping it onto a grid of nodes. Second, equations (A.1) are approximated in each subdomain by – generally nonlinear – algebraic equations, which involve values of the unknown functions only at the nodes. In total, this leads to a relatively large algebraic problem. Third, this system needs to be solved, numerically.

A.2 Discretization of the stationary device problem

The procedure of numerically solving the set of partial differential equations in a semiconductor device can only be an approximate to the real solution. The accuracy of this approximation depends on both the appropriateness of the approximating functions for the dependent variables in the subdomains and the size of the subdomains. The most suitable methods for partitioning a *semiconductor* device into suitable subdomains are the finite differences method (FDM), and the finite element method (FEM). Even though no preference for either of these methods can be given from the mathematical point of view, the FDM has proven to be slightly superior to the FEM in experiment [Sel84]. It is applied for all solar cell simulations performed in this work (Chapter 6 and Chapter 7) and hence, we focus on this method, here. The two methods are essentially different from the beginning but may though lead to identical results if a proper mesh is chosen. The FEM solves the set of differential equations within a subdomain, whereas the FDM searches for solutions at the grid points. This imposes relatively stringent constraints on the mesh for the FDM. The classical FDM uses meshlines which are parallel to the coordinate axes. These continuous lines start from one boundary of the domain and end at its opposite. Here, we use the FD discretization based on the box-method [For60]. We consider a rectangular device and use a tensor product mesh

$$\mathbf{M} = \{(x_i, y_j)\}, \quad 0 \leq i \leq n+1, 0 \leq j \leq m+1. \tag{A.3}$$

Assuming the set of equations to be in divergence form [Eng83]

$$\nabla \vec{f} = s, \tag{A.4}$$

and choosing a 2-D problem (the 3-D case is analogous), the divergence theorem yields

$$\iint\limits_A \mathrm{d}x\mathrm{d}y \; \nabla \vec{f} = \oint\limits_C f_1 \mathrm{d}y - f_2 \mathrm{d}x. \tag{A.5}$$

Here, C is the boundary curve of a region A in the x, y-plane (Fig. A.1). The edges of the box intersect the meshlines at midpoints between two nodes. We refer to a midpoint between node (x_i, x_j) and (x_{i+1}, y_j) by $(x_{i'}, y_j)$, or shortly by (i', j) and abbreviate the distances between two nodes by $h_i = x_i - x_{j-1}$, $k_j = y_j - y_{j-1}$. Inserting Eq. (A.4) into Eq. (A.5) and subdividing the integral along C into the paths along the four edges of the box (dashed lines in Fig. A.1) yields:

$$I_{i-1',j} + I_{i,j-1'} + I_{i',j} + I_{i,j'} = \iint\limits_{A_{\mathrm{Box}}} \mathrm{d}x\mathrm{d}y \; s, \tag{A.6}$$

where

$$I_{i',j} \;=\; \int\limits_{y_j - k_j/2}^{y_j + k_{j+1}/2} \mathrm{d}y \; f_1(x_{i'}, y), \qquad I_{i,j-1'} \;=\; -\int\limits_{x_i - h_j/2}^{x_i + h_{i+1}/2} \mathrm{d}x \; f_2(x, y_{i-1'}), \tag{A.7}$$

and $I_{i,j'}$, $I_{i,j-1'}$ analogously. So far, Eq. (A.6) is exact. The integrals in Eq. (A.7) can be approximated by A_{Box}:

$$\hat{I}_{i',j} \;=\; \frac{k_j + k_{j+1}}{2} f_1(x_{i'}, y_j), \qquad \hat{I}_{i,j-1'} \;=\; -\frac{h_i + h_{i+1}}{2} f_2(x_i, y_{i-1'}). \tag{A.8}$$

The functions f_1, f_2 need to be evaluated at the nodes. However, to solve these, typically derivatives or other dependencies are required, and so, f_1, f_2 are further approximated by functions $\tilde{f}_1$, $\tilde{f}_2$ using centered difference quotients and interpolated values of mesh functions [Ban83].

The right hand side of Eq. (A.6) can be approximated by the area of the box multiplied by the function value in its center:

$$\iint\limits_{A_{\text{Box}}} \mathrm{d}x\mathrm{d}y \; s \approx s(x_i, x_j)\frac{(k_j + k_{j+1})(h_j + h_{i+1})}{4}. \tag{A.9}$$

For all mesh points where a box can be defined – these are all points except those on the boundaries, where Dirichlet BCs need to be applied – the FD equations read:

$$s(x_i, x_j)\frac{(k_j + k_{j+1})(h_j + h_{i+1})}{4} = \tilde{I}_{i-1',j} + \tilde{I}_{i,j-1'} + \tilde{I}_{i',j} + \tilde{I}_{i,j'}. \tag{A.10}$$

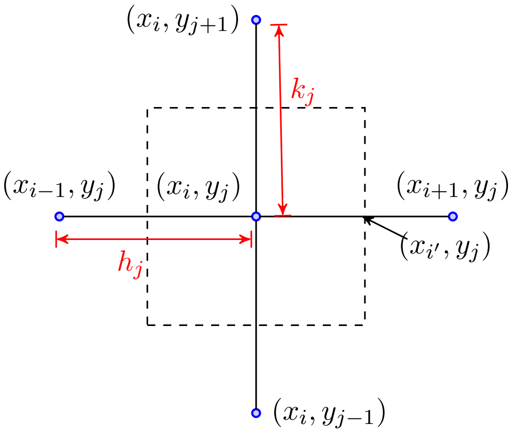

Figure A.1: Sketch of the finite-difference box method. The dashed lines indicate the finite-difference box.

Note that these mesh-points also include Neumann BCs (i.e. the derivative of an unknown is given at the interface) which are handled by the so called “mirror imaging” [e.g. Sel84]. Neumann BCs are applied to all interfaces apart from metalized interfaces where the unknown itself is given (i.e. $E_{fn} - E_i = E_i - E_{fp}$).

For example, underneath contacts or local diffusions, strong gradients in the dependent variables may be expected depending on the operating conditions. Therefore, a very fine meshing is required in these regions. According to the classical FDM, such a mesh refinement requires an enormous number of mesh-points since the lines are only allowed to start and terminate at the edges of the domains. A first improvement to the classical approach was proposed by Adler [Adl80] who introduced meshlines which are allowed to terminate into one direction. Franz *et al.* [Fra83] improved this method by allowing the meshlines to stop in any direction parallel to the coordinate

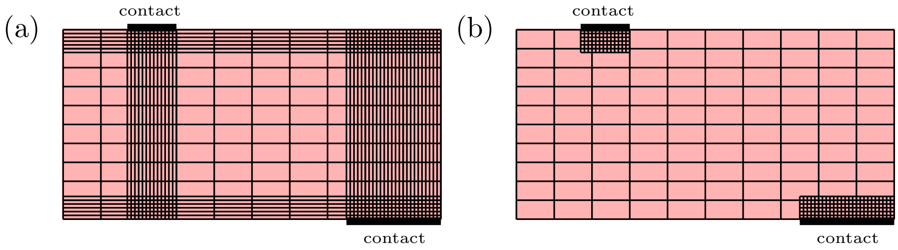

Figure A.2: Oversimplified comparison of mesh generation with the classical FDM (left) and the method of finite boxes (right).

axes. An oversimplified example of the reduction in node numbers obtained by this approach is shown in Fig. A.2.

A further improvement of the mesh is obtained by delaunization. Thereby, a Delaunay triangulation is performed to create a Delaunay grid without any obtuse angles.

A.3 Linearizing and solving the semiconductor equations

The final solution of the coupled set of Eqs. (2.1) and (2.3) can be solved in either a coupled or a decoupled approach. When ramping a parameter during the simulation, e.g. the voltage, typically, a combination of both is used: during a plugin-loop, an initial solution is found using Gummel's decoupled algorithm [Gum64]. This initial solution is then used as an input to the subsequent coupled solver. When ramping through the voltage, this solver uses each previous solution as an initial guess for the next voltage step. Therefore, the voltage ramping must be performed in suitable small steps.

Figure A.3 shows Gummel's algorithm which successively solves the Poisson equation and the continuity equations. First, Poisson's equation (2.1) is solved using a guess of φ_n and φ_p (or n, p depending on the choice of the dependent variables). Next, the continuity equations (2.3) are solved with Ψ obtained during the solution of (2.1). This loop is repeated successively until the desired convergence or a maximal number of iterations is reached. This plugin-sequence is typically solved for low-injection conditions (i.e. low voltages and possibly low illumination), when the coupling between the semiconductor equations is low. At higher voltages or strong illumination, when the minority carrier density approaches the majority carrier density, Eqs. (2.1) and (2.3) become strongly coupled and the convergence is strongly reduced [Man74]. This problem can be overcome if the semiconductor

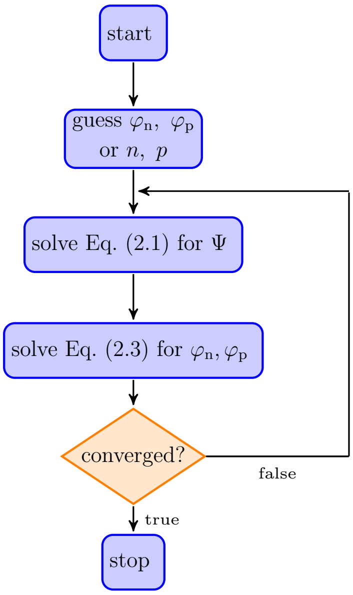

Figure A.3: Gummel's decoupled algorithm [Gum64] for solving the semiconductor equations. Sketch after [Eng83].

equations are solved simultaneously rather than iteratively. The coupling is taken into account, e.g. by using a Newton iteration scheme.

In the following, an example of avoiding typical convergence problems is provided.

Example:
Convergence problems are often observed when simulating the illuminated I-V curve of solar cells featuring strongly charged interfaces, such as SiN$_x$ or Al$_2$O$_3$ passivated surfaces (Chapter 6 and Chapter 7). To overcome this, we start by determining the thermal equilibrium solution using the decoupled approach, and subsequently ramp the intensity in small steps using the coupled solver until the desired value is reached. Taking this solution as a start value for voltage ramping, convergence problems are typically eliminated.

In the following, we detail the iteration algorithm. Numerically solving the semiconductor equations implies that they are solved discretized and thus, approximately. Here, we consider the linear approximation:

$$\vec{f}(\vec{x}) = \vec{f}(\vec{p}) + \mathbf{J_f}(\vec{p})(\vec{x} - \vec{p}) + \mathcal{O}(\|\vec{x} - \vec{p}\|). \tag{A.11}$$

to the vector $\vec{f}$ near a given point $\vec{p} \subset \mathbb{R}^n$ by the Jacobian matrix:

$$\mathbf{J_f} = \frac{\partial(f_1, \ldots, f_m)^T}{\partial(x_1, \ldots, x_n)^T} = \left(\frac{\partial f_i}{\partial x_j}\right)_{i=1,\ldots,m;\ j=1,\ldots,n}, \tag{A.12}$$

Here, $\vec{x} = (x_1, \ldots, x_n)^T \subset \mathbb{R}^n$, and $\vec{f} = (f_1, \ldots, f_m)^T$ is a differentiable component function.

In the following, the Jacobian is applied to the semiconductor equations which are considered in a scaled form. Therefore, we write all voltages in units of $(q\beta)^{-1}$, all spatial dimensions in terms of the Debye $L_D := (\varepsilon_0\varepsilon_\mathrm{r}/(q\beta n_i))^{1/2}$, and all densities in units of n_i [Fic83]. The dimensionless properties are labeled with a star.
For the carrier densities this results in:

$$n^* \;=\; \mathrm{e}^{\Psi^*-\varphi_n^*}, \qquad p^* \;=\; \mathrm{e}^{\varphi_p^*-\Psi^*}. \tag{A.13}$$

Abbreviating $qN + \varrho_\mathrm{trap} =: C$ and making use of Eq. (2.5), it follows for the semiconductor equations in steady state [Ban83, Fic83]:

$$\begin{aligned} g_1 &= \Delta\Psi^* + \mathrm{e}^{\Psi^*-\varphi_n^*} - \exp(\varphi_p^* - \Psi^*) - C^* &&= 0 \\ g_2 &= \nabla\left(\mu_n\,\mathrm{e}^{\Psi^*-\varphi_n^*}\vec{\nabla}\varphi_n^*\right) + R_\mathrm{net}^*(\Psi,n,p) &&= 0 \\ g_3 &= \nabla\left(\mu_p\,\mathrm{e}^{\varphi_p^*-\Psi^*}\vec{\nabla}\varphi_p^*\right) + R_\mathrm{net}^*(\Psi,n,p) &&= 0. \end{aligned} \tag{A.14}$$

Substituting further $u^* = \exp(-\varphi_n^*)$, $v^* = \exp(\varphi_p^*)$, and choosing $R_\mathrm{net} = 0$ for convenience, the Jacobian matrix of the vector $\vec{g} = (g_1, g_2, g_3)^T$ (Eq. (A.14)) reads in similar form as in Bank *et al.* [Ban83]:

$$\mathbf{J_g} = \begin{bmatrix} -\Delta\,\Box + \left(\mathrm{e}^{\Psi^*}u^* + v^*\,\mathrm{e}^{-\Psi^*}\right)\Box & -\,\mathrm{e}^{\Psi^*}u^*\,\Box & -v^*\,\mathrm{e}^{-\Psi^*}\,\Box \\ \nabla(-\mu_n\,\Box\,\mathrm{e}^{\Psi^*}u^*\vec{\nabla}(\ln(u^*))) & \nabla\left(\mu_n\,\mathrm{e}^{\Psi^*}\vec{\nabla}(u^*\,\Box\,)\right) & 0 \\ \nabla(-\mu_p\,\Box\,v^*\,\mathrm{e}^{-\Psi^*}\vec{\nabla}(\ln(v^*))) & 0 & \nabla\left(\mu_p\,\mathrm{e}^{-\Psi^*}\vec{\nabla}(v^*\,\Box\,)\right) \end{bmatrix}, \tag{A.15}$$

where the $\Box$-symbols are placeholders for the components of the vector $\mathbf{J_g}$ acts on. Different to Bank *et al.* [Ban83], we include u^* and v^* explicitly into the Jacobian $\mathbf{J_g}$ Eq. (A.15). Note that in Eq. (A.15) it was assumed that μ_n and μ_p are independent of Ψ. Indeed, the inclusion of this dependence has typically small influence [Ban83] and can therefore be neglected.
Iterative methods are required to solve systems of nonlinear algebraic equations. The most famous approach is Newton's method [New71], which is applied here according to Bank and Rose [Ban81]:

$$\mathbf{J_g}_k\vec{x} \;=\; -\vec{g} \tag{A.16a}$$

$$\vec{z}_{k+1} - \vec{z}_k \;=\; \lambda_k\vec{x}_k. \tag{A.16b}$$

Here, $\vec{z} = (\Psi^*, u, v)^T$ and $\vec{x} = (\delta\Psi^*, \delta u, \delta v)^T$. The interested reader finds background information about Newton's method e.g. in [Sel84] (rather phenomenological) or [Ort70] (rather elaborate).

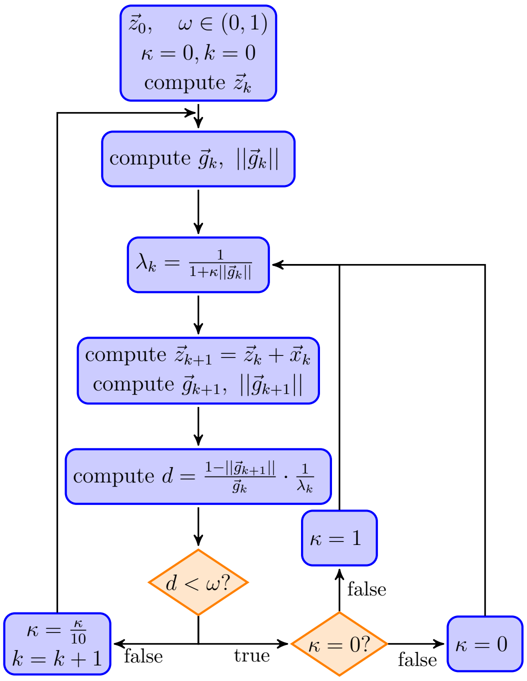

Figure A.4: The damped Newton iteration scheme using Bank-Rose iterations [Ban81]. In the example shown here, $\kappa_k/10$ is taken as an initial estimate for κ_{k+1} [Ban81]. A description of the algorithm is given in the text.

Applying Newton's iteration scheme to the semiconductor equations, convergence of the Newton scheme is obtainable only for very small time steps, so methods to enhance the convergence are applied.

For the FDM, we apply the so called Bank-Rose method [Ban81] for applications using FDM discretization, which is typically used for applications using the FDM discretization (Fig. A.4). The convergence of the Newton scheme is controlled by the damping factor λ_k which is determined in an iterative way. Thereby, λ_k is chosen such that $||\vec{g}_{k+1}/\vec{g}_k|| < 1$, but as close as possible to unity.

The Bank-Rose algorithm searches in the vicinity of initial solutions $\vec{z}_k$ for the shortest path through the basin of attraction of the zeros of $\vec{g}_k$ to obtain an improved approximation for $\vec{z}_{k+1}$. If $\vec{z}_k$ approaches the solution (i.e. $\vec{z} \to \vec{z}^*$), λ_k approaches unity if κ is bounded. Only if the convergence of λ is approximately as fast as the convergence of $\vec{z}$, superlinear convergence of the suggested algorithm can be expected [Ban81]. In case κ is unbounded, κ may grow infinitely such that no improved approximation $\mathbf{z}_{k+1}$ can be found and convergence fails. Note that for FEM discretizations, typically a different method, e.g. the approximate Newton-multilevel iteration scheme [Ban81, Ban83], has to be applied.

The abstract view of the solution process in Eqs. (A.15) and Eq. (A.16) is advantageous for several reasons: On the one hand, the divergence form of $\mathbf{J}_g$ is optimal for applications to FDM and FEM discretizations which are well suitable for semiconductor device modeling (Sec. A.2). Furthermore, the diagonal operators of $\mathbf{J}_g$ are self-adjoint, which is advantageous because high standards in efficiently solving such equations are established. This is in particular important for the application of block iteration methods in solving Newton's equations since the linear systems corresponding to the diagonal of $\mathbf{J}_g$ has to be solved repeatedly in each inner loop. Bank *et al.* [Ban83] suggest to view the lower triangular part of $\mathbf{J_k}$ (Eq. (A.17)) as a block iterative method for the discretized block system arising from Eq. (A.16):

$$\mathbf{L_k}(\vec{x}_n - \vec{x}_{n-1}) = -(\mathbf{J_k}\vec{x}_n + \vec{g}_k). \tag{A.17}$$

It should be remarked that regarding the combination with a Newton-iteration scheme, block iteration is superior to sparse direct methods [Ban83].

Bibliography

[Abe95b] A. G. Aberle, T. Lauinger, J. Schmidt, and R. Hezel. Injection-level dependent surface recombination velocities at the silicon-plasma silicon nitride interface. *Appl. Phys. Lett.*, 66: 2828–2830, 1995b.

[Abe95a] A. G. Aberle, P. P. Altermatt, G. Heiser, S. J. Robinson, A. Wang, J. Zhao, U. Krumbein, and M. A. Green. Limiting loss mechanisms in 23% efficient silicon solar cells. *J. Appl. Phys.*, 77: 3491–4004, 1995a.

[Abe97] A. G. Aberle and R. Hezel. Progress in Low-Temperature Surface Passivation of Silicon Solar Cells using Remote-Plasma Silicon Nitride. *Prog. Photovoltaics*, 5: 29–50, 1997.

[Abe99] A. G. Aberle. *Crystalline Silicon Solar Cells - Advanced Surface Passivation and Analysis.* Center for Photovoltaic Engineering, University of New South Wales, Australia, 1999.

[Abe00] A. G. Aberle. Surface Passivation of Crystalline Silicon Solar Cells: A Review. *Prog. Photovoltaics: Res. Appl.*, 8: 473–487, 2000.

[Adl80] M. S. Adler. A Method for Termination Mesh Lines in Finite Difference Formulations of the Semiconductor Device Equations. *Solid State Electron.*, 23: 845–853, 1980.

[Ako10] M. Akorede, H. Izam, I. Aris, and M. A. Kadir. A Review of Strategies for Optimal Placement of Distributed Generation in Power Distribution Systems. *Research Journal of Applied Sciences*, 5: 137–145, 2010.

[Alj90] S. Aljishi, J. Cohen, S. Jin, and L. Ley. Band tails in hydrogenated amorphous silicon and silicon-germanium alloys. *Phys. Rev. Lett.*, 64: 2811–2814, 1990.

[Alt96] P. P. Altermatt, G. Heiser, A. G. Aberle, A. Wang, J. Zhao, S. J. Robinson, S. Bowden, and M. A. Green. Spatially resolved analysis and minimization of resistive losses in high-efficiency Si solar cells. *Prog. Photovoltaics*, 4: 399–414, 1996.

[Alt97] P. P. Altermatt, J. Schmidt, G. Heiser, and A. G. Aberle. Assessment and parameterisation of Coulomb-enhanced Auger recombination coefficients in lowly injected crystalline silicon. *J. Appl. Phys.*, 82: 4938–4944, 1997.

[Alt02a] P. P. Altermatt and G. Heiser. Predicted electronic properties of polycrystalline silicon from three-dimensional device modeling combined with defect-pool model. *J. Appl. Phys.*, 92: 2561–2574, 2002a.

[Alt02b] P. P. Altermatt, A. G. Aberle, J. Zhao, A. Wang, and G. Heiser. A numerical model of p-n junctions bordering on surfaces. *Sol. Energy Mat. Sol. Cells*, 74: 165–174, 2002b.

[Alt02c] P. P. Altermatt, J. O. Schumacher, A. Cuevas, M. J. Kerr, S. W. Glunz, R. R. King, G. Heiser, and A. Schenk. Numerical modeling of highly doped Si:P emitters based on Fermi-Dirac statistics and self-consistent material parameters. *J. Appl. Phys.*, 92: 3187–3197, 2002c.

[Alt03] P. P. Altermatt, A. Schenk, and F. Geelhaar. Reassessment of the intrinsic carrier density in crystalline silicon in view of band-gap narrowing. *J. Appl. Phys.*, 93: 1598–1604, 2003.

[Alt05b] P. P. Altermatt, A. Schenk, and R. Schmidthüsen. The impact of incomplete ionisation on Si solar cells. In *Proc. 20th EU PVSEC*, pages 1267–1270, Barcelona, Spain, 2005b.

[Alt05a] P. P. Altermatt, F. Geelhaar, T. Trupke, X. Day, A. Neisser, and E. Daub. Injection dependence of spontaneous radiative recombination in c-Si: experiment, theoretical analysis, and simulation. In *Proc. 5th International Conference on Numerical Simulation of Optoelectronic Devices (NUSOD05)*, pages 47–48. IEEE, New York, 2005a.

[Alt06c] P. P. Altermatt, A. Schenk, B. Schmithüsen, and G.Heiser. An empirical model for the density-of-states and for incomplete ionization in crystalline silicon. I: Establishing the model in Si:P. *J. Appl. Phys.*, 100: 113714, 2006c.

[Alt06d] P. P. Altermatt, A. Schenk, B. Schmithüsen, and G. Heiser. A simulation model for the density of states and for incomplete ionization in crystalline silicon. II. Investigation of Si:As and Si:B and usage in device simulation. *J. Appl. Phys.*, 100: 113715, 2006d.

[Alt06b] P. P. Altermatt, H. Plagwitz, R. Bock, J. Schmidt, R. Brendel, M. J. Kerr, and A. Cuevas. The surface recombination velocity at boron-doped emitters: Comparison between various passivation techniques. In *Proc. 21st EU PVSEC*, Dresden, Germany, 2006b. IEEE, New York.

[Alt06a] P. P. Altermatt, F. Geelhaar, T. Trupke, X. Dai, A. Neisser, and E. Daub. Injection dependence of spontaneous radiative recombination in crystalline silicon: Experimental verification and theoretical analysis. *Appl. Phys. Lett.*, 88: 261901, 2006a.

[Alt09] P. P. Altermatt, S. Steingrube, Y. Yang, C. Sprodowski, T. Dezhdar, S. Koc, B. Veith, S. Hermann, R. Bock, K. Bothe, J. Schmidt, and R. Brendel. Highly Predictive Modelling of Entire Si Solar Cells for Industrial Applications. In *Proc. 24th EU PVSEC*, pages 901–906, Hamburg, Germany, 2009. WIP, Munich.

[And77] P. J. Anderson and M. J. Buckingham. Theory of depletion-layer recombination in silicon p–n junctions. *Electron. Lett.*, 13: 496–498, 1977.

[Bäh04] M. Bähr, S. Dauwe, L. Mittelstädt, J. Schmidt, and G. Gobsch. Surface passivation and contact resistance on various emitters of screen-printed crystalline silicon solar cells. In *Proc. 19th EU PVSEC*, pages 955–958, Paris, France, 2004.

[Bal93] I. Balberg and I. Lubianiker. Evidence for the defect-pool model from induced recombination shifts in undoped a-Si:H. *Phys. Rev. B*, 48: 8709–8714, 1993.

[Ban81] R. E. Bank and D. J. Rose. Global Approximate Newton Methods. *Numer. Math.*, 37: 279–295, 1981.

[Ban83] R. E. Bank, D. J. Rose, and W. Fichtner. Numerical Methods for Semiconductor Device Simulation. *IEEE Trans. Electron Devices*, ED-30: 1031–1041, 1983.

[Bar54] N. A. Barricelli. Esempi numerici di processi di evoluzione. *Methodos*, pages 45–68, 1954.

[Bec96] N. Beck, N. Wyrsch, C. Hof, and A. Shah. Mobility lifetime product – A tool for correlating a-Si:H film properties and solar cell performances. *J. Appl. Phys.*, 79: 9361–9368, 1996.

[Bei93] J. Beier and B. Voss. Humps in dark I-V-curves-analysis and explanation. In *Proc. 23th IEEE PVSC*, pages 321–324, Louisville, KY, 1993.

[Ber98a] C. Berge, J. Schmidt, B. Lenkeit, H. Nagel, and A. G. Aberle. Comparison of Effective Carrier Lifetimes in Silicon Determined by Transient and Quasi-Steady-State Photoconductance Measurements. In *Proc. 2nd WPSEC*, pages 1426–1429, Vienna, Austria, 1998a.

[Ber98b] N. Bernstein, M. J. Aziz, and E. Kaxiras. Amorphous-crystal interface in silicon: A tight-binding simulation. *Phys. Rev. B*, 58: 4579–4583, 1998b.

[Bin74] R. Bindemann and K. Unger. On the spectral density distribution of Donor-Acceptor pair recombination in GaP. *Phys. Status Solidi B*, 66: 133, 1974.

[Bla82] J. Blakemore. Approximations for Fermi-Dirac intergrals, especially the function $F_{1/2}(\eta)$ used to describe the electron density in a semiconductor. *Solid State Electron.*, 25: 1067–1076, 1982.

[Bol80] B. Bolzano. Rein analytischer Beweis des Lehrsatzes dass zwischen je zwey Werthen, die ein entgegengesetztes Resultat gewaehren, wenigstens eine reele Wurzel der Gleichung liege, Prague, 1817 English translation in. *Russ, S. B. "A Translation of Bolzano's Paper on the Intermediate Value Theorem." Hist. Math.*, 7: 156–185, 1980.

[Bot05] K. Bothe, R. Sinton, and J. Schmidt. Fundamental boron–oxygen-related carrier lifetime limit in mono- and multicrystalline silicon. *Prog. Photovoltaics: Res. Appl.*, 13: 287–296, 2005.

[Bra53] W. H. Brattain and J. Bardeen. Surface Properties of Germanium. *Bell Syst. Tech. J.*, 32: 1–41, 1953.

[Bre73] R. Brent. *Algorithms for Minimization without Derivatives*, chapter 4. Prentice-Hall, Englewood Cliffs, NJ, 1973.

[Bre94] O. Breitenstein and J. Heydenreich. Non-Ideal I-V-Characteristics of Block-Cast Silicon Solar Cells. *Solid State Phenomena*, 37–38: 139–144, 1994.

[Bre01a] O. Breitenstein, M. Langenkamp, O. Lang, and A. Schirrmacher. Shunts due to laser scribing of solar cells evaluated by highly sensitive lock-in thermography. *Sol. Energy Mat. Sol. Cells*, 65: 55–62, 2001a.

[Bre01b] O. Breitenstein, M. Langenkamp, J. P. Rakoniaina, and J. Zettner. The imaging of shunts in solar cells by infrared Lock-In Thermography. In *Proc. 17th EU PVSEC*, pages 1499–1502, Munich, Germany, 2001b.

[Bre03] O. Breitenstein and M. Langenkamp. *Lock-in Thermography - Basics and Use for Functional Diagnostics of Electronic Components.* Springer, Berlin, Heidelberg, 2003.

[Bre06b] O. Breitenstein, P. P. Altermatt, K. Ramspeck, and A. Schenk. The origin of ideality factors $n > 2$ of shunts and surfaces in the dark I-V curves of silicon solar cells. In *Proc. 21st EU PVSEC*, pages 625–628, Dresden, Germany, 2006b.

[Bre06a] O. Breitenstein, P. P. Altermatt, K. Ramspeck, M. A. Green, J. Zhao, and A. Schenk. Interpretation of the Commonly Observed I-V Characteristics of c-Si Cells Having Ideality Factor Larger Than Two. In *Proc. 4th WPSEC*, pages 879–884, Hawaii, 2006a. IEEE, Piscataway, NJ.

[Bre09] O. Breitenstein, J. Bauer, A. Lotnyk, and J.-M. Wagner. Defect induced non-ideal dark *I-V* characteristics of solar cells. *Superlattices Microstruct.*, 45: 182–189, 2009.

[BY87] Y. Bar-Yam and J. D. Joannopoulos. Theories of defects in amorphous semiconductors. *J. Non-Cryst. Solids*, 97–98, Part I: 467–474, 1987.

[Che94] Z. Chen, A. Rohatgi, and D. Ruby. Silicon surface and bulk defect passivation by low temperature PECVD oxides and nitrides. In *Proc. 1st IEEE WCPEC*, pages 1331–1334, Waikaloa, HI, 1994.

[Cho86] S. C. Choo. Carrier generation-recombination in the space-charge region of an asymmetrical p-n junction. *Solid State Electron.*, 11: 1069–1077, 1986.

[Cor96] R. Corkish and M. A. Green. Junction recombination current in abrupt junction diodes under forward bias. *J. Appl. Phys.*, 80: 3083–3090, 1996.

[Cue11] A. Cuevas. Modelling Silicon Characterisation. In *Proc. 1st Silicon PV*, Freiburg, Germany, 2011. *accepted* for publication in Energia Procedia.

[Dau02a] S. Dauwe, L. Mittelstädt, A. Metz, and R. Hezel. Experimental Evidence of Parasitic Shunting in Silicon Nitride Rear Surface Passivated Solar Cells. *Prog. Photovolt: Res. Appl.*, 10: 271–278, 2002a.

[Dau02c] S. Dauwe, J. Schmidt, A. Metz, and R. Hezel. Fixed charge density in silicon nitride films on crystalline silicon surfaces under illumination. In *Proc. 29th IEEE PVSC*, pages 162–165, New Orleans, LA, 2002c.

[Dau02b] S. Dauwe, J. Schmidt, and R. Hezel. Very low surface recombination velocities on p- and n-type silicon wafers passivated with hydrogenated amorphous silicon films. In *Proc. 29th IEEE PVSC*, pages 1246–1249, New Orleans, LA, 2002b.

[Dau03] S. Dauwe, L. Mittelstädt, A. Metz, J. Schmidt, and R. Hezel. Low-temperature rear surface passivation schemes for $> 20\,\%$ efficient silicon solar cells. In *Proc. 3rd WCPEC*, pages 1395–1398, Osaka, Japan, 2003.

[Dau04] S. Dauwe. *Low-temperature passivation of crystalline silicon and its application to the rear side of solar cells.* PhD thesis, Leibzniz University of Hannover, 2004.

[de 09] S. de Wolf and M. Kondo. Nature of doped a-Si:H/c-Si interface recombination. *J. Appl. Phys.*, 105: 103707, 2009.

[Dea93] S. C. Deane and M. J. Powell. Defect chemical potential and the density of states in amorphous silicon. *Phys. Rev. Lett.*, 70: 1654–1657, 1993.

[Dek69] T. J. Dekker. *Constructive Aspects of the Fundamental Theorem of Algebra*, chapter *Finding a zero by means of successive linear interpolation.* Wiley-Interscience, London, 1969.

[DeM68] A. DeMari. An accurate numerical steady-state one-dimensional solution of the P-N junction. *Solid State Electron.*, 11: 33–58, 1968.

[Dju97] A. Djurišić, J. Elazar, and A. Rakic. Simulated-annealing-based genetic algorithm for modeling the optical constants of solids. *Appl. Opt.*, 36: 7097–7103, 1997.

[Don98] J. Dong and D. A. Drabold. Atomistic Structure of Band-Tail States in Amorphous Silicon. *Phys. Rev. Lett.*, 80: 1928–1931, 1998.

[Dra91] D. A. Drabold, P. A. Fedders, S. Klemm, and O. F. Sankey. Finite-temperature properties of amorphous silicon. *Phys. Rev. Lett.*, 67: 2179–2182, 1991.

[Dun92] S. T. Dunham. A quantitative model for the coupled diffusion of phosphorus and point defects in silicon. *J. Electrochem. Soc.*, 139: 2628–2636, 1992.

[Dzi77] J. Dziewior and W. Schmid. Auger coefficients for highly doped and highly excited silicon. *Appl. Phys. Lett.*, 31: 346–348, 1977.

[Elm97] J. R. Elmiger, R. Schieck, and M. Kunst. Recombination at the silicon nitride/silicon interface. *J. Vac. Sci. Technol.*, 15: 2418–2425, 1997.

[Eng83] W. E. Engl, H. K. Dirks, and B. Meinerzhagen. Device Modeling. In *Proc. IEEE*, volume 71, pages 10–31, 1983.

[Fef95] E. Fefer, Y. Shapira, and I. Balberga. Direct determination of the band-gap states in hydrogenated amorphous silicon using surface photovoltage spectroscopy. *Appl. Phys. Lett*, 67: 371–373, 1995.

[Fic83] W. Fichtner, D. J. Rose, and R. E. Bank. Semiconductor Device Simulation. *IEEE Trans. Electron Devices*, ED-30: 1018–1030, 1983.

[For60] G. E. Forsythe and W. R. Wasow. *Finite Difference Methods for Partial Differential Equations.* Wiley, New York, 1960.

[Fra83] A. F. Franz, G. A. Franz, S. Selberherr, C. Ringhofer, and P. Markovich. Finite Boxes – A Generalization of the Finite Difference Method Suitable for Semiconductor Device Simulation. *IEEE Trans. Electron Devices*, ED-30: 1070–1082, 1983.

[Fuj85] S. Fujita and A. Sasaki. Dangling Bonds in Memory-Quality Silicon Nitride Films. *J. Electrochem. Soc.*, 132: 398–402, 1985.

[Gan05] M. Gandomkar, M. Vakilian, and M. Ehsan. A combination of genetic algorithms and simulated annealing for optimal DG allocation in distribution networks. In *Proc. Canadian Conference on Electrical and Computational Engineering*, pages 645–648, Sakskatoon, Sask., 2005.

[Gar05] M. Garin, U. Rau, W. Brendle, I. Martin, and R. Alcubilla. Characterization of a-Si:H/c-Si interfaces by effective-lifetime measurements. *J. Appl. Phys.*, 98: 093711–9, 2005.

[Gas74] S. Gasiorowicz. *Quantum Physics*. John Wiley and Sons, Inc., New York, London, Sydney, Toronto, 1974.

[Gat11a] Gatz. to be submitted(!), TODO!!, 2011a.

[Gat11c] S. Gatz, H. Hannebauer, R. Hesse, F. Werner, A. Schmidt, T. Dullweber, J. Schmidt, K. Bothe, and R. Brendel. 19.4%–efficient large-area fully screen-printed silicon solar cells. *Phys. Status Solidi RRL*, 5: 147–149, 2011c.

[Gat11b] S. Gatz, K. Bothe, J. Müller, T. Dullweber, and R. Brendel. Analysis of local Al-doped back surface fields for high efficiency screen-printed solar cells. In *Proc. 1st Silicon PV*, Freiburg, Germany, 2011b. *accepted* for publication in Energia Procedia.

[Gha89] M. Y. Ghannam and R. P. Mertens. Surface recombination current with a nonideality factor greater than 2. *IEEE Electr. Device. L.*, 10: 4740–4754, 1989.

[Glu99a] S. W. Glunz, D. Biro, S. Rein, and W. Warta. Field-effect passivation of the SiO_2–Si interface. *J. Appl. Phys.*, 86: 683–691, 1999a.

[Glu99b] S. W. Glunz, S. Rein, J. Knobloch, W. Wettling, and T. Abe. Comparison of boron- and gallium-doped p-type Czochralski silicon for photovoltaic application. *Prog. Photovoltaics: Res. Appl.*, 7: 463–469, 1999b.

[Glu01] S. W. Glunz, S. Rein, W. Warta, J. Knobloch, and W. Wettling. Degradation of carrier lifetime in Cz silicon solar cells. *Sol. Energy Mater. Sol. Cells*, 65: 219–229, 2001.

[Gre90] M. Green. Intrinsic concentration, effective densities of states, and effective mass in silicon. *J. Appl. Phys.*, 67: 2944–2954, 1990.

[Gre94] M. Green and K. Emery. Solar cell efficiency tables (version 3). *Progr. Photovolt.*, 2: 27–34, 1994.

[Gre95] M. A. Green. *Silicon Solar Cells: Advanced Principles & practice.* Centre Photovoltaic Devices & Systems, 1995.

[Gre08] M. A. Green. Self-consistent optical parameters of intrinsic silicon at 300 K including temperature coefficients. *Sol. Energy Mat. Sol. Cells*, 92: 1305–1310, 2008.

[Gro66] A. S. Grove and D. J. Fitzgerald. Surface effects on p-n junctions: Characteristics of surface space-charge regions under non-equilibrium conditions. *Solid State Electron.*, 9: 783–806, 1966.

[Gum64] H. K. Gummel. A self-consistent iterative scheme for one-dimensional steady state transistor calculations. *IEEE Trans. Electron Devices*, ED-11: 455–465, 1964.

[Hac81b] G. D. Hachtel, M. H. Mack, R. R. O'Brien, and B. Speelpenning. Semiconductor Analysis Using Finite Elements - Part 1: Computational Aspcets. *IBM J. Res. Dev.*, 25: 232–245, 1981b.

[Hac81a] G. D. Hachtel, M. H. Mack, and R. R. O'Brien. Semiconductor Analysis Using Finite Elements - Part 2: IGFET and BJT Case Studies. *IBM J. Res. Dev.*, 25: 246–260, 1981a.

[Hal52] R. N. Hall. Electron-Hole Recombination in Germanium. *Phys. Rev.*, 87: 387, 1952.

[Hal86] V. Halpern. The statistics of recombination via dangling bonds in amorphous silicon. *Philos. Mag. B*, 54: 473–482, 1986.

[Han67] R. J. Handy. Theoretical analysis of the series resistance of a solar cell. *Solid State Electron.*, 10: 765–775, 1967.

[Har09] N. Harder and S. Hermann. private communications, 2009.

[Hat95] K. Hattori, M. Anzai, H. Okamoto, and Y. Hamakawa. Distribution of light-induced defect states in undoped amorphous silicon. *J. Appl. Phys.*, 77: 2989–2992, 1995.

[Hau01] A. Hauser, G. Hahn, M. Spiegel, H. Feist, O. Breitenstein, and P. Rakotoniaina. Comparison of Different Techniques for Edge Isolation. In *Proc. 17th EU PVSEC*, page 1739, Munich, Germany, 2001.

[Hei80] V. Heine. In H. Ehrenreich, F. Seitz, and D. Turnbull, editors, *Solid State Physics*, volume 35, pages 118–119. Academic, New York, 1980.

[Hez89] R. Hezel and K. Jaeger. Low-Temperature Surface Passivation of Silicon for Solar Cells. *J. Electrochem. Soc.*, 136: 518–523, 1989.

[Hoe08a] B. Hoex, J. J. H. Gielis, M. C. M. van de Sanden, and W. M. M. Kessels. On the c-Si surface passivation mechanism by the negative-charge-dielectric Al_2O_3. *J. Appl. Phys.*, 104: 113703, 2008a.

[Hoe08b] B. Hoex, J. Schmidt, P. Pohl, M. C. M. van de Sanden, and W. M. M. Kessels. Silicon surface passivation by atomic layer deposited Al_2O_3. *J. Appl. Phys.*, 104: 044903, 2008b.

[Hol75] J. H. Holland. *Adaptation in Natural and Artificial Systems.* University of Michigan Press, Ann Arbor, 1975.

[Hop63] J. J. Hopfield, D. G. Thomas, and M. Gershenzon. Pair Spectra in GaP. *Phys. Rev. Lett.*, 10: 162, 1963.

[Hub92] J. Hubin, A. V. Shah, and E. Sauvain. Effects of dangling bonds on the recombination function in amorphous semiconductors. *Phil. Mag. Lett.*, 66: 115–125, 1992.

[Iba02] H. Ibach and H. Lüth. *Festkörperphysik.* Springer, Berlin, Heidelberg, 6 edition, 2002.

[Jac82] W. B. Jackson. The correlation energy of the dangling silicon bond in a-Si:H. *Solid State Commun.*, 44: 477–480, 1982.

[Jac90] W. B. Jackson. Role of hydrogen complexes in the metastability of hydrogenated amorphous silicon. *Phys. Rev. B*, 41: 10257–10260, 1990.

[Jac92] W. B. Jackson and C. C. Tsaik. Hydrogen transport in amorphous silicon. *Phys. Rev. B*, 45: 6564–6580, 1992.

[Jee58] T. Jeeves. Secant modification of Newton's method. *Comm. Assoc. Comp. Mach. 1*, 8: 9–10, 1958.

[Joh87] N. M. Johnson, F. A. Ponce, R. A. Street, and R. J. Nemanich. Defects in single-crystal silicon induced by hydrogenation. *Phys. Rev. B*, 35: 4166–4169, 1987.

[Joy77] W. B. Joyce and R. W. Dixon. Analytic approximations for the Fermi energy of an ideal Fermi gas. *Appl. Phys. Lett.*, 31: 354–356, 1977.

[Kak87] J. Kakalios, R. A. Street, and W. B. Jackson. Stretched-exponential relaxation arising from dispersive diffusion of hydrogen in amorphous silicon. *Phys. Rev. Lett.*, 59: 1037–1040, 1987.

[Kam96] A. Kaminski, J. J. Marchand, H. E. Omari, A. Laugier, Q. N. Le, and D. Sarti. Conduction processes in silicon solar cells. In *Proc. 25th IEEE PVSC*, pages 573–576, Washington, D. C., 1996.

[Kan63] E. O. Kane. Thomas-Fermi Approach to Impure Semiconductor Band Structure. *Phys. Rev.*, 131: 79–88, 1963.

[Kaz04] A. G. Kazanskiĭ and K. Y. Khabarova. Distribution of the Density of Electronic States in the Energy Gap of Microcrystalline Hydrogenated Silicon. *Semiconductors*, 38: 1221–1224, 2004.

[Ker02b] M. J. Kerr and A. Cuevas. Recombination at the interface between silicon and stoichiometric plasma silicon nitride. *Semicond. Sci. Technol.*, 17: 166–172, 2002b.

[Ker02a] M. J. Kerr and A. Cuevas. General parameterization of Auger recombination in crystalline silicon. *J. Appl. Phys.*, 91: 2473–2480, 2002a.

[Kin55] R. H. Kingston and S. F. Neustadter. Calculation of the Space Charge, Electric Field, and Free Carrier Concentration at the Surface of a Semiconductor. *J. Appl. Phys.*, 26: 718–720, 1955.

[Kit01] C. Kittel and H. Krömer. *Thermodynamik*, chapter 2, pages 55–57. Oldenbourg, München, Wien, 5 edition, 2001.

[Kla92a] D. Klaassen. A unified mobility model for device simulation – I. Model equations and concentration dependence. *Solid State Electron.*, 35: 953–959, 1992a.

[Kla92b] D. Klaassen. A unified mobility model for device simulation –II. Temperature Dependence of Carrier Mobility and Lifetime. *Solid State Electron.*, 35: 961–967, 1992b.

[Kli02] E. Klimkovsky, J. K. Rath, R. E. I. Schropp, and F. A. Rubinelli. Errors introduced in a-Si:H-based solar cell modeling when dangling bonds are approximated by decoupled states. *Thin Solid Films*, 422: 211–219, 2002.

[Kon08] M. Kondo, S. D. Wolf, and H. Fujiwara. Understanding of Passivation Mechanism in Heterojunction c-Si Solar Cells. In *Mater. Res. Soc. Symp. Proc.*, volume 1066. MRS, 2008.

[Kor06a] L. Korte. *Die elektronische Struktur des amorph-kristallinen Silizium-Heterostruktur-Kontakts*. PhD thesis, University of Marburg, 2006a.

[Kor06b] L. Korte, A. Laades, and M. Schmidt. Electronic states in a-Si:H/c-Si heterostructures. *J. Non-Cryst. Solids*, 352: 1217–1220, 2006b.

[Kot95] D. E. Kotecki and J. D. Chapple-Sokol. Hydrogen incorporation in silicon nitride films deposited by electron-cyclotron-resonance chemical vapor deposition. *J. Appl. Phys.*, 77: 1284–1293, 1995.

[Kri88] D. T. Krick and P. M. Lenahan. Nature of the dominant deep trap in amorphous silicon nitride. *Phys. Rev. B*, 38: 8226–8229, 1988.

[Kuh95] B. Kuhlmann, A. G. Aberle, and R. Hezel. Two-dimensional numerical optimisation study of inversion layer emitters of silicon solar cells. In *Proc. 13th EU PVSEC*, pages 1209–1212, Nice, France, 1995.

[Küh00] R. Kühn, P. Fath, and E. Bucher. Effects of pn-junction bordering on surfaces investigated by means of 2Dmodeling. In *Proc. 28th IEEE PVSC*, pages 116–119, Anchorage, AL, 2000.

[Lan02] M. Langenkamp and O. Breitenstein. Classification of shunting mechanisms in crystalline silicon solar cells. *Sol. Energy Mater. Sol. Cells*, 72: 433–440, 2002.

[Lau73a] S. E. Laux. *Two-Dimensional Simulation of Gallium-Arsenide MEFSET's Using the Finit-Element Method.* PhD thesis, University of Michigan, 1973a.

[Lau73b] S. E. Laux and R. J. Lomax. Effect of Mesh Spacing on Static Negative Resistance in GaAs MESFET Simulation. *IEEE Trans. Electron Devices*, ED-28: 708–714, 1973b.

[Lau96] T. Lauinger, J. Schmidt, A. G. Aberle, and R. Hezel. Record low surface recombination velocities on 1 Ωcm p-type silicon using remote plasma silicon nitride passivation. *Appl. Phys. Lett.*, 68: 1232–1234, 1996.

[Lax59] M. Lax. Giant traps. *J. Phys. Chem. Solids*, 8: 66–73, 1959.

[Lee80] K. Lee and A. Nussbaum. The influences of traps on the generation-recombination current in silicon diodes. *Solid State Electron.*, 23: 655–660, 1980.

[Lee10b] C. Leendertz, R. Stangl, T. F. Schulze, M. Schmidt, and L. Korte. A recombination model for a-Si:H/c-Si heterostructures. *Phys. Status Solidi C*, 7: 1005–1010, 2010b.

[Lee10a] C. Leendertz, N. Mingirulli, T. F. Schulze, J.-P. Kleider, B. Rech, and L. Korte. Physical insight into interface passivation of a-Si:H/c-Si heterostructures by analysis of injection-dependent lifetime and band bending. In *Proc. 25th EU PVSEC*, pages 1377–1381, Valencia, Spain, 2010a. WIP, Munich.

[Leg96] C. Leguijt, P. Lölgen, J. A. Eikelboom, A. W. Weeber, F. M. Schuurmans, W. C. Sinke, P. F. A. Alkemade, P. M. Sarro, C. H. M. Maree, and L. A. Verhoef. Low temperature surface passivation for silicon solar cells. *Sol. Energy Mater. Sol. Cells*, 40: 297–345, 1996.

[Li08] T.-T. A. Li, K. R. McIntosh, and A. Cuevas. Limitations of a simplified dangling bond recombination model for a-Si:H. *J. Appl. Phys.*, 104: 113718, 2008.

[Lim10] B. Lim, F. Rougieux, D. Macdonald, K. Bothe, and J. Schmidt. Generation and annihilation of boron–oxygen-related recombination centers in compensated p- and n-type silicon. *J. Appl. Phys.*, 108: 103722, 2010.

[Mac00] D. Macdonald and A. Cuevas. The trade-off between phosphorus gettering and thermal degradation in multicrystalline silicon. In *Proc. 16th EU PVSEC*, pages 1707–1710, Glasgow, UK, 2000.

[Mac04a] D. Macdonald and L. J. Geerligs. Recombination activity of interstitial iron and other transition metal point defects in p- and n-type crystalline silicon. *Appl. Phys. Lett.*, 85: 4061–4063, 2004a.

[Mac04b] D. H. Macdonald, L. J. Geerligs, and A. Azzizi. Iron detection in crystalline silicon by carrier lifetime measurements for arbitrary injection and doping. *J. Appl. Phys.*, 95: 1021–1028, 2004b.

[Mah80] G. Mahan. Energy gap in Si and Ge: Impurity dependence. *J. Appl. Phys.*, 51: 2634–2646, 1980.

[Man65] A. Many, Y. Goldstein, and N. B. Grove. *Semiconductor Surfaces.* North-Holland Publishing Company, Amsterdam, Netherlands, 1965.

[Man74] O. Manck, H. H. Heimeier, and W. L. Engl. High injection in a two-dimensional transistor. *IEEE Trans. Electron Devices*, ED-21: 403–409, 1974.

[Mar74] M. Marsden. Cubic spline interpolation of continuous functions. *J. Approx. Theory*, 10: 103–111, 1974.

[Mar82] P. A. Markowich, C. A. Ringhofer, S. Selberherr, and E. Langer. A singularly perturbed boundary value problem modelling a semiconductor device. Report 2482, MRC, *University of Wisconsin*, 1982.

[Mar83] P. A. Markowich, C. A. Ringhofer, E. Langer, and S. Selberherr. An asymptotic analysis of single-junction semiconductor devices. Report 2527, MRC, *University of Wisconsin*, 1983.

[McI00a] K. R. McIntosh and C. B. Honsberg. In *Proc. 16th EU PVSEC*, pages 1651–1654, Glasgow, UK, 2000a. James & James, London, UK.

[McI00b] K. R. McIntosh, P. P. Altermatt, and G. Heiser. In *Proc. 16th EU PVSEC*, pages 243–246, Glasgow, UK, 2000b. James & James.

[McI01] K. R. McIntosh. *Lumps, humps and bumps: three detrimental effects in the current-voltage curve of silicon solar cells.* PhD thesis, UNSW, School of Electrical Engineering, Sydney, 2001.

[Mer01] A. Merazga, A. F. Meftah, A. M. Meftah, C. Main, and S. Reynolds. Defect pool model based transient photoconductivity and the condution band tail profile in a–Si:H. *J. Phys.: Condens. Matter*, 13: 10969–10977, 2001.

[Mön01] W. Mönch. *Semiconductor Surfaces and Interfaces.* Springer Series in surfaces sciences. Springer, Berlin, Heidelberg, 3rd edition, 2001.

[Mot90] N. Mott. *Metal-Insulator Transitions.* Taylor & Francis, London, 1990.

[N9́7] V. Nádaždy, R. Durný, and E. Pinčik. Evidence for the Improved Defect-Pool Model for Gap States in Amorphous Silicon from Charge DLTS Experiments on Undoped a-Si:H. *Phys. Rev. Lett.*, 78: 1102–1105, 1997.

[Nag99] H. Nagel, C. Berge, and A. G. Aberle. Generalized analysis of quasi-steady-state and quasi-transient measurements of carrier lifetimes in semiconductors. *J. Appl. Phys.*, 86: 6218–6221, 1999.

[New71] I. Newton. Methodus fluxionum et serierum infinitarum, 1664–1671.

[New91] R. C. Newman, J. H. Tucker, A. R. Brown, and S. A. McQuaid. Hydrogen diffusion and the catalysis of enhanced oxygen diffusion in silicon at temperatures below 500 °C. *J. Appl. Phys*, 70: 3061–3070, 1991.

[Nor89] J. E. Northrup. Effective correlation energy of a Si dangling bond calculated with the local-spin-density approximation. *Phys. Rev. B*, 40: 5875–5878, 1989.

[Nus73] A. Nussbaum. Generation-recombination characteristic behavior of silicon diodes. *Phys. Status Solidi A*, 19: 441–450, 1973.

[Ohr11] T. Ohrdes, S. Steingrube, H. Wagner, C. Zechner, G. Letay, R. Chen, S. T. Dunham, and P. P. Altermatt. Solar cell emitter design with PV-tailored implantation. In *Proc. 1st Silicon PV*, Freiburg, Germany, 2011. *accepted* for publication in Energia Procedia.

[Oli07] S. Olibet, E. Vallat-Sauvain, and C. Ballif. Model for a-Si:H/c-Si interface recombination based on the amphoteric nature of silicon dangling bonds. *Phys. Rev. B*, 76: 035326, 2007.

[Ort70] J. M. Ortega and W. C. Rheinboldt. *Iterative Solution of Nonlinear Equations in Several Variables.* Academic Press, New York, 1970.

[Ove87] R. J. V. Overstraeten and R. P. Mertens. Heavy doping effects in silicon. *Solid State Electron.*, 30: 1077–1087, 1987.

[Pal97] J. Pallarès, L. F. Marsal, X. Correig, J. Calderer, and R. Alcubilla. Space charge recombination in p–n junctions with a discrete and continuous trap distribution. *Solid State Electron.*, 41: 17–23, 1997.

[Pap08] L. M. G. J. Papaioannou, D. N. Kouvatsos, and A. T. Voutsas. An experimental study of band gap states electrical properties in poly-Si TFTs by the analysis of the transient currents. *Phys. Status Solidi C*, 5: 3613–3616, 2008.

[Pla07] H. Plagwitz. *Surface passivation of crystalline silicon solar cells by amorphous silicon films.* PhD thesis, Leibniz University of Hannover, 2007.

[Pla08] H. Plagwitz, B. Terheiden, and R. Brendel. Staebler-Wronski-like formation of defects at the amorphous-silicon-crystalline silicon interface during illumination. *J. Appl. Phys.*, 103: 094506, 2008.

[Pow93] M. J. Powell and S. C. Deane. Improved defect-pool model for charged defects in amorphous silicon. *Phys. Rev. B*, 48: 10815–10827, 1993.

[Pow96] M. J. Powell and S. C. Deane. Defect-pool model and the hydrogen density of states in hydrogenated amorphous silicon. *Phys. Rev. B*, 53: 10121–10131, 1996.

[Que62] H. J. Queisser. Forward characteristics and efficiencies of silicon solar cells. *Solid State Electron.*, 1: 1–10, 1962.

[Reb96] M. Rebaudengo and M. Reorda. A genetic algorithm for floorplan area optimization. *Comput. Aided Des.*, 15: 911–1000, 1996.

[Rei03] S. Rein and S. W. Glunz. Electronic Properties of the Metastable Defect in Boron-Doped Czochralski Silicon: Unambiguous Determination by Advanced Lifetime Spectroscopy. *Appl. Phys. Lett.*, 82: 1054–1056, 2003.

[Rei05b] S. Rein and S. W. Glunz. Electronic properties of interstitial iron and iron-boron pairs determined by means of advanced lifetime spectroscopy. *J. Appl. Phys.*, 98: 113711, 2005b.

[Rei05a] S. Rein and S. W. Glunz. Advanced lifetime spectroscopy - defect parameters of iron in silicon and a new fingerprint. In *Proc. 20th EU-PVSEC*, pages 753–756, Barcelona, Spain, 2005a.

[Rho88] E. H. Rhoderick and R. H. Williams. *Metal-Semiconductor Contacts.* Clarendon (Oxford, UK), 1988.

[Riz91] R. Rizk, P. de Mierry, D. Ballutaud, and M. Aucouturier. Hydrogen diffusion and passivation processes in p- and n-type crystalline silicon. *Phys. Rev. B*, 44: 6141–6151, 1991.

[Rob95] S. J. Robinson, S. R. Wenham, P. P. Altermatt, A. G. Aberle, G. Heiser, and M. A. Green. Recombination rate saturation mechanisms at oxidized surfaces of high-efficiency silicon solar cells. *J. Appl. Phys.*, 78: 4740–4754, 1995.

[Ros55] A. Rose. Recombination Processes in Insulators and Semiconductors. *Phys. Rev. B*, 97: 322–333, 1955.

[Ros63] A. Rose. *Concepts in photoconductivity and allied problems.* Interscience Publ., New York, NY, 1963.

[Rüd11] M. Rüdiger, M. Rauer, C. Schmiga, M. Hermle, and S. W. Glunz. Accurate modeling of aluminum-doped silicon. In *Proc. 1st Silicon PV*, Freiburg, Germany, 2011. *accepted* for publication in Energia Procedia.

[Sah57] C.-T. Sah, R. N. Noyce, and W. Shockley. *Proc. of the IRE*, 45: 1228–1243, 1957.

[Sah58] C.-T. Sah and W. Shockley. Electron-Hole Recombination Statistics in Semiconductors through Flaws with Many Charge Conditions. *Phys. Rev.*, 109: 1103–1115, 1958.

[Sak86] I. Sakata and Y. Hayashi. Theoretical Analysis on the Limitations of the Open-Circuit Voltage of a Hydrogenated Amorphous Silicon p-i-n Solar Cell. *Appl. Phys. A*, 39: 277–286, 1986.

[Sch92] A. Schenk. A model for the field and temperature dependence of Schockley-Read-Hall lifetimes in Silicon. *Solid State Electron.*, 35: 1558–1596, 1992.

[Sch94a] D. Schroeder. *Modelling of Interface Carrier Transport for Device Simulation.* Springer, Wien, New York, 1994a.

[Sch94b] G. Schumm. Chemical equilibrium description of stable and metastable defect structures in a-Si:H. *Phys. Rev. B*, 49: 2427–2442, 1994b.

[Sch95] A. Schenk and U. Krumbein. Coupled defect-level recombination: Theory and application to anomalous diode characteristics. *J. Appl. Phys.*, 78: 3185–3192, 1995.

[Sch96] J. Schmal. Defect-pool model for doped a-Si:H. *J. Non-Cryst. Solids*, 198–200, Part 1 and 2: 387–390, 1996.

[Sch97] J. Schmidt, F. M. Schuurmans, W. C. Sinke, S. W. Glunz, and A. G. Aberle. Observation of multiple defect states at silicon-silicon nitride interfaces fabricated by low-frequency plasma-enhanced chemical vapor deposition. *Appl. Phys. Lett.*, 71: 252–254, 1997.

[Sch98a] A. Schenk. *Advanced physical models for silicon device simulation.* Computational Microelectronics. Springer, Wien, New-York, 1998a.

[Sch98b] A. Schenk. Finite-temperature full random-phase approximation model of band gap narrowing for silicon device simulation. *J. Appl. Phys.*, 84: 3684–3695, 1998b.

[Sch99a] J. Schmidt and A. G. Aberle. Carrier recombination at silicon-silicon nitride interfaces fabricated by plasma-enhanced chemical vapor deposition. *J. Appl. Phys.*, 85: 3626–3633, 1999a.

[Sch99b] J. Schmidt and A. Cuevas. Electronic properties of light-induced recombination centers in boron-doped Czochralski silicon. *J. Appl. Phys.*, 86: 3175–3180, 1999b.

[Sch01] J. O. Schumacher, P. P. Altermatt, G. Heiser, and A. G. Aberle. Application of an improved band-gap narrowing model to the numerical simulation of recombination properties of phosphorus-doped silicon emitters. *Sol. Energy Mater. Sol. Cells*, 65: 95–103, 2001.

[Sch04b] C. Schmiga, H. Nagel, S. Steckemetz, and R. Hezel. 17% efficient multicrystalline silicon solar cells with rear thermal oxide passivation. In *Proc. 19th EU PVSEC*, pages 1060–1063, Paris, France, 2004b.

[Sch04a] J. Schmidt, J. D. Moschner, J. Henze, S. D. S, and R. Hezel. Recent progress in the surface passivation of silicon solar cells using silicon nitride. In *Proc. 19th EU PVSEC*, pages 391–396, Paris, France, 2004a.

[Sch06] A. Schenk, P. P. Altermatt, and B. Schmithusen. Physical Model of Incomplete Ionization for Silicon Device Simulation. In *International Conference on Simulation of Semiconductor Processes and Devices*, 2006.

[Sch07b] M. Schmidt, L. Korte, A. Laades, R. Stangl, C. Schubert, H. Angermann, E. Conrad, and K. v Maydell. Physical aspects of a-Si:H/c-Si heterojunction solar cells. *Thin Solid Films*, 515: 7475–7480, 2007b.

[Sch07a] J. Schmidt, K. Bothe, R. Bock, C. Schmiga, R. Krain, and R. Brendel. N-type silicon – the better material choice for industrial high-efficiency solar cells? In *Proc. 22nd EU PVSEC*, pages 998–1001, Milan, Italy, 2007a.

[Sch08c] M. F. Schubert, F. W. Mont, S. Chhajed, D. J. Poxson, J. K. Kim, and E. F. Schubert. Design of multilayer antireflection coatings made from co-sputtered and low-refractive-index materials by genetic algorithm. *Opt. Express*, 16: 5290–5298, 2008c.

[Sch08a] J. Schmidt, A. Merkle, R. Brendel, B. Hoex, M. C. M. van de Sanden, and W. M. M. Kessels. Surface Passivation of High-efficiency Silicon Solar Cells by Atomic-layer-deposited Al_2O_3. *Prog. Photovoltaics: Res. Appl.*, 16: 461–466, 2008a.

[Sch08b] J. Schmidt, A. Merkle, B. Hoex, M. C. M. van de Sanden, W. M. M. Kessel, and R. Brendel. Atomic-layer-deposited aluminum oxide for the atomic-layer-deposited aluminum oxide for the surface passivation of high-efficiency silicon solar cells. In *33rd IEEE PVSC*, San Diego, CA, 2008b.

[Sch09] J. Schmidt, N. Thiemann, R. Bock, and R. Brendel. Recombination lifetimes in highly aluminum-doped silicon. *J. Appl. Phys.*, 106: 093707, 2009.

[Sch11] T. F. Schulze, C. Leendertz, N. Mingirulli, L. Korte, and B. Rech. Impact of Fermi-level dependent defect equilibration on V_{oc} of amorphous/crystalline silicon heterojunction solar cells. In *Proc. 1st Silicon PV*, Freiburg, Germany, 2011. *accepted* for publication in Energia Procedia.

[SD] Sentaurus-Device. Synopsys Inc., Mountain View, CA. URL `www.synopsys.com/products/tcad/tcad.html`.

[Sei10] M. Seibt. private communications, 2010. University of Göttingen.

[Sel84] S. Selberherr. *Analysis and Simulation of Semiconductor Devices.* Springer, Wien, New-York, 1984.

[Shi80] E. Shiles, T. Sasaki, M. Inokuti, and D. Y. Smith. Self-consistency and sum-rule tests in the Kramers-Kronig analysis of optical data: Application to aluminium. *Phys. Rev. B*, 22: 1612–1628, 1980.

[Sho49] W. Shockley. The theory of p-n junctions in semiconductors and p-n junction transistors. *Bell Sys. Tech. J.*, 28: 435–489, 1949.

[Sho52] W. Shockley and W. T. Read. Statistics of the Recombination of Holes and Electrons. *Phys. Rev.*, 87: 835–842, 1952.

[Sik82] K. Sikorski. Bisection is optimal. *Numeri. Math.*, 40: 111–117, 1982.

[Sim71] J. G. Simmons and G. W. Taylor. Nonequilibrium Steady-State Statistics and Associated Effects for Insulators and Semiconductors Containing an Arbitrary Distribution of Traps. *Phys. Rev. B*, 4: 502–511, 1971.

[Sin96] R. A. Sinton, A. Cuevas, and M. Stuckings. Quasi-Steady-State Photoconductance, A New Method for Solar Cell Material and Device Characterization. In *Proc. 25th IEEE PVSC*, pages 457–460, Washington, D. C., 1996.

[Smi87] Z. E. Smith and S. Wagner. Band tails, entropy, and equilibrium defects in hydrogenated amorphous silicon. *Phys. Rev. Lett.*, 59: 688–691, 1987.

[Sno86] C. M. Snowden and E. Snowden. *Introduction to Semiconductor Device Modelling.* World Scientific, Singapore, 1986.

[Sop02] B. Sopori, Y. Zhang, R. Reedy, K. Jones, N. M. Ravindra, S. Rangan, and S. Ashok. Trapping and Detrapping of H in Si: Impact on Diffusion Properties and Solar Cell Processing. In *Mat. Rs. Soc. Symp. Proc.*, volume 719, pages 125–131, 2002.

[Sop05] B. Sopori, R. Reedy, K. Jones, Y. Yan, M. Al-Jassim, Y. Zhang, B. Bathey, and J. Kalejs. A Comprehensive Model of Hydrogen Transport into a Solar Cell During Silicon Nitride Processing for Fire-Through Metallization. In *Proc. 31st IEEE PVSC*, Orlando, Florida, 2005. IEEE, New York.

[SP] Sentaurus-Process. Synopsys Inc., Mountain View, CA. URL `www.synopsys.com/products/tcad/tcad.html`.

[Spr94] A. B. Sproul. Dimensionless solution of the equation describing the effect of surface recombination on carrier decay in semiconductors. *J. Appl. Phys.*, 76: 2851–2854, 1994.

[Sta77] D. L. Staebler and C. R. Wronski. Reversible conductivity changes in discharge-produced amorphous Si. *Appl. Phys. Lett.*, 31: 292–294, 1977.

[Sta03] R. Stangl, A. Froitzheim, M. Schmidt, and W. Fuhs. Design criteria for amorphous/crystalline silicon heterojunction solar cells - a simulation study. In *Proc. 3rd WCPEC*, volume 2, pages 1005–1008, Osaka, Japan, 2003. IEEE, New York.

[Ste10a] S. Steingrube, P. P. Altermatt, J. Schmidt, and R. Brendel. Modelling c-Si/SiN$_x$ interface recombination by surface damage. *Phys. Status Solidi RRL*, 4: 91–93, 2010a.

[Ste10b] S. Steingrube, P. P. Altermatt, D. S. Steingrube, J. Schmidt, and R. Brendel. Interpretation of recombination at c-Si/SiN$_x$ interfaces by surface damage. *J. Appl. Phys.*, 108: 014506, 2010b.

[Ste10c] S. Steingrube, P. P. Altermatt, D. Zielke, F. Werner, J. Schmidt, and R. Brendel. Reduced passivation of silicon surfaces at low injection densities caused by H-induced defects. In *Proc. 25th EU PVSEC*, pages 1748–1754, Valencia, Spain, 2010c.

[Ste10d] S. Steingrube, D. S. Steingrube, R. Brendel, and P. P. Altermatt. Comprehensive model for recombination at a-Si:H/c-Si interfaces based on amphoteric defects. *Phys. Status Solidi C*, 7: 276–279, 2010d.

[Ste11b] S. Steingrube, R. Brendel, and P. P. Altermatt. Limits to Shockley-Read-Hall (SRH) statistics for quantifying recombination via amphoteric defects. *submitted to* Phys. Status Solidi A, 2011b.

[Ste11a] S. Steingrube, O. Breitenstein, K. Ramspeck, S. Glunz, A. Schenk, and P. P. Altermatt. Explanation of commonly observed shunt currents in c-Si solar cells by means of recombination statistics beyond the Shockley-Read-Hall approximation. *J. Appl. Phys*, 2011a. in press.

[Ste11c] S. Steingrube, H. Wagner, H. Hannebauer, S. Gatz, R. Chen, T. Dullweber, S. T. Dunham, P. P. Altermatt, and R. Brendel. Loss analysis and improvements of industrially fabricated Cz-Si solar cells by means of process and device simulations. In *Proc. 1st Silicon PV*, Freiburg, Germany, 2011c. *accepted* for publication in Energia Procedia.

[Sto98] M. Stocks and A. Cuevas. Surface recombination velocity of thermally oxidised multicrystalline silicon. In *Proc. 2nd WCPEC*, pages 1623–1626, Vienna, Austria, 1998.

[Str84] R. A. Street. Disorder effects on deep trapping in amorphous semiconductors. *Philos. Mag. B*, 49: L15–L20, 1984.

[Str89] R. A. Street and K. Winer. Defect equilibria in undoped a-Si:H. *Phys. Rev. B*, 40: 6236–6249, 1989.

[Str91b] R. A. Street. *Hydrogenated amorphous silicon.* Cambridge Solid State Science Series, 1991b.

[Str91a] R. A. Street. Hydrogen chemical potential and structure of a-Si:H. *Phys. Rev. B*, 43: 2454–2457, 1991a.

[Stu85] M. Stutzmann, W. B. Jackson, and C. C. Tsai. Light-induced metastable defects in hydrogenated amorphous silicon: A systematic study. *Phys. Rev. B*, 32: 23–47, 1985.

[Stu86] M. Stutzmann. Annealing of metastable defects in hydrogenated amporphous silicon. *Phys. Rev. B*, 34: 63–72, 1986.

[Stu89] M. Stutzmann. The defect density in amorphous silicon. *Philos. Mag. B*, 60: 531–546, 1989.

[Stu92] M. Stutzmann. A comment on thermal defect creation in hydrogenated amorphous silicon. *Philos. Mag. Lett.*, 66: 147–150, 1992.

[Sun94] V. Suntharalingam and V. M. Branz. On modeling trivalent dangling bonds with bivalent levels. In E. A. Schiff, M. Hack, A. Madan, M. Powell, and A. Matsuda, editors, *Amorphous Silicon Technology, Materials research society symposium proceedings*, volume 336, pages 153–158, 1994.

[Sze81] S. M. Sze. *Physics of Semiconductor Devices.* Wiley, New York, 2 edition, 1981.

[Tag00] M. Taguchi, K. Kawamoto, S. Tsuge, T. Baba, H. Sakata, M. Morizane, K. Uchihashi, N. Nakamura, S. Kiyama, and O. Oota. HIT$^{\mathrm{TM}}$ Cells — High-Efficiency Crystalline Si Cells with novel Structure. *Prog. Photovolt. Res. Appl.*, 8: 503–513, 2000.

[Tan92] M. Tanaka, M. Taguchi, T. Matsuyama, T. Sawada, S. Tsuda, S. Nakano, H. Hanafusa, and Y. Kuwano. Development of New a-Si/c-Si Heterojunction Solar Cells: ACJ-HIT (Artificially Constructed Junction-Heterojunction with Intrinsic Thin-Layer). *Jpn. J. Appl. Phys.*, 31: 3518–3522, 1992.

[Tan99] K. Tanaka, E. Maruyama, T. Shimada, and H. Okamoto. *Amorphous Silicon*, volume 148–155. John Wiley & Sons, Chichester, 1999.

[Tho65] D. G. Thomas, J. J. Hopfield, and W. M. Augistyniak. Kinetics of radiative recombination at randomly distributed donors and acceptors. *Phys. Rev.*, 140: A202–A220, 1965.

[Thu80a] W. R. Thurber, R. L. Mattis, Y. M. Liu, and J. J. Filiben. Resistivity-dopant density relationship for boron-doped silicon. *J. Electrochem. Soc.*, 127: 2291–2294, 1980a.

[Thu80b] W. R. Thurber, R. L. Mattis, Y. M. Liu, and J. J. Filiben. Resistivity-dopant density relationship for phosphorus-doped silicon. *J. Electrochem. Soc.*, 127: 1807–1812, 1980b.

[Tru03] T. Trupke, M. A. Green, P. Würfel, P. P. Altermatt, A. Wang, J. Zhao, and R. Corkish. Temperature dependence of the radiative recombination coefficient of intrinsic crystalline silicon. *J. Appl. Phys.*, 94: 4930–4937, 2003.

[Vai86] F. Vaillant and D. Jousse. Recombination at dangling bonds and steady-state photoconductivity in a-Si:H. *Phys. Rev. B*, 34: 4088–4098, 1986.

[Vas77] A. B. Vasil'eva and V. G. Stel'makh. Singularly disturbed systems of the theory of semiconductor devices. *Math. Fiz.*, 17: 339–348, 1977.

[Vas78] A. B. Vasil'eva and V. F. Butuzov. Singularly perturbed equations in the critical case. Translated Report 2039, MRC, *University of Wisconsin*, 1978.

[vC97] M. W. M. van Cleef, J. K. Rath, F. A. Rubinelli, C. H. M. van der Werf, R. E. I. Schropp, and W. F. van der Weg. Performance of heterojunction p^+ microcrystalline silicon n crystalline silicon solar cells. *J. Appl. Phys.*, 82: 6089–6905, 1997.

[vdH05] A. S. H. van der Heide, A. Schönecker, J. H. Bultman, and W. C. Sinke. Explanation of high solar cell diode factors by nonuniform contact resistance. *Prog. Photovolt. Res. Appl.*, 13: 3–16, 2005.

[vM06] K. v Maydell, E. Conrad, and M. Schmidt. Efficient Silicon Heterojunction Solar Cells Based on p- and n-type Substrates Processed at Temperatures $< 220\,^\circ$C. *Prog. Photovolt: Res. Appl.*, 14: 289–295, 2006.

[Wan90] A. Wang, J. Zhao, and M. A. Green. 24% efficient silicon solar cells. *Appl. Phys. Lett.*, 57: 602–604, 1990.

[Wan04] T. H. Wang, E. Iwaniczko, M. R. Page, D. H. Levi, Y. Yan, H. M. Branz, Q. Wang, V. Yelundur, and A. Rohatgi. Hydrogenated Amorphous Silicon Emitter and Back-Surface-Field Contacts for Crystalline Silicon Solar Cells. In *Proc. DOE Solar Energy Technologies*, volume CP-520-37033. NREL, 2004.

[Web94] K. J. Weber and H. Jin. Improved silicon surface passivation achieved by negatively charged silicon nitride films. *Appl. Phys. Lett.*, 94: 0635091–3, 1994.

[Web08] J. Weber. Hydrogen in semiconductors: From basic physics to technology. *Phys. Status Solidi C*, 5: 535–538, 2008.

[Web09] K. J. Weber and H. Jin. Improved silicon surface passivation achieved by negatively charged silicon nitride films. *Appl. Phys. Lett.*, 94: 063509, 2009.

[Wen85] S. R. Wenham, M. R. Willison, S. Narayanan, and M. A. Green. Efficiency improvement in screen printed polycrystalline silicon solar cells by plasma treatments. In *Proc. 18th IEEE PVSC*, pages 1008–1013, Las Vegas, NV, 1985. IEEE, New York.

[Wer10] F. Werner, B. Veith, D. Zielke, L. Kühnemund, C. Tegenkamp, M. Seibt, J. Schmidt, and R. Brendel. Improved understanding of recombination at the Si/Al_2O_3 interface. In *Proc. 25th EU PVSEC*, pages 1121–1124, Valencia, Spain, 2010. WIP, Munich.

[Wik11] Wikipedia. Brent's method — Wikipedia, The Free Encyclopedia, 2011. URL `http://en.wikipedia.org/w/index.php?title=Brent$%$27s_method$&$oldid=410708027`. [Online; accessed 28-February-2011].

[Wil98] J. A. Willemen. *Modelling of amorphous silicon single- and multi-junction solar cells*. PhD thesis, TU Delft, 1998.

[Win90] K. Winer. Defect formation in a-Si:H. *Phys. Rev. B*, 41: 12150–12161, 1990.

[Wol63] M. Wolf and H. Rauschenbach. Series resistance effects on solar cell measurements. *Advanced Energy Conversion*, 3: 455–479, 1963.

[Wyr91] N. Wyrsch and A. Shah. Depth profiles of mobility lifetime products and capture cross-sections in a-Si:H. *J. Non-Cryst. Solids*, 137–138: 431–434, 1991.

[You61] C. E. Young. Extended Curves of the Space Charge, Electric Field, and Free Carrier Concentration at the Surface of a Semiconductor, and Curves of the Electrostatic Potential Inside a Semiconductor. *J. Appl. Phys.*, 32: 329–332, 1961.

[Zie10a] D. Zielke. *private communications*, 2010a.

[Zie10b] D. Zielke. Rückseitenpassivierung von kristallinen Siliciumsolarzellen mit Aluminiumoxid, 2010b.

Abbreviations and symbols

Abbreviations

abbreviation	**meaning**
ALD	atomic layer deposition
alnealed	aluminum annealed
Al_2O_3	stoichiometric aluminum oxide
Al–p^+	highly aluminum doped
a-Si	amorphous silicon
a-Si:H	hydrogenated amorphous silicon
a-Si:H(i), a-Si:H(n), a-Si:H(p)	intrinsic, n-type, p-type hydrogenated amorphous silicon
BGN	bandgap narrowing
BSF	back surface field
CCS	capture cross sections
c-Si	crystalline silicon
c-Si(n), c-Si(p)	n-type, p-type crystalline silicon
Cz	Czochralski grown
DAP	donor-acceptor pair
DB	dangling bond
DL	demarcation level
DPM	defect-pool model
EA	evolutionary algorithm
ECV	electrochemical capacitance-voltage
FDM	finite differences method
FZ	float-zone silicon
GA	genetic algorithm
HRTEM	high resolution transmission electron microscopy
I-V	current voltage characteristics
ISFH	Institute for Solar Energy Research Hamelin
LPCVD	low-pressure chemical vapor deposition

MPP	maximum power point
n-Si, p-Si	n-type, p-type silicon
PA-ALD	plasma assisted ALD
PECVD	plasma enhanced chemical vapor deposition
PERC	Passivated Emitter and Rear Cell
PERL	Passivated Emitter and Rear Locally-diffused
PV	photovoltaics
QFL	quasi-Fermi level
QSSPC	quasi-steady-state photoconductance method
SCR	surface-charge region
SDR	surface-damage region
SEM	scanning electron microscope
SRH	Shockley-Read-Hall
SiN_x	amorphous silicon nitride
SiO_2	stoichiometric silicon oxide
1 sun	illumination of an AM1.5G spectrum with an intensity of $100\,mW/cm^2$
th-ALD	thermal ALD
TQFL	trap quasi-Fermi level
WB	weak bond

Table A.1: Abbreviations.

Mathematical symbols

abbreviation	value	description
$E_\mathrm{g}^\text{c-Si}$	1.12 eV	c-Si energy bandgap
β	$1/k_BT$	thermal energy
h	$6.62606896(33) \times 10^{-34}$ Js	Planck's constant
k_B	$1.3806504(24) \times 10^{-23}$ JK^{-1}	Boltzmann's constant
N_c	2.86×10^{19} cm^{-3}	conduction band effective density of states at 300 K in Si
N_v	3.10×10^{19} cm^{-3}	valence band effective density of states at 300 K in Si
q	$1.602176487 \times 10^{-19}$ As	elementary charge
ε_r	11.9	relative permittivity of c-Si and a-Si
ε_0	$8.854187817 \times 10^{-12}$As/(Vm)	vacuum permittivity

Table A.2: Quantities taken as constants.

abbreviation	unit	description
A	cm^2	area
φ_s	V	surface band-bending
c_n, c_p	s^{-1}	capture coefficient of electrons and holes
$c_\mathrm{n,0}$, $c_\mathrm{p,0}$	s^{-1}	capture coefficient of electrons and holes in thermal equilibrium
$c_\mathrm{n,0}^+$, $c_\mathrm{n,0}^0$	s^{-1}	equilibrium capture coefficient of electrons for positively charged and neutral states
c_n^+, c_n^0	s^{-1}	capture coefficient of electrons for positively charged and neutral states
$c_\mathrm{p,0}^-$, $c_\mathrm{p,0}^0$	s^{-1}	equilibrium capture coefficient of holes for negatively charged and neutral states
c_p^-, c_p^0	s^{-1}	capture coefficient of holes for negatively charged and neutral states
Δn	cm^{-3}	excess carrier density / injection density
D_it	cm^{-2}eV^{-1}	interface defect distribution
D_it^A, D_it^D	cm^{-2}eV^{-1}	interface defect distribution of acceptors and donors
$D_\mathrm{it}^\mathrm{corr}$	cm^{-2}eV^{-1}	interface defect distribution of correlated defects
$D_\mathrm{it}^\mathrm{DB}$	cm^{-2}eV^{-1}	DB interface defect distribution
E_c0, E_v0	eV	conduction and valence band edge of the intrinsic semiconductor
E_c, $E_\mathrm{c}^\text{c-Si}$	eV	conduction band edge of c-Si

$E_\mathrm{c}^\text{a-Si}$	eV	conduction band mobility edge of a-Si
E_d	eV	defect energy
$E_\mathrm{Dn}, E_\mathrm{Dp}$	eV	demarcation level for electrons and holes
$E_\mathrm{Dn}^\mathrm{a}, E_\mathrm{Dp}^\mathrm{a}$	eV	demarcation level for electrons and holes in amphoteric statistics
$E_\mathrm{Dn}^{-,\mathrm{a}}, E_\mathrm{Dn}^{0,\mathrm{a}}$	eV	demarcation level for electrons for negatively charged and neutral states in amphoteric statistics
$E_\mathrm{Dp}^{+,\mathrm{a}}, E_\mathrm{Dp}^{0,\mathrm{a}}$	eV	demarcation level for holes for positively charged and neutral states in amphoteric statistics
$E_\mathrm{Dn}^\mathrm{SRH}, E_\mathrm{Dp}^\mathrm{SRH}$	eV	demarcation for electrons and holes in SRH statistics
$E_\mathrm{Dn}^{-,\mathrm{SRH}}, E_\mathrm{Dn}^{0,\mathrm{SRH}}$	eV	demarcation level for electrons for negatively charged and neutral states in SRH statistics
$E_\mathrm{Dp}^{+,\mathrm{SRH}}, E_\mathrm{Dp}^{0,\mathrm{SRH}}$	eV	demarcation level for holes for positively charged and neutral states in SRH statistics
E_i	eV	Fermi energy of intrinsic material
E_corr	eV	correlation energy
E_f	eV	Fermi energy
E_fn, E_fp	eV	electron and hole quasi-Fermi energy
E_f^eq	eV	equilibration Fermi energy of a-Si:H
$E_\mathrm{f,i}^\mathrm{eq}$	eV	equilibration Fermi energy of a-Si:H(i)
$E_\mathrm{fn}^\text{c-Si}$, $E_\mathrm{fp}^\text{c-Si}$	eV	quasi-Fermi level in c-Si
$E_\mathrm{f,sh}$	eV	shift of E_f^eq in the DPM from $E_\mathrm{f,i}^\mathrm{eq}$
$E_\mathrm{f,sh}$	eV	shift of E_f^eq in the DPM from $E_\mathrm{f,i}^\mathrm{eq}$
E_g, $E_\mathrm{g}^\text{c-Si}$	eV	energy bandgap of c-Si
$E_\mathrm{g}^\text{a-Si}$	eV	energy bandgap a-Si
e_n, e_p	s^{-1}	emission coefficient of electrons and holes
$e_\mathrm{n}^\mathrm{SRH}$, $e_\mathrm{p}^\mathrm{SRH}$	s^{-1}	emission coefficient of electrons and holes for SRH statistics
$e_\mathrm{n,a}^{-}, e_\mathrm{n,a}^{0}$	s^{-1}	emission coefficient of electrons for negatively charged and neutral states for amphoteric statistics
$e_\mathrm{n,SRH}^{-}, e_\mathrm{n,SRH}^{0}$	s^{-1}	emission coefficient of electrons for negatively charged and neutral states
$e_\mathrm{p,a}^{+}$, $e_\mathrm{p,a}^{0}$	s^{-1}	emission coefficient of electrons for positively charged and neutral states for amphoteric statistics
$e_\mathrm{p,SRH}^{0}$, $e_\mathrm{p,SRH}^{+}$	s^{-1}	emission coefficient of holes for positively charged and neutral states
η	1	cell efficiency

$E_{\mathrm{Tn}}, E_{\mathrm{Tp}}$	eV	trap quasi-Fermi level for electrons and holes
$E_{\mathrm{Tn}}^{-}, E_{\mathrm{Tn}}^{0}$	eV	trap quasi-Fermi level for electrons for negatively charged and neutral states
$E_{\mathrm{Tp}}^{+}, E_{\mathrm{Tp}}^{0}$	eV	trap quasi-Fermi level for holes for positively charged and neutral states
$E_{\mathrm{Tn}}^{-,\mathrm{a}}, E_{\mathrm{Tn}}^{0,\mathrm{a}}$	eV	trap quasi-Fermi level for electrons for negatively charged and neutral states in amphoteric statistics
$E_{\mathrm{Tp}}^{+,\mathrm{a}}, E_{\mathrm{Tp}}^{0,\mathrm{a}}$	eV	trap quasi-Fermi level for holes for positively charged and neutral states in amphoteric statistics
$E_{\mathrm{Tn}}^{\mathrm{SRH}}, E_{\mathrm{Tp}}^{\mathrm{SRH}}$	eV	trap quasi-Fermi level for electrons and holes in SRH statistics
$E_{\mathrm{Tn}}^{-,\mathrm{SRH}}, E_{\mathrm{Tn}}^{0,\mathrm{SRH}}$	eV	trap quasi-Fermi level for electrons for negatively charged and neutral states in SRH statistics
$E_{\mathrm{Tp}}^{+,\mathrm{SRH}}, E_{\mathrm{Tp}}^{0,\mathrm{SRH}}$	eV	trap quasi-Fermi level for holes for positively charged and neutral states in SRH statistics
E_{v}, $E_{\mathrm{v}}^{\text{c-Si}}$	eV	valence band edge of c-Si
$E_{\mathrm{v}}^{\text{a-Si}}$	eV	valence band mobility edge of a-Si
FF	1	fill factor
I	mA	current
j	mA/cm^2	current density
j_{mpp}	mA/cm^2	maximum power point current density
$\vec{j}_{\mathrm{n}}$, $\vec{j}_{\mathrm{p}}$	A	current of electrons and holes
j_{sc}	mA/cm^2	short circuit current density
μ_{d}	J/mole	defect chemical potential
n_{D}	1	diode ideality factor
n, p	cm^{-3}	electron and hole density
n_0, p_0	cm^{-3}	electron and hole density in thermal equilibrium
n_{i}	cm^{-3}	intrinsic density
$n_{\mathrm{i,eff}}$	cm^{-3}	effective intrinsic density
N_{A}	cm^{-3}	acceptor density
N_{c0}	cm^{-3}eV^{-1}	conduction-band tail-state distribution
N_{d}	cm^{-3}	defect density
D^{DB}	cm^{-3}eV^{-1}	DB distribution
$D_{\mathrm{tot}}^{\mathrm{DB}}$	cm^{-3}	DB distribution D^{DB} integrated over energy
N_{D}	cm^{-3}	donor density
N_{dop}	cm^{-3}	dopant density
D_{Gauss}	cm^{-2}eV^{-1}	Gaussian surface defect distribution
N_{imp}	cm^{-3}	impurity density
N_{s}	cm^{-2}	surface defect density
N_{v0}	cm^{-3}eV^{-1}	valence-band tail-state distribution

P_{mpp}	$\mathrm{mW/cm^2}$	maximum power point power density
Q_{it}	$\mathrm{q/cm^2}$	effective interface charge density
$Q_{\mathrm{it}}^{\mathrm{A}}, Q_{\mathrm{it}}^{\mathrm{D}}$	$\mathrm{q/cm^2}$	charge density of acceptors and donors
$Q_{\mathrm{it}}^{\mathrm{corr}}$	$\mathrm{q/cm^2}$	charge density of correlated defects
Q_{f}	$\mathrm{q/cm^2}$	fixed surface charge density
Q_{it}^{*}	$\mathrm{q/cm^2}$	charge density at the actual interface
R_{Aug}	$\mathrm{cm^{-3}s^{-1}}$	Auger recombination rate
R_{Rad}	$\mathrm{cm^{-3}s^{-1}}$	radiative recombination rate
R_{SRH}	$\mathrm{cm^{-3}s^{-1}}$	SRH recombination rate
R_{surf}	$\mathrm{cm^{-2}s^{-1}}$	surface recombination rate
$\mathcal{S}$	$\mathrm{eVK^{-1}}$	entropy
S_{eff}	cm/s	effective surface recombination velocity
$S_{\mathrm{eff,deg}}$	cm/s	contribution of the SDR to the effective surface recombination velocity
$S_{\mathrm{eff,surf}}$	cm/s	contribution of the surface to the effective surface recombination velocity
σ_{DP}	eV	width of the Gaussian function in the DPM
σ_{n}, σ_{p}	$\mathrm{cm^2}$	CCS for electrons and holes
σ^{c}, σ^{0}	$\mathrm{cm^2}$	CCS of of charged or neutral states
σ_{n}^{+}, σ_{n}^{0}	$\mathrm{cm^2}$	CCS of positively charged or neutral states for electrons
σ_{p}^{-}, σ_{p}^{0}	$\mathrm{cm^2}$	CCS of negatively charged or neutral states for holes
$S_{\mathrm{n}}, S_{\mathrm{p}}$	cm/s	surface recombination velocity parameter
T	°C	temperature
τ, τ_{n}, τ_{p}	s	SRH lifetime parameter (of electrons and holes)
τ_{0}	s	substrate lifetime parameter
τ_{b}	s	charge carrier lifetime in the bulk
τ_{eff}	s	effective charge carrier lifetime
τ_{Aug}	s	Auger lifetime
τ_{surf}, $\tau_{\mathrm{surf,n}}$ $\tau_{\mathrm{surf,p}}$	s	lifetime parameters (for electrons and holes) at the surface of an SDR
τ_{Rad}	s	radiative lifetime
τ_{SRH}	s	SRH lifetime
$u_{\mathrm{n}}^{\mathrm{c}}$, $u_{\mathrm{p}}^{\mathrm{c}}$	$\mathrm{cm^{-3}s^{-1}}$	capture rate of electrons and holes
$u_{\mathrm{n}}^{\mathrm{e}}$, $u_{\mathrm{p}}^{\mathrm{e}}$	$\mathrm{cm^{-3}s^{-1}}$	emission rate of electrons and holes
$u_{\mathrm{SRH}}^{\mathrm{D,c}}$, $u_{\mathrm{SRH}}^{\mathrm{A,c}}$	$\mathrm{cm^{-3}s^{-1}}$	capture rates of donor-and acceptor like states for SRH statistics
$u_{\mathrm{SRH}}^{\mathrm{D,e}}$, $u_{\mathrm{SRH}}^{\mathrm{A,e}}$	$\mathrm{cm^{-3}s^{-1}}$	emission rates of donor-and acceptor like states for SRH statistics

$u_{\mathrm{a}}^{\mathrm{D,c}}$, $u_{\mathrm{a}}^{\mathrm{A,c}}$	$\mathrm{cm}^{-3}\mathrm{s}^{-1}$	capture rates of donor-and acceptor like states for amphoteric statistics
$u_{\mathrm{a}}^{\mathrm{D,e}}$, $u_{\mathrm{a}}^{\mathrm{A,e}}$	$\mathrm{cm}^{-3}\mathrm{s}^{-1}$	emission rates of donor-and acceptor like states for amphoteric statistics
V_{mpp}	mV	maximum power point voltage
V_{oc}	mV	open circuit voltage
v_{th}, $v_{\mathrm{th,n}}$, $v_{\mathrm{th,p}}$	cm/s	thermal velocity (of electrons and holes)
z_{deg}	µm	extension of the SDR
z_{SCR}	µm	extension of the SCR

Table A.3: Symbols. The units are given as used in this work.

List of Figures

List of Tables

Acknowledgments

First of all, I would like to thank Dr. P. P. Altermatt (Leibniz University, Hanover) for his encouraging and dedicated support, for his confidence, for the inspiring research environment, and for the pleasant atmosphere in his working group. I learnt so much from him during the past three years.

I thank Prof. Dr. R. Brendel (Leibniz University, Hanover; ISFH) for providing me the opportunity to work at the Institute for Solar Energy Research Hamelin (ISFH) and in the department for Solar Energy Research at the Leibniz University of Hanover, and for the possibility to conduct my PhD studies under his supervision.

I further thank my co-referee PD Dr. C. Tegenkamp (Leibniz University, Hanover), and the chairman of the examination committee Prof. Dr. D. Ristau (Leibniz University, Hanover).

I am grateful to all who contributed to this work by providing essential measured data and with whom I held fruitful discussions. In particular, I would like to thank Prof. Dr. A. Cuevas (Australian National University, Canberra), and Dr. M. J. Kerr (Transform Solar Pty Ltd.) for providing their τ_{eff}-measurements of SiN_x passivated samples and for interesting conversations. I also thank PD Dr. M. Seibt and A. Urban (both Georg-August-University, Göttingen) for providing HRTEM images of SiN_x passivated silicon substrates. I am grateful to B. Veith, D. Zielke, M. Kessler, L. Vorspel, and Prof. Dr. J. Schmidt (all ISFH) for preparing and providing the Al_2O_3 passivated wafers, for performing the τ_{eff} measurements of these samples, and for inspiring discussions.

I acknowledge the experimental cooperation with Dr. S. W. Glunz (Fraunhofer ISE, Freiburg) who provided the PERL solar cells, PD Dr. H. S. Leipner (Martin-Luther-University of Halle-Wittenberg) for performing the variable load scratching of these cells, and Dr. O. Breitenstein (Max Planck Institute of Microstructure Physics, Halle) for performing the cleavage and laser-scribing experiments. I further thank Prof. Dr. A. Schenk (Swiss Federal Institute of Technology (ETH), Zurich) for helpful hints and discussions regarding the DAP model.

For providing detailed measurements of their fabricated screen-printed solar cells, I would like to show my gratitude to S. Gatz, H. Hannebauer and Dr. T. Dullweber (all ISFH).

I appreciate the never-ending work of the reading committee, my supervisor Dr. P. P. Altermatt (Leibniz University, Hanover), my colleague S. Eidelloth (ISFH), my brother I. Dreißigacker (Leibniz University, Hanover), and my dear husband D. S. Steingrube (Leibniz University, Hanover).

Last but not least, my thanks go to my parents and all other members of my family for their support and care.

Curriculum Vitae

Name: Silke Steingrube
Maiden name: Silke Dreißigacker
E-mail: steingrube@solar.uni-hannover.de
Date of birth: 08/08/1982, Hanover, Germany
Family status: married

Education

10/2002 - 09/2007	**Georg-August-University Göttingen** Studies of physics 09/2007: Diplom in physics, graduation: with excellence 10/2004: Vordiplom in physics, graduation: very good	**Göttingen, Germany**
09/2005 - 02/2006	**University of Helsinki** Studies of physics and research projects (ERASMUS term)	**Helsinki, Finland**
1995 - 2002	**Käthe-Kollwitz-Gymnasium** A-levels Graduation (grade 1.3)	**Hanover, Germany**
1993-1995	**Gottfried-Keller-Schule** Secondary school	**Hanover, Germany**
1989-1993	**Brüder-Grimm-Schule** Primary school	**Hanover, Germany**

Awards and honors

09/2007	**Georg-August-University Göttingen** **Faculty of Physics** Dr. Berliner - Dr. Ungewitter - Award for excellent graduation Award for excellent examination performance and excellent diploma thesis	**Göttingen, Germany**
09/2005 - 09/2007	**Fellowship of the** **German National Academic Foundation** **(Studienstiftung des Deutschen Volkes)** Scholarship of the German National Academic Foundation (Acceptance after excellent merits during the pre-diploma)	**Göttingen, Germany**
06/2002	**Certificate of approval for extraordinary dedication** Approval for extraordinary dedication to the energy- and climate protection project of the Käthe-Kollwitz-Gymnasium.	**Hanover, Germany**
06/2002	**Honorship for outstanding examination in physics** Book-Price of the DPG (German Physics Society) Free membership in the DPG (German Physics Society)	**Hanover, Germany**

Publications

Scientific Publications

(1) K. O. E. Henriksson, K. Vörtler, S. Dreißigacker, K. Nordlund and J. Keinonen
Sticking of atomic hydrogen on the tungsten (0 0 1) surface
Surface Science **600**, 3167 (2006)

(2) R. Brendel, S. Dreissigacker, N.-P. Harder and P. P. Altermatt
Theory of analyzing free energy losses in solar cells
Applied Physics Letters **93**, 173503 (2008)

(3) S. Steingrube, M. Timme, F. Wörgötter and P. Manoonpong
Self-organized adaptation of a simple neural circuit enables complex robot behaviour
Nature Physics **6**, 224 (2010)

(4) S. Steingrube, D. S. Steingrube, R. Brendel and P. P. Altermatt
Comprehensive model for recombination at a-Si:H/c-Si interfaces based on amphoteric defects
Physica Status Solidi C **7**, 276 (2010)
see also entry (12) in *Contributions at international conferences*

(5) S. Steingrube, P. P. Altermatt, J. Schmidt and R. Brendel
Modelling c-Si/SiN$_x$ interface recombination by surface damage
Physica Status Solidi – Rapid Research Letters **4**, 91 (2010)

(6) S. Steingrube, P. P. Altermatt, D. S. Steingrube, J. Schmidt and R. Brendel
Interpretation of recombination at c-Si/SiN$_x$ interfaces by surface damage
Journal of Applied Physics **108**, 014506 (2010)

(7) S. Steingrube, O. Breitenstein, K. Ramspeck, S. Glunz, A. Schenk, and P. P. Altermatt
Explanation of commonly observed shunt currents in c-Si solar cells by means of recombination statistics beyond the Shockley-Read-Hall approximation
Journal of Applied Physics **110** (2011), in press

(8) S. Steingrube, R. Brendel and P. P. Altermatt
Limits to Shockley-Read-Hall (SRH) statistics for quantifying recombination via amphoteric defects
submitted to Physica Status Solidi A (2011)

(9) S. Gatz, T. Dullweber, S. Steingrube, V. Mertens, F. Einsele and R. Brendel
Firing stability of a-SiN$_y$:H/SiN$_x$ surface passivation stacks for crystalline silicon solar cells
in preparation (2011)

(10) S. Steingrube, F. Wörgötter, D. S. Steingrube, P. Manoonpong and M. Timme
Adaptive Neuronal Chaos Control and Applications in Robotics
in preparation (2011)

Contributions at International Conferences

(11) U. Köster, A. Hyvarinen and S. Dreissigacker
Visual: *Estimation of two-layer statistical model of natural images using score matching leads to complex cell properties*
Computational and Systems Neuroscience, Salt Lake City, Utah (2007)

(12) S. Steingrube, D. S. Steingrube, R. Brendel and P. P. Altermatt
Oral: *Comprehensive model for recombination at a-Si:H/c-Si interfaces based on amphoteric defects*
12th International Conference on the Formation of Semiconductor Interfaces, Weimar, Germany (2009)
see also entry (4) in *Scientific Publications*

(13) P. P. Altermatt, S. Dreissigacker, Y. Yang, C. Sprodowski, T. Dezhdar, S. Koc, B. Veith, S. Hermann, R. Bock, K. Bothe, J. Schmidt and R. Brendel
Oral: *Highly predictive modelling of entire Si solar cells for industrial applications*
24th European Photovoltaic Solar Energy Conference, Hamburg, Germany (2009)

(14) S. Steingrube, P. P. Altermatt, D. Zielke, F. Werner, J. Schmidt and R. Brendel
Visual: *Reduced passivation of silicon surfaces at low injection densities caused by H-induced defects*
25th European Photovoltaic Solar Energy Conference, Valencia, Spain (2010)

(15) S. Eidelloth, U. Eitner, S. Steingrube and R. Brendel
Visual: *Open source graphical user interface in MATLAB for two-dimensional simulations solving the fully coupled semiconductor equations using COMSOL*
25th European Photovoltaic Solar Energy Conference, Valencia, Spain (2010)

(16) S. Steingrube, H. Wagner, H. Hannebauer, S. Gatz, R. Chen, T. Dullweber, S. T. Dunham, P. P. Altermatt and R. Brendel
Oral: *Loss analysis and improvements of industrially fabricated Cz-Si solar cells by means of process and device simulations*,
1st Silicon PV, Freiburg, Germany (2011), accepted for publication in Energy Procedia

(17) T. Ohrdes, S. Steingrube, H. Wagner, C. Zechner, G. Letay, R. Chen, S. T. Dunham and P. P. Altermatt

Visual: *Solar cell emitter design with PV-tailored implantation*,
1st Silicon PV, Freiburg, Germany (2011), accepted for publication in Energy Procedia

(18) J. Schmidt, F. Werner, B. Veith, D. Zielke, S. Steingrube, P. P. Altermatt, S. Gatz, T. Dullweber, R. Brendel
Oral: *Advances in the surface passivation of silicon solar cells*,
International Conference on Materials for Advanced Technologies 2011, Symposium O, submitted to Energy Procedia